



Leibniz
Universität
Hannover

Gottfried Wilhelm Leibniz Universität Hannover

Fakultät für Mathematik und Physik

Development of semiconductor light sources for photonic-enabled quantum communication

genehmigte

Dissertation zur Erlangung des
akademischen Grades

Doktor der Naturwissenschaften

(Dr. rer. nat.)

vorgelegt von

M. Sc. Jingzhong Yang

geboren am 27. September 1991 in Liaoning, China

2023

Referent:

Prof. Dr. Fei Ding (Leibniz Universität Hannover, Germany)

Korreferent:

Prof. Dr. Oliver G. Schmidt (Technische Universität Chemnitz)

Tag der Promotion: 22. Sep 2022

Prediction is very difficult, especially about the future

Niels Bohr (1885-1962)

This page intentionally left blank.

Bibliographic record

Jingzhong Yang

Development of semiconductor light sources for photonic-enabled quantum communication

Fakultät für Mathematik und Physik der Gottfried Wilhelm Leibniz Universität Hannover

Dissertation, 2022

181 Seiten

77 Abbildungen

5 Tabellen

316 Literaturzitate

Keywords: quantum communication, non-classical light sources, quantum dots, entanglement swapping, optical antenna, photoneutralization

This page intentionally left blank.

Erklärung kumulative Dissertation

aus:

Die Naturwissenschaftliche Fakultät, die Fakultät für Mathematik und Physik, die Fakultät für Elektrotechnik und Informatik, die QUEST-Leibniz-Forschungsschule sowie die Leibniz-Forschungsschule für Optik und Photonik (LSO) der Gottfried Wilhelm Leibniz Universität Hannover haben die Änderung der nachstehende Gemeinsame Ordnung für die Promotion zur Doktorin der Naturwissenschaften oder zum Doktor der Naturwissenschaften (Dr. rer. nat.) an der Gottfried Wilhelm Leibniz Universität Hannover beschlossen. (19.04.2022).

§ 8 Dissertation (3)

... ³Es ist eine ausführliche Darstellung voranzustellen, die eine kritische Einordnung der Forschungsthemen und wichtigsten Erkenntnisse aus den Publikationen in den Kontext der wissenschaftlichen Literatur zum Thema vornimmt sowie die individuellen eigenen Beiträge und ggf. die Beiträge weiterer Autoren an den jeweiligen Publikationen darlegt.

Publication 1 (Chapter 3)

Michael Zopf, Robert Keil, Yan Chen, Jingzhong Yang, Disheng Chen, Fei Ding, and Oliver G. Schmidt

Entanglement Swapping with Semiconductor-Generated Photons Violates Bells Inequality. *Phys. Rev. Lett.* 123, 160502 (2019)

O. G. Schmidt and F. Ding conceived and supervised the project. J. Yang and M. Zopf designed and implemented the optical setup and performed first measurements. R. Keil carried out the growth of the GaAs QD. Y. Chen fabricated the high-brightness dielectric antenna device. D. Chen contributed to the analysis and the interpretation of the results. M. Zopf performed the data collection/analysis and wrote the manuscript with the help from F. Ding, O. G. Schmidt, J. Yang and the other co-authors.

Hartmut Michael Zopf

Semiconductor-generated entangled photons for hybrid quantum networks. PhD Dissertation (2020)

Publication 2 (Chapter 4)

Jingzhong Yang, Michael Zopf, Pengji Li, Nand Lal Sharma, Weijie Nie, Frederik Benthin, Tom Fandrich, Eddy P. Rugeramigabo, Caspar Hopfmann, Robert Keil, Oliver G. Schmidt, and Fei Ding

Statistical limits for entanglement swapping with semiconductor entangled photon sources. *Phys. Rev. B* 105, 235305 (2022)

F. Ding and O. G. Schmidt conceived and supervised the project. J. Yang designed and implemented the optical setup and performed initial measurements. J. Yang, P. Li and F. Benthin performed the optical experiments and collected the data. N. L. Sharma and R. Keil executed the GaAs QD sample growth. W. Nie carried out the fabrication of the high-brightness dielectric antenna device. C. Hopfmann contributed to the analysis and interpretation of the results. J. Yang and T. Fandrich carried out the data analysis. J. Yang and M. Zopf wrote the manuscript with the help from E. P. Rugeramigabo, C. Hopfmann, O. G. Schmidt, F. Ding and the other co-authors.

Publication 3 (Chapter 5)

Jingzhong Yang, Cornelius Nawrath, Robert Keil, Raphael Joos, Xi Zhang, Bianca Höfer, Yan Chen, Michael Zopf, Michael Jetter, Simone Luca Portalupi, Fei Ding, Peter Michler, and Oliver G. Schmidt

Quantum dot-based broadband optical antenna for efficient extraction of single photons in the

telecom O-band. *Opt. Express* 28, 13, 19457-19468 (2020)

F. Ding, P. Michler and O. G. Schmidt conceived and supervised the project. J. Yang and Y. Chen designed and fabricated the dielectric antenna device. J. Yang, R. Keil and B. Höfer carried out the photoluminescence characterization. J. Yang and X. Zhang performed the simulation. C. Nawrath and R. Joos performed the single photon characterization. M. Jetter implemented the growth of the as-grown sample. S. L. Portalupi and M. Zopf contributed to the analysis and interpretation of the results. J. Yang and C. Nawrath wrote the manuscript with the help from S. L. Portalupi, M. Zopf, F. Ding, P. Michler, and O. G. Schmidt, and the other co-authors.

Publication 4 (Chapter 6)

Jingzhong Yang, Tom Fandrich, Frederik Benthin, Robert Keil, Nand Lal Sharma, Weijie Nie, Caspar Hopfmann, Oliver G. Schmidt, Michael Zopf, and Fei Ding
Photonneutralization of charges in GaAs quantum dot based entangled photon emitters. *Phys. Rev. B* 105, 115301 (2022)

F. Ding, M. Zopf and O. G. Schmidt conceived and supervised the project. J. Yang, T. Fandrich and F. Benthin performed the experiment and data collection. J. Yang and T. Fandrich executed the data analysis. N. L. Sharma and R. Keil grew the GaAs QD sample. W. Nie fabricated the high-brightness dielectric antenna device. J. Yang wrote the manuscript with the help from M. Zopf, C. Hopfmann, O. G. Schmidt, F. Ding, and the other co-authors.

Publication 5 (Chapter 6)

Xin Cao, Jingzhong Yang, Pengji Li, Yiteng Zhang, Eddy P. Rugeramigabo, Benedikt Brechtken, Rolf J. Haug, Michael Zopf, and Fei Ding
Single photon emission from ODT passivated near-surface GaAs quantum dots. *Appl. Phys. Lett* 118, 221107 (2021)

F. Ding conceived the project. X. Cao, Y. Zhang and E. P. Rugeramigabo carried out the near-surface QDs sample growth. X. Cao and P. Li performed and optimised the passivation process. X. Cao and J. Yang implemented the optical characterization, data collection/analysis. B. Brechtken and R. J. Haug implemented AFM measurements and contributed to the data interpretation. X. Cao wrote the manuscript with input from M. Zopf, F. Ding, and the other co-authors.

Xin Cao

Growth and characterization of epitaxial quantum dots: from visible to telecom wavelength range. PhD Dissertation (2022)

Author's detail

Authors	Affiliation
Mr. Jingzhong Yang Prof. Dr. Fei Ding Dr. Michael Zopf Dr. Eddy Patrick Rugermigabo Dr. Xin Cao Mr. Pengji Li Mr. Frederik Benthin Mr. Tom Fandrich	Leibniz University of Hannover
Prof. Dr. Oliver. G. Schmidt Dr. Robert Keil Ms. Bianca Höfer Dr. Xi Zhang Dr. Yan Chen Dr. Disheng Chen Dr. Caspar Hopfmann Dr. Nand Lal Sharma Dr. Weijie Nie	Chemnitz University of Technology Leibniz Institute for Solid State and Materials Research in Dresden
Prof. Dr. Peter Michler Dr. Simone Luca Portalupi Dr. Michael Jetter Mr. Cornelius Nawrath Mr. Raphael Joos	University of Stuttgart

Abstract

Quantum information technologies have attracted tremendous attentions and development efforts by worldwide research organizations and governments in the past decades. It comprises the generation, manipulation, and transfer of quantum bits ‘qubits’ based on the laws of quantum mechanics, enabling the applications of quantum metrology, quantum computation, quantum communication, etc. As one of the frontier quantum technologies, quantum communication features unconditionally secure data transfer between parties over long distance in theory, which can be accomplished through quantum state of light photons, due to their weak interaction with the environment and their remaining coherence over long distance. Meanwhile, quantum repeaters, similar as amplifier in classical communication are believed to be indispensable components to address the photon absorption and decoherence in noisy quantum channels, which scales exponentially with the distance. Quantum repeaters generally consist of three basic elements, namely entanglement swapping, entanglement purification, and quantum memories. In spite of significant breakthroughs achieved with a variety of optical protocols theoretically and experimentally, lack of near-perfect deterministic light sources with fast repetition rates, high degree of single photon purity, indistinguishability, and entanglement still impedes the practical applications.

Semiconductor quantum dots are one of the leading system that have exhibited their potential for on-demand generation of high-quality single and entangled photon pairs for above applications. In this work, epitaxially grown III-V semiconductor quantum dots are investigated for driving their application in future quantum networks. First, an individual quantum dot emitting two pairs of entangled photons under pulsed two-photon resonant excitation has been utilized for realization of entanglement swapping, with the swapped photon pairs yielding a fidelity of 0.81 ± 0.04 to the Bell state Ψ^+ . To explore the practical limits of future quantum networks featuring multiple semiconductor based sources, we scrutinize the consequences of device fabrication, dynamic tuning techniques, time evolution of entanglement, and statistical effects on two separated quantum dot devices adapted in an entanglement swapping scheme. A numerical model based on the observed experimental data is proposed, serving not only as a benchmark for scalability of quantum dot devices, but also laying a roadmap for optimization of solid-state quantum emitters in quantum networks.

For real-world quantum applications envisioned with quantum dots, the brightness of the quantum light sources is one of the key enabling factors, which is determined by the source excitation and extraction efficiency, as well as system detection system efficiency. Usually, the

primary issue restricting the extraction of photons from III-V semiconductor quantum dots is the high-refractive index material of the host matrix which causes at the semiconductor-vacuum interface. To improve the photon extraction efficiency, a simple and efficient structure based on the principle of optical antennas is developed, resulting in an observed extraction of 17% of single photons in the telecom O-band, and a broadband enhancement of up to 180 times compared to the as-grown sample.

A further limiting factor in the source efficiency is caused by the presence of charges in the solid-state environment. Charge fluctuation occur that quench radiative emission processes in resonant excitation schemes and induce fluorescence intermittence (blinking) that deteriorates the quantum yield. The photo-neutralization of GaAs/AlGaAs quantum dots excited by two-photon resonant pumping is investigated. Applying weak gate laser light to the quantum dot allows for controlling the charges capture processes. By adjusting the gate laser power and wavelength, an increase in excitation efficiency of 30% is observed compared to the two-photon resonant excitation without optical gating. The transition rates between the neutral and charged ground state are investigated by means of auto-/cross- correlation measurements. Furthermore, by studying a series of surface-passivated samples with different dot-to-surface distance as close to 20 nm, octadecanethiol (ODT) was found to be an effective compound to neutralize the surface states, leading to reduced formation of non-radiative transition channels. It is anticipated that such a passivation method paves the way of near-field coupling related nano-photonic devices, or elimination of surface states for well-preserved emission properties towards the development of uncapped structure, fundamentally getting rid of total internal reflection to the maximum extent.

Contents

Bibliographic record	v
Erklärung kumulative Dissertation	vii
Abstract	xi
Abbreviations and Constants	xvii
1 Introduction	1
1.1 Quantum information science	1
1.1.1 Photon states and representation	2
1.1.2 Quantum communication	8
1.1.3 Entanglement swapping	11
1.1.4 Entanglement purification	13
1.1.5 Quantum memories	14
1.1.6 Quantum repeaters	15
1.2 Quantum light sources	17
1.2.1 Single photon emitters	18
1.2.2 Entangled photon emitters	20
1.3 Semiconductor quantum dots	21
1.3.1 Electronic states	23
1.3.2 Generation of entangled photons	24
1.3.3 Optical gate effect on charge states	27
1.4 Overview of this thesis	29
2 Background and fundamental methods	31
2.1 Sample growth and fabrication	31
2.1.1 Epitaxial quantum dots	31

2.1.2	Strain-tunable quantum dots based devices	32
2.2	Optical excitation setup	35
2.3	Optical characterization for quantum dots emission	37
2.3.1	Micro-photoluminescence spectroscopy	38
2.3.2	Coherence time measurement	40
2.3.3	Coincidence measurement	43
2.3.4	Radiative lifetime measurement	44
2.3.5	Second-order intensity autocorrelation	46
2.3.6	Quantum tomography	50
2.3.7	Photon indistinguishability	54
2.4	Calibration of optical components	59
2.4.1	Extinction ratio of notch filters	59
2.4.2	Retardance of waveplates	60
2.4.3	Mueller matrix measurement	61
2.4.4	Decomposition of Mueller matrix	65
2.5	Quantum states transformation	68
2.5.1	Jones Matrix of mirrors	68
2.5.2	Quantum mechanics at BS and PBS	69
2.5.3	Phase retarders and Hadamard gate	71
2.5.4	Mach-Zehnder interferometer	72
2.5.5	Hong-Ou-Mandel interferometer	73
2.5.6	Entanglement teleportation with BS	78
2.5.7	Entanglement swapping with BS or PBS	80
3	Entanglement swapping with single quantum dot	83
3.1	Overview of the experimental setup	84
3.2	Sample information	85
3.3	Entanglement swapping with a single quantum dot	87
3.4	Influence of indistinguishability on entanglement swapping fidelity	88
3.5	Conclusion	90
4	Statistical limits for entanglement swapping with independent quantum dots	93
4.1	Spectral overlap between devices	95
4.2	Repeater-relevant device characteristics	96

4.3	Necessity of fine structure tuning	98
4.4	Prediction for a real-world quantum network	101
5	High-brightness telecom O-band optical antenna	107
5.1	Device fabrication	108
5.2	Simulation method for the antenna structure	110
5.3	Brightness enhancement	111
5.4	Evaluation of the single-photon purity	113
5.5	Evaluation of extraction efficiency	115
6	Neutralization of charge states for GaAs quantum dots	119
6.1	Dynamics of blinking in GaAs quantum dots	121
6.2	Photoluminescence characterization of blinking	122
6.2.1	Photoluminescence excitation spectroscopy	123
6.2.2	Influence of gate-laser on photoluminescence intensity	124
6.3	Second-order intensity correlation characterization	125
6.3.1	Auto-correlation of neutral exciton	126
6.3.2	Cross-correlation between neutral and charged exciton	127
6.4	Influence of photoneutralization on entangled states	128
6.5	ODT passivation for near-surface quantum dots	130
7	Conclusions and Outlook	135
7.1	Conclusions	135
7.1.1	Entanglement swapping with a single semiconductor QDs	135
7.1.2	Predicating the outcome of swapping with two QDs devices	136
7.1.3	Extraction of photons at telecom waveband	136
7.1.4	Efficient excitation of the source	136
7.2	Outlook	137
7.2.1	Optimization of the device performance	137
7.2.2	On-chip integrated photonic circuits	137
7.2.3	Quantum communication in real-world	137
	Appendix	139
	Bibliography	147

Contents

Publications and Presentations	175
Acknowledgements	177
Selbstständigkeitserklärung	179
Curriculum Vitae	181

Abbreviations and Constants

Abbreviations

BS	beam splitter
BSM	Bell state measurement
CCD	charge-coupled device
DOS	density of states
EPR	Einstein, Podolsky, and Rosen
FSS	fine structure splitting
HBT	Hanbury Brown and Twiss
HF	hydrofluoric
HOM	Hong-Ou-Mandel
HWP	half-wave plate
MBE	Molecular beam epitaxy
MZI	Mach-Zehnder interferometer
IRF	instrument response function
ODT	octadecanethiol
PBS	polarizing beam splitter
PCM	passive-choice-measurement
PL	photoluminescence
PLE	photoluminescence excitation
PMMA	polymethyl methacrylate
QD	quantum dot
QKD	quantum key distribution
QM	quantum memory
QWP	quarter-wave plate

SNSPD	superconducting nanowire single photon detector
SPD	single photon detector
SPDC	spontaneous parametric down conversion
TCSPC	time-correlated single photon counting
TIP	total internal reflection
TPE	two photon excitation
TPI	two-photon interference
X	neutral exciton
XX	neutral biexciton
ZPL	zero-phonon line

Constants

c	speed of light
\hbar	reduced Planck constant
ε_0	vacuum electric permittivity
k	Wave vector
k_B	Boltzmann constant
ϵ_0	Vacuum permittivity

Introduction

In the past decades, quantum information science has attracted intensive research interests from the research institutes and governments. It is usually classified into three main subbranches, e.g., quantum cryptography, quantum computing and quantum teleportation, which are related with transmission or manipulation of data based on the properties of quantum mechanics. This chapter starts from an overview of the main quantum information applications, in particular quantum communication, as one of the promising topic to be discussed with the emerging issues and solutions ('quantum repeaters'). The physics of semiconductor quantum dots are reviewed as single- and entangled- photon sources, rendering it to be one of the promising candidates in photonic quantum communication schemes.

1.1 Quantum information science

'Photon', the term introduced by Lewis in 1926 [1] for revealing both wave-like and particle-like properties of light ('wave-particle duality'), is the consequence of a long term argument about the nature of light among plenty of talent scientists over several centuries. Quantum optics was therefore established based on consecutive experimental demonstrations, i.e., Young-type experiment by Taylor (1909) [2], single photon interference by Grangier, Roger, and Aspect (1986) [3], photon-counting/correlation experiment by Hanbury Brown and Twiss (1956) [4], 'Bell experiment' by Freedman and Clauser (1972) [5, 6, 7, 8] for testing Einstein, Podolsky, and Rosen (EPR) paradox [9], etc. By convention, the development of science always promotes practical applications. Quantum information processing (QIP) was started after the experimental studies of entanglement of quantum states on the basis of atomic science, utilizing superposition principle and non-classical correlations of quantum mechanics for qubits transferring and processing in computation and communication.

It is well-known that the conventional computers are constructed based on silicon microprocessing technology, in which the number of operation increase as polynomial power

of the number of transistors. According to Moore's law [10], it becomes more and more difficult to produce chips with exponential growth of the number of transistors, taking into account of the cost of fabrication plans. The revolutionary idea of running computer with the law of quantum mechanics was firstly proposed by Richard Feynman in 1982 [11], targeting to efficiently solve sophisticated problems with qubits, quantum logic gates, and circuits. Benefiting from its advantage that the computation power increase exponentially with the number of qubits, quantum computer can be adapted in many applications with corresponding algorithms, i.e., determine balance of unknown function (Deutsch algorithm) [12], database searching (Grover's algorithm) [13], factorize large numbers (Shor's algorithm) [14], simulation of quantum system [11], etc.

The concept of quantum communication was developed in the 1980s [15] and firstly demonstrated by cryptography experiment in 1992 [16], which provide a confidential way of transmitting private key via quantum channels over long distances based on the established telecommunication infrastructures. The communication parties get rid of the risk of undetectable eavesdropper from the third party due to quantum no-cloning theorem. Moreover, quantum teleportation proposed by Bennett in 1993 [17] enables the transmission of an unknown state from one partner to the other with the aid of entangled states as the media. Then the first test in experiment was demonstrated in 1997 [18] with polarization-entangled photons generated by a spontaneous parametric down conversion (SPDC) source [19].

1.1.1 Photon states and representation

Benefitting from the nature of high resistance to decoherence from the environment and fastest 'flying' qubits, photons are considered as the best quantum information carriers for transferring and manipulation in the applications of global quantum communication [20, 21] and linear photonic quantum computing [22, 23, 24]. A pure qubit is usually written as the superposition state of two orthogonal base vectors $|0\rangle$ and $|1\rangle$ in Hilbert space [25]. Here we would like to encode the logic qubits using the horizontal $|H\rangle$ and vertical $|V\rangle$ polarization of single-photons,

$$|0\rangle \equiv |H\rangle, \quad |1\rangle \equiv |V\rangle \quad (1.1.1)$$

Therefore, the superposition state of a single photon is presented as,

$$|\psi\rangle = \alpha |H\rangle + \beta |V\rangle \quad (1.1.2)$$

where the normalization condition on $|\psi\rangle$ requires that,

$$\alpha^2 + \beta^2 = 1 \quad (1.1.3)$$

It is convenient to present the state of polarization via a spherical coordinate system as shown in Fig. 1.1(a), where linear polarization of light is located in the equatorial plane with states of $|H\rangle$, $|D\rangle$, $|V\rangle$, $|A\rangle$ at the end points of two orthogonal diameters. Two circularly polarized light $|R\rangle$ and $|L\rangle$ are at two poles of the sphere. The end of vector must be inside or on surface of sphere, representing degree of polarization.

$$\begin{aligned} |D\rangle &= \frac{1}{\sqrt{2}}(|H\rangle + |V\rangle) \\ |A\rangle &= \frac{1}{\sqrt{2}}(|H\rangle - |V\rangle) \\ |R\rangle &= \frac{1}{\sqrt{2}}(|H\rangle - i|V\rangle) \\ |L\rangle &= \frac{1}{\sqrt{2}}(|H\rangle + i|V\rangle) \end{aligned} \quad (1.1.4)$$

Apart from the form of superposition of base vectors, the polarization states can also be represented by Jones matrices in the following,

$$|H\rangle = \begin{pmatrix} 1 \\ 0 \end{pmatrix}, \quad |V\rangle = \begin{pmatrix} 0 \\ 1 \end{pmatrix} \quad (1.1.5)$$

or in form of density matrix notions,

$$\rho_H = \begin{pmatrix} 1 & 0 \\ 0 & 0 \end{pmatrix}, \quad \rho_V = \begin{pmatrix} 0 & 0 \\ 0 & 1 \end{pmatrix} \quad (1.1.6)$$

The density matrix of an arbitrary mixed state $|\psi\rangle$ can be represented as,

$$\rho_{|\psi\rangle} = \sum_i P_i |\psi_i\rangle \langle\psi_i| = \begin{pmatrix} A & Be^{i\phi} \\ Be^{-i\phi} & 1 - A \end{pmatrix} \quad (1.1.7)$$

where P_i is the probabilistic weighting, A and B are real and positive with the relation $0 \leq A \leq 1$, $B \leq \sqrt{A(1-A)}$. The density matrix $\rho_{|\psi\rangle}$ can also be represented with three stokes parameters $\{S_1, S_2, S_3\}$ [26],

$$\rho_{|\psi\rangle} = \frac{1}{2} \sum_{i=0}^3 S_i \vec{\sigma}_i \quad (1.1.8)$$

with σ_i matrices,

$$\sigma_0 \equiv \begin{pmatrix} 1 & 0 \\ 0 & 1 \end{pmatrix}, \quad \sigma_1 \equiv \begin{pmatrix} 0 & 1 \\ 1 & 0 \end{pmatrix}, \quad \sigma_2 \equiv \begin{pmatrix} 0 & -i \\ i & 0 \end{pmatrix}, \quad \sigma_3 \equiv \begin{pmatrix} 1 & 0 \\ 0 & -1 \end{pmatrix} \quad (1.1.9)$$

The components of $\{S_1, S_2, S_3\}$ give the degree of polarization in $|D\rangle$ and $|A\rangle$, $|R\rangle$ and $|L\rangle$ bases, $|H\rangle$ and $|V\rangle$, and S_0 always equals to one for normalization. Each of the parameters

corresponds to the probability contrast of a series of orthogonal polarization projection measurements:

$$\begin{aligned}
 S_0 &= P_{|H\rangle} + P_{|V\rangle} \\
 S_1 &= P_{|D\rangle} - P_{|A\rangle} \\
 S_2 &= P_{|R\rangle} - P_{|L\rangle} \\
 S_3 &= P_{|H\rangle} - P_{|V\rangle}
 \end{aligned} \tag{1.1.10}$$

where $P_{|\psi\rangle}$ is the probability of projection measurement on $|\psi\rangle$ state. For pure states, $\sum_{i=1}^3 S_i^2 = 1$; for mixed states, $0 \leq \sum_{i=1}^3 S_i^2 < 1$.

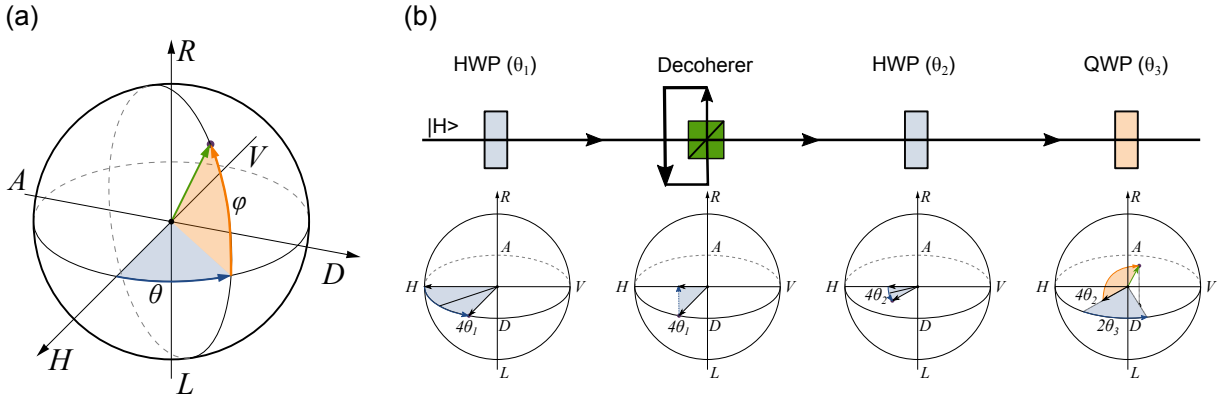


Figure 1.1: (a) Poincaré sphere representation of an arbitrary single photon state, located at the surface of the sphere with a certain azimuthal angle θ and elliptical angle φ . $|H\rangle$, $|D\rangle$, $|V\rangle$, $|A\rangle$, $|R\rangle$ and $|L\rangle$ represent horizontal, vertical, diagonal, anti-diagonal, right-circular and left circular polarization. (b) Exemplary manipulation of a single photon state by a series of linear optics started from $|H\rangle$ polarization (top), and corresponding processing of state represented by poincaré sphere (bottom). After passing through a half-wave plate (HWP) with an angle of θ_1 between fast axis and horizontal polarization, the initial state in poincaré sphere is flipped by 180° clockwise around the axis at an angle of $2\theta_1$. A decoherer, made of a polarizing beam splitter (PBS) splitting $|H\rangle$ and $|V\rangle$ components of light with a path difference longer than coherence length of photons, will degrade the degree of polarization. A HWP with an angle of θ_2 then flips the remaining $|H\rangle$ -polarized light by 180° . Finally, when the light pass through a quarter-wave plate (QWP) with a fast-axis angle of θ_3 relative to current polarization, the state of light is flipped by 90° clockwise around the axis $2\theta_3$ away from current state.

Fig. 1.1(b) shows an exemplary generation of arbitrary polarization states based on $|H\rangle$ polarized light, via a HWP, a decoherer (e.g., thick birefringent optics), a HWP and a QWP. The operation action on the density matrix of the states can be represented by Jones matrix,

$$\begin{aligned}
 U_{HWP}(\theta) &= e^{-\frac{i\pi}{2}} \begin{pmatrix} \cos 2\theta & \sin 2\theta \\ \sin 2\theta & -\cos 2\theta \end{pmatrix} \\
 U_{QWP}(\theta) &= e^{-\frac{i\pi}{4}} \begin{pmatrix} \cos^2 \theta + i \sin^2 \theta & (1-i) \sin \theta \cos \theta \\ (1-i) \sin \theta \cos \theta & \sin^2 \theta + i \cos^2 \theta \end{pmatrix}
 \end{aligned} \tag{1.1.11}$$

with θ the fast axis angle of the wave plates. The state of light after the first HWP becomes,

$$\rho = U_{HWP}(\theta_1)\rho_H U_{HWP}^T(\theta_1) = \begin{pmatrix} \cos^2\theta_1 & \sin\theta_1 \cos\theta_1 \\ \sin\theta_1 \cos\theta_1 & \sin^2\theta_1 \end{pmatrix} \quad (1.1.12)$$

After the decoherer, the degree of polarization will be degraded, resulting in the elimination of anti-diagonal elements,

$$\rho = \begin{pmatrix} \cos^2\theta_1 & 0 \\ 0 & \sin^2\theta_1 \end{pmatrix} = \cos^2\theta_1 |H\rangle\langle H| + \sin^2\theta_1 \cdot \sigma_0 \quad (1.1.13)$$

Therefore the amount of decoherence can be tuned by the rotation angle θ_1 of the first HWP. In the next, the state can be deterministically rotated to a position in the poincaré sphere by a HWP and QWP combination. There are usually two ways for evaluating whether a state is pure or mixed. Assuming that the density matrix of a state after diagonalization is,

$$\rho = \begin{matrix} & \langle\psi| & \langle\psi^*| \\ \begin{matrix} |\psi\rangle \\ |\psi^*\rangle \end{matrix} & \begin{pmatrix} E_1 & 0 \\ 0 & E_2 \end{pmatrix} \end{matrix} = E_1 |\psi\rangle\langle\psi| + E_2 |\psi^*\rangle\langle\psi^*| \quad (1.1.14)$$

In case neither eigenvalues E_1 and E_2 are equal to zero, the state is a mixed state. Either E_1 or E_2 is zero indicate a pure state. Moreover, the state can also be classified, according to the idempotence of the density matrix, where $\rho^2 = \rho$ for a pure state, and $\rho^2 \neq \rho$ for a mixed state. For a deterministic target state,

$$\rho_t = (1 - \varepsilon)\rho_s + \frac{\varepsilon}{N}\mathbb{1} \quad (1.1.15)$$

with ε the strength of depolarization, ρ_s the specific pure state, N the number of qubits, and $\mathbb{1}$ the identity matrix, the information of the state can be extracted by a variety of methods. ‘Fidelity’ is one of the measures, representing the degree of overlap between the target state $|\psi_t\rangle$ and a specific pure state $|\psi_s\rangle$, as $F(|\psi_t, \psi_s\rangle) \equiv |\langle\psi_t|\psi_s\rangle|^2$ [27]. The value of fidelity usually can be calculated with density matrix ρ_t, ρ_s as,

$$F(\rho_t, \rho_s) \equiv \left| \text{Tr}(\sqrt{\sqrt{\rho_t}\rho_s\sqrt{\rho_t}}) \right|^2 \quad (1.1.16)$$

or $f(\rho_t, \rho_s) \equiv \sqrt{F(\rho_t, \rho_s)}$

where the fidelity is zero for two orthogonal states and one for two identical states. For the calibration of the depolarization degree of a mixed state, fidelity is sensitive to the square of depolarized term ε when the number of nonzero eigenvalues of the matrix n_{eigen} is equal to N , but linearly varies with ε in case of $n_{eigen} < N$ [28]. Apart from fidelity,

there are other standard benchmarks characterizing a depolarized state,

Concurrence [29] and *Tangle* [29, 30]: Measures defined to evaluate the non-classical feature of quantum states. The concurrence C is,

$$C(\rho_t) \equiv \max \left\{ 0, \sqrt{\lambda_1} - \sqrt{\lambda_2} - \sqrt{\lambda_3} - \sqrt{\lambda_4} \right\} \quad (1.1.17)$$

where λ_i are the eigenvalues of $\rho_t \rho'_t$, with $\rho'_t \equiv (\sigma_2 \otimes \sigma_2) \rho_t^* (\sigma_2 \otimes \sigma_2)$. Tangle $T(\rho_t)$ is simply the square of the concurrence, which is usually sensitive to first order of the perturbation of ε .

Trace distance [31]: A similar measure as fidelity for comparing two states defined as,

$$D(\rho_t, \rho_s) = \frac{1}{2} \text{Tr} |\rho_t - \rho_s| \quad (1.1.18)$$

which is linearly sensitive to the strength of depolarization ε .

Von Neumann entropy [32] and *linear entropy* [33]: The measures can be used to evaluate the degree of mixed states. For von Neumann,

$$S_v(\rho_t) = -\text{Tr}(\rho_t \cdot \ln \rho_t) \quad (1.1.19)$$

and linear entropy,

$$S_L(\rho) \equiv \frac{N}{N-1} \left[1 - \text{Tr}(\rho^2) \right] \quad (1.1.20)$$

both are linearly sensitive to the depolarization, and von Neumann start to vary with $\varepsilon \ln \varepsilon$ when the density matrix ρ_t is not fully rank. Besides, other benchmarks such as entanglement of formation (EOF) [29] and negativity [34] are used for calibrating the degree of entanglement on arbitrary two qubits system.

Entanglement of quantum states depicts the correlation property between quantum systems based on superposition principle, originally comes from the EPR paradox arguing that quantum mechanics is incomplete. It was recognized as a philosophical issue due to the lack of experimental demonstration. Nevertheless, with the remarkable breakthrough proposed by Bell in 1964 ('Bell's inequality') [35], various verification in experiments are achieved [5, 6, 7], e.g., polarization entangled photon pairs from atomic cascade or SPDC, revealing that the correlation between two particles disobey local realistic model [36]. The degree of freedom of entanglement for photons can be multiple forms, i.e., position-momentum [37], time-frequency [38], orbital angular frequency [39], time-bin entanglement [40]. In this thesis, we focus on polarization-based entanglement. For a

2-qubits pure polarization entanglement, there are four common Bell states described as,

$$\begin{aligned} |\Phi^\pm\rangle &= \frac{1}{\sqrt{2}}(|HH\rangle \pm |VV\rangle) \\ |\Psi^\pm\rangle &= \frac{1}{\sqrt{2}}(|HV\rangle \pm |VH\rangle) \end{aligned} \quad (1.1.21)$$

As same as the single photon polarization states, 2-qubits entangled states can be presented likewise with Jones matrices,

$$|\phi^\pm\rangle = \frac{1}{\sqrt{2}} \begin{pmatrix} 1 \\ 0 \\ 0 \\ \pm 1 \end{pmatrix} \otimes \begin{pmatrix} 1 \\ 0 \\ 0 \\ \pm 1 \end{pmatrix} \pm \begin{pmatrix} 0 \\ 1 \\ 1 \\ 0 \end{pmatrix} \otimes \begin{pmatrix} 0 \\ 1 \\ 1 \\ 0 \end{pmatrix} = \frac{1}{\sqrt{2}} \begin{pmatrix} 1 \\ 0 \\ 0 \\ \pm 1 \end{pmatrix} \quad (1.1.22)$$

$$|\psi^\pm\rangle = \frac{1}{\sqrt{2}} \begin{pmatrix} 1 \\ 0 \\ 0 \\ \pm 1 \end{pmatrix} \otimes \begin{pmatrix} 0 \\ 1 \\ 1 \\ 0 \end{pmatrix} \pm \begin{pmatrix} 0 \\ 1 \\ 1 \\ 0 \end{pmatrix} \otimes \begin{pmatrix} 1 \\ 0 \\ 0 \\ \pm 1 \end{pmatrix} = \frac{1}{\sqrt{2}} \begin{pmatrix} 0 \\ 1 \\ \pm 1 \\ 0 \end{pmatrix} \quad (1.1.23)$$

or in the form of 4×4 density matrix constructed by Stokes parameters,

$$\rho = \frac{1}{4} \sum_{i,j=0}^3 S_{i,j} \vec{\sigma}_i \vec{\sigma}_j \quad (1.1.24)$$

Extending the density matrix representation of one and two qubits, any n-qubits state can be represented as,

$$\rho = \frac{1}{2^n} \sum_{i_1, i_2, \dots, i_n=0}^3 \vec{S}_{i_1, i_2, \dots, i_n} \vec{\sigma}_{i_1} \otimes \vec{\sigma}_{i_2} \otimes \dots \otimes \vec{\sigma}_{i_n} \quad (1.1.25)$$

with $S_{0,0,\dots,0} = 1$ for normalization. The dimension of the density matrix is $2^n \times 2^n$. Typical example of multiple photon entanglement is GHZ states [41],

$$\begin{aligned} |\psi\rangle^{(3)} &= \frac{1}{\sqrt{2}}(|HHH\rangle + |VVV\rangle) && \text{(3-photon qubits)} \\ |\psi\rangle^{(4)} &= \frac{1}{\sqrt{2}}(|HHHH\rangle + |VVVV\rangle) && \text{(4-photon qubits)} \\ |\psi\rangle^{(n)} &= \frac{1}{\sqrt{2}}(|H\rangle^{(1)} \otimes \dots \otimes |H\rangle^{(n)} + |V\rangle^{(1)} \otimes \dots \otimes |V\rangle^{(n)}) && \text{(n-photon qubits)} \end{aligned} \quad (1.1.26)$$

1.1.2 Quantum communication

Faithful and confidential systems for information transmission are of great importance and interest from governments, militaries, or financial organizations over the centuries. Classical cryptography is the method used to send messages among parties with some sophisticated encryption algorithms to defend the ‘listen in’ risk from decipher. One-time-pad encryption was firstly proposed by Gilbert Vernam in 1917 [42], which is perfectly secure in principle because new codes are always generated for new messages, but impractical for use due to the eavesdropping of the key. The other well-known example is the RSA encryption scheme [31, 43] based on the mechanism that the time for finding prime factors of large integer increase exponentially with the number of digits. However, this is physically insecure, because a potentially efficient algorithm or powerful computation ability (i.e., quantum computer) will easily decode the key.

Quantum cryptography is one typical application in quantum communication, aiming at providing a method for transmitting a secure key and detecting the presence of eavesdropper [44]. According to quantum mechanics, it is impossible to extract the information from single particle, and then make a quantum copy of it (‘quantum no-cloning theorem’). The process of sharing a secure key between the parties (e.g., Alice and Bob) is called ‘quantum key distribution (QKD)’ [35, 45].

Fig. 1.2(a) shows the QKD according to BB84 protocol, a typical scheme proposed by C. Bennett and G. Brassard in 1984 using single photon source [15]. By projecting the polarization of photons on randomly chosen bases without telling anyone, The sender (Alice) transmits the photons to Bob with regular time intervals. When the receiver (Bob) obtains the photons, he will perform the polarization measurement with a random choice of projection bases and record the results. By exchanging the projection bases information via public channel, a set of sifted bits are discovered between Alice and Bob by keeping the results measured from the same detection bases and discarding others. Afterwards, the presence of eavesdropper (Eve) can be detected by checking the error rate of key, when Bob shared a subset of the sifted key to Alice for comparison, thereby identifying the quantum key distribution channel is secure or not. A basic understanding is that Eve is similar as Bob, capable of detecting the accurate results with success probability of 50 % due to random choice of projection bases, and 50 % probability of detecting correct bits from wrong projection bases. Then she has to send her detection results to Bob with a decreased accuracy of 75 %,

$$\begin{aligned} P &= P_{\text{correct basis}} + P_{\text{wrong basis}} \times P_{\text{correct results}} \\ &= 50 \% + 50 \% \times 50 \% \\ &= 75 \% \end{aligned} \tag{1.1.27}$$

meaning that the communication channel has probably been intercepted if the error rate is higher than 25 %.

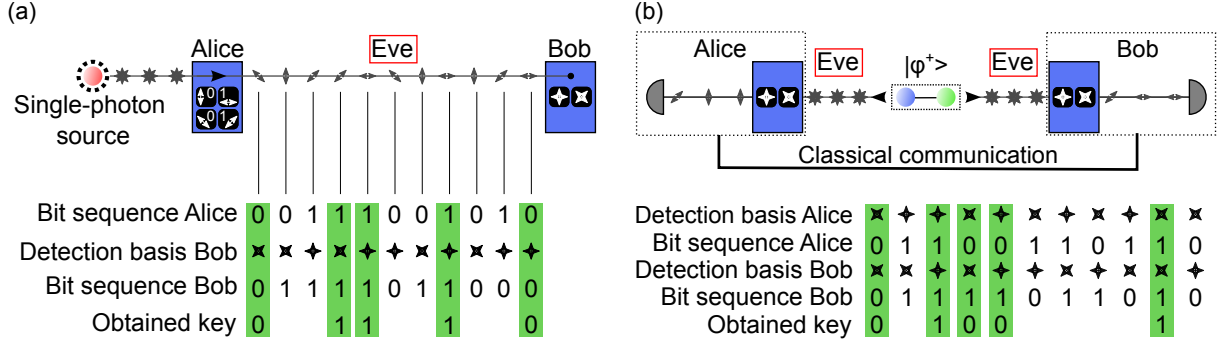


Figure 1.2: Schematic of QKD with of BB84 and Ekert protocols, based on single-photon and entangled-photon sources, respectively. (a) Alice encodes a sequence of data bits by randomly setting the polarization bases, which is only known by herself. Then she transmits the photons to Bob. A secure key will be shared to both after the exchange of information with respect to the measurement bases. (b) Polarization-entangled photon pairs are shared to Alice and Bob at different locations, followed by polarization projection measurement on randomly chosen bases. A secure key will be obtained by both parties after exchanging the measurement bases via the classical communication channel.

Apart from BB84 protocol based on single photon sources, the other well-known schemes such as Ekert protocol [45] with entangled photon sources is illustrated in Fig. 1.2(b). Streams of entangled photon pairs with the state of $|\varphi^+\rangle$ are shared to Alice and Bob via quantum channels for projection measurements on random choice of bases, respectively. To obtain the sifted key, they then communicate with classical channel to exchange the information of choice of projection bases, leaving the bits resulting from commonly chosen bases and discarding others. The correlation coefficients are available by sharing a subset of measurement results together with corresponding projection bases. Thus, the presence of eavesdropper will be revealed due to the destruction of entanglement, calibrated by Bell-CHSH inequality.

Quantum teleportation was firstly proposed by Bennett in 1993 [17] and experimentally demonstrated in 1997 [18], allowing for the fundamental study of transferring the unknown quantum state of one photon to other particles by assist of entangled states. The basic idea of teleportation can be expressed by a schematic as displayed in Fig. 1.3, assuming the polarization state of input photon 1 from single photon source is given by,

$$|\psi\rangle_1 = \alpha |H\rangle_1 + \beta |V\rangle_1 = \begin{pmatrix} \alpha \\ \beta \end{pmatrix} \quad (1.1.28)$$

where $\alpha^2 + \beta^2 = 1$ is used for normalization. Photon 2 and 3 are generated from an EPR photon source could be any of four Bell states. Here we consider a specific case of the state in the form of,

$$|\Psi^+\rangle_{23} = \frac{1}{\sqrt{2}}(|H\rangle_2 |H\rangle_3 + |V\rangle_2 |V\rangle_3) \quad (1.1.29)$$

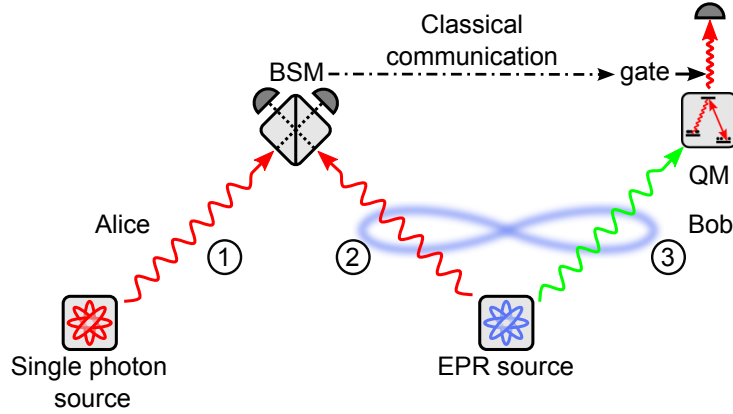


Figure 1.3: Schematic of quantum teleportation. Polarization state $|\psi\rangle_1$ of photon 1 from single photon source in Alice is to be teleported to photon 3 at Bob. Firstly, Alice performs the Bell state measurement (BSM) on photon 1 and 2 and send the results to Bob using classical channel. The initial state $|\psi\rangle$ can then be retrieved by carrying out a unitary operation for photon 3, according to the outcome of BSM. Photon 3 was stored in quantum memory (QM) awaiting the BSM results.

Therefore, the complete polarization state of the three particle system can be described as,

$$\begin{aligned}
 |\Psi\rangle_{123} &= |\psi\rangle_1 \otimes |\Psi^+\rangle_{23} \\
 &= \frac{1}{\sqrt{2}}(\alpha |H\rangle_1 |H\rangle_2 |H\rangle_3 + \alpha |H\rangle_1 |V\rangle_2 |V\rangle_3 \\
 &\quad + \beta |V\rangle_1 |H\rangle_2 |H\rangle_3 + \beta |V\rangle_1 |V\rangle_2 |V\rangle_3)
 \end{aligned} \tag{1.1.30}$$

And this can also be rewritten as,

$$\begin{aligned}
 |\Psi\rangle_{123} &= \frac{1}{2}(|\Phi^+\rangle_{12} \otimes (\alpha |H\rangle_3 + \beta |V\rangle_3) \\
 &\quad + |\Phi^-\rangle_{12} \otimes (\alpha |H\rangle_3 - \beta |V\rangle_3) \\
 &\quad + |\Psi^+\rangle_{12} \otimes (\beta |H\rangle_3 + \alpha |V\rangle_3) \\
 &\quad + |\Psi^-\rangle_{12} \otimes (-\beta |H\rangle_3 + \alpha |V\rangle_3))
 \end{aligned} \tag{1.1.31}$$

where $|\Phi^+\rangle$, $|\Phi^-\rangle$, $|\Psi^+\rangle$ and $|\Psi^-\rangle$ are the Bell states in Equ. 1.1.21, which can be distinguished by BSM. Due to the collapse of quantum system from measurement, the state of photon 3 is always projected to specific polarization, correlated with the BSM results, i.e., when $|\Psi^+\rangle$ is measured in Alice, the polarization of photon 3 will be

$$|\psi\rangle_3 = \beta |H\rangle_3 + \alpha |V\rangle_3 \tag{1.1.32}$$

Then Bob should do a specific unitary operation using operation gates (HWP and QWP

combination for photon qubits) according to the result from Alice, to retrieve the initial state of photon 1,

$$\begin{aligned} |\psi\rangle_3^{\text{gated}} &= \sigma_1^{\text{gate}} \cdot |\psi\rangle_3 \\ &= \begin{pmatrix} 0 & 1 \\ 1 & 0 \end{pmatrix} \cdot \begin{pmatrix} \beta \\ \alpha \end{pmatrix} = \begin{pmatrix} \alpha \\ \beta \end{pmatrix} \end{aligned} \quad (1.1.33)$$

In classical data transmission applications, repeater is an essential ingredient to counteract the intensity loss owing to absorption and scattering over a long distance. This is an analogous task for quantum communication or quantum computation, where the loss and decoherence of photons are the main obstacle in establishing large-scale quantum networks at present, thus necessitating the local amplifiers to boost the signals during data transmission, called ‘quantum repeater’ [46]. Typical quantum repeaters consist of three components, i.e., entangled swapping, entanglement purification, and quantum memory, which target to address the problem of loss, decoherence, and synchronization of timing for gate operation at the individual nodes, respectively. [47].

1.1.3 Entanglement swapping

The concept of entanglement swapping was the earliest proposed by Zukowski in 1993 [48], providing a solution of entangling two uncorrelated particles which never interact, is also understood as teleportation of entanglement. Entanglement swapping is the key element in quantum repeater, in order to overcome the distance limitation caused by loss of photons, by constructing entanglement connection among number of local nodes [44].

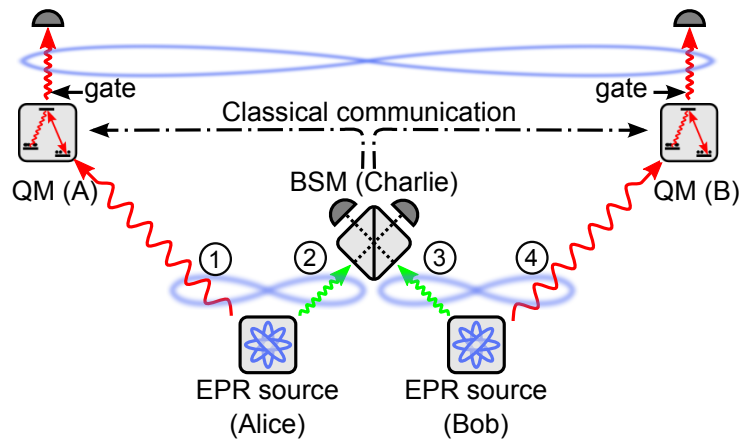


Figure 1.4: Schematic of entanglement swapping. One of the photon in entangled photon pair generated from each EPR source in Alice and Bob (Photon 2 and 3) are sent to Charlie using long-distance transmission channel for BSM. The remaining photons (Photon 1 and 4) at each party are locally stored in the quantum memory, awaiting the BSM results from Charlie for gate operation.

The arrangement of entanglement swapping is analogical to quantum teleportation, as

displayed in Fig. 1.4 [49]. Assuming pairs of polarization-entangled photons are generated by EPR sources at two remote parties Alice and Bob with the state,

$$\begin{aligned} |\Phi^+\rangle_{12} &= \frac{1}{\sqrt{2}}(|H\rangle_1 |H\rangle_2 + |V\rangle_1 |V\rangle_2) \\ |\Phi^+\rangle_{34} &= \frac{1}{\sqrt{2}}(|H\rangle_3 |H\rangle_4 + |V\rangle_3 |V\rangle_4) \end{aligned} \quad (1.1.34)$$

Then the polarization state of the four-photon system can be written as,

$$\begin{aligned} |\Psi\rangle_{1234} &= |\Phi^+\rangle_{12} \otimes |\Phi^+\rangle_{34} \\ &= \frac{1}{2}(|H\rangle_1 |H\rangle_2 |H\rangle_3 |H\rangle_4 + |H\rangle_1 |H\rangle_2 |V\rangle_3 |V\rangle_4 \\ &\quad + |V\rangle_1 |V\rangle_2 |V\rangle_3 |H\rangle_4 + |V\rangle_1 |V\rangle_2 |V\rangle_3 |V\rangle_4) \end{aligned} \quad (1.1.35)$$

The above state can also be rewritten as a sum of productions of Bell states between photon 1 and 4, photon 2 and 3,

$$\begin{aligned} |\Psi\rangle_{1234} &= \frac{1}{2}(|\Phi^+\rangle_{14} \otimes |\Phi^+\rangle_{23} + |\Phi^-\rangle_{14} \otimes |\Phi^-\rangle_{23} \\ &\quad + |\Psi^+\rangle_{14} \otimes |\Psi^+\rangle_{23} + |\Psi^-\rangle_{14} \otimes |\Psi^-\rangle_{23}) \end{aligned} \quad (1.1.36)$$

After sending photon 2 and 3 to Charlie for a subsequent BSM, the four-photon quantum system collapse, resulting in the generation of entanglement between photon 1 and 4, which correlated with the BSM results. By performing specific gate operation on photon 1 and 4 depending on the results from Charlie, a specific polarization entangled state can be obtained between photon 1 and 4. For example, if $|\Phi^-\rangle_{14}$ is the desired Bell state for Alice and Bob, but result $|\Psi^+\rangle_{23}$ is measured in Charlie, corresponding to the entangled state $|\Psi^+\rangle_{14}$ of photon 1 and 4. Gate operation ought to be proceeded on the photons extracted from QM(A) and QM(B) as follows,

$$\begin{aligned} |\Phi^-\rangle_{14} &= \sigma^{\text{gate (A)}} \otimes \sigma^{\text{gate (B)}} \cdot |\Psi^+\rangle_{14} \\ &= \frac{1}{\sqrt{2}} \begin{pmatrix} 1 & 1 \\ 1 & -1 \end{pmatrix}_{(A)} \otimes \frac{1}{\sqrt{2}} \begin{pmatrix} 1 & 1 \\ 1 & -1 \end{pmatrix}_{(B)} \cdot \frac{1}{\sqrt{2}} \left(\begin{pmatrix} 1 \\ 0 \end{pmatrix}_1 \otimes \begin{pmatrix} 0 \\ 1 \end{pmatrix}_4 + \begin{pmatrix} 0 \\ 1 \end{pmatrix}_1 \otimes \begin{pmatrix} 1 \\ 0 \end{pmatrix}_4 \right) \\ &= \frac{1}{\sqrt{2}} \left(\begin{pmatrix} 1 \\ 0 \end{pmatrix}_1 \otimes \begin{pmatrix} 1 \\ 0 \end{pmatrix}_4 - \begin{pmatrix} 0 \\ 1 \end{pmatrix}_1 \otimes \begin{pmatrix} 0 \\ 1 \end{pmatrix}_4 \right) \end{aligned} \quad (1.1.37)$$

Instead, if the measurement result in Charlie is $|\Phi^-\rangle_{23}$, then there is no need of any gate operation applied on photon 1 and 4.

1.1.4 Entanglement purification

To address the loss of photons in transmission, entanglement swapping realizes the construction of entanglement between remote parties by a number of local nodes in between. While decoherence effect of photons from the environment, which deviate the initial state of the quantum system to be a mixed state, leads to exponential degradation of fidelity of the distributed entanglement as the propagation distance. The scheme of entanglement purification is proposed in 1996 by Bennett [50], Deutsch [51] and experimentally achieved by Pan [52, 53]. A subset of high entanglement can be extracted from a large set of unknown mixed state by sacrificing a subset of photons.

Fig. 1.5(a) shows the optical operation of perfect PBS on different polarization of input photons, where only identically polarized photons come out from different output ports (Panel (I)-(II)). For a better understanding of purification, it can be simply assumed that a pure Bell state $|\Phi^+\rangle$ transmitted in a long distance is mixed with the Bell state $|\Psi^+\rangle$. The state of the quantum system can be expressed as,

$$\rho_{mix} = F |\Phi^+\rangle \langle \Phi^+| + (1 - F) |\Psi^+\rangle \langle \Psi^+| \quad (1.1.38)$$

with F the fidelity of $|\Phi^+\rangle$ in the mixed-state system.

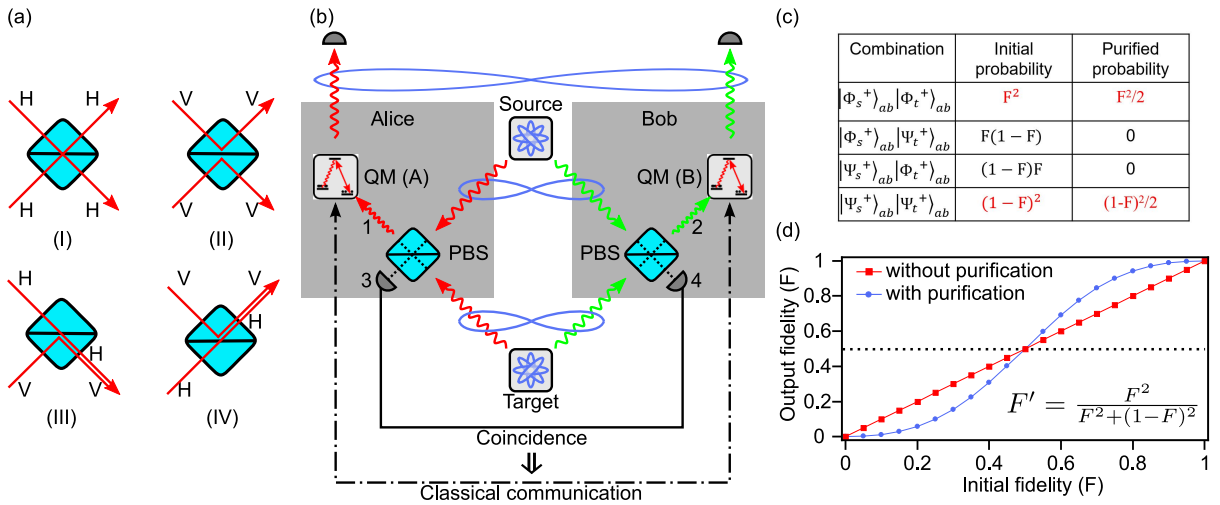


Figure 1.5: (a) Output mode selection of PBS depending on the input polarization of photons. Horizontally and vertically polarized photons are transmitted and reflected, respectively. (b) Schematic of entanglement purification. (c) Possible combinations of four photon states of the quantum system. Only two combinations lead to the outcome of single photons from each port of two PBSs, which are marked as red. (d) Comparison of entanglement fidelity before (red) and after (blue) purification.

To realized purification, two pairs of entangled photons are separated as source and target as illustrated in Fig. 1.5(b). The density matrix of the states of the quantum

system then would be,

$$\begin{aligned}\rho_s &= F |\Phi_s^+\rangle \langle \Phi_s^+| + (1 - F) |\Psi_s^+\rangle \langle \Psi_s^+| \\ \rho_t &= F |\Phi_t^+\rangle \langle \Phi_t^+| + (1 - F) |\Psi_t^+\rangle \langle \Psi_t^+|\end{aligned}\tag{1.1.39}$$

When two photons from each entangled photon pairs of source and target are separated, and interfered at two PBSs (Alice and Bob). The combinations of four-photon state is displayed in Fig. 1.5(c). However, due to optical property of PBS illustrated in Fig. 1.5(a), only states combinations $|\Phi_s^+\rangle |\Phi_t^+\rangle$ and $|\Psi_s^+\rangle |\Psi_t^+\rangle$ result in output of single photons from four ports of PBSs simultaneously, which can be labelled as photon 1, 2 3, and 4. By checking the coincidences of photon 3 and 4 on different polarization measurement bases. The purified entangled state can be obtained by performing proper gate operation on photon 1 and 2, according to the measurement results on photon 3 and 4. The resultant density matrix of entangled photon 1 and 2 is then,

$$\rho_{12} = F'(|\Phi^+\rangle \langle \Phi^+|) + (1 - F')(|\Psi^+\rangle \langle \Psi^+|)\tag{1.1.40}$$

where $F' = F^2/[F^2 + (1 - F)^2]$. Fig. 1.5(d) shows the fidelity of output entanglement between photon 1 and 2, as a function of initial fidelity of the quantum system with (blue) and without (red) entanglement purification. The fidelity after purification is enhanced, in case that the initial fidelity is over the classical-quantum limit ($F > 0.5$).

1.1.5 Quantum memories

The central goal of quantum networks is the construction of connection among remote nodes using single- or entangled- photons as medium. It relies on high-quality and efficiency quantum interface between light and matters. QMs are the key elements of photonic quantum technologies, such as quantum repeaters, linear-photonic quantum computation, which enable the capability to coherently manipulate, buffer, and re-time photonic signals [54, 55, 56, 57]. The promising material systems are mainly classified into several groups: rare-earth-ion doped solids [58], diamond color centers [59, 60], crystalline solids [61], alkali metal vapors [62, 63, 64], and molecules [65]. To date, depending on requirements of applications, various types of QM have been demonstrated using different protocols and material systems by means of engineered coupling to hybrid degrees of freedom. For example, time-bandwidth and multimode capacity might be important for local quantum processing, whereas a long storage time is extremely essential for long-haul quantum communication. Taking into account of a typical entanglement distribution by a standard quantum repeater over 1000 km [47], a timescale of milliseconds is required to cover the waiting time for transmission of classical signals.

1.1.6 Quantum repeaters

As have been discussed in Sec. 1.1.2, quantum repeaters are indispensable components to extend the data propagation distance in global-scale quantum communication. As a typical verification, quantum nested purification [66] consisting of entanglement swapping and purification and purification has demonstrated the feasibility of a quantum repeater, despite the lack of effective QMs.

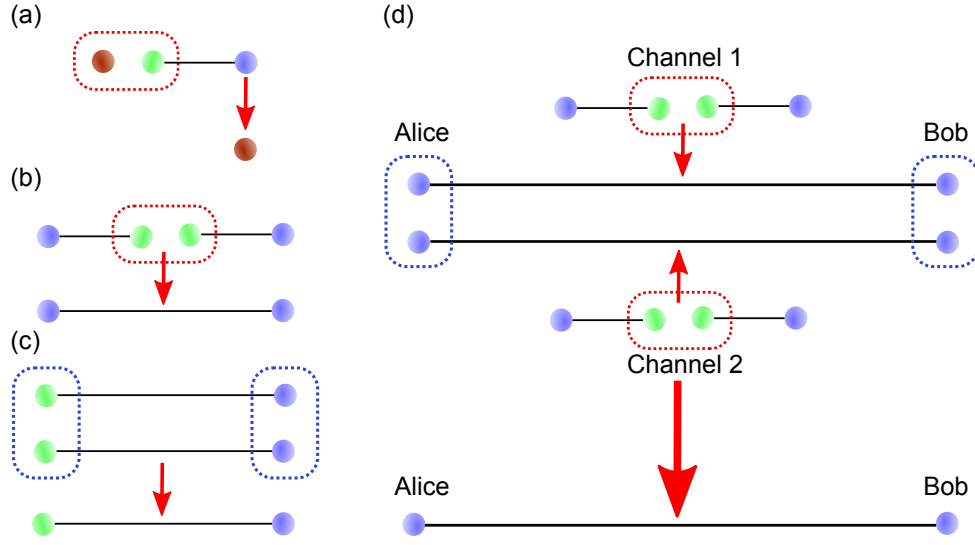


Figure 1.6: Diagram of entanglement (a) teleportation, (b) swapping, (c) purification, and (d) nested purification for a linear optical repeater.

Fig. 1.6 (a)-(c) illustrate the schematic diagram of components for a standard quantum repeater. In case BSM (red dash box) is applied on the photon at a pre-defined state (brown) and one of the photon of EPR photon pairs, the initial state will be teleported to the remaining photon after unitary operation in terms of BSM (Fig. 1.6(a)). Similarly, a renewed entanglement between two initially uncorrelated photons is established, if one of two photons from two individual EPR pairs are selected for BSM (Fig. 1.6(b)). Fig. 1.6(c) shows the simplified diagram of physical principle of entanglement purification presented in Fig. 1.5(b). After the coincidence measurement between the photons coming out from the PBS (blue dash box), the entanglement fidelity of the left photons are enhanced. A nested purification scheme is proposed by combining entanglement swapping and purification as presented in Fig. 1.6(d). Two parallel entanglement swapping are first carried out at the intermedia node (‘Charlie’) in between two end nodes (‘Alice’ and ‘Bob’), followed by the purification operation on the remaining two EPR pairs. Entangled photons possessing a higher purity are thus generated between Alice and Bob. High-quality QMs will directly enable the nested purification to be the linear quantum repeaters for practical quantum communication.

In conventional quantum repeater scheme, the goal is to create entanglement between

the QMs in the end nodes via BSM at the intermedia nodes. Apart from the function of storing qubits in the end nodes for waiting the classical measurement results, QMs also enable the functions of hub in the intermedia nodes in a multiple parallel transmission channels (Fig. 1.7(a)). The local QMs in the intermedia nodes C_i keep the entanglement until they are informed whether successful or failed entanglement generation with its neighbor nodes (red photons between Alice and C1, Bob and C2) are made. Selective BSM are executed only on successfully entangled pairs. In contrast, all-photonic quantum repeaters (Fig. 1.7(b)) allow the implementation of the functions by using the graph states [67], in which projection measurements are carried out either on X basis or Z basis between signal photon (red) and graph state photon (blue) to disentangle the distant nodes or establish the entanglement, depending on the measurement results. Such a scheme provides the advantage of a higher connection efficiency ($M^{N+1}\epsilon^{N+1}$) than conventional quantum repeaters ($M\epsilon^{N+1}$) with parallel entanglement swapping, where M denotes the number of channels, N is the number of the intermedia nodes, ϵ is the survival probability of EPR pairs during transmission.

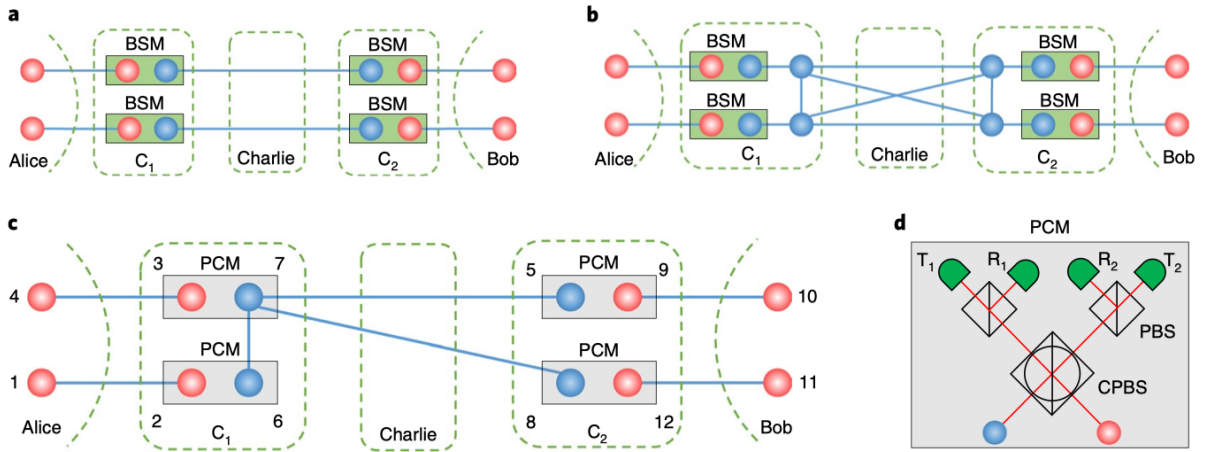


Figure 1.7: Diagram of memory-based or all-photonic quantum repeaters. (a) Conventional memory-based quantum repeaters with two parallel transmission channels and one intermedia node. (b) All-photonic quantum repeaters. Graph state is induced in the intermedia node in order to construct joint entanglement with the entangled photons from end nodes. (c) An exemplary all-photonic repeater using GHZ state. (d) passive-choice-measurement (PCM) enables the functions of selective BSM in (c) via a passive manner. Reprinted figure with permission from [68]. Copyright 2019.

Fig. 1.7(c) display a simplified all-photonic quantum repeater by a substitution of GHZ state for the graph state, along with the PCMs to passively execute the switching function between entanglement or disentanglement. In the end, at least one of entanglement combinations between photon 4&10, 4&11, 1&10, or 1&11 will be established. Fig. 1.7(d) illustrates the sketch of the PCM, composed of circular PBS (CPBS) and two normal PBSs [68]. When no heralding information of entanglement arrives the intermedia nodes C_i (e.g.,

red photon is lost during transmission), only one photon will be subjected into CPBS, leading to the photon detected by either right or left port of CPBS. The measurement of the photon will collapse the quantum system of n-particle GHZ state $|GHZ_N^+\rangle$ to be a smaller GHZ state $|GHZ_{N-1}^+\rangle$ or $|GHZ_{N-1}^-\rangle$, corresponding to a projection measurement on X basis that disentangles one photon in the GHZ state with the others. When the photon from the neighbor nodes successfully arrive PCM, the CPBS will server as either bell state analyzer or projector in X basis, depending on the correlation between the four detectors (Details about PCM can be found in the supplementary of [68]).

1.2 Quantum light sources

The task of quantum optics is to study the nature of light as streams of photons, instead of classical electromagnetic wave. According to the observation of statistical properties of photon streams, light sources can be classified into three types: Thermal (chaotic) light, Coherent light, and non-classical light, with respect to photon statistics of super-Poissonian, Poissonian, and sub-Poissonian distribution, respectively.

Thermal (chaotic) light: The light comes from electromagnetic radiation by a hot body (thermal light), a single spectral line of a discharged lamp (chaotic light), or an ensemble of incoherent emitters. In such types of sources, the probabilistic distribution of photons in terms of mean photon number \bar{n} can be written as [69],

$$P(n) = \frac{\bar{n}^n}{(1 + \bar{n})^{(1+n)}} \quad (1.2.1)$$

This distribution is called the Bose-Einstein distribution, where the variance of statistics distribution is $(\Delta n)^2 = \bar{n}^2 + \bar{n}$ [70]. The fluctuation of photon number $\Delta n < \bar{n}$.

Coherent light: Typical coherent light is a laser, in which the uncertainty product of energy and time follow the minimal value in Heisenberg uncertainty principle ($\Delta E \cdot \Delta t \geq \hbar/2$) [71]. A perfect coherent source emits a constant intensity of light, with the probability distribution of photon numbers in terms of mean photon number \bar{n} following Poissonian distribution,

$$P(n) = \frac{\bar{n}^n}{n!} e^{-\bar{n}} \quad (1.2.2)$$

The standard deviation of photon number is $\Delta n = \sqrt{\bar{n}}$ [69]. Since the uncertainty of zero can only be achieved in case \bar{n} is equal to zero, apparently it is never possible to generate on-demand single photons by attenuating Thermal and coherent light.

Non-classical light: Non-classical (quantum) light is generated by single photon sources, resulting in successive single photons with a deterministic interval between the photon events. The statistics distribution is called ‘sub-Poissonian’ [72, 73], with the fluctuation of photon number $\Delta n < \bar{n}$. The sub-Poissonian statistics of such a source reveals the

direct confirmation of quantum nature of light, enabling many photonic-based quantum information applications.

1.2.1 Single photon emitters

Single photon emitters play as a fundamental resource in the realm of leading photonic quantum information technologies [74, 75, 76], emitting photons following ‘sub-Poissonian’ statistics. Ideal single photon sources necessitate the emission of photons with high repetition rates, a high and constant quantum efficiency into spatiotemporal mode, a high indistinguishability, and a high single photon purity. Although plenty of material systems have been developed, there are no ideal single photon emitters satisfying all prerequisites. Herein, we are going to briefly review the advantages and disadvantages for prevalent single photon emitters as follows [77],

Trapped atoms and ions: The first experimental demonstration of single photon emission was observed from the atomic transition of sodium atoms in 1977 [78], in spite of low stability and efficiency. To date, single photon emission from cold atoms features high efficiency and lifetime-limited linewidth due to negligible inhomogeneous broadening [79]. However, such sources require complex trapping setups as well as long dynamics process of transition, giving rise to high cost and low operation rates.

SPDCs: Study of such a type of sources was earliest began by Klyshko and Zel’dovich, with first experimental demonstration of quantum correlation by Burnham and Weinberg in 1970 [19]. One of two photons produced in a non-linear process shows the nature of single photons [80]. However, such a frequency conversion process suffer an intrinsic drawback of non-deterministic emission with increase of pumping power, unambiguously degrading the security in the above-mentioned quantum communication schemes [81, 82] (Details in the following Section 1.2.2).

Color centers: Color centers are low-density fluorescent point defects existing in crystals or nanocrystals. The biggest advantage of these material system is the stable room-temperature operation once the ground and excited states of the emitters are far away from the valence and conduction bands of the host. Nitrogen vacancy (NV) and Silicon vacancy (SiV) are two emitters mostly studies in diamond with well-established understanding of crystallographic and electronic structures [83]. Both emitters can be fabricated by ion implementation and subsequent annealing, exhibiting narrow emission lines at cryogenic temperatures. Different from NV, SiV center is less influenced by the fluctuation of environment due to its inversion symmetry property [84]. Apart from defects in diamond, there are other color centers (Fig. 1.8(a)) such as SiC centers in the compound semiconductors [85, 86], rare-earth-ions impurities in crystals YAG [87, 88], and II-IV compound semiconductor ZnO [89, 90], being of particular interests but need to be further investigated more in detail.

Semiconductor quantum dots: In comparison with other single photon emission plat-

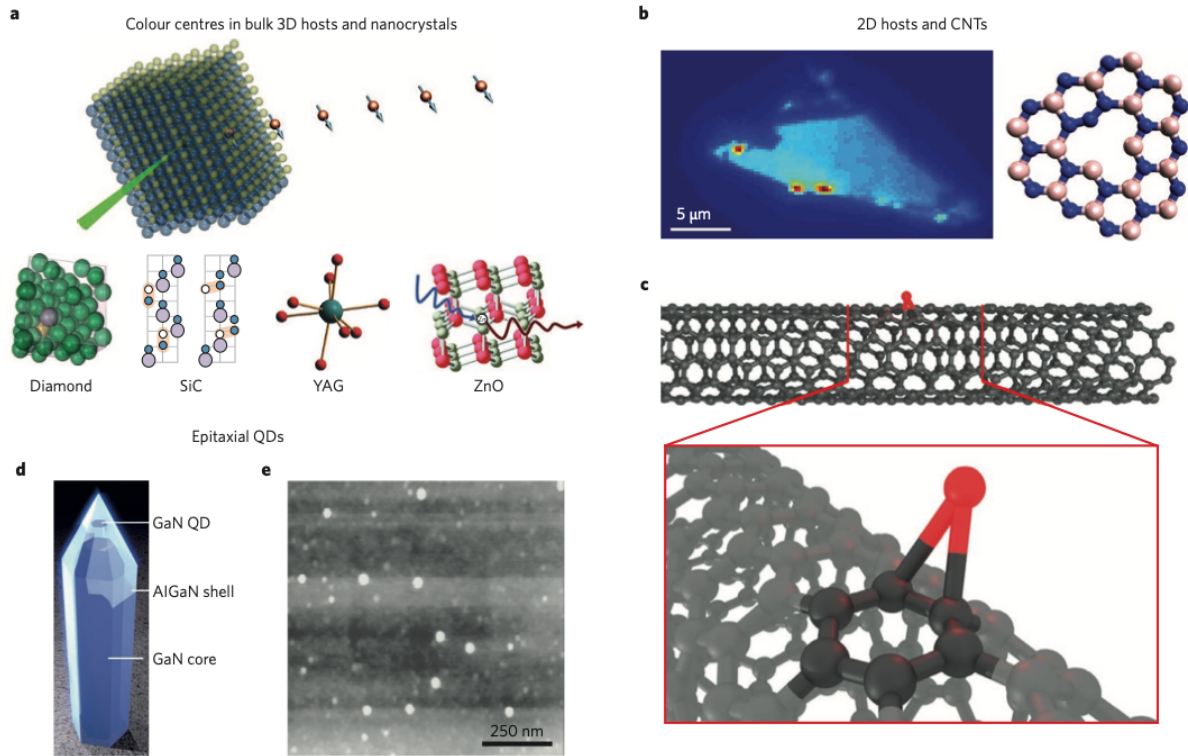


Figure 1.8: Solid-state single photon emitters. (a) Color centers in 3D bulk crystals or nanocrystals emitting single photons under the excitation by green laser beam. (Insets: Broadly studied hosts, e.g., diamond, Silicon carbide (SiC), yttrium aluminum garnet (YAG), and zinc oxide (ZnO).) (b) Single photon emitters in 2D hosts. Confocal map (left) of single photon emission at cryogenic temperatures, resulting from localized excitons in transition metal dichalcogenides involving MoSe_2 and WSe_2 . Defects in monolayer hexagonal boron nitride (hBN) and flakes of hBN allow the operation of single photon emitters at room-temperature. (c) Single photon emission was observed from localized excitons, generated by oxide-related defects in carbon nanotubes (CNTs). (d) Nitride QDs in nanowire waveguide and (e) Self-assembled InAs QDs, grown by epitaxial methods. Reprinted figure with permission from [77]. Copyright 2016.

forms, semiconductor quantum dots (QDs) e.g., InAs/GaAs (Fig. 1.8(e)) show the best overall performance [91, 92] achieving high quantum efficiency, photon purity, indistinguishability, spin-photon entanglement, and two-photon entanglement at cryogenic temperatures. Moreover, a variety of semiconductor manufacturing technologies enable the optimization of such a source towards ideal single photon emitters. On the other hand, III-Nitride QDs (Fig. 1.8(d)) operating at room temperature simplifies the requirements for complicate cooling systems [93, 94].

Except for above material platforms, amounts of two-dimensional materials have represented single photon emission such as quantum defects in transition metal dichalcogenides [95, 96] and hexagonal boron nitride [97] (Fig. 1.8(c)). Semiconductor CNTs is a potential single photon emitter for integrated photonic circuits due to its inherent property as

1D resonator, or telecom technologies because the zero-phonon line (ZPL) located above $1 \mu\text{m}$ [98, 99, 100].

1.2.2 Entangled photon emitters

Starting from late 1980s till nowadays, SPDCs based on non-linear optical process have been the workhorse in plenty of demonstrations of quantum applications [81]. It provides a convenient and robust method to produce highly indistinguishable polarization-entangled photons at room temperatures. As illustrated in Fig. 1.9(a) of type-II SPDC sources [101], an ultraviolet pump laser beam is impinging a non-linear crystal (e.g., BBO). Then two cone-shaped light beams with orthogonally polarized photons are generated, leading to observation of daughter photons at two intersection points of cones.

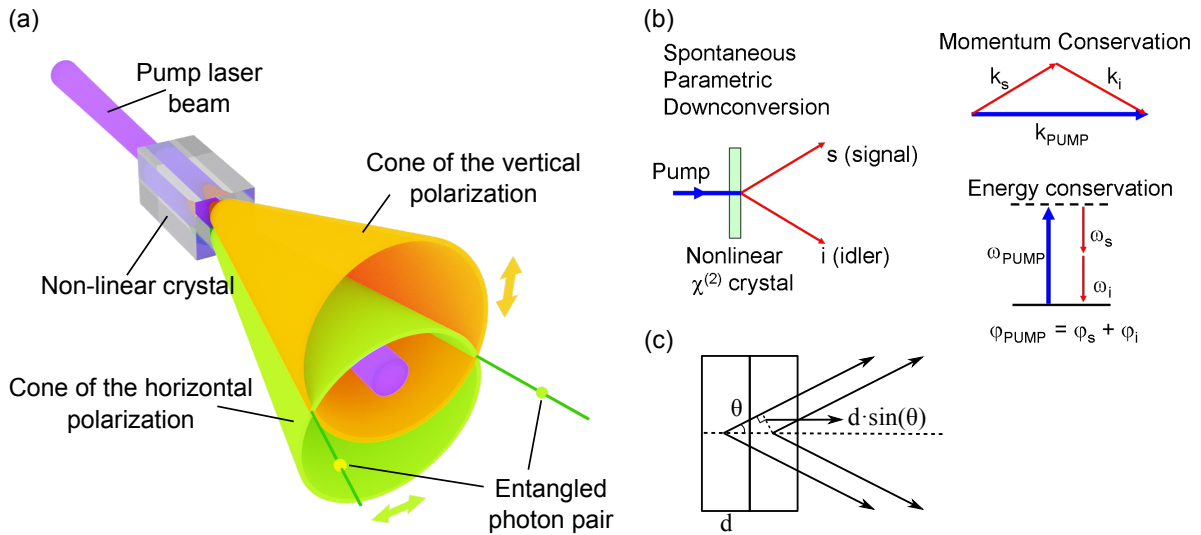


Figure 1.9: Generation of polarization entangled photon pairs based on SPDC sources. (a) An ultraviolet pump laser is employed to excite type-II non-linear crystal. Owing to the phase-matching conditions, two beams with opposite polarization emerge after the crystal in the shape of cones. Entangled photon pairs appear at the intersection lines of two cones. (b) Physical diagram of SPDC sources. (c) Generation of entangled photon pairs using type-I SPDC source, with transverse shift of cones $d \sin \theta$. Panel (a) and (b) are reprinted copyright CC By 4.0 [102] and CC By 3.0 [103] from Wikipedia without any changes made.

In non-linear optics, the non-linear components for electromagnetic field in the non-linear materials can not be ignored under a high electric field, resulting in an expansion of electric susceptibility (χ) in powers of electric fields (E_i),

$$\begin{aligned}
 P(\omega) &= P_L(\omega) + P_{NL}(\omega) \\
 &= P^{(1)}(\omega) + P^{(2)}(\omega) + \dots \\
 &= \varepsilon_0(\chi^{(1)}(\omega) \cdot E(\omega) + \chi^{(2)}(\omega_1, \omega_2) \cdot E(\omega_1)E(\omega_2) + \dots)
 \end{aligned}
 \tag{1.2.3}$$

with ε_0 the vacuum electric permittivity. Generally, non-linear effect is mainly governed

by the first two order electric susceptibilities. The state of pairwise photons yielded by SPDCs is,

$$|\Psi\rangle = |00\rangle + \varepsilon |11\rangle + \varepsilon^2 |22\rangle + \dots \quad (1.2.4)$$

where $|00\rangle$ and $|11\rangle$ represent no photon state and one photon in each of two intersection points. The probability of $|11\rangle$ state is determined by ε^2 relevant with $\chi^{(2)}$ and phase matching conditions. In practice, other variables such as the length of crystal, intensity of the pumping power also determine the generation efficiency of single entangled photon pairs.

Fig. 1.9(b) shows the diagram of SPDC sources (left), assuming photons in pump laser possessing energy $\hbar\omega_{PUMP}$ and momentum $\hbar k_{PUMP}$ interface with crystal, yielding two entangled photons (signal and idler). Momentum and energy conservations are required in the process (Fig. 1.9) following,

$$\begin{aligned} \vec{k}_{PUMP} &= \vec{k}_s + \vec{k}_i \\ \omega_{PUMP} &= \omega_s + \omega_i \end{aligned} \quad (1.2.5)$$

with phase matching condition $\varphi_{PUMP} = \varphi_s + \varphi_i$. Polarization states of entangled photon pairs are usually determined by the types of crystal materials, and orientation of the electromagnetic field with respect to the material, etc. For type-II SPDC as Fig. 1.9(a), polarization of signal and idler are usually orthogonal, whereas the polarization of pump photon is orthogonal to signal and idler photons sharing identical polarization in type-I SPDC sources (Fig. 1.9(c)). Two pieces of thin non-linear crystals are combined with the optical axes oriented perpendicularly. High-fidelity entanglement is obtained in case that the crystals are thin enough ($d \ll$ coherence length of pump photons), so that one can not tell from which crystals that photons are generated. Once pump light with polarization angle of θ_p is induced to interface with the crystal, the polarization-entangled state of generated photon pairs can be represented as [28],

$$|\Psi\rangle = \cos\theta_p |HH\rangle + e^{i\varphi} \sin\theta_p |VV\rangle \quad (1.2.6)$$

where φ results from the birefringence of the crystals. However, as we discuss above, number of photons produced in the non-linear process are affected by the crystal material and pumping power. High power of pump laser for a higher source efficiency will induce bigger portion of other states, e.g., $|22\rangle, |33\rangle \dots$ thereby degrading the purity of sources.

1.3 Semiconductor quantum dots

Low dimensional materials are of great interests owing to the convenient control of optical and electronic properties solely by the size [104, 105, 106, 107]. Depending on the size of the nanocrystals along the axes in space, the structures are generally classified into no

confinement, 1D confinement, 2D confinement, and 3D confinement as shown in Fig. 1.10. The different types of confinement corresponding to various density of states (DOSs) will determine the carriers concentrations and energy distribution (figures in the bottom line). The form of DOS ($\rho(E) = dN(E)/dE$) can be deduced as [108],

$$\rho(E) = \frac{dN(E)}{dE} = \frac{dN}{dk} \cdot \frac{dk}{dE} \quad (1.3.1)$$

$$E = \frac{\hbar^2 k^2}{2m^*}$$

with $N(E)$ being the number of states, E the energy, k the wave vector, \hbar the reduced Planck constant, and m^* the effective mass of carriers. On the other hand, the number of states are determined by the dimension of confinement, i.e., 3D bulk materials,

$$N_{3D} = \frac{V_{3D}}{V_s} \cdot 2 \cdot \left(\frac{1}{2}\right)^3 = \frac{k^3}{3\pi^2} \quad (1.3.2)$$

where $V_{3D} = 4\pi k^3/3$ is the volume of space spanned by k , V_s is the area occupied by single state, a factor 2 is double electron spins in each state, $(1/2)^3$ is the correction factor for counting identical states along the axes of n_x, n_y, n_z . Herein we conclude that DOS for low-dimensional materials as increase of confinement,

$$\rho_{3D}(E) = \frac{1}{2\pi^2} \left(\frac{2m^*}{\hbar^2}\right)^{3/2} (E - E_c)^{1/2}$$

$$\rho_{2D}(E) = \sum_{i=1}^n \frac{m^*}{\pi \hbar^2} H(E - E_c) \quad (1.3.3)$$

$$\rho_{1D}(E) = \frac{1}{\pi \hbar} \left(\frac{1}{2m^*(E - E_c)} \right)$$

$$\rho_{0D}(E) = 2\delta(E - E_c)$$

Where H is the Heaviside step function, E_c denotes the band energy of carriers in conduction band, δ accounts for the delta function. For 3D-confinement materials e.g., QDs, delta function of DOS indicates a discrete distribution of energy levels as similar as hydrogen atom, constraining electrons, holes, or electron-pairs to zero dimensions.

In addition, the prerequisites of spatial size of a QD relative to the wavefunction of the charge carrier is given by de-Broglie wavelength,

$$\lambda_B = \frac{h}{\sqrt{2k_B T \cdot m^*}} \quad (1.3.4)$$

where h is the Planck constant, k_B is the Boltzmann constant, T is the temperature. For GaAs QDs, in which the effective mass of an electron in the conduction band is $0.066m_0$ (m_0 is the mass of a free electron), the de-Broglie wavelength is around 30 nm at room temperature, necessitate the size of GaAs QDs in the order of tens of nanometers.

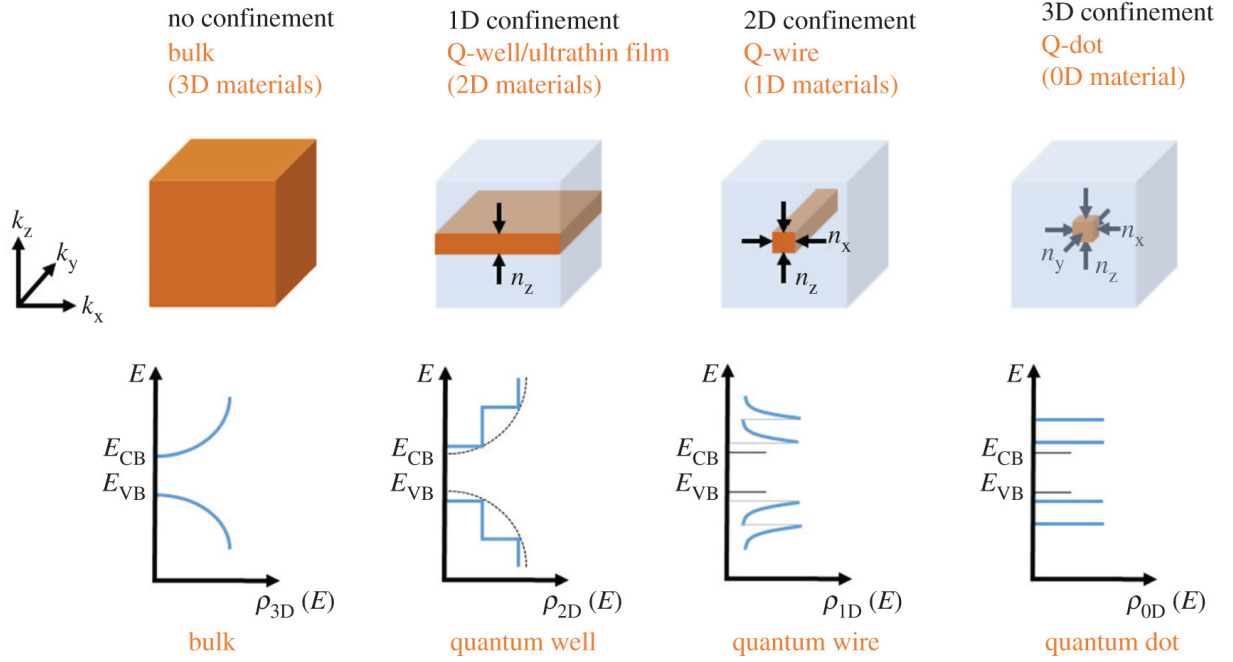


Figure 1.10: DOS of semiconductors with different configurations of confinement, i.e., 3D bulk without confinement, 2D quantum well/ultra-thin film with confinement in one direction, 1D quantum wire with two-dimensional confinement, and 0D quantum dots three-dimensional confinement. Reprinted figure from [108]. Copyright CC BY 4.0 [102], Royal Society, without any changes made.

1.3.1 Electronic states

Semiconductor QDs are also referred as ‘artificial atoms’, not only allow for an on-demand generation of high-purity single photons [109], they also show high performance in terms of pairwise entanglement fidelity [110], large radiative decay rates and internal quantum efficiencies in contrast to other quantum systems [111, 112] (e.g., atoms and diamond defect centers).

The discrete band structure and photoluminescence emission of a QD is represented in the inset of Fig. 1.11 with orange background. A low band gap nanostructure e.g., QD is embedded in the middle of high band gap structure e.g. barrier layer. By means of optical excitation schemes, cluster of free electrons and holes are formed in conduction and valence band of barrier layer, respectively. In case a pair of electron and hole is trapped by the QD after energy relaxation through the interaction with phonon or carrier scattering, a neutral exciton (X) occupying discrete energy level of the QD forms (grey inset at the left). The recombination of electron and hole in the following radiative process give rise to the emission of a single photon.

However, different forms of occupancy of electrons and holes within the energy levels of a QD usually yield a number of transition states. Fig. 1.11 shows the PL spectrum of a single photon including three dominant types of transitions, i.e., $|X\rangle$, $|X^+\rangle$, and $|XX\rangle$

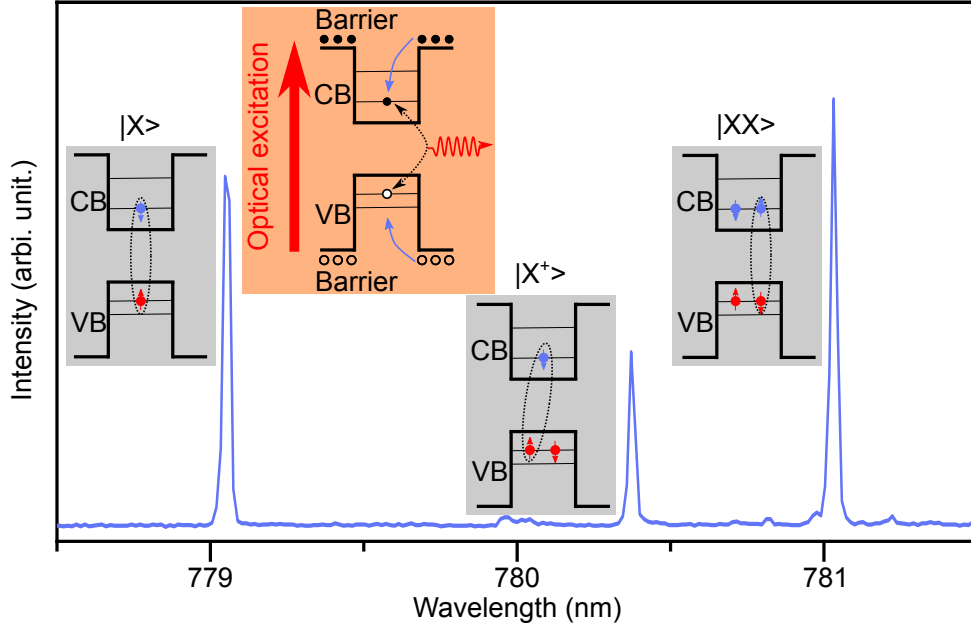


Figure 1.11: photoluminescence (PL) spectrum of a GaAs QD with multiple electronic states. Panel with orange background illustrates the diagram of photoluminescence process in the band structure consisting barriers, valence, and conduction band. Panels with grey background illustrate different forms of occupancy of electrons (blue) and holes (red) in conduction and valence band, corresponding to three dominant transitions in the spectrum.

under two photon excitation (TPE) (Details in the Sec. 2). Apart from a pair of electron and hole at excited state, the appearance of an additional hole with opposite spin direction in the valence band of the QD leads to $|X^+\rangle$ state. Similarly, the configuration involving two pairs of electrons and holes along opposite spin direction within the energy levels is called $|XX\rangle$ state, resulting in the generation of polarization-entangled photons in the cascade process.

1.3.2 Generation of entangled photons

The cascade process for generating entangled-photon pairs in QDs was the earliest predicted in 2000 [113], and experimentally demonstrated in the year of 2006 [114]. The physical mechanism is illustrated in Fig. 1.12(a), illustrating the radiative cascade process from excited biexciton states $|XX\rangle$ ($|\downarrow\uparrow\uparrow\downarrow\rangle$) in a QD, with the sequential recombination of two degenerate pairs of inverse spin combinations of electron and hole ($|\downarrow\uparrow\rangle$ and $|\uparrow\downarrow\rangle$), which explains the generation of entangled photon pairs [115].

Since the projection of electron (heavy hole) is either $1/2(3/2)$ or $-1/2(-3/2)$, two bright states of $|XX\rangle$ ($|\downarrow\uparrow\uparrow\downarrow\rangle$) can be represented as $|-1/2, 3/2\rangle$ ($|\downarrow\uparrow\rangle$) and $|1/2, -3/2\rangle$ ($|\uparrow\downarrow\rangle$), resulting in total z-spin of $|+1\rangle$ and $|-1\rangle$ coupled to a right (R) and left (L) hand circularly polarized photon according to the selection rules. Fig. 1.12(a) illustrates the generation of polarization-entangled photons with two possible decay channels from

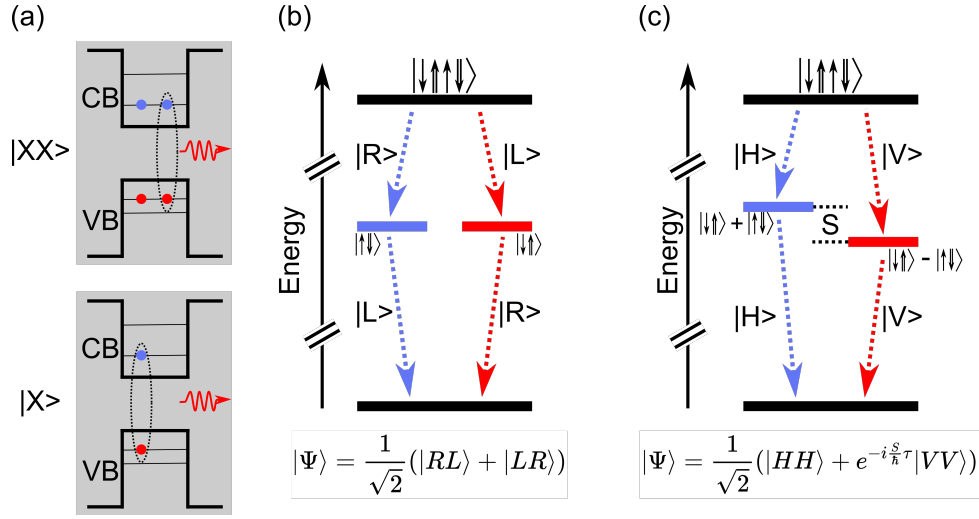


Figure 1.12: Cascade of radiative decay process of neutral biexciton (XX) states from a single QD. (a) Recombination of electrons and holes lead to generation of a pair of entangled photons via intermedia X state. (b) and (c) illustrate the formation of entangled state of emitted photon pairs, without and with the existence of fine structure splitting (FSS) (S). \uparrow, \downarrow and \uparrow, \downarrow denote the electron and hole spins, respectively.

the biexciton (blue and red). In the case that the dot maintains a perfect cylindrical symmetry along its growth axis, the exchange interaction between spin of electron and hole is negligible. Suppose $-1/2$ electron and $3/2$ recombine first, a $|R\rangle$ polarized photon is produced, leaving a X trapped in the dot which subsequently recombine to emit a $|L\rangle$ photon. Generation of photons with opposite order of polarization is started by the first combination of $|1/2, -3/2\rangle$ to emit a $|L\rangle$ photon, followed by a $|R\rangle$ photon. Since the channels are coherent at a superposition state and there is no way to distinguish two degenerated states, the polarization of two photons should be described by the entangled state,

$$|\Psi\rangle = \frac{1}{\sqrt{2}}(|RL\rangle + |LR\rangle) \equiv \frac{1}{\sqrt{2}}(|HH\rangle + |VV\rangle) \equiv \frac{1}{\sqrt{2}}(|DD\rangle + |AA\rangle) \quad (1.3.5)$$

However, the QDs in practice are usually asymmetric, causing a lift-up doublet degenerated structure with an energy difference of S due to electron-hole interaction, called ‘FSS’ (Fig. 1.12). As a consequence, the state of entangled photon pairs is evolving with the radiative lifetime (τ) of the X photon, in the form of [116],

$$|\Psi(S, \tau)\rangle = \frac{1}{\sqrt{2}}(|H_{XX}H_X\rangle + e^{-i\frac{S}{\hbar}\tau} |V_{XX}V_X\rangle) \quad (1.3.6)$$

where $|H\rangle$ and $|V\rangle$ represent horizontally and vertically polarized photons, aligned with the substrate cleave direction. It is obvious that the phase of entangled state is evaluating as a function of X photon lifetime for a finite FSS.

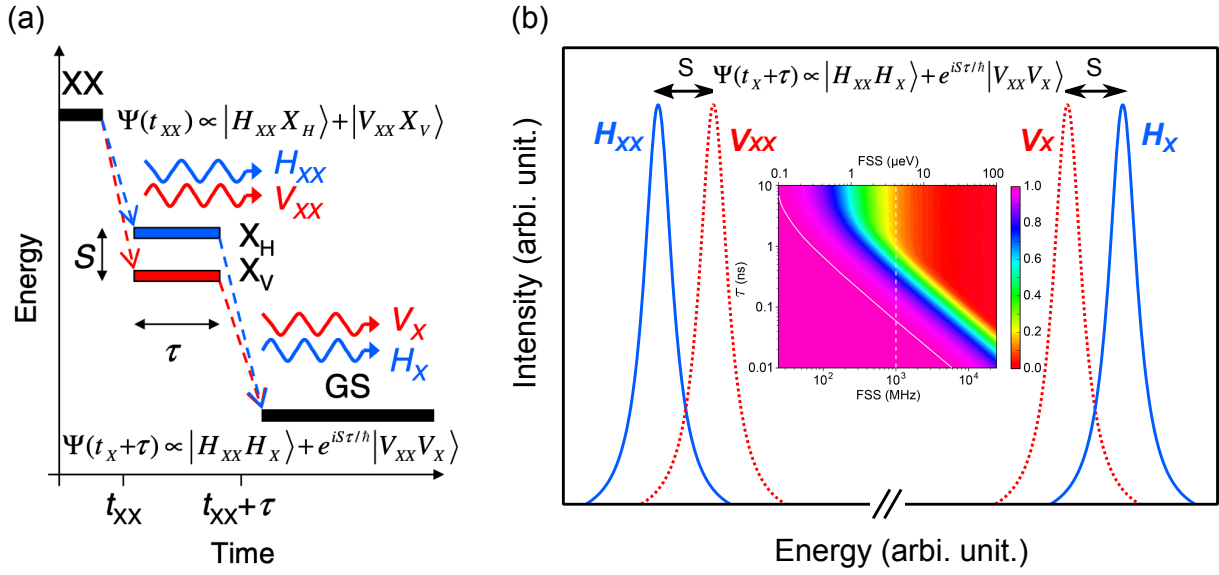


Figure 1.13: (a) Evolution of entangled state in the QD as a function of time during the XX cascade process. (b) Exemplary illustration of spectrum from a single QD, exhibiting energy splitting relative to photon polarization, which is caused by FSS. Colormap in the inset figure represents the average concurrence as a function of detector resolution and FSS in case of a X lifetime of ($\tau = 1$ ns). Reprinted figure (a) with permission from [116]. Copyright 2008. Reprinted inset in figure (b) from [117]. Copyright CC BY 4.0 [102], Optical Society of America, without any changes made.

Fig. 1.13(a) schematically display the evolution of the entangled state in the quantum system on a timeline of a single cascade process. Due to spin-orbit interaction, two $|X\rangle$ states mix and create new eigenfunction in the form of $1/\sqrt{2}(|+1\rangle - |-1\rangle)$ and $1/\sqrt{2}(|+1\rangle + |-1\rangle)$ [118]. The recombination of first pairs of electrons and holes yield a horizontally or vertically polarized XX photons (H_{XX} or V_{XX}), leaving an X_H (or X_V) in the dot. The mutual wavefunction is thus given by,

$$|\Psi\rangle = \frac{1}{\sqrt{2}}(|H_{XX}X_V\rangle + |V_{XX}X_V\rangle) \quad (1.3.7)$$

The energy separation between decay channels gives rise to a time-dependent phase ($e^{-iS\tau/\hbar}$), producing an entangled state after the decay of $|X\rangle$ to ground state (GS) by emitting X photons,

$$|\Psi\rangle = \frac{1}{\sqrt{2}}(|H_{XX}H_X\rangle + e^{-\frac{iS\tau}{\hbar}} |V_{XX}V_X\rangle) \quad (1.3.8)$$

Fig. 1.13 shows the exemplary spectrum corresponding to the energy of photons from different excitons in Fig. 1.13(a), where the FSS can be distinguished by polarization-dependent measurement. A large FSS leads to two-photon states that oscillate between two Bell states with an exponentially evolving phase as a function of X lifetime. However,

slow detection system ($\tau_d \gg \hbar/S$) will also average the exponential phase term, causing only classical correlations detected even with a finite FSS [119]. While a fast detection system with a higher detection resolution ($\tau_d \ll \hbar/S$) will render two cascade channel indistinguishable again, owing to Heisenberg uncertainty relationship ($\Delta E \geq \hbar/2\tau_d$) [117]. Therefore, the solution of obtaining high fidelity of polarization entanglement from a single QD is to eliminate the FSS [120] or develop fast detection systems [117, 121] as shown in the inset of Fig. 1.13(b). The color map manifests that a highly entangled photons with average concurrence close to unity would be obtained as small as FSS and time bins of detectors.

1.3.3 Optical gate effect on charge states

Although semiconductor QDs have been demonstrated to be the promising candidate to generate single photons and entangled photon pairs truly on-demand, providing high-purity single photons, high-fidelity entangle photon pairs etc., the imperfection of quantum efficiency still inhibits the application of such a source in quantum information processing.

The overall brightness of QDs based photon sources is further influenced by the excitation efficiency, corresponding to the probability of QDs being occupied at the desired state under resonant excitation [122, 123]. The physical reasons behind are mostly explained by the intrinsic Coulomb blockade due to the charge carrier capture process [124, 125]. Fig. 1.14(a) presents the blinking dynamics of the photon emission from the QD within the charge and neutralization process of the ground state. The QD stays neutral and single photons are continuously emitted from the spontaneous transition processes in a time range of τ_{on} . However, neutral exciton photon emission is quenched once the QD is charged, leading to photon emission from the transition of other excitonic states within τ_{off} .

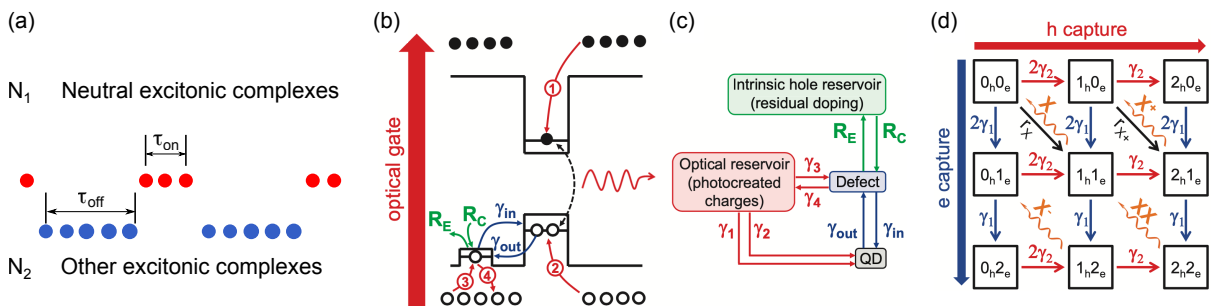


Figure 1.14: (a) Sketch of optical blinking of the QD emission. (b) Diagram of optical gate effect on InAs QDs. Charge carriers from GaAs barrier are captured by the QD and the defect. (c) Diagram of carrier capture process in the QDs system, involving photon-created charges by optical gate laser. (d) Diagram of population model. Reprinted figures (b), (c), and (d) with permission from [125]. Copyright 2012, American Physics Society, without any changes made.

An all-optical approach to stabilize the solid-state charge environment for a resonantly

excited QD is the concept of photoneutralization of charges by illumination with an additional weak gate laser as illustrated in Fig. 1.14(b). Intrinsic charges (e.g., holes) introduced by residual doping of the sample will prefer to be trapped (or de-trapped) by the defect with capture (escape) rate of R_C (R_E). In the case that the defect is located in the vicinity of the QD, the defect state will interface with the hole state of the QDs via a tunneling channel corresponding to injection rate of γ_{in} and inverse rate γ_{out} . The appearance of gate laser will excite additional electrons and holes injected into the QD (process 1 and 2) and the defect (process 3 and 4). The overall diagram of interaction in such a system is shown in Fig. 1.14(c). Apart from the transitions between defect and intrinsic reservoir QD, optical gate laser provide additional two channels between the barrier and the defect with the QD. The population of average number of electrons and holes in the defect and the QD can be described in the following equations,

$$\begin{aligned}
 \frac{dn_p}{dt} &= R_C(2 - n_p) - R_E n_p - \gamma_{in}(2 - n_h)n_p + \gamma_{out}(2 - n_p)n_h + \gamma_3(2 - n_p) - \gamma_4 n_p \\
 \frac{dn_h}{dt} &= \gamma_{in}(2 - n_h)n_p - \gamma_{out}(2 - n_p)n_h + \gamma_2(2 - n_h) - \gamma n_h n_e \\
 \frac{dn_e}{dt} &= \gamma_1(2 - n_e) - \gamma n_h n_e
 \end{aligned}
 \tag{1.3.9}$$

where n_p represents the average number of holes in the defect, n_h, n_e are the average number of holes and electrons in the QD, $\gamma_1(\gamma_2)$ stand for the electrons(holes) capture rate in the QD from the barrier, $\gamma_3(\gamma_4)$ is the hole capture (escape) rate from the defect, γ corresponds to radiative decay rate in excitonic state recombination process. By assuming the relationship as below,

$$R_C, R_E, \gamma_1, \gamma_2, \gamma_3, \gamma_4, \gamma \gg \gamma_{in} \gg \gamma_{out}
 \tag{1.3.10}$$

the model in Equ. 1.3.9 can generally explain physical dynamics of chargers of the QD system under gate laser. To gives a deep understanding of the population of various charge configuration of the QD, Fig. 1.14(d) schematize the process considering the X, positive and negative exciton X^\pm , and XX state corresponding to the radiative rates of γ_X , γ_{X^\pm} , and γ_{XX} , respectively. The probability of charge configuration in the QD can be calculated by replacing second and third terms of Equ. 1.3.9 with following equations:

$$\frac{dP}{dt} = T \cdot P
 \tag{1.3.11}$$

where P is,

$$P = \begin{pmatrix} P_{0h,0e} \\ P_{0h,1e} \\ P_{0h,2e} \\ P_{1h,1e} \\ P_{1h,2e} \\ P_{2h,1e} \\ P_{2h,2e} \\ P_{2h,0e} \\ P_{1h,0e} \end{pmatrix}, \text{ with } \sum P_{i_h,j_e} = 1 \quad (1.3.12)$$

T is the tensor of transition rates of different charge configurations in the QD under resonant pumping [125, 126]. γ_{in} and γ_{out} are negligible in this model since they are far slower than transition rates γ_1 and γ_2 . Taking into account that the population of electrons and holes created in barriers by gate laser are captured by optical phonon emission and Auger processes, γ_1 and γ_2 can be effectively tuned in terms of power of weak gate laser to control the population of charges in the QD.

1.4 Overview of this thesis

The general scope of this thesis is to depict how semiconductor QD-based single or entangled photon sources are developed towards the realization of quantum communication.

Chapter 2: We show how to prepare and characterize a QD-based optical device from sample growth, fabrication and optical measurements. Fundamental knowledge for optical elements calibration and photon polarization state manipulation are discussed for a better understanding of entanglement swapping by the use of a single QD as the entangled photon source.

Chapter 3: To overcome optical losses in telecommunication fiber or free space for long-distance transmission, quantum repeater schemes are proposed as a quantum-mechanical equivalent of a classical signal amplifier. Core feature of such a repeater is entanglement swapping. Here we show the first experimental evidence of entanglement swapping achieved with a single GaAs/AlGaAs quantum dot. Entangled photon pairs are obtained after performing a Bell state measurement on two photons, one from each of two pairs of entangled photons. We believe that this achievement is a milestone in the development of hybrid semiconductor quantum repeaters for quantum communication applications.

Chapter 4: We propose the discussion of challenges of quantum networks with semiconductor entangled photon sources. We stress the necessity of tuning the exciton fine structure, and explain why the often observed time evolution of photonic entanglement in quantum dots is not applicable for large quantum networks. The consequences of device fabrication, dynamic tuning techniques and statistical effects for practical network

applications are also investigated.

Chapter 5: To realize a long-distance quantum communication in practice, quantum light sources emitting high-rate photon at telecom band is essential. A dielectric antenna structure is presented to extract single photons at telecom O-band from InGaAs/GaAs QDs. An efficiency of 17 % is experimentally determined. By measuring 57 QDs, we can observe a brightness enhancement of up to 180 times compared to the as-grown sample. Extraction efficiencies of up to ~ 38 % are obtainable, confirmed by finite-difference time-domain (FDTD) simulations.

Chapter 6: Apart from low collection efficiency on account of high contrast of refractive indices between the semiconductor matrix and the vacuum space, the imperfect excitation efficiency caused by Coulomb blockade owing to the defects in the vicinity of the QD inhibits the overall brightness of the source. We report, for the first time, on the photo-neutralization of GaAs/AlGaAs quantum dots excited by two-photon resonant pumping. By appropriate control of power and wavelength of gate laser, we observe an increase in excitation efficiency of 30 % with a stable entanglement fidelity. Moreover, A surface passivation method using octadecanethiol (ODT) is introduced to circumvent the quenching of PL intensity and linewidth broadening effect, provided that the QDs are close to the top surface, thereby suffering charge fluctuation and trap states on the surface. From the investigation of different thickness of the capping layers on top of the QDs, we find that the degraded intensity and coherence of QDs emission can be partially restored, implying the elimination of additional charge state and tunneling channels at the surface.

Chapter 7: Achievements of this thesis are summarized, together with some discussions regarding the perspective, challenges and solutions in the current research field.

Background and fundamental methods

In this chapter, the basic knowledge of experimental methods in this thesis will be introduced, starting from the growth of the semiconductor QDs as-grown sample. By means of feed-forward strain tuning techniques, along with experimental methods of characterizing the quality of photon emission from QDs, it is possible to develop the QD to be the promising single or entangled photon sources. Finally, the demonstration of an essential quantum application, i.e., entanglement swapping based on one single quantum dot is discussed, laying the foundations for scalable semiconductor based quantum networks.

2.1 Sample growth and fabrication

To implement quantum information science using semiconductor based photon sources, it is mandatory that the photon emission of the sources possess the properties of high quantum efficiency, single photon purity, indistinguishability, scalability, and high entanglement fidelity of entangled photon pairs. Thus, it proposes high demands for sample growth and additional tuning methods to counteract the imperfections. In this section, description of sample growth and corresponding sample structure are discussed, followed by the strain-induced tuning techniques for quantum dots (QDs).

2.1.1 Epitaxial quantum dots

Molecular beam epitaxy (MBE) is a technique which is the earliest developed in the late 1960 [127], allowing the growth of high-quality single crystal layers with low impurity. QDs grown by MBE [128] have so far shown the greatest potential for semiconductor light sources due to their high reproducibility and photon coherence. Fig. 2.1(a) shows the photograph of a MBE machine for developing III-V semiconductor QDs by *in-situ* local droplet etching and nanoholes infilling methods (Fig. 2.1(b)). Al droplets form at the surface of AlGaAs (001) bottom layer after the deposition of a layer of Al, followed by

As content in the AlGaAs bottom layer dissolved from the diffusion of Al. Self-assembled nanoholes with ultra-high in-plane symmetry are created, which are subsequently filled by deposition of GaAs and capped with a layer of AlGaAs. A low density of quantum emitters with a magnitude of $1 \times 10^8 \sim 1 \times 10^9 \text{ cm}^{-2}$ is therefore formed.

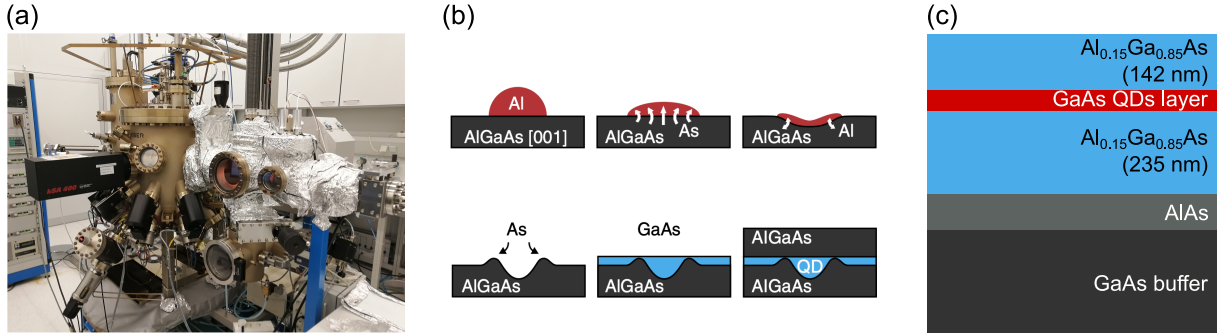


Figure 2.1: Growth of epitaxial QDs. (a) Photograph of the MBE machine. (b) Growth procedures of GaAs/AlGaAs QDs. (c) Sketch of cross-section of as-grown sample structure. Reprinted figure (b) from [128]. Copyright CC BY 4.0 [102], Springer Nature, without any changes made.

The whole as-grown sample structure is displayed in Fig. 2.1(c), where AlAs is grown as sacrificial layer between GaAs buffer and the AlGaAs bottom layer for the further sample processing. By carefully optimizing the size of QDs, the emission wavelength can be manipulated in a broad spectra range by controlling of confinement [129]. The manipulation of Al content in AlGaAs top and bottom layers are an effective tool to lift the band gap of barrier layer up the GaAs QDs. The optimal extraction efficiency of photons from the QDs is obtained through the design of thickness of the top and bottom layers, in terms cavity effect [130].

2.1.2 Strain-tunable quantum dots based devices

Although semiconductor QDs-based emitters potentially exhibit unbeatable performance with respect to the deterministic non-classical photon emission with no physical limits in contrast to SPDCs, ‘no two snowflakes are alike’ is a principle that also seems to hold for QDs. Their growth is governed by randomness in shape, material composition, and internal strain fields. This inability to grow perfect QDs is a major challenge: As an example, key elements in quantum information processing [131, 132, 133] such as two-photon interference (TPI) require photons from different sources to be indistinguishable. In order to modify the electronic and optical properties of QDs to e.g., counteract the broad emission wavelength distribution, several post-growth tuning techniques were exploited, via such as temperature [134, 135], electric field [136], or magnetic field [137].

In this subsection, we recapitulate fabrication of strain-induced hybrid devices for the independent tuning of semiconductor III-V QDs [120, 139, 140, 141, 142, 143, 144, 145,

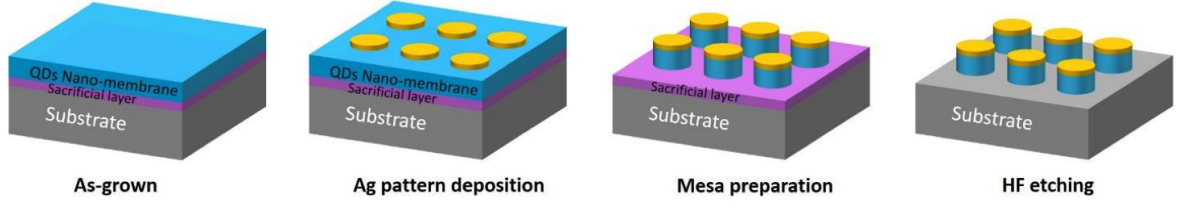


Figure 2.2: Fabrication of free-standing QDs containing nanomembranes. Reprinted figure from [138]. Copyright CC BY 4.0 [102], Springer Nature, without any changes made.

146], starting from the fabrication of free-standing QDs containing nanomembranes (Fig. 2.2). Photolithography is performed on the as-grown sample to define an array of circle (or rectangular) pattern, followed by the deposition of a layer of silver (or gold) and a subsequent lift-off process. Ag pattern is formed at the surface of the as-grown sample. Next, a solution of sulfuric acid, hydrogen peroxide and deionized water (ratio 1:8:200) is applied to vertically etch the substrate in order to expose the AlAs sacrificial layer. The latter is then removed using 25% hydrofluoric (HF) acid solution to create free-standing membranes [138, 140]. Panel (I) and (II) in Fig. 2.3(a) show the images of membranes (size of $160\ \mu\text{m} \times 120\ \mu\text{m}$ of each piece) on the substrate taken by optical microscope. Most of the membranes in panel (I) are tidily laid out on the substrate with a sunk sign in the center of each membrane, indicating an insufficient selective etching time by HF solution. In contrast, randomly drifted membranes on the substrate illustrated in panel II imply that QDs containing membranes are released from the substrate.

To understand the energy band structure and optical properties of semiconductors as a function of induced strain, $k \cdot p$ perturbation theory is commonly employed [147]. The band structure of a semiconductor is modified under a uniform deformation of the semiconductor caused by the internal or external stress. The effect of strain on the Hamiltonian was investigated by Pikus and Bir in the 1960s [148, 149]. The changes observed in semiconductor lattices subject to strain fields allow manipulating the excitonic states and optical emission features of semiconductor QDs. Panel (III) and (IV) show the images of transferred membranes on the commercial $[\text{Pb}(\text{Mg}_{1/3}\text{Nb}_{2/3})\text{O}_3]_{0.72} - [\text{PbTiO}_3]_{0.28}$ (PMN-PT), which is usually coated by gold layers at the top and bottom. In panel (III), free-standing membranes in panel (I) are transferred on PMN-PT via kirkendall effect between gold layers of nanomembranes and PMN-PT under a certain pressure in a $300\ \text{°C}$ environment for 30 mins (Fineplacer from Finetech company). Since the pressure induced in the transfer process will deform the QDs, an additional layer of polymethyl methacrylate (PMMA) is deposited between PMN-PT and membranes for releasing applied force, followed by a bake process (panel (IV)). Fig. 2.3(b) displays the sketch of strain tunable device, where the PMN-PT carried QDs nanomembranes is placed on a copper sample holder, along with silver glue as the adhesive layer. External voltage is biased on the PMN-PT via the gold layers as the electrodes. Additional solid-immersion lens is then put on top of the

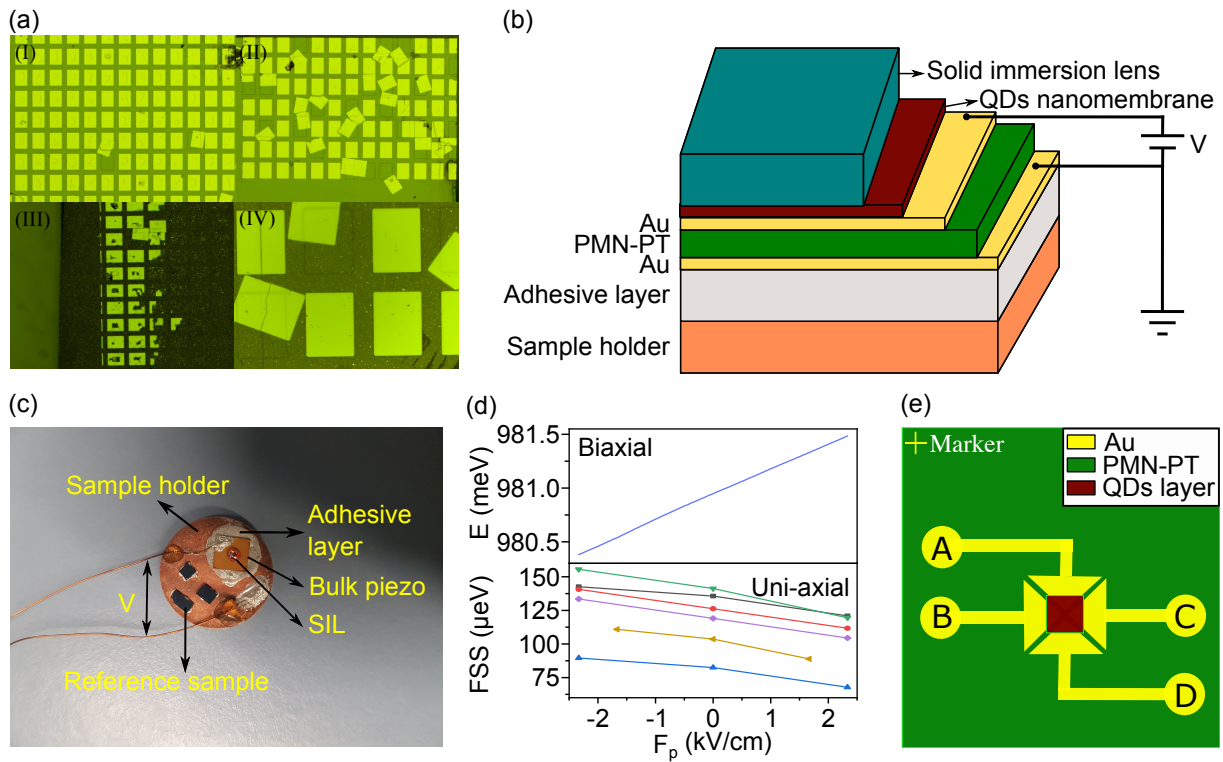


Figure 2.3: (a) QDs containing membranes after HF etching within different time duration. (b) Perspective and (c) photograph of a nanomembrane-based strain tunable device covered by a solid immersion lens. (d) Optical response of the QDs emission under different types of strain. Colorful lines in the lower panel illustrate the tuning effect for a series of QDs (e) Sketch of an isotropic strain tunable device.

hybrid structure to extract more photons from the QDs. Fig. 2.3(c) shows the photograph of the top view of the device. Several reference samples are additionally placed next to the lens for calibrating the performance of device. In the experiment, the device is loaded in a 4 K Helium cryostat biased by an external source meter unit, with a tunable voltage from (-700 V to 700 V) resulting in compressive or tensile strain. The types of PMN-PT determine the orientation of strain transferred to the QDs in the membranes. As represented in the upper panel of Fig. 2.3(d), bi-axially applied compressive (tensile) strain deforms the size of a QD uniformly, leading to linear tuning of the emission wavelength as a function of the strain field. Biaxial strain tuning is a reliable method to engineer the QD electric structure in a precise and reversible way [139, 140, 141]. The strain-tuning of the photon emission wavelength can resolve the scalability difficulty in quantum interference-related experiments using different semiconductor sources. Instead of adjusting the size of QDs, the employed uni-axial actuator employs strain to the membranes along single axis [131, 150, 151]. An appropriate uni-axial strain to the QDs improves the symmetry of the confinement potential so that the fine structure splitting (FSS) can be adjusted as shown in the lower panel of Fig. 2.3(d) [120, 145].

Although uni-axial or bi-axial strain enables the wavelength-tuning of single photons or the generation of high-fidelity entangled photons from QDs, wavelength-tunable entangled photon emission has to be demonstrated to ensure the indistinguishable photons from separate emitters towards the application of such sources in quantum information networks, e.g., entanglement swapping. Fig. 2.3(e) shows a strain tunable quantum dot entangled photon source fulfilling this task. A layer of gold pattern is deposited on the Si-based commercial PMN-PT by photolithography, followed by vertical etching approximately 10-15 μm via reactive-ion etching (RIE). Then, focused ion beam (FIB) is employed to penetrate the piezoelectric crystal into four parts in a shape of ‘ \times ’. A piece of QDs containing nanomembrane is finally placed at the center with PMMA as the glue layer. The emission wavelength and FSS can be independently tuned by strain induced along two orthogonal directions of such a thin film PMN-PT with two independent pairs of electrodes [143] (A-D and B-C). Hence, a silicon-integrated wavelength-tunable QDs-based source emitting high-fidelity entangled photon pairs has been realized.

2.2 Optical excitation setup

Apart from the preparation of the QDs sample, customized optical setups are also necessitated to accomplish the functionalities of characterizing the qualities of photon emission from the QDs, which are the excitation and collection setups. Fig. 2.4 illustrates the sketch of self-built excitation setup with various functionalities, i.e., doubling of frequency and repetition rate, pulse slicing/shaping, and simultaneous excitation of multiple QDs by pulsed and continuous-wave (cw) lasers.

The part of optical setup in the top right corner of Fig. 2.4(a) is constructed to distribute the wavelength-tunable cw laser (Ti-Sapphire from M2 company) to many branches for above-band excitation, quasi-resonant excitation, photoluminescence excitation (PLE), etc., or as benchmark to calibrate the quality of optical instruments and setups. To excite the QDs on-demand, a wavelength-tunable Ti-Sapphire pulsed laser (Coherent Chameleon Ultra II) with pulse duration shorter than the radiative decay time of QDs is employed. In the top left frame of 2.4(a), the laser is switched to go either frequency doubling path through BBO crystal with up-conversion of frequency, or pulse slicer setup for narrowing down the laser linewidth from 12 nm to 1 nm.

The main body of the optical excitation setup consist of three functionalities, which can be simplified in 2.4(b). When the pulsed laser pass through the BS, the intensity of a single pulse will be divided into two pulses for the excitation of separated QDs (Panel 1). As a consequence, the photon emission from these QDs will be synced with an adjustable time delay via a linear stage in one path between the BS and the QD. To realize the amplification of the repetition rate (period of pulse $T = 12.5$ ns), a Mach-Zehnder interferometer is built as shown in panel 2. A single laser pulse is split into two by the first BS. One pulse propagates along the length-tunable path controlled by a linear stage,

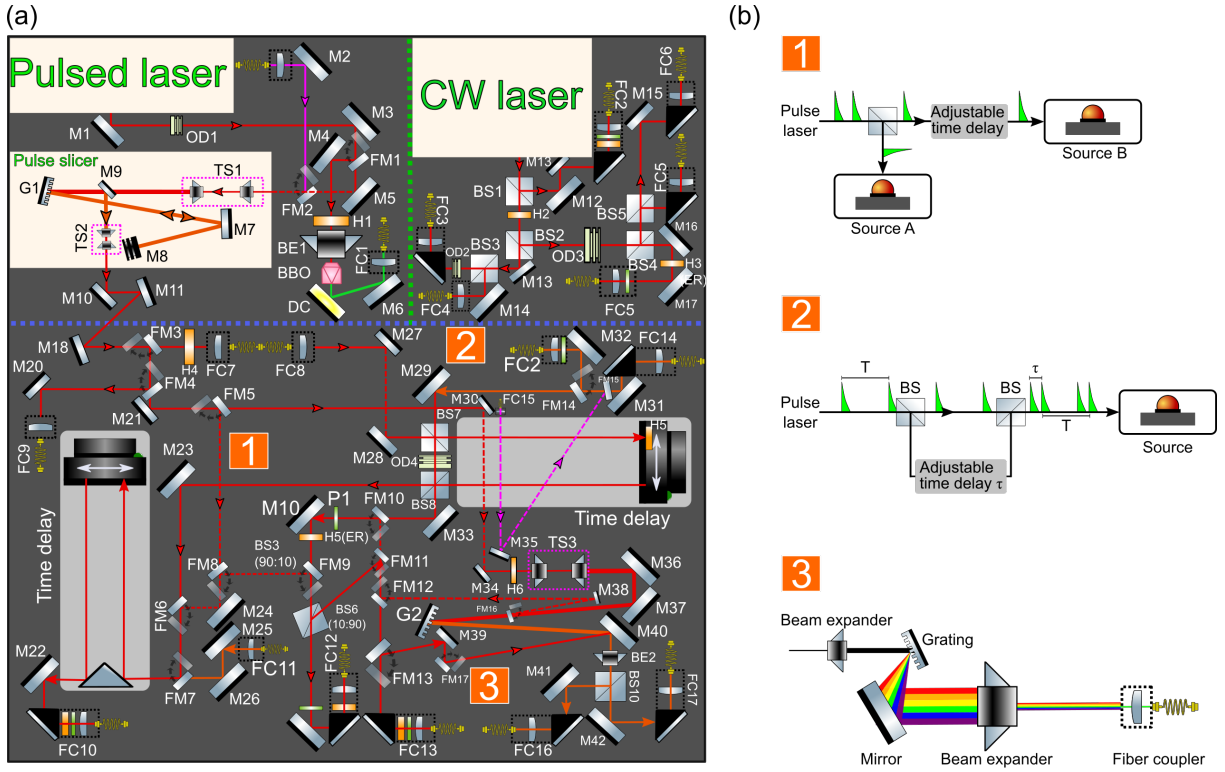


Figure 2.4: Schematic of the excitation setup for the QDs characterization. (a) Overview of the self-built optical excitation setup powered by a pulsed laser with a repetition rate of 80 MHz, pulse duration of 140 fs, wavelength tuning range from 680 nm to 1080 nm, and a cw laser with linewidth of 100 kHz, wavelength tuning range of 723 nm ~ 1080 nm. (b) Schematic of the components of the excitation setup used to customize the pulses from the laser, allowing for specific excitation schemes.

giving rise to a time delay of τ after the pulse entering the other path. Then laser pulses from two paths are coherently coupled at the second BS, with repetition rate of 160 MHz pulses coming from the two output ports of second BS. Such an optical setup enable the enhancement of brightness from QDs and further characterization of indistinguishability of photon emissions. Panel 3 in Fig. 2.4 shows the sketch of pulse shaping setup as similar as pulse slicing [152, 153], which is introduced to further narrow down the linewidth of the pulsed laser for TPE. To efficiently scatter the laser light on the grating, a beam expander is first used to broaden the beam size for 3 times. After the diffraction of the grating, a sequence of laser beams spatially distributed in wavelengths are created. A fiber coupler is placed behind a second beam expander for picking out preferred excitation wavelength and linewidth by adjusting the position of the fiber coupler. For GaAs/AlGaAs QDs, the binding energy between XX and X photons is around 4 meV corresponding to ~ 2 nm, so that TPE requests the laser energy to be half of the total energy of X and XX photons,

$$\lambda_{laser} = \frac{2\lambda_X \cdot \lambda_{XX}}{\lambda_X + \lambda_{XX}} \quad (2.2.1)$$

The linewidth of the pulsed laser coming out from such a pulsing shaping setup is usually below 0.1 nm (~ 3 ps), which is sufficient to avoid interactions with either X or XX photon signals.

2.3 Optical characterization for quantum dots emission

To adapt semiconductor QDs to be the optical sources in quantum information applications, it is essential to evaluate the photon emission quality from the QDs-based as-grown sample or devices by various measurement methods. Fig. 2.5 presents the overview of optical characterization setup. After the optical illumination by pulsed or cw lasers, a QD is pumped to the excited state, emitting single photons or entangled photon pairs in the next radiative decay process. The excitation laser is then blocked out from the light path by the use of optical filters, leaving the photoluminescence (PL) signals entering into the characterization setup. When all the flip mirrors in the light path are flipped down, the signal is directly sent to spectrometer from the bottom light path. The signals will arrive charge-coupled device (CCD) of spectrometer 2 passing through the grating stage of spectrometer 1, leading to a high resolution calibration for the spectrum of signals. However, suppose the first flip mirror in the bottom light path is on, the light will be directly guided into spectrometer 2 for spectroscopy measurements.

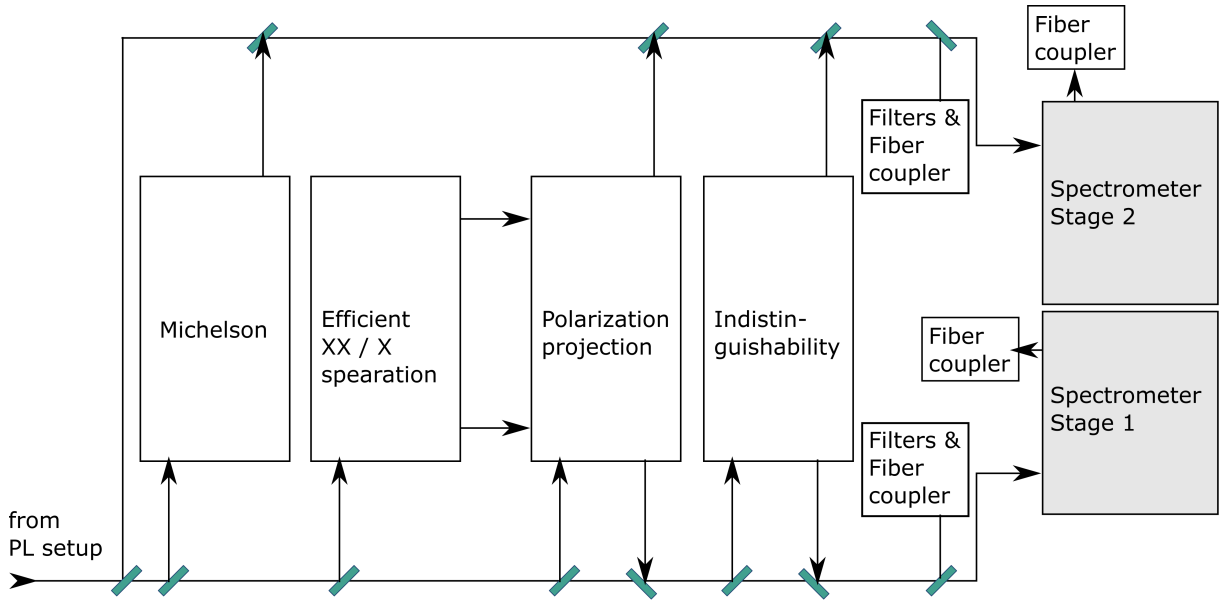


Figure 2.5: Overview of the signal characterization setup for the QDs. Specific characterization tasks are executed by switching specific flip mirrors (green blocks) on and off.

The other deterministic measurements are carried out by switching on both flip mirrors at top and bottom of corresponding characterization setup box, i.e., Michelson setup, indistinguishability setup. For polarization projection measurement, there are two possi-

bilities. One is to guide the signals into efficient XX/X separation setup, and XX and X photons are independently filled into projection setup for measurement. After polarization projection, the signals are then coupled into the fiber couplers in front of spectrometers which are connected with superconducting nanowire single photon detectors (SNSPDs). The other convenient but inefficient way is to first send the signals into the projection setup. Signals coming out from top and bottom paths are then individually sent to two spectrometers for spectrum selection. The picked out XX and X signals in terms of wavelengths are then coupled into the fiber couplers after spectrometers for the further single photon detection. In the following subsections, the discussion about these measurements will be introduced more in details.

2.3.1 Micro-photoluminescence spectroscopy

Micro-PL spectroscopy, as a basic optical approach in the study of quantum optics, is an effective tool for extracting the dynamic information of quanta in QDs. To characterize the cryogenic PL, the laser is applied to excite the QDs-based sample loaded in the low temperature cryostat (Montana Instrument C2 cryostation in our system). By collecting the signals emitted from the sample and guide them into the spectrometer, we are able to perform a sequence of analysis measurements (Fig. 2.6(a)). To characterize the statistics of the QDs, the sample is mounted on the positioning stages from Attocube with the degrees of freedom along x, y, and z directions in a range of 5 cm of each, and the whole stages are loaded in a vacuum environment of 4 K. Three gratings with different resolution (300/1200/1800 lines/mm) are configured inside the spectrometer, allowing the extraction of spectrum information depending on the requirements.

Fig. 2.6(b) shows the exemplary PL spectra acquired from a QD under above-band excitation from a cw laser (red), or TPE of pulsed laser (blue). From above-band excitation spectrum, a cluster of transition peaks appear around the XX peak due to the probabilistic capture of electrons and holes by the QDs generated in the barrier layer. This leads to the possible observation of odd and even number of carriers occupied in the potential energetic level of the dot. In contrast to non-resonant excitation scheme, π -pulsed resonant excitation of the *s*-shell of the QD is the ultimate method in order to obtain optical bright excitons with an excitation efficiency of unity. Apart from the advantage of deterministic excitation of the specific state, the time jitter and phonon scattering process are avoided as well, giving rise of the high photon indistinguishability and repetition rate of photon generation. The blue spectrum in Fig. 2.6(b) presents the PL of the same QD under TPE with pulsed laser energy in the middle of XX and X photon peaks. The laser background is blocked out by a series of notch filters, whose linewidth is approximately $\Delta\lambda_{notch} = 0.3$ nm. The other complex excitonic transition states disappear comparing with the spectrum under the non-resonant excitation (Fig. 2.6(a)).

A typical characteristic of resonant excitation is the rabi oscillation in the power depen-

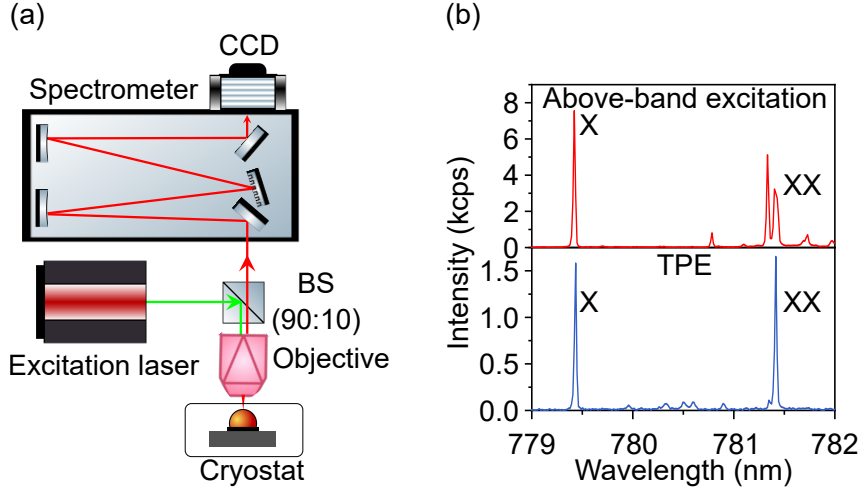


Figure 2.6: (a) Sketch of experimental setup for characterizing the PL spectrum from QDs samples. The excitation laser beam is reflected by a 90:10 BS (T:90, R:10), and hit on an optical objective which has a magnification of $\times 100$, numerical aperture of 0.7, and working distance of 10 mm in a wavelength range from 480 ~ 1800 nm. The laser beam is then focused on the sample loaded in a 4K close-cycle gas helium cryostat. The PL signals from the QDs and reflected laser are then collected by the objective, and sent to the spectrometer. The spectrum information of the signal is thus adapted by the CCD, after the dispersion of a grating. Laser signals are blocked in the transmission light path after BS by some long pass or notch filters (not shown). (b) PL spectra from a single QD under above-band excitation by a cw laser (upper panel), and TPE by pulsed laser (lower panel).

dent intensity measurement. The occupation probability of the excited state is written as,

$$P = \frac{\Omega_R^2}{\Omega^2} \sin^2(\Omega t/2) \quad (2.3.1)$$

and

$$\begin{aligned} \Omega^2 &= \Omega_R^2 + \Delta\omega \\ \Omega_R^2 &= |\mu E_0/\hbar|^2 \end{aligned} \quad (2.3.2)$$

where Ω_R denotes the rabi oscillation frequency, $\Delta\omega$ is the detuning frequency of excitation laser off from the resonance, μ is the dipole moment, E is the amplitude of the electromagnetic wave. For perfect resonant excitation ($\Delta\omega = 0$), the transition probability varies as a function of the electric field amplitude in a form of sinusoidal oscillation. The pulse area Θ is defined according to,

$$\Theta = \left| \frac{\mu}{\hbar} \int_{-\infty}^{\infty} E(t) dt \right| \quad (2.3.3)$$

which is a dimensionless parameter determined by pulse energy. An excitation pulse with pulse area equal to π is called as π -pulse, promoting the system to excited state.

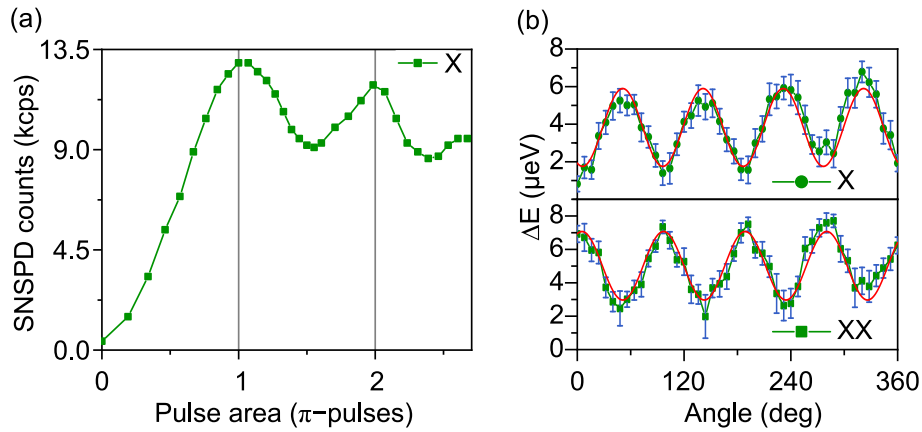


Figure 2.7: (a) PL intensity fluctuation as a function of pulse area. (b) Oscillation of the emission energy of X and XX photons, as a function of polarizer rotation angle in polarization dependent measurement with fitting curves (red lines).

The oscillation period at the low excitation power is longer than the spontaneous radiative lifetime causing inefficient pumping probability, while a high power excitation for shorting the period is impossible in practice due to damping mechanism, which usually consists of population decay and population-conserving scattering processes (or called ‘dephasing’). At the presence of the damping process, the spontaneous radiative rate is negligible and the rates of stimulated emission and absorption equal out, resulting in asymptotic limit at a high power. Fig. 2.7(a) displays the phenomenon of Rabi oscillation, in which the PL intensity of the QD oscillates as a function of the pulse area depending on the excitation power.

On the other hand, the information of FSS can be acquired by implementing the polarization dependent measurement. In the experiment, an electronically rotatable polarizer is put after the BS in Fig. 2.6(a). As described in the previous chapter, the FSSs caused by the asymmetry of the QDs yield the energy splitting of the single transition peak correlated with polarization of photons. Therefore, the energy splitting of emitted photons can be detected as a function of the polarization as Fig. 2.7(b). By rotating the polarizer from 0° to 360° uniformly, the emission energy of transmitted XX or X photons after polarizer will wander in an energy difference range, in corresponding to two perpendicular polarization states. The XX and X states show same oscillation amplitude equal to S but inverted phase, owing to the conservation of the total z-spin momentum of the bright excitons. The FSS value S is then extracted from the amplitude by fitting of the oscillation curves.

2.3.2 Coherence time measurement

Coherence in quantum optics is generally referred to describe the stability of the light, classified into temporal and spatial coherence. The temporal coherence of light, called

‘coherence time’ (T_2), represents the time duration over which the phase of the electromagnetic wave train to be stable. In a classical view of light as electromagnetic wave, the coherence time can be accurately determined by the first-order correlation function $g^{(1)}(\tau)$,

$$g^{(1)}(\tau) = \frac{\langle E^*(t)E(t+\tau) \rangle}{\langle |E(t)|^2 \rangle} \quad (2.3.4)$$

where E and $E^*(t)$ denote the electric field and its conjugated value, and $\langle \dots \rangle$ indicate the average over a long time interval T , defined as:

$$\langle E^*(t)E(t+\tau) \rangle = \frac{1}{T} \int_T E^*(t)E(t+\tau)dt \quad (2.3.5)$$

In case that we assume a quasi-monochromatic light field with a central frequency of ω_0 is $E(t) = E_0 e^{-i\omega_0 t + \phi(t)}$, then,

$$g^{(1)}(\tau) = e^{-i\omega_0 \tau} \langle e^{i[\phi(t+\tau) - \phi(t)]} \rangle \quad (2.3.6)$$

The first term at the right of the equation indicates that the real part of $g^{(1)}$ oscillate in a period of $2\pi/\omega_0$, and the second term reveals the relationship between time t and $t+\tau$, corresponding to coherence time. For light with the Lorentzian shape of linewidth $\Delta\omega$, $g^{(1)}(\tau)$ is given by,

$$g^{(1)}(\tau) = e^{-i\omega_0 \tau} e^{-\frac{|\tau|}{T_2}} \quad (2.3.7)$$

and the coherence time T_2 is defined at when $g^{(1)}(T_2) = g^{(1)(0)}/e$,

$$T_2 = \frac{1}{\Delta\omega} \quad (2.3.8)$$

For light with the Gaussian shape of linewidth $\Delta\omega$, $g^{(1)}(\tau)$ is given by,

$$g^{(1)}(\tau) = e^{-i\omega_0 \tau} e^{-\frac{\pi}{2} \left(\frac{\tau}{T_2} \right)^2} \quad (2.3.9)$$

where the coherence time T_2 is,

$$T_2 = \frac{(8\pi \ln 2)^{\frac{1}{2}}}{\Delta\omega} \quad (2.3.10)$$

In the Michelson interference measurement (Fig. 2.8(a)), the single photon stream is first split into two paths by a beam splitter (BS). One beam is reflected by a reflector and hit on the BS after passing through a fixed length of light path. The other transmitted beam is reflected by a 180°-reflector placed on a movable piezo stage that is loaded on an electronically controllable linear stage. The spatially overlapped reflected beams are finally sent to the spectrometer for spectra analysis, by scanning the time delay between two arms. Fig. 2.8(b) displays the photography of the Michelson interferometer

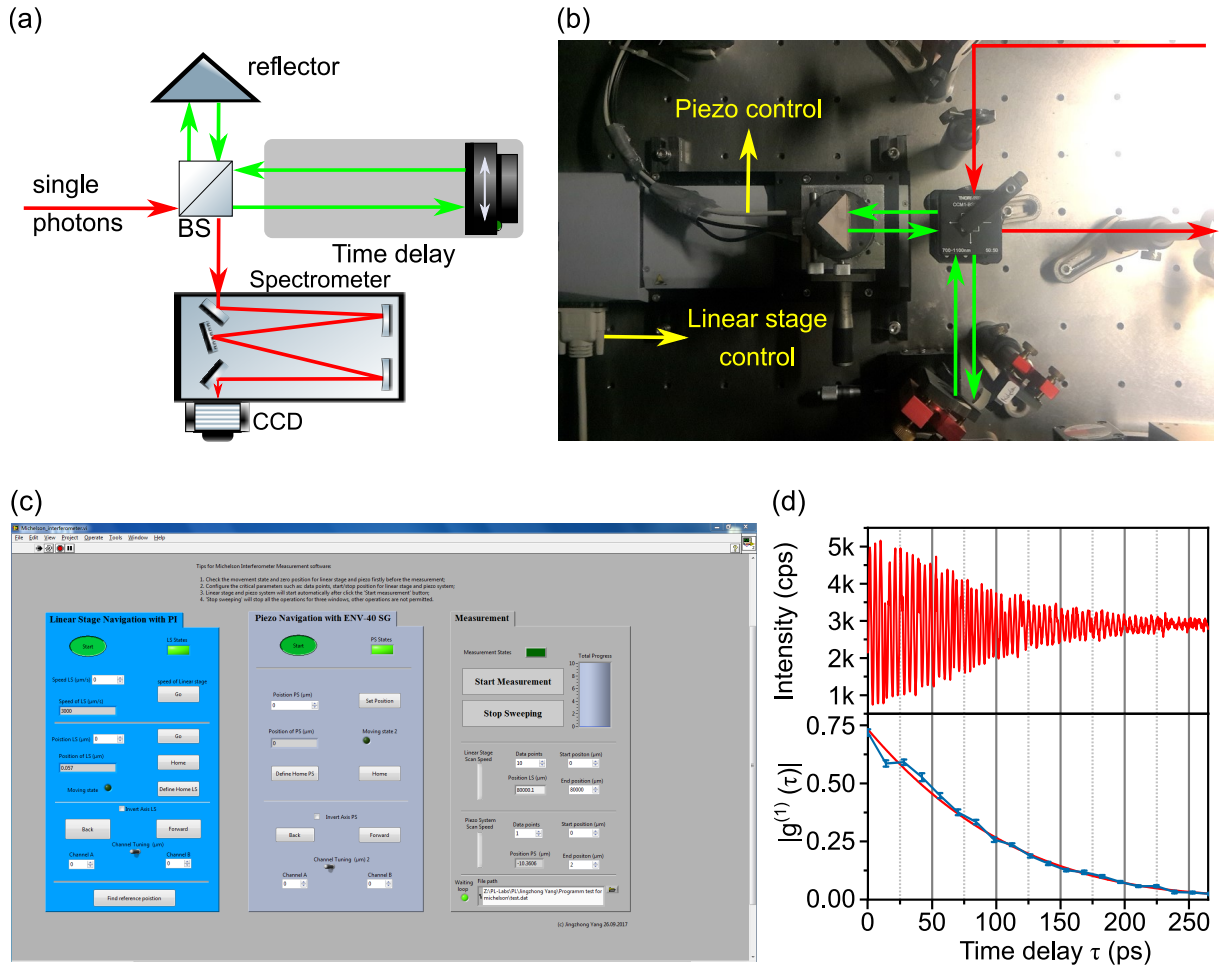


Figure 2.8: (a) Sketch, (b) photograph, and control software (c) of Michelson interferometer for characterizing the coherence time of photons. (d) Exemplary measurement result for the first-order correlation function of a single QD.

in experiment. The read lines denote the input and output light path, and green lines imply two separated light paths of the interferometer. The linear stage and piezo stage are independently controlled by computer via self-programmed control software based on Labview (Fig. 2.8(c)). As shown in the graphic user interface, the software is comprised of three panels. From the left to the right, these panels are used to independently control the position of linear stage, piezo stage, and automatic scanning of time delay for coherence time measurement. In the experiment, the electric field of light coming out from the interferometer can be expressed as,

$$E^{(out)}(t) = \frac{1}{\sqrt{2}}(E(t) - E(t + \tau)) \quad (2.3.11)$$

The average intensity of the light is thus [115, 154],

$$\begin{aligned} I^{(out)} &= 2 \cdot I_0 \cdot [1 + \text{Re}(g^{(1)}(\tau))] \\ &= 2 \cdot I_0 \cdot [1 + |g^{(1)}(\tau)| \cdot \cos\phi(\tau)] \end{aligned} \quad (2.3.12)$$

where I_0 is the intensity of single photon signal, τ is the time delay between two light paths in the Michelson interferometer ($\tau = \Delta L/c$). According to Equ. 2.3.12, the interference fringes in intensity appear as a function of τ , and the visibility of interference $V(\tau)$ is defined as,

$$\begin{aligned} V(\tau) &= \frac{I_{max} - I_{min}}{I_{max} + I_{min}} \\ &= |g^{(1)}(\tau)| \end{aligned} \quad (2.3.13)$$

where I_{max} and I_{min} are the maximal and minimal intensity of photon fluxes from the transition of studied state, respectively. To obtain the first-order correlation function in experiment, visibility as a function of time delay is measured by scanning the position of movable arm of interferometer. At the beginning, the time delay is set to be zero ($\Delta L = 0$) by the linear stage, and the spectra mapping starts with the movement of piezo stage in a small range such as $1.2 \mu\text{m}$ by 50 data points. An oscillatory graph of intensity as a function of time delay of piezo stage is obtained, allowing the extraction of visibility at zero delay of linear stage by performing sinusoidal fitting for the oscillation of intensity as a function of piezo stage position. Then linear stage move the piezo stage and reflector to the next position away from zero position, followed by a new round of PL spectroscopy mapping to extract the visibility at time delay τ of linear stage. With the scanning of the linear stage position in a range of such as 10 cm by 12 data points, the oscillatory graph of intensity and extracted visibility as a function of time delay induced by linear stage is represented in the upper and lower panel of Fig. 2.8(d), respectively. The latter is then fitted by Equ. 2.3.9, where the amplitude is lower than 1 due to the imperfect overlap of interference beams. This does not affect the correctness of extracted coherence time T_2 .

2.3.3 Coincidence measurement

Coincidence measurement is not only significant for understanding the quantum picture of light, but also a tool for the data processing in quantum applications [155]. The counting of coincidence usually include more than two single photon detectors (SPDs) and a time-correlated single photon counting (TCSPC) system. The TCSPC receives the signals from all the SPDs, and count the number of coincidence of registered signals among independent detectors at certain time delay. The accidental coincidence count rate can be approximately estimated with the formula [156, 157],

$$R_{coincidence} = \tau^{(n-1)} \cdot R_1 \cdot R_2 \cdots R_n \quad (2.3.14)$$

where n is the number of detectors. τ is the repetition period of the pulsed laser, or time bin of the histogram of time-tagging device, and N_1, \dots, N_n are the photon count rates of the SPDs. Taking into account of the dark counts from each detector, the real 2-photon coincidence counts,

$$R_{real} = R_{coincidence} - \tau \cdot (R_1 \cdot R_{2,dark} + R_{1,dark} \cdot R_2 + R_{1,dark} \cdot R_{2,dark}) \quad (2.3.15)$$

with $R_{1,dark}, R_{2,dark}$ the dark count rates of the detectors.

2.3.4 Radiative lifetime measurement

The radiative lifetime is defined as the characteristic feature of the two-level system in atom, depicting the radiation process of the photons due to the relaxation of exciton from the high to the lower energy levels. The rate of such a transition process is governed by the Einstein A coefficient. Assuming the population of the excited state to be denoted as N_e , the dynamic of the radiative process can be expressed by,

$$\frac{dN_e}{dt} = -A \cdot N_e \quad (2.3.16)$$

therefore,

$$\begin{aligned} N_e(t) &= N_e(0) \cdot e^{(-t/T_1)} \\ T_1 &= \frac{1}{A} \end{aligned} \quad (2.3.17)$$

with T_1 the radiative lifetime. The transition rate of spontaneous emission for a free-space dipole can be given by Fermi's golden rule [158]:

$$A = \frac{2\pi}{\hbar^2} |M|^2 g(\omega) \quad (2.3.18)$$

and,

$$M = \sqrt{\frac{\mu^2 \hbar \omega}{6\epsilon_0 V_0}} \quad , \quad g(\omega) = \frac{\omega^2 V_0}{\pi^2 c^3} \quad (2.3.19)$$

where M is the transition matrix, $g(\omega)$ is the density of the states in free space, \hbar is the reduced Planck constant, V_0 is the model volume, ω is the angular frequency of the light, μ is the dipole moment, c is the speed of light, and ϵ_0 is the vacuum permittivity. Thus, the lifetime of an emitter in free-space is,

$$T_1 = \frac{3\pi\epsilon_0 \hbar c^3}{\mu^2 \omega^3} \quad (2.3.20)$$

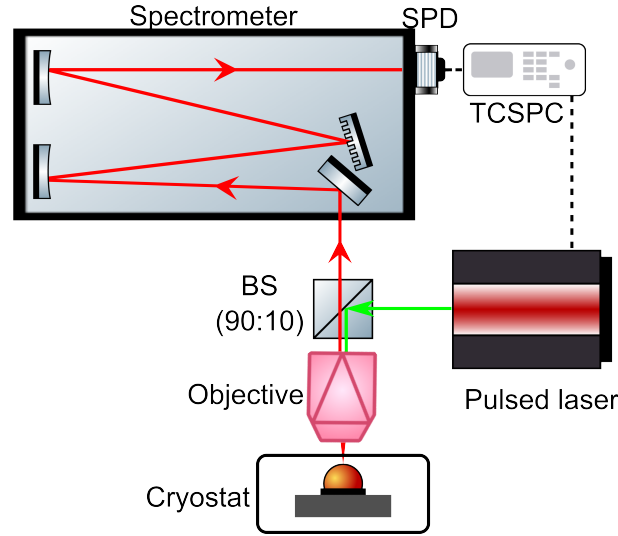


Figure 2.9: Sketch of experimental setup for characterizing the lifetime of QDs.

In the experiment, lifetime is measured by counting the coincidence statistics between the electric triggering signals from pulsed laser and the arrival time of generated photons to the SPD. The recombination of electrons and holes typically possess the lifetime in the time scale of a few hundreds of picoseconds to ~ 1 ns. To get rid of time jitter solely in the radiative lifetime measurement, pulsed laser is employed to resonantly excite the QDs-based as-grown sample as presented in Fig. 2.9, which is loaded in the 4 K cryostat. The emitted photons from the QD is collected by the objective and guided into the spectrometer for a selection of the studied PL transition peak via the grating. The single photons then hit on the SPD, resulting in generation of electronic pulses sent to TCSPC device. The arrival time of each photon is registered by the device working like a timer. Simultaneously, every time the laser sending out an optical pulse, an electronic pulsed signal is directly sent to the TCSPC device.

The coincidence histogram as a function of time delay between the arrival times of the optical signals from XX and X transitions and the electronic signals from pulsed laser are illustrated in Fig. 2.10(a). It reveals the population probability of excitons (N_e) in a form of exponential decay as described in Equ. 2.3.17. For XX state in a three-level ladder system, the modeling function for population probability ($T_{1,XX}$) is given by,

$$I_{XX}(t) = \left[I_0 \cdot e^{-\frac{t}{T_{1,XX}}} \cdot H(t) \right] * I_{IRF}^{(1)} + I_{bg} \quad (2.3.21)$$

with the first term at the right of the equation being the lifetime-related exponential decay. I_0 is the normalization factor of the coincidence counts, I_{bg} is the background of the coincidence, and $H(\tau)$ is the Heaviside function. ‘IRF’ ($I_{IRF}^{(1)}$), the parameter standing for the overall time resolution of the detection system including ramp of pulsed laser, optics, SPDs, and TCSPC, is convoluted with ‘real’ decay in time domain [159]. Fig.

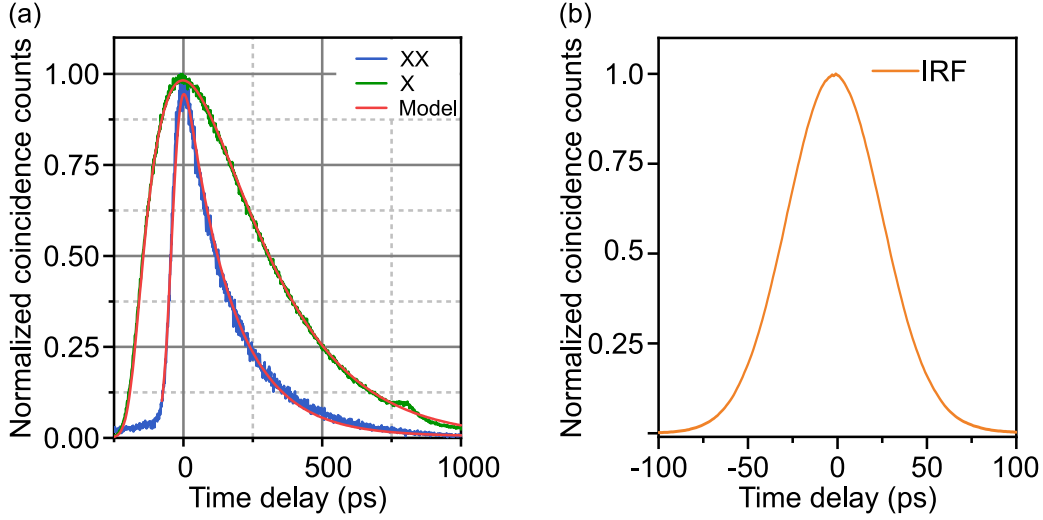


Figure 2.10: (a) Histogram of lifetime measurement for XX (blue) and X (green), fitted with analytical model (red). (b) Exemplary instrument response function (IRF) of the optical system, taking into account of the optics, the SNSPD, and the TCSPC system.

2.10(b) shows the Gaussian-shape IRF in experiment detected by a SPD, by counting the coincidence histogram of the 140 fs pulsed laser signal through the detection system, with the electronic pulses from the laser. The degradation of the time resolution of system is mainly introduced by time jitters of the SPD and TCSPC devices. The fitting of X state is special in the cascade process due to the time jitter correlated with lifetime of XX state. The modeling equation for X is,

$$I_X(t) = \left[I_0 \cdot \frac{T_{1,X}}{T_{1,X} - T_{1,XX}} \cdot \left(e^{-\frac{t}{T_{1,X}}} - e^{-\frac{t}{T_{1,XX}}} \right) \right] * I_{IRF} + I_{bg} \quad (2.3.22)$$

By introducing $T_{1,XX}$ acquired from Equ. 2.3.21 for fitting, the lifetime of X photons ($T_{1,X}$) is extracted.

2.3.5 Second-order intensity autocorrelation

In the Sec. 1.2, the classification of light in terms of the photon statistics is discussed. Herein we illustrate the approach of qualifying light based on the second-order correlation function $g^{(2)}(\tau)$, which reveals the amplitude correlations by use of Hanbury Brown and Twiss (HBT) setup. The photon emitters can therefore be classified as *anti-bunched*, *coherent*, and *bunched* sources.

Hanbury Brown and Twiss were astronomers working in measuring the diameters of stars. However, limited by the physical limit of Michelson stellar interferometer in collection efficiency and resolution, they developed the intensity interferometer to measure the correlations between the photocurrent generated by the starlight that impinges on the two photomultipliers, which enables another easier way to determine the spread angle of

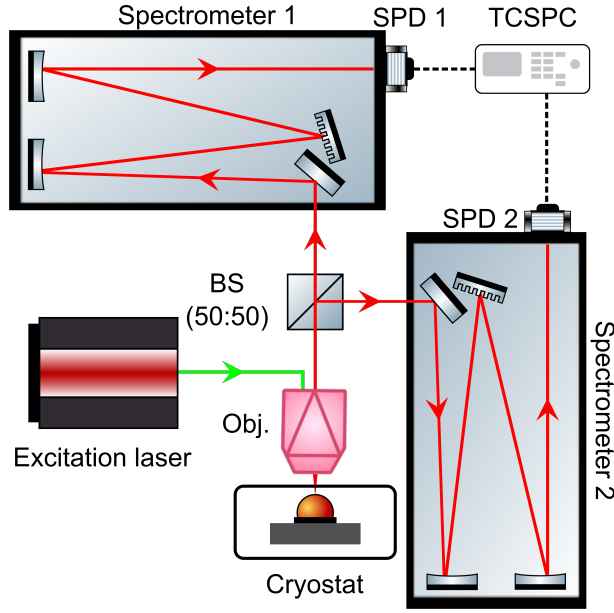


Figure 2.11: Sketch of the HBT setup for measuring the second-order intensity autocorrelation.

light from the star. Fig. 2.11 shows the HBT setup for measuring $g^{(2)}(\tau)$ of light emitted by the QDs. After the laser excitation, emitted photons are collected by the objective and split by an 50:50 BS. Then, two streams of single photons are individually fed into the spectrometers for the selection of a specific transition peak, i.e., X photons. In the end, the TCSPC system will register the arrival times of photons from each SPD and perform the coincidence counting process. The essence of HBT experiment is the intensity fluctuation of a beam of photons relative to its coherence. Which means, if the photons detected by two SPDs are coherent, the intensity fluctuations from each other will also be correlated. From a classical perspective, the intensity of each detector is given by,

$$I_1(t) = I_2(t) \equiv \langle I \rangle + \Delta I(t) \quad (2.3.23)$$

where $\langle I \rangle$ is the mean intensity, and $\Delta I(t)$ is the fluctuation of intensity. With identical intensities on the detectors, the output of HBT is proportional to $\langle \Delta I(t)\Delta I(t + \tau) \rangle$, in which τ is the time delay of photons registered on the different detectors. When τ equals to zero, the output of HBT is,

$$\langle \Delta I(t)\Delta I(t + \tau) \rangle_{\tau=0} = \langle \Delta I(t)^2 \rangle \quad (2.3.24)$$

where $\langle I(t) \rangle$ is zero by definition. $\langle I(t)^2 \rangle$ is not due to the intensity fluctuations for chaotic light. When the time delay $\tau \gg T_2$, the output tend to be zero because of completely uncorrelated intensity fluctuation [158].

The mathematic definition of the second-order correlation function $g^{(2)}(\tau)$ is analogue of the first-order correlation function $g^{(1)}(\tau)$ that determines the visibility of single photon

interference, or in another word, the fluctuation of electric field in time. $g^{(2)}(\tau)$ quantifies the intensity fluctuation, which is defined as,

$$g^{(2)}(\tau) = \frac{\langle E^*(t)E^*(t+\tau)E(t+\tau)E(t) \rangle}{\langle E^*(t)E(t) \rangle \langle E^*(t+\tau)E(t+\tau) \rangle} = \frac{\langle I(t)I(t+\tau) \rangle}{\langle I(t) \rangle \langle I(t+\tau) \rangle} \quad (2.3.25)$$

with $E(t)$ and $I(t)$ the electric field and intensity of the photon beam, $\langle \dots \rangle$ the time average symbol. When the time delay τ is ultra-longer than the coherence time T_2 , the intensity correlation can be written as,

$$\begin{aligned} \langle I(t)I(t+\tau) \rangle_{\tau \gg T_2} &= \langle (\langle I \rangle + \Delta I(t))(\langle I \rangle + \Delta I(t+\tau)) \rangle \\ &= \langle I \rangle^2 + \langle I \rangle (\langle \Delta I(t) \rangle + \langle \Delta I(t+\tau) \rangle) \\ &\quad + \langle \Delta I(t) \rangle \langle \Delta I(t+\tau) \rangle \\ &= \langle I \rangle^2 \end{aligned} \quad (2.3.26)$$

The second-order correlation function is,

$$g^{(2)}(\tau \gg T_2) = \frac{\langle I(t)I(t+\tau) \rangle}{\langle I(t) \rangle^2} = \frac{\langle I(t) \rangle^2}{\langle I(t) \rangle^2} = 1 \quad (2.3.27)$$

When the time delay $\tau \ll T_2$, particularly $\tau = 0$

$$g^{(2)}(0) = \frac{\langle I(t)^2 \rangle}{\langle I(t) \rangle^2} \geq 1 = g^{(2)}(\tau) \quad (2.3.28)$$

For perfect coherent source with a time-independent intensity, $g^{(2)}(\tau) = 1$ for all τ . But for any other classical chaotic sources with time-varying intensity, $\langle I(t)^2 \rangle$ is larger than $\langle I(t) \rangle^2$ due to intensity fluctuation, i.e., Atomic discharge lamp with spectral line of Gaussian shape, the second-order correlation function is,

$$g^{(2)}(\tau) = 1 + e^{-\pi(\frac{\tau}{T_2})^2} \quad (2.3.29)$$

or for Lorentzian chaotic light,

$$g^{(2)}(\tau) = 1 + e^{-2\frac{|\tau|}{T_1}} \quad (2.3.30)$$

As the number of photons registered by the detectors are proportional to the intensity, the definition of $g^{(2)}(\tau)$ can be re-written as,

$$g^{(2)}(\tau) = \frac{\langle n_1(t)n_2(t+\tau) \rangle}{\langle n_1(t) \rangle \langle n_2(t+\tau) \rangle} \quad (2.3.31)$$

where $n_i(t)$ is the number of photon counts detected at time t , and $g^{(2)}(\tau)$ is proportional to the probability of simultaneously detecting one photon at t and the other photon at

$t + \tau$, which is the coincidence. In the case of light sources emitting photons with sub-Poissonian statistics where single photons are separated with a long time interval, it is apparent that it is impossible to detect two photons at $\tau = 0$, corresponding to $g^{(2)}(\tau) = 0$. As the increase of τ , the probability of obtaining the coincidence increase, resulting in an anti-bunched behavior for $g^{(2)}(\tau)$.

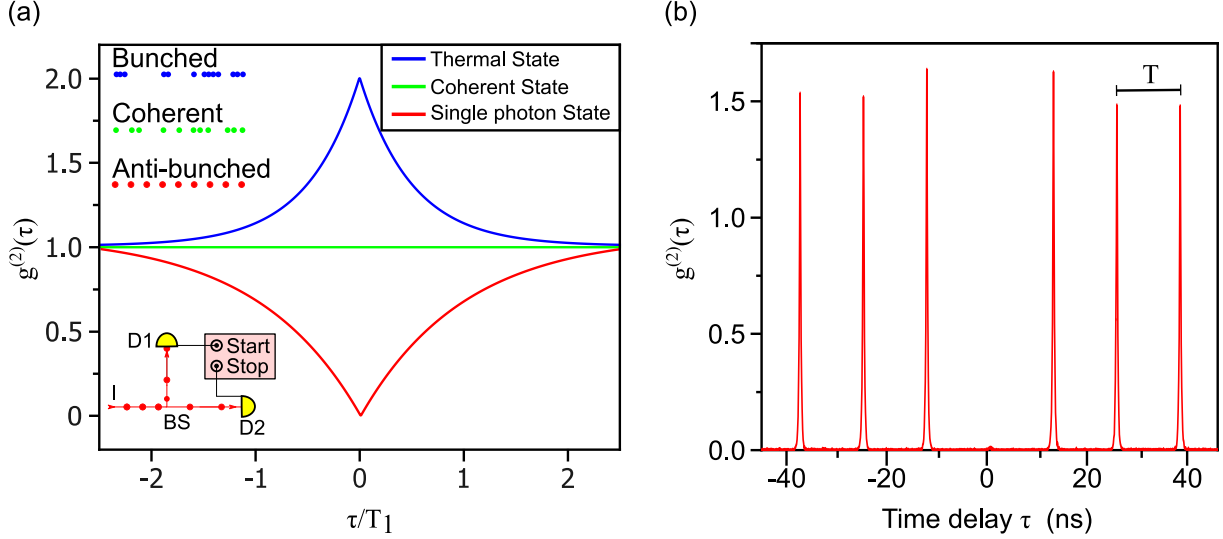


Figure 2.12: (a) Continuous coincidence histogram of second-order intensity autocorrelation function for thermal light, coherent light, and non-classical light. (b) Normalized pulsed coincidence histogram of second-order intensity autocorrelation function with a repetition rate of $1/T$.

Fig. 2.12(a) shows continuous second-order intensity correlation ($g^{(2)}(\tau)$) as function of time delay τ for three different type of sources as described in the last chapter. When the time delay is equal to zero,

1. Super-Poissonian light:

$$g^{(2)}(0) = 1 + \frac{(\Delta n)^2 - \langle n \rangle}{\langle n \rangle^2} = 2 \quad (2.3.32)$$

2. Coherent light:

$$g^{(2)}(0) = 1 \quad (2.3.33)$$

3. Sub-Poissonian light:

$$g^{(2)}(0) = 1 - \frac{1}{n} \quad (2.3.34)$$

In a summary, we conclude that the intensity correlation at zero is determined by the type of light sources as,

- **Bunched light:** $g^{(2)}(0) > 1$

- **Coherent light:** $g^{(2)}(0) = 1$
- **Anti-bunched light:** $g^{(2)}(0) < 1$

In addition of criteria of classifying the type of sources, second-order intensity correlation function at time delay $\tau = 0$ is a signature for evaluating the single photon purity of the quantum light sources, meaning that the lower of $g^{(2)}(0)$ value is, the higher of the purity would be. For the continuous stream of photons emitted by the QD under cw laser excitation, $g^{(2)}(0)$ can be extracted by fitting the histogram with the following equation:

$$g^{(2)}(\tau) = \left[1 - \left(1 - g^{(2)}(0) \right) \cdot e^{-\frac{|\tau|}{T_{tot}}} \right] * I_{IRF}^{(2)} \quad (2.3.35)$$

where the first term at the right of equation indicates the ideal second-order correlation function, with $1/T_{tot} = (1/T_1 + 1/T_P)$ related with radiative lifetime T_1 and pumping time T_P of the QD. The second term $I_{IRF}^{(2)}$ is the system response function of two detection channels, which can be measured by counting the coincidence of two short-duration laser pulses.

When the QD is excited by the pulsed laser, the time interval between emitted photons are determined by the repetition rate excitation pulses (R_{rep}). Therefore, coincidence are only detected at the time delay of integral folds of pulse period as illustrated in 2.12(b), with period of laser pulses to be $T = 1/R_{rep} = 12.5$ ns. The single photon purity is defined by the ratio of coincidence at zero time delay and the average coincidence of far away peaks with the same counting time window $\Delta\tau$,

$$g^{(2)}(0, \Delta\tau) = \frac{I(0, \Delta\tau)}{\frac{1}{k} \sum_i^{i+k} I(i \cdot T, \Delta\tau)} \quad (2.3.36)$$

where I is the coincidence counts of a certain peak, i is the index of the peak at a far away time delay, k is the number of peaks for averaging the coincidence, T is the the laser pulse period, $\Delta\tau$ is the size of time window for counting the coincidence. To get rid of the coincidence background from the noise, a proper size of window τ in data analysis are usually applied only including the dominant peak area.

2.3.6 Quantum tomography

Apart from a potential single photon source, QDs are also one of the promising candidates as entangled photon sources, emitting polarization-entangled photon pairs via the cascade of XX states. As similar as the evaluation of single photon purity $g^{(2)}(0)$ by second-order correlation measurement, the entangled states of photons from the QDs can be despicted with the density matrix, obtained by ‘Quantum tomography’ [26]. Specific information about the entangled states such as ‘fidelity’, ‘negativity’, ‘concurrence’, ‘linear entropy’ are then available from the density matrix, as detailed in Sec. 1.1.1.

The construction of a two-qubits density matrix can be completed by performing a series of probability measurements on particular projection basis as shown in Equ. 1.1.24, with 2-dimensional Stokes parameters determined as [26],

$$S_{i,j} = S_i \otimes S_j \quad (2.3.37)$$

As an example,

$$\begin{aligned} S_{0,3} &= (P_{(H)} + P_{(V)}) \otimes (P_{(H)} - P_{(V)}) \\ &= P_{|HH\rangle} - P_{|HV\rangle} + P_{|VH\rangle} - P_{|VV\rangle} \end{aligned} \quad (2.3.38)$$

where $P_{|\psi_1, \psi_2\rangle}$ denote the probability of measuring the coincidence on polarization basis combinations $|\psi_1\rangle$ and $|\psi_2\rangle$, corresponding to the coincidence at zero time delay of second-order intensity correlation measurement in experiment.

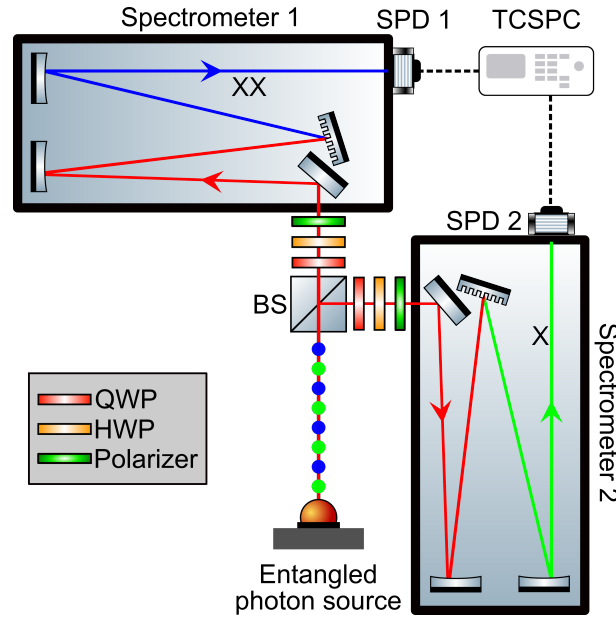


Figure 2.13: Optical setup for characterizing the density matrix of polarization entangled photons from QDs.

Fig. 2.13 display the sketch of optical characterization setup for the quantum tomography. By the use of two photon excitation (TPE) approach, the QD is resonantly pumped to the XX state followed by the cascade process emitting pairs of polarization-entangled photons, in the form of one of the Bell states,

$$\begin{aligned} |\Psi\rangle &= \frac{1}{\sqrt{2}} (|H_{xx}H_x\rangle + |V_{xx}V_x\rangle) \\ &\equiv \frac{1}{\sqrt{2}} (|D_{xx}D_x\rangle + |A_{xx}A_x\rangle) \\ &\equiv \frac{1}{\sqrt{2}} (|R_{xx}L_x\rangle + |L_{xx}R_x\rangle) \end{aligned} \quad (2.3.39)$$

The stream of emitted photon pairs are then collected and splitted into two beams by BS for projection measurement, with each beam passing a HWP, QWP, and polarizer. In Chap. 1, we have discussed that the combination of HWP and QWP can rotate an arbitrary state to a deterministic state on Poincaré sphere. Inversely, a deterministic state would be detected by putting a polarizer orientated at a fixed angle, and adjust the Specific rotation angle of waveplates. Two spectrometers in the transmission and reflection path of BS are utilized to select the XX and X photons peaks for single photon detection, respectively. Depending on the polarization determined by the HWP/QWP combinations in these two paths, correlation of various polarization combinations between XX and X photons can be measured by second-order cross-correlation measurement.

As mentioned in previous chapter, density matrix is useful to calculate the degree of overlap between an unknown target state $|\psi_t\rangle$ and expected maximally-entangled state $|\psi_s\rangle$ ('fidelity') with the relation,

$$f = \langle \psi_s | \rho_t | \psi_s \rangle \quad (2.3.40)$$

Assuming a general form of two-qubits density matrix [115],

$$\rho_t = \begin{pmatrix} \rho_{11} & \rho_{12} & \rho_{13} & \rho_{14} \\ \rho_{12}^* & \rho_{22} & \rho_{23} & \rho_{24} \\ \rho_{13}^* & \rho_{23}^* & \rho_{33} & \rho_{34} \\ \rho_{14}^* & \rho_{24}^* & \rho_{34}^* & \rho_{44} \end{pmatrix} \quad (2.3.41)$$

The fidelity to the Bell state $|\Phi^+\rangle$ is,

$$\begin{aligned} f = \langle \psi_s | \rho_t | \psi_s \rangle &= \frac{1}{2}(\rho_{11} + \rho_{44}) + Re\{\rho_{14}\} \\ &= \frac{1}{4}(1 + E_R + E_D - E_C) \end{aligned} \quad (2.3.42)$$

where $\{E_R, E_D, E_C\}$ indicate the correlation contrast along rectilinear, diagonal, and circular polarization combinations defined as,

$$E_R = \frac{g_{H,H}^{(2)}(0) - g_{H,V}^{(2)}(0)}{g_{H,H}^{(2)}(0) + g_{H,V}^{(2)}(0)} \quad E_D = \frac{g_{D,D}^{(2)}(0) - g_{D,A}^{(2)}(0)}{g_{D,D}^{(2)}(0) + g_{D,A}^{(2)}(0)} \quad E_C = \frac{g_{R,R}^{(2)}(0) - g_{R,L}^{(2)}(0)}{g_{R,R}^{(2)}(0) + g_{R,L}^{(2)}(0)} \quad (2.3.43)$$

Fig. 2.14(a) shows the results of the second-order cross-correlation measurement on three pairs of polarization bases. Strong bunched correlations $g^{(2)}(0) > 1$ between $H - H, D - D$, and $R - L$ bases are obtained in contrast to anti-bunched correlation between $H - V, D - A$, and $R - R$ polarization bases with $g^{(2)}(0) < 1$. According to Equ. 2.3.42 and 2.3.43, the fidelity exceeding 0.5 with respect to Φ^+ is calculated, demonstrating the

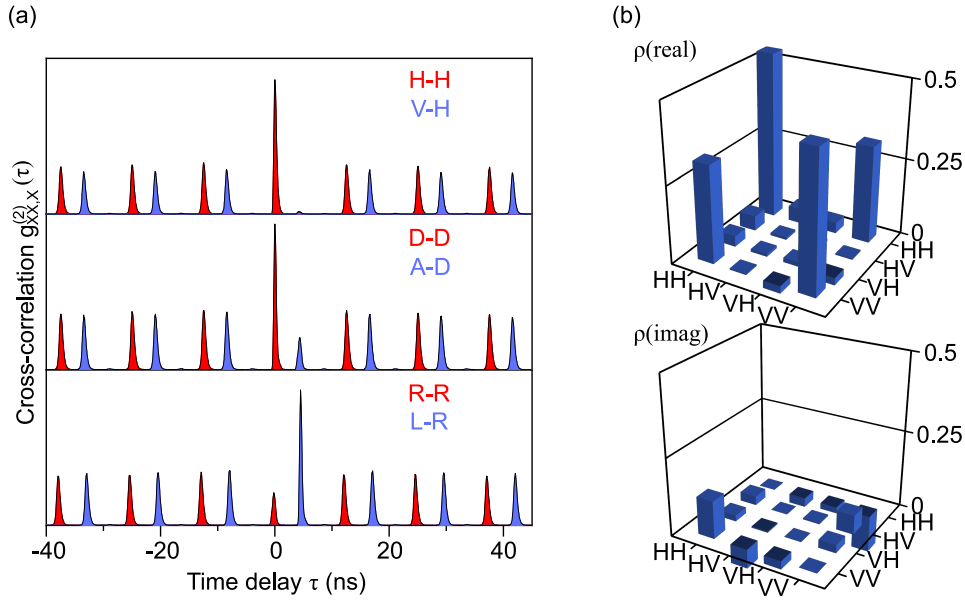


Figure 2.14: (a) Pulsed cross-correlation histogram between XX and X photons projected at different polarization basis (H-H/V, D-D/A, R-R/L). The second-order cross-correlation histogram between orthogonal polarization bases (blue) is positively shifted by a few ns for a clear view in contrast to the collinear bases. (b) Real and imaginary part of an exemplary density matrix of entangled photon pairs from a QD.

emission of entangled photons. Second-order correlation measurement on a number of 4^n polarization bases combinations necessitate the full construction of a density matrix by Stokes parameters [26] (n is the number of entanglement qubits). Tab. 2.1 shows the exemplary projection measurement list for XX and X photons, from which the density matrix of an arbitrary state can be constructed via the detected coincidence and Equ. 1.1.24.

No.	Polarization basis (XX)	Polarization basis (X)	No.	Polarization basis (XX)	Polarization basis (X)
1	$ H\rangle$	$ H\rangle$	9	$ D\rangle$	$ R\rangle$
2	$ H\rangle$	$ V\rangle$	10	$ D\rangle$	$ D\rangle$
3	$ V\rangle$	$ V\rangle$	11	$ R\rangle$	$ D\rangle$
4	$ V\rangle$	$ H\rangle$	12	$ H\rangle$	$ D\rangle$
5	$ R\rangle$	$ H\rangle$	13	$ V\rangle$	$ D\rangle$
6	$ R\rangle$	$ V\rangle$	14	$ V\rangle$	$ L\rangle$
7	$ D\rangle$	$ V\rangle$	15	$ H\rangle$	$ L\rangle$
8	$ D\rangle$	$ H\rangle$	16	$ R\rangle$	$ L\rangle$

Table 2.1: Polarization projection bases combinations for quantum state tomography.

Nevertheless, the statistical drift cause inevitable outcome of non-physical result in the construction of density matrix photon counting, owing to errors such as: Poissonian counting fluctuation, drift of emission/detection efficiency, wave-plates uncertainty, etc. A physical density matrix need to meet the demand of three cardinal properties: normal-

ization, positive semi-definiteness, and hermiticity. Therefore, the maximum likelihood estimation method [160] is employed to determine the physical density matrix, taking into account of the imperfection of experimental system. A numerical model developed by the quantum information group of Prof. Paul G. Kwiat [161] facilitates the maximum likelihood estimation of physical density matrix as shown in Fig. 2.14(b).

The detection efficiency of the measurement system η_{det} and pair generation efficiency ϵ can also be estimated from the cross-correlation measurements, according to the literatures [162, 163]. Assuming a pulsed laser with a repetition rate of M is used to excite the QD to the XX state, and the XX state will decay to the ground state with the emissions of XX and X photons. Each photon will then be detected by the single photon detector with detection efficiency of η_{det} . The single photon rate I for XX or X photons can be written as,

$$I = \epsilon \cdot M \cdot \eta \quad (2.3.44)$$

The coincidence count rate $I^{(2)}$ between XX and X photons at time delay of zero denotes the detected pair rate,

$$I^{(2)}(0) = \epsilon \cdot M \cdot \eta_{det}^2 \quad (2.3.45)$$

According to Equ. 2.3.14, the coincidence count rate between XX and X photons at an arbitrary time delay, which is the integer pulse period, can be written as,

$$I^{(2)}(\tau) = \epsilon^2 \cdot M \cdot \eta_{det}^2 \quad (2.3.46)$$

Therefore, by measuring the single photon count rate (I) and coincidence count rate between XX and X photons at time delay of zero and τ ($I^{(2)}(0)$ and $I^{(2)}(\tau)$), the photon pair excitation efficiency can be determined as,

$$\epsilon = \frac{I^2}{M \cdot I^{(2)}(0)} \quad \text{or} \quad \epsilon = \frac{I^{(2)}(\tau)}{I^2(0)} \quad (2.3.47)$$

Similarly, the detection efficiency (η_{det}) can be estimated as,

$$\eta_{det} = \frac{I^{(2)}(0)}{I} \quad \text{or} \quad \eta_{det} = \frac{I^{(2)}(0)}{\sqrt{M} \cdot \sqrt{I^{(2)}(\tau)}} \quad (2.3.48)$$

2.3.7 Photon indistinguishability

The indistinguishability of emitted photons from single photon sources is the critical parameter for the interference related quantum information applications based on quantum gate operation. The indistinguishability indicates that two photons are both Fourier-transform limited, possessing same wavelength, polarization, pulse width, bandwidth, etc., in every degree of freedom. The characterization of photon indistinguishability can

be carried out in terms of the boson nature of photons in Hong-Ou-Mandel (HOM) measurement [164].

The physical description of HOM can be explained by Fig. 2.15. When one photon hits on the 50:50 BS, the photon will be either transmitted or reflected. When two photons are sent into the individual input port of a BS, there are four possibilities of the behaviors of photons. Either two photons are both transmitted (panel I) or reflected (II), or one photon is reflected, and the other is transmitted (panel III and IV). However, in case that two identical photons with all the degrees of freedom arrive at the BS simultaneously, they will always come out from the same output port (panel III~IV in Fig. 2.15), owing to the boson nature of photons. The mathematic expression of HOM effect is explained in the Sec. 2.5.

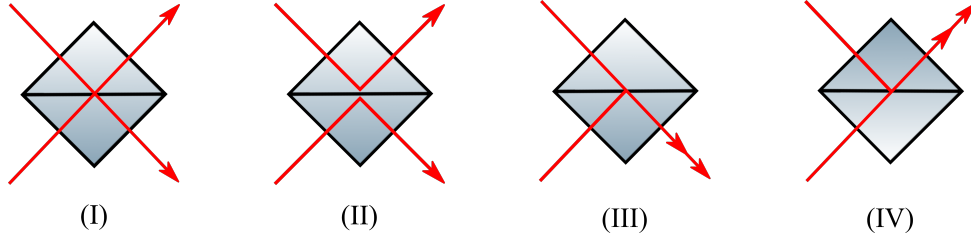


Figure 2.15: Four possible behavior of two-photon reflection and transmission at a 50:50 BS.

As the generation of single photons from the emitter is correlated with the excitation and recombination process of electron-hole pairs. The properties of emitted photons is determined by the parameters of the sources. If radiative process strictly obey the dynamics from an upper energy state to a lower level ground state with spontaneous emission, the linewidth is subject to the homogeneous broadening mechanism due to natural broadening. It gives rise to a Fourier-transform limited temporal coherence time $T_2 = 2/\Delta\omega$, with $\Delta\omega$ the natural linewidth in angular frequency, whereas the linewidth will show the inhomogeneous broadening in the presence of dephasing process. For the case of QDs embedded in the solid-state matrix, the impurities in the environment will generate electric field around the QD by the capture of charge carriers. Such an exemplary process will reduce the temporal coherence of photons with the relationship of,

$$\frac{1}{T_2} = \frac{1}{2T_1} + \frac{1}{T_2^*} = \frac{1}{2}\gamma_{T_1} + \gamma^* \quad (2.3.49)$$

with T_2 the coherence time, T_1 the radiative lifetime, T_2^* the dephasing time related with exciton scattering, exciton-phonon interactions, or charge noise from impurities. γ_{T_1} is the spontaneous decay rate, γ^* denotes the dephasing rate corresponding to dephasing time T_2^* . In the case of resonant excitation, the degraded indistinguishability caused by the energy jittering from charge noise of an individual QD can be quantitatively defined

as [115],

$$V_{\delta E} = \frac{T_2}{2T_1} \quad (2.3.50)$$

Apart from the limited coherence usually attributed to dephasing due to charge and spin noise or phonon scattering [165], it has been demonstrated that the ratio of the lifetimes of $T_{1,XX}$ and $T_{1,X}$ is related to limited indistinguishability even further, because of intrinsic dephasing stemming from cascade emission in the three-level quantum ladder system under TPE, given by [166, 167, 168],

$$V_{casc} = \frac{1}{1 + T_{1,XX}/T_{1,X}} \quad (2.3.51)$$

Thus, we can give an approximation on the indistinguishability of an individual QD [167],

$$V = V_{\delta E} \cdot V_{casc} \quad (2.3.52)$$

Fig. 2.16 shows the sketch of an unbalanced Mach-Zehnder interferometer (MZI) used for measuring the indistinguishability of single photons emitted by the QD in the cryostat. By means of the double pulses generation setup shown in the panel 2 of Fig. 2.4(b), consecutive pairs of photons with a time delay of τ and repetition period of $T = 12.5$ ns are emitted from the QD. As the PBS splits the light paths depending on the polarization of photons (H-transmitted, V-reflected), each circularly-polarized photon emitted from XX or X transition states possess equal possibility to be transmitted or reflected. A HWP is inserted in the transmission path for switching the photons to be either indistinguishable or distinguishable comparing with the reflected photons in relation to polarization. When the fast axis of HWP is at 0° , polarization of two photons arriving at the BS is perpendicular. If the fast axis angle of HWP is 45° with respect to the transmitted H-polarized photons, the polarization of photons is rotated to be V polarization, which are the same as the reflected photons by the PBS. A fix-length difference between the reflected and transmitted path is employed on purpose with the relationship of,

$$L_R - L_T = c \cdot \tau \quad (2.3.53)$$

where L_R denotes the length of reflection path, L_T denotes the transmission path, c is the speed of light, and τ is the time delay between the photons excited by the double pulses. Two spectrometers behind the BS are used to deterministically select the studied photon peaks by grating (XX or X) for coincidence measurement.

The physical principle of the indistinguishability measurement is depicted as the simplified schematic diagram in the upper panel of Fig. 2.17. Assuming that a pair of single photons with a time delay of τ arrive at the first BS (or PBS), there are four possibilities of the behaviors of two photons.

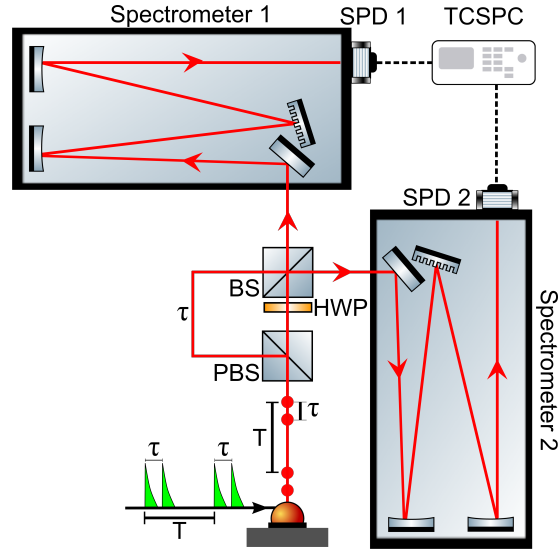


Figure 2.16: Sketch of optical characterization setup for the indistinguishability of the single photons from an exemplary QD, using an unbalanced MZI with a fixed time delay τ .

- The earlier photons are reflected, the latter photons are transmitted.
- Both of earlier and latter photons are either transmitted or reflected.
- The earlier photons are transmitted, and the latter photons are reflected.

For the first case, the earlier and latter photons will arrive at the second BS at the same time. No coincidence counts at zero time delay can be detected, if these two photons are completely indistinguishable due to HOM effect. In contrast, there are 50% probability of generating coincidence counts for distinguishable photons as panel I~II of Fig. 2.15. For the second case, there are two possibilities that coincidence counts will be recorded at time delay of $|\tau|$. Depending on the configurations of photons registered by the detectors, i.e., (earlier photon-D1, latter photon-D2) or (earlier photon-D2, latter photon-D1), the coincidence counts are averaged at time delay $+\tau$ and $-\tau$. However, there is still one possibility that coincidence counts between earlier and latter photons are recorded at $\pm 2\tau$. The lower panel of Fig. 2.17(a) shows the probabilities of time delay between earlier and latter photons after the MZI, and the relative ratio of coincidence as a function of time delay for distinguishable photons.

Fig. 2.17(b) presents the measurement results of indistinguishability for the earlier and latter photons with co-polarized \parallel and cross-polarized \perp cases, by setting the fast axis of HWP in Fig. 2.16 to be 45 deg and 0 deg. The obvious disappearance of peak at zero time delay for indistinguishable (\parallel) photons imply the HOM effect. The indistinguishability of photon emission from a QD is experimentally determined by the contrast of coincidence counts at zero time delay peak area between co-polarized (I_{\parallel}) and cross-polarized I_{\perp} cases

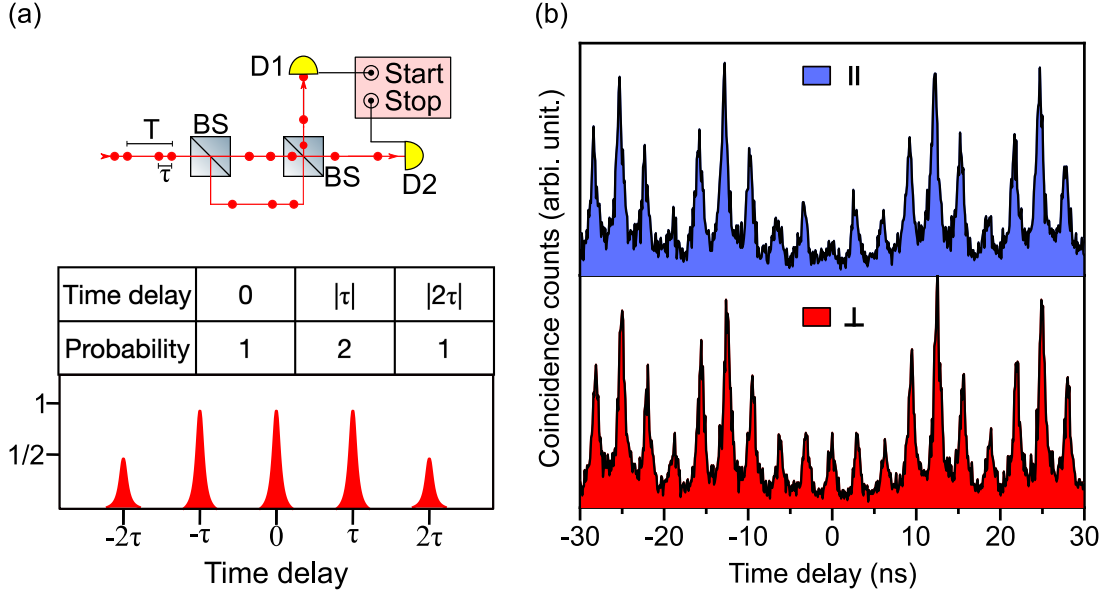


Figure 2.17: (a) Simplified sketch of photon indistinguishability measurement setup (upper panel). Probability of coincidence as a function of time delay in a photon indistinguishability measurement (lower panel). (b) Second-order correlation measurement on parallelly (blue) and perpendicularly (red) polarized photons impinging on the BS.

[169],

$$V = \frac{I_{\perp} - I_{\parallel}}{I_{\perp}} \quad (2.3.54)$$

Due to imperfections of the optics, the polarizations cannot be set to be fully orthogonal for measuring the case of distinguishable photons. The unbalanced beam splitter transmission and reflection also degrades the visibility [170]. The photon indistinguishability involving the correction of these effects is,

$$V = \frac{R^2 + T^2}{2RT} - \frac{I_{\parallel} \cdot (1 - V_{dis})}{I_{\perp} - I_{\parallel} \cdot V_{dis}} \quad (2.3.55)$$

where R and T are the reflection and transmission efficiency of the second BS, respectively. V_{dis} denotes the ratio of peak areas at time delay of zero and τ for distinguishable histogram.

In real-world quantum applications, two photon interference at the BS request indistinguishable photons from two independent photon emitters. The visibility of TPI (call 'HOM' visibility) between photons from QD A and QD B is given by [170],

$$M = \frac{\gamma_A \gamma_B}{\gamma_A + \gamma_B} \cdot \frac{\gamma_A + \gamma_B + \gamma_{A(effect)}^* + \gamma_{B(effect)}^*}{\Delta\omega^2 + [(\gamma_A + \gamma_B + \gamma_{A(effect)}^* + \gamma_{B(effect)}^*)/2]^2} \quad (2.3.56)$$

where γ_A and γ_B denote the radiative decay rates of two QDs. $\Delta\omega$ is the mismatch of

angular frequency of QDs. γ_{effect}^* is the effective dephasing rate, estimated by substituting Equ. 2.3.52 and 2.3.50 into Equ. 2.3.49,

$$\gamma_{effect}^* = \frac{\gamma_{T_1}(1 - V)}{2V} \quad (2.3.57)$$

2.4 Calibration of optical components

In the real quantum optics experiment, there are no perfect optical elements for transferring or manipulating photon qubits, causing absorption and decoherence of data signals. Herein we discuss the calibration of optical properties for typical optical components used in the optical measurements such as wavelength-dependent notch filters, birefringent wave-plates, dielectric mirrors. Different from Jones matrices used to express the operation of photonic components on photon qubits, Mueller matrices has the advantages of containing the depolarization information of components and light. In this section, we introduce the method of calibration and interpretation of Mueller matrices for the optical elements in our laboratory.

2.4.1 Extinction ratio of notch filters

To achieve the TPE discussed in the Sec. 2.2, the laser wavelength is demanded to be in-between the emission wavelengths of XX and X photon. Ultra-narrow bandwidth notch filters are employed in order to block the laser light out from the light collection path. Apart from the bandwidth, the extinction ratio (ER) is an essential parameter allowing the extraction of signals with high efficiency and purity.

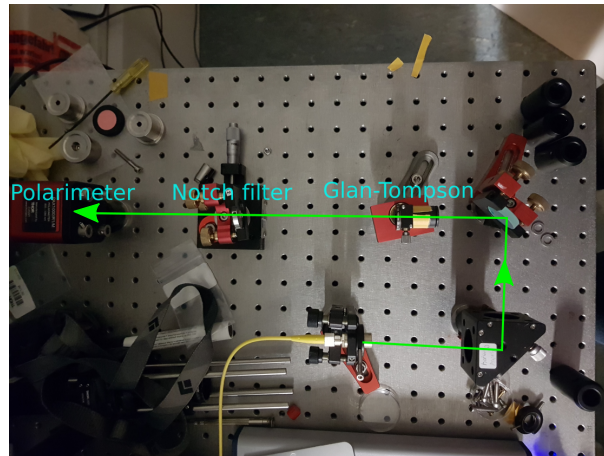


Figure 2.18: Optical setup for calibrating the extinction ratio of a notch filter.

Fig. 2.18 shows the photography of experimental setup for extinction ratio calibration of a notch filter. In the TPE, the laser background with the wavelength in the middle of

XX and X is usually blocked by the notch filters with high extinction ratio. Therefore, it is essential to learn the specification of this value by testing. The laser light from the fiber coupler possessing TPE wavelength is reflected by two mirrors and sent through a Glan-Thompson polarizer ($ER > 10^5$). The laser beam then hit the center of the notch filter tilted by a certain angle for reflecting most of the light. A Thorlabs polarimeter (PAX1000IR/M) is placed in the transmission path after the calibrated notch filter for power detection. Since the working wavelength of the notch filter is relevant with the tilted angle relative to the incident beam, we can switch the maximal and minimal transmission of laser light by adjusting the horizontal node of the mirror mount. The extinction ratio of the notch filter is then determined with the measured maximal and minimal transmission power (T_{max}/T_{min}). Moreover, polarization-dependent extinction ratio can be measured by rotating the angle of the Glan-Thompson polarizer.

2.4.2 Retardance of waveplates

Birefringent retarders are the materials introducing phase shift for polarized light, in which widely used components are the waveplates for controlling the states of photonic qubits. In order to calibrate the typical qualities of half- and quarter- waveplates purchased from the market. We establish the setup as displayed in Fig. 2.19 for the calibration of retardance of waveplates.

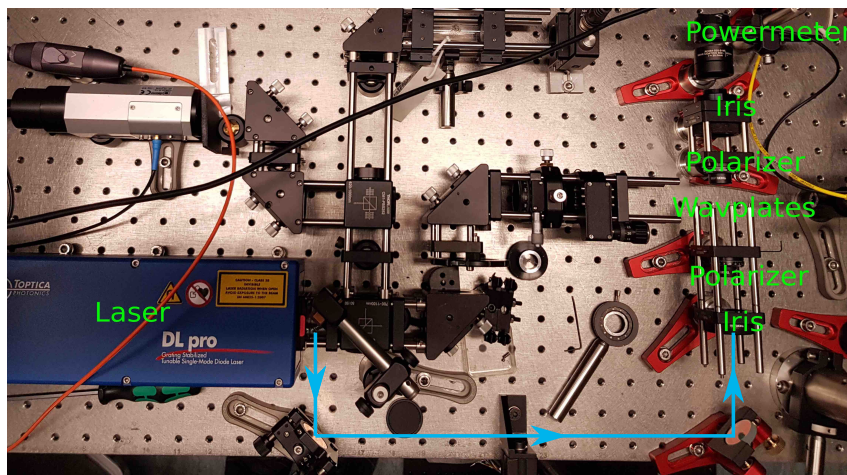


Figure 2.19: Optical setup for calibrating the retardance of waveplates.

A powermeter is first employed for the detection of laser power passing through the optical components. Along the coming direction of laser beam, the calibration procedure is,

- Add the first polarizer in the light path and rotate it to 0° or 180°
- Add the second polarizer in the light path and rotate it to a certain angle with the minimal power transmitted through.

- Rotate the second polarizer by 180° for check the obtained maximal power.
- Rotate the first polarizer by 180° . The obtained power should be as same as the minimal power as above.
- Insert the calibrated HWP or QWP in-between the polarizers, and rotate them to obtain the maximal power.

First polarizer (deg)	Second polarizer (deg)	Actual degree of second polarizer (deg)	Minimum (uW)	Maximum (mW)
0	0	253.0	321	11.86
0	180	73.0	319	
180	180	73.0	319	
180	0	253.0	321	
Plates Type	Number		Maximal power (mW)	Percentage
Half Wave Plate	1		11.62	97.976%
	2		11.79	99.410%
	3		11.71	98.735%
	4		11.77	99.241%
	5		11.82	99.663%
	6		11.78	99.325%
	7		11.78	99.325%
	8		11.81	99.578%
Quarter Wave Plate	1		5.03	42.411%
	2		5.14	43.339%
	3		5.00	42.159%

Table 2.2: Calibration results of retardance of waveplates purchased in the market.

For perfect waveplates, the obtained maximal laser power during the rotation should be equal to (100 %) or half (50 %) of the maximal power for half-wave plate (HWP) or quarter-wave plate (QWP), in contrast to the power without the waveplates (ignoring the low transmission loss $\sim 0.1\%$ at the working wavelength). Tab. 2.2 shows the calibration results of retardance for waveplates working at the designed wavelengths, from which we can conclude that most of the HWPs satisfy the declared specification with retardance fluctuation of $< \lambda/300$ corresponding to power deviation of 0.67 %. However, the retardance fluctuation of QWP is over the specification $< \lambda/300$ corresponding to power deviation of 1.33 %.

2.4.3 Mueller matrix measurement

Mueller matrix [171] is an effective tool to calibrate the typical performance of optical components such as diattenuation, retardance, and degree of depolarization [172, 173, 174]. In the following, we show the experimental calibration approach to obtain the Mueller matrix of commonly used optical elements such as the optical filter, dielectric

mirror. As the output state of light expressed with Stokes parameters (S_0, S_1, S_2, S_3) is determined by the Mueller matrix applied on the initial state, we employ the least squares linear regression analysis to fit the matrix by comparing the Stokes parameters without and with the calibrated optical element for different input states.

Number	Stokes Vector			Spherical Coordinate		Polarization Ellipse	
	S1	S2	S3	Polar (°)	Azimuth (°)	Ellipticity (°)	Azimuthal (°)
1	0	1.618034	0.618034	69.09484255	90	10.45257872	45
2	0	-1.618034	0.618034	69.09484255	-90	10.45257872	-45
3	0	1.618034	-0.618034	110.9051574	90	-10.45257872	45
4	0	-1.618034	-0.618034	110.9051574	-90	-10.45257872	-45
5	1.618034	0	0.618034	69.09484255	0	10.45257872	0
6	-1.618034	0	0.618034	69.09484255	180	10.45257872	90
7	1.618034	0	-0.618034	110.9051574	0	-10.45257872	0
8	-1.618034	0	-0.618034	110.9051574	180	-10.45257872	90
9	1.618034	0.618034	0	90	20.90515745	0	10.45257872
10	-1.618034	0.618034	0	90	159.0948426	0	79.54742128
11	1.618034	-0.618034	0	90	339.0948426	0	-10.45257872
12	-1.618034	-0.618034	0	90	200.9051574	0	-79.54742128
13	-1	1	1	54.73561032	135	17.63219484	67.5
14	1	-1	-1	125.2643897	315	-17.63219484	-22.5
15	1	-1	1	54.73561032	315	17.63219484	-22.5
16	-1	1	-1	125.2643897	135	-17.63219484	67.5
17	1	1	-1	125.2643897	45	-17.63219484	22.5
18	-1	-1	1	54.73561032	225	17.63219484	-67.5
19	1	1	1	54.73561032	45	17.63219484	22.5
20	-1	-1	-1	125.2643897	225	-17.63219484	-67.5

Table 2.3: Polarization reference points for calibrating the Mueller matrix of optical elements.

Table. 2.3 illustrates 20 polarization reference points uniformly distributed on the surface of Poincaré sphere as the initial states, which are described by Stokes vector, spherical coordinate, and polarization ellipse, respectively. Different from Fig. 2.18 for extinction ratio measurement, a pair of HWP and QWP is placed behind the Glan-Thompson polarizer for creating these reference states deterministically. The measurement step for transmission Mueller matrix of notch filter is as follows,

- Remove the notch filter away from the light path.
- Rotate the HWP and QWP combination to generate laser polarization to be the ones at the reference points. Record the real Stokes vector parameters \vec{S} (S_0, S_1, S_2, S_3) from polarimeter, and the rotation angle of the waveplates for each point.
- Insert the calibrated notch filter back to the light path. Rotate the waveplates combination to the recorded angle for each reference point, and record the new Stokes vector parameters \vec{S}' (S'_0, S'_1, S'_2, S'_3).
- Utilize the least squares regression fitting approach to model the Mueller matrix, which transforms the list of initial states \vec{S} to final states \vec{S}' .

Here we get the transmission Mueller matrix for an notch filter,

$$M_{notch}^{(T)} = \begin{pmatrix} 0.9508 & -0.0012 & -0.0016 & 0.0031 \\ -2.8070e^{-4} & 0.9515 & 0.0029 & -0.0012 \\ -3.8920e^{-4} & -0.017 & 0.9518 & -0.0094 \\ 0.0011 & 7.4403e^{-4} & 0.0301 & 0.9513 \end{pmatrix} \quad (2.4.1)$$

Fig. 2.20 shows the distance between the Stokes vectors \vec{S}' transmitted from the notch filter and the resultant Stokes vectors by applying the fitted matrix on the Stokes vectors \vec{S} of initial reference points, in order to evaluate the uncertainty of the matrix. A maximal deviation of < 0.025 in Fig. 2.20 indicates a beyond accuracy of fitting for the real performance of notch filter transmission, because the accuracy of polarimeter in the specification is 0.25. Enhancement of the number of reference points gives rise to higher figure of merit for the fitted Mueller matrix.

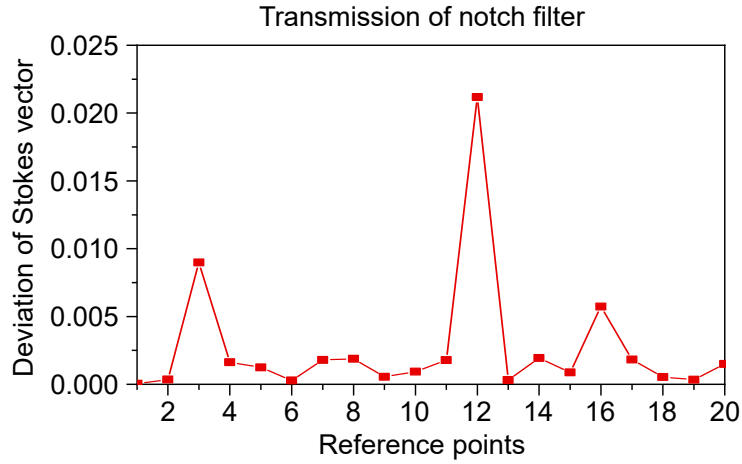


Figure 2.20: Deviation of the Stokes vectors induced by transmission of the notch filter, in contrast to the ones resulting from the application of fitted matrix on the reference points.

Apart from the transmission of signal for laser filtering, the notch filter can also be employed as the wavelength-dependent reflection mirror for signals with high-efficiency and purity according to the specification. Therefore, we calibrate the reflection Mueller matrix of notch filter using the setup shown in Fig. 2.21(a), along with the steps as follows,

- Put the cage module consisting of the polarizer, QWP and HWP in the reflection path of the notch filter. The position is labeled as *position 2* in the above picture.
- Rotate the HWP and QWP to the polarization reference point on the poincaré sphere, record the rotation angles of waveplates for each point and corresponding stokes vectors \vec{S} (S_0, S_1, S_2, S_3) in the polarimeter.
- Put the cage system in front of the notch filter and label the position as *position 1*.

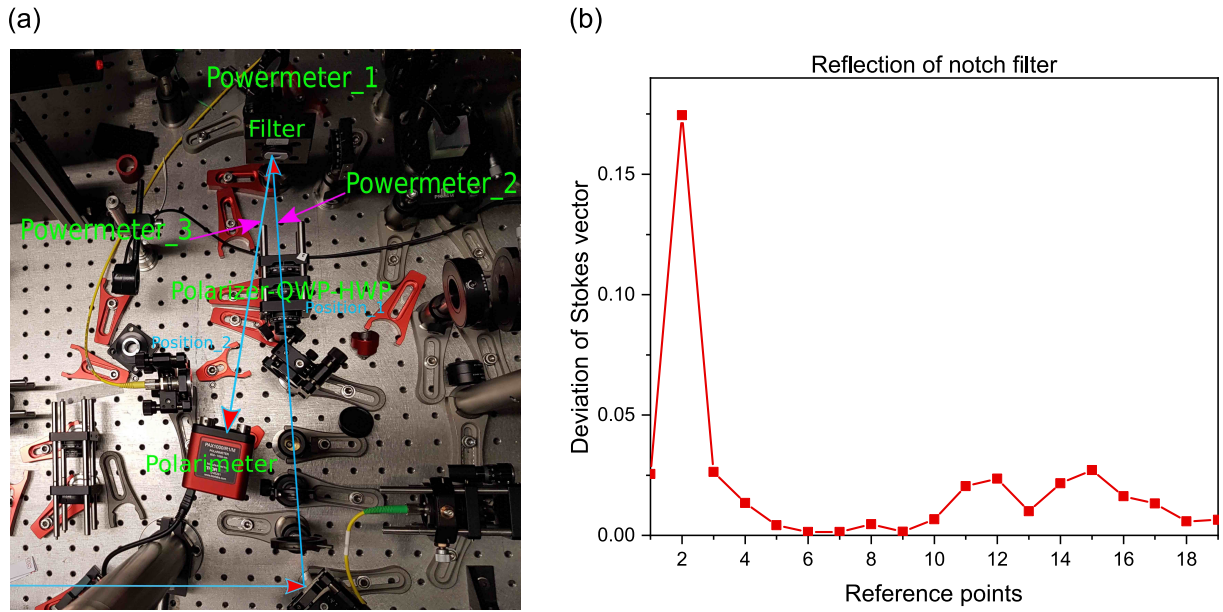


Figure 2.21: (a) Calibration of Mueller matrix for the reflection of notch filter. (b) Deviation of the Stokes vectors induced by the reflection of the notch filter, in contrast to the ones resulting from the application of fitted matrix on the reference points.

- Rotate the waveplates to each recorded angle and read the Stokes vectors from polarimeter as \vec{S}' (S'_0, S'_1, S'_2, S'_3). Simultaneously, the powers before and after the reflection of the notch filter is also recorded for correcting S_0 for each polarization, in order to calculate the reflectance of the notch filter.

As the same as the fitting of the transmission case, the reflection Mueller matrix of the notch filter is,

$$M_{notch}^{(R)} = \begin{pmatrix} 0.9032 & 0.8843 & -0.0077 & 0.0021 \\ 0.0031 & 0.8998 & 0.0709 & -0.0086 \\ -0.0068 & 0.0479 & -0.9025 & 4.594e^{-04} \\ 0.0028 & -0.0054 & -0.0118 & -0.8932 \end{pmatrix} \quad (2.4.2)$$

Fig. 2.22(b) illustrates the deviation of resultant Stokes vectors \vec{S}' after the reflection the notch filter comparing with the ones calculated by applying the fitted Mueller matrix on the initial stokes vectors \vec{S} of light in the Tab. 2.3. The maximal deviation close to 0.175 still manifests a high figure of merit of the fitted matrix, in terms of low performance of the polarimeter over 0.25.

With the same approach, the Mueller matrix of dielectric mirror is measured by comparing the list of Stokes vectors before and after the reflection of the calibrated mirror

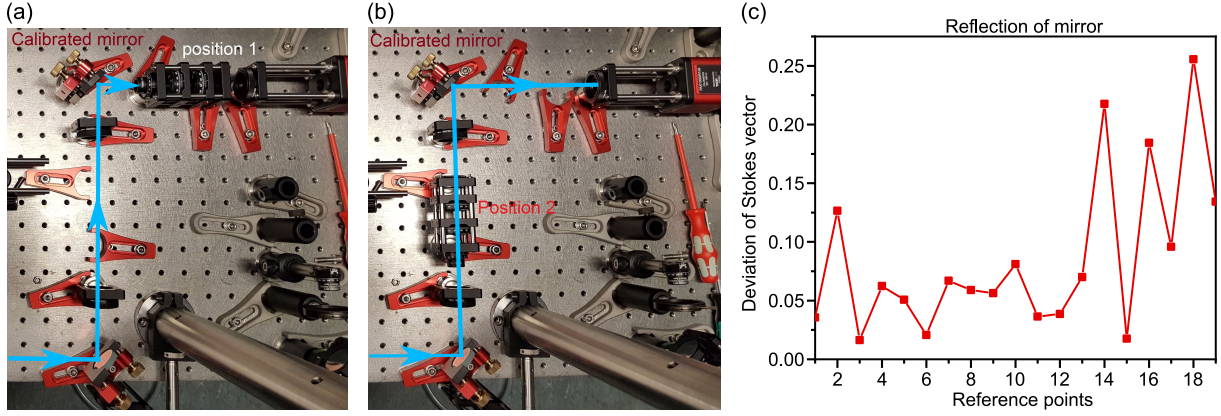


Figure 2.22: (a) Calibration of Mueller matrix for dielectric mirror. (b) Deviation of the Stokes vectors induced by reflection of the mirror, in contrast to the ones resulting from the application of fitted matrix on the reference points.

(Fig. 2.22). An exemplary Mueller matrix of a dielectric mirror is,

$$M_{mirror} = \begin{pmatrix} 0.9884 & 0.0015 & -0.0026 & 0.0190 \\ -0.0042 & 0.9808 & 0.0638 & -0.0248 \\ -0.0115 & 0.0589 & -0.9516 & 0.2463 \\ -0.0071 & 0.0089 & -0.2439 & -0.9527 \end{pmatrix} \quad (2.4.3)$$

2.4.4 Decomposition of Mueller matrix

The decomposition of Mueller matrix has been addressed in many literatures [172, 175, 176, 177]. Here we introduce the polar decomposition algorithm [172, 173], proven to be feasible for determining the diattenuation and retardance of a Mueller matrix. Using such an algorithm [174], we are capable to decompose the Mueller matrix of an optical element (M) into three matrices, evaluating the depolarization (M_{Δ}), retardance (M_R), and diattenuation (M_D).

$$\begin{aligned} M &= M_{\Delta} M_R M_D \\ &= T_u \begin{pmatrix} 1 & \vec{D}^T \\ \vec{P} & \mathbf{m} \end{pmatrix} \\ &= \begin{pmatrix} m_{00} & m_{01} & m_{02} & m_{03} \\ m_{10} & m_{11} & m_{12} & m_{13} \\ m_{20} & m_{21} & m_{22} & m_{23} \\ m_{30} & m_{31} & m_{32} & m_{33} \end{pmatrix} \end{aligned} \quad (2.4.4)$$

where $T_u = m_{00}$ is the transmittance of unpolarized light, \vec{D}^T is the transposed \vec{D} vector,

$$\vec{D} = \begin{pmatrix} D_{|H\rangle} \\ D_{|D\rangle} \\ D_{|C\rangle} \end{pmatrix} = \frac{1}{m_{00}} \begin{pmatrix} m_{01} \\ m_{02} \\ m_{03} \end{pmatrix} \quad (2.4.5)$$

$D_{|\psi\rangle}$ denotes the visibility of transmittance T for horizontally, diagonally, and circularly polarized light in contrast to their orthogonal polarization, which are determined as,

$$D_{|\psi\rangle} = \frac{T_{|\psi\rangle} - T_{|\psi^\perp\rangle}}{T_{|\psi\rangle} + T_{|\psi^\perp\rangle}}, \quad 0 \leq D_{|\psi\rangle} \leq 1 \quad (2.4.6)$$

\vec{P} denotes the polarizance, which is the degree of polarization (DOP) of this exiting light resulting from unpolarized light, given by,

$$\vec{P} = \begin{pmatrix} P_{|H\rangle} \\ P_{|D\rangle} \\ P_{|C\rangle} \end{pmatrix} = \frac{1}{m_{00}} \begin{pmatrix} m_{10} \\ m_{20} \\ m_{30} \end{pmatrix}, \quad 0 \leq |\vec{P}| = \bar{P} \leq 1 \quad (2.4.7)$$

The diattenuation matrix is,

$$M_D = T_u \begin{pmatrix} 1 & \vec{D}^T \\ \vec{D} & \mathbf{m}_D \end{pmatrix} \quad (2.4.8)$$

$$\mathbf{m}_D = \sqrt{1 - D^2} \mathbf{1} + (1 - \sqrt{1 - D^2}) \hat{D} \hat{D}^T$$

with $\mathbf{1}$ the 3×3 identity matrix, \hat{D} the unit vector along \vec{D} . In the case that M_D is non-singular matrix, the Mueller matrix containing the depolarization and retardance components is,

$$M' = M M_D^{-1} = \begin{pmatrix} 1 & \vec{0}^T \\ \vec{P}_\Delta & \mathbf{m}' \end{pmatrix}$$

$$= M_\Delta \cdot M_R \equiv \begin{pmatrix} 1 & \vec{0}^T \\ \vec{P}_\Delta & \mathbf{m}_\Delta \end{pmatrix} \cdot \begin{pmatrix} 1 & \vec{0}^T \\ \vec{0}^T & \mathbf{m}_R \end{pmatrix} \quad (2.4.9)$$

$$\vec{P}_\Delta = \frac{\vec{P} - \mathbf{m} \vec{D}}{1 - D^2}$$

$$\mathbf{m}' = \mathbf{m}_\Delta \mathbf{m}_R$$

where \mathbf{m}_Δ can be obtained by,

$$m_\Delta = \pm \left[\mathbf{m}' (\mathbf{m}')^T + \left(\sqrt{\lambda_1 \lambda_2} + \sqrt{\lambda_2 \lambda_3} + \sqrt{\lambda_3 \lambda_1} \right) \mathbf{1} \right]^{-1}$$

$$\times \left[\left(\sqrt{\lambda_1} + \sqrt{\lambda_2} + \sqrt{\lambda_3} \right) \mathbf{m}' (\mathbf{m}')^T + \sqrt{\lambda_1 \lambda_2 \lambda_3} \mathbf{1} \right] \quad (2.4.10)$$

with minus sign applied for negative determinant of \mathbf{m}' , but plus sign for positive determinant. $\lambda_1, \lambda_2, \lambda_3$ are the eigenvalues of $\mathbf{m}'(\mathbf{m}')^T$. After the calculation of M_Δ , M_R can be calculated by,

$$M_R = M_\Delta^{-1} M' \quad (2.4.11)$$

The depolarization power Δ of an element is given by [174],

$$\Delta = 1 - \frac{|Tr(\mathbf{m}_\Delta)|}{3}, \quad 0 \leq \Delta \leq 1 \quad (2.4.12)$$

The retardance R is [174],

$$R = \cos^{-1} \left[\frac{Tr(M_R)}{2} - 1 \right], \quad 0 \leq R \leq \pi \quad (2.4.13)$$

For the special cases such as analyzer or polarizer, decomposition of Mueller matrix for the elements are detailed in the literature [174]. By using this approach, we evaluate the performance of the transmission of notch filter regarding diattenuation, retardance, and depolarization. Corresponding information are extracted from the fitted Mueller matrix Equ. 2.4.1 as,

- Diattenuation:

$$D_{notch}^{(T)} \equiv \frac{T_{max} - T_{min}}{T_{max} + T_{min}} = 0.0039 \quad (2.4.14)$$

- Retardance:

$$R_{notch}^{(T)} \equiv |R_{fast} - R_{slow}| = 0.0209 \quad (2.4.15)$$

- Power of depolarization:

$$\Delta_{notch}^{(T)} = 0.0483 \quad (2.4.16)$$

where T_{max} and T_{min} are the maximal and minimal transmittance of the orthogonal eigen polarizations, characterizing the dependence of transmission upon the incident polarization. It is obvious that the notch filter has negligible diattenuation on the transmitted light. R_{fast} and R_{slow} denote the retardance along the eigen polarizations, and a small fraction of retardance is induced on the transmitted light from the notch filter. A low power of depolarization reveal the non-depolarizing nature of the transmission of the notch filter.

Apart from the decomposition of transmission Mueller matrix of notch filter, we are capable of evaluating the influence of mirrors of the polarization state of light. As an example, we decompose the fitted Mueller matrix from the dielectric mirror (Equ. 2.4.3), resulting in,

- Diattenuation:

$$D_{mirror} \equiv \frac{T_{max} - T_{min}}{T_{max} + T_{min}} = 0.0195 \quad (2.4.17)$$

- Retardance:

$$R_{mirror} \equiv |R_{fast} - R_{slow}| = 2.8893 \quad (2.4.18)$$

- Power of depolarization:

$$\Delta_{mirror} = 0.0161 \quad (2.4.19)$$

Therefore, we can conclude that the dielectric mirror will introduce negligible diattenuation and depolarization effect on the polarization of input light, while an additional retardance of 2.8893 is applied. For an ideal mirror, a phase of π should be implemented between H- and V- polarization on the coherent state of input light after reflection. The insufficient phase shift of the dielectric mirror should be compensated in some rigid polarization states investigation.

2.5 Quantum states transformation

Different from Mueller matrix manipulating the Stokes vectors, which represents the degree of polarization, Jones matrix is used to model the effect of a medium on the polarization of light [178]. It helps us to understand the quantum state of light and perform the manipulation of optical qubits by means of photonic elements. The density matrix of quantum states can be derived from Jones matrix. As discussed in the Chap. 1, the polarization state for,

Single qubits:

$$|\psi\rangle = \alpha|H\rangle + \beta|V\rangle = \begin{pmatrix} \alpha \\ 0 \end{pmatrix} + \begin{pmatrix} 0 \\ \beta \end{pmatrix} = \begin{pmatrix} \alpha \\ \beta \end{pmatrix} \quad (2.5.1)$$

Two qubits:

$$|\psi\rangle = \alpha|HH\rangle + \beta|VV\rangle = \alpha \begin{pmatrix} 1 \\ 0 \end{pmatrix} \otimes \begin{pmatrix} 1 \\ 0 \end{pmatrix} + \beta \begin{pmatrix} 0 \\ 1 \end{pmatrix} \begin{pmatrix} 0 \\ 1 \end{pmatrix} = \begin{pmatrix} \alpha \\ 0 \\ 0 \\ \beta \end{pmatrix} \quad (2.5.2)$$

with $\alpha^2 + \beta^2 = 1$ for normalization.

2.5.1 Jones Matrix of mirrors

Optical mirrors are the most commonly used components in the applications of light, which are generally classified into two types, i.e., dielectric mirrors and metal mirrors.

Concerning the dielectric mirror, the high reflection is achieved by the use of dielectric bragger reflection (DBR) structure. The more pairs of high/low dielectric layers are, the higher the total reflection of the mirror is. When the effective refractive index $n_{effective}$ of the DBR medium is ultra-larger than the one of free-space n_{air} , the Brewster angle

θ_B approach 90° . A π phase shift will be solely applied on the vertical polarization after reflection, if the incident angle is smaller than Brewster angle. The ideal Jones matrix for dielectric mirror is,

$$J_{mirror} = \begin{pmatrix} 1 & 0 \\ 0 & -1 \end{pmatrix} \quad (2.5.3)$$

However, the metal mirror is not recommended being used in the polarization relevant experiments because of the change of polarization of the light in theory. Considering a beam incident on a metal with an arbitrary angle, an evanescent wave forms and propagates a short distance on the surface. The reflection/transmission coefficient (r and t) for the horizontal (p) and vertical (s) polarization will be complex value,

$$\begin{aligned} r_s &= |r_s| e^{i\varphi_{rs}} \\ t_s &= |t_s| e^{i\varphi_{ts}} \\ r_p &= |r_p| e^{i\varphi_{rp}} \\ t_p &= |t_p| e^{i\varphi_{tp}} \end{aligned} \quad (2.5.4)$$

where the absolute value of reflection and transmission coefficients are determined by Fresnel equations, while φ_{rs} and φ_{ts} depend on the metal characteristics such as conductivity, magnetic permeability, and wave frequency. Therefore, the phase difference between horizontal and vertical polarization of reflected light is $\Delta\varphi = \varphi_{rs} - \varphi_{rp}$, leading to an arbitrary polarization like ellipse polarization. In practical applications, the polarization measurement on the reflected beam helps to understand the features of a metal.

2.5.2 Quantum mechanics at BS and PBS

Unlike the optical components such as mirrors, waveplates, BS and PBS do not only manipulate the polarization mode of photon qubits, but also the spatial mode. Our discussion in the following are mainly inspired by the literature [179], The state of a qubit with spatial and polarization mode is,

$$|\psi\rangle = \begin{pmatrix} \alpha \\ \beta \end{pmatrix}_{pol} \otimes \begin{pmatrix} a \\ b \end{pmatrix}_{spat} \quad (2.5.5)$$

where $a^2 + b^2 = 1$ and $\alpha^2 + \beta^2 = 1$ denote the normalization factor for the spatial mode ‘s’ and polarization mode ‘pol’ on orthonormal basis, respectively. The two qubits state for photon 1 and 2 can be expressed as,

$$|\psi\rangle_{12} = \begin{pmatrix} \alpha_1 \\ \beta_1 \end{pmatrix}_{pol} \otimes \begin{pmatrix} a_1 \\ b_1 \end{pmatrix}_{spat} \otimes \begin{pmatrix} \alpha_2 \\ \beta_2 \end{pmatrix}_{pol} \otimes \begin{pmatrix} a_2 \\ b_2 \end{pmatrix}_{spat} \quad (2.5.6)$$

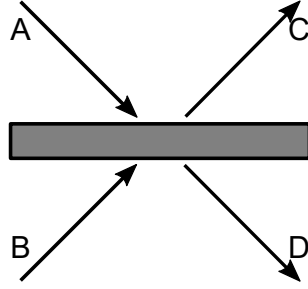


Figure 2.23: Sketch of a beam splitter.

As shown in Fig. 2.23, the spatial mode operation of a beam splitter on the single-qubit state can be explained as the application of a linear transformation matrix \mathbf{R}_{BS} applied on the photon state $\begin{pmatrix} a \\ b \end{pmatrix}$. The basis vector $\begin{pmatrix} 1 \\ 0 \end{pmatrix}$ is for a photon in input port A and $\begin{pmatrix} 0 \\ 1 \end{pmatrix}$ is for a photon in port B. The transformation process is,

$$\begin{pmatrix} c \\ d \end{pmatrix} = \mathbf{R}_{BS} \cdot \begin{pmatrix} a \\ b \end{pmatrix} \quad (2.5.7)$$

with the transformation matrix for BS being,

$$\mathbf{R}_{BS}^{(A)} = \begin{pmatrix} ir & t \\ t & ir \end{pmatrix} \quad (2.5.8)$$

r and t are the reflection and transmission coefficients of the BS relative to input port A. The spatial mode of Jones matrix for input port B of BS is,

$$\mathbf{R}_{BS}^{(B)} = \begin{pmatrix} t & ir \\ ir & t \end{pmatrix} \quad (2.5.9)$$

Then the transformation matrix of the BS, including the polarization degree of freedom, becomes,

$$\begin{aligned} \mathbf{R}_{BS} &= \begin{pmatrix} t_H & 0 \\ 0 & t_V \end{pmatrix}_{spat} \otimes \begin{pmatrix} 1 & 0 \\ 0 & 1 \end{pmatrix}_{pol} + \begin{pmatrix} r_H & 0 \\ 0 & r_V \end{pmatrix}_{spat} \otimes \begin{pmatrix} 0 & i \\ i & 0 \end{pmatrix}_{pol} \\ &= \begin{pmatrix} t_H & ir_H & 0 & 0 \\ ir_H & t_H & 0 & 0 \\ 0 & 0 & t_V & ir_V \\ 0 & 0 & ir_V & t_V \end{pmatrix} \end{aligned} \quad (2.5.10)$$

where t_H , t_V , r_H , and r_V are the transmission and reflection coefficients for horizontal (H) and vertical (V) polarization. However, the polarization operation of BS is usually

negligible, as it does not affect the polarization state of the photons.

For the ordinary polarizing beam splitter (PBS), which possess full transmission of H -polarized ($t_H = 1$, $t_V = 0$) and reflection of V -polarized light ($r_H = 0$, $r_V = 1$), the transformation matrix (similar to Equ. 2.5.10) can be written as

$$\begin{aligned} \mathbf{R}_{PBS} &= \begin{pmatrix} 1 & 0 \\ 0 & 0 \end{pmatrix}_{pol} \otimes \begin{pmatrix} 1 & 0 \\ 0 & 1 \end{pmatrix}_{spat} + \begin{pmatrix} 0 & 0 \\ 0 & 1 \end{pmatrix}_{pol} \otimes \begin{pmatrix} 0 & i \\ i & 0 \end{pmatrix}_{spat} \\ &= \begin{pmatrix} 1 & 0 & 0 & 0 \\ 0 & 1 & 0 & 0 \\ 0 & 0 & 0 & i \\ 0 & 0 & i & 0 \end{pmatrix} \end{aligned} \quad (2.5.11)$$

It is apparent that the form of this matrix align with the one of a controlled-NOT (CNOT) gate in quantum logic circuits [31, 180]. It has been demonstrated that the CNOT gate to be an essential element in the entanglement purification scheme (Sec. 1.1.4).

2.5.3 Phase retarders and Hadamard gate

Phase retarders are the optical elements, made of birefringent uni-axial crystals, introducing a phase shift between the horizontal and vertical polarization. The Jones matrix of any phase retarder with fast axis equal to either H or V axis of the electric field can be conveniently expressed as,

$$\mathbf{R}_{phase} = \begin{pmatrix} e^{i\eta_H} & 0 \\ 0 & e^{i\eta_V} \end{pmatrix}_{pol} \quad (2.5.12)$$

with η_H and η_V the phase offsets of the electric field along H and V directions, respectively.

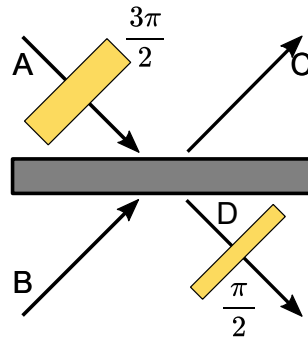


Figure 2.24: Sketch of a beam splitter with phase retarders.

For a combination of phase retarder and BS as illustrated in Fig. 2.24, a photon passes through a $3\pi/2$ retarder and goes into the 50:50 BS from port A. A $\pi/2$ retarder is placed at the output port D of BS. First, we can calculate the output state before the $\pi/2$

retarder as,

$$\begin{aligned}
 |\varphi\rangle_d &= R_{BS} \cdot R_{3\pi/2} \cdot |\varphi\rangle_a \\
 &= \frac{1}{\sqrt{2}} \begin{pmatrix} i & 1 \\ 1 & i \end{pmatrix}_{BS} \cdot \begin{pmatrix} -i & 0 \\ 0 & -i \end{pmatrix}_{3\pi/2} \cdot \begin{pmatrix} 1 \\ 0 \end{pmatrix}_a \\
 &= \frac{1}{\sqrt{2}} \begin{pmatrix} 1 \\ -i \end{pmatrix} = \frac{1}{\sqrt{2}} \left[\begin{pmatrix} 1 \\ 0 \end{pmatrix}_c + \begin{pmatrix} 0 \\ -i \end{pmatrix}_d \right]
 \end{aligned} \tag{2.5.13}$$

Since the $\pi/2$ phase retarder will implement an additional phase on the photons at port D of BS, the resultant state is,

$$\begin{aligned}
 |\varphi\rangle &= \frac{1}{\sqrt{2}} \left[\begin{pmatrix} 1 \\ 0 \end{pmatrix}_c + \begin{pmatrix} i & 0 \\ 0 & i \end{pmatrix}_{\pi/2} \begin{pmatrix} 0 \\ -i \end{pmatrix}_d \right] \\
 &= \frac{1}{\sqrt{2}} \begin{pmatrix} 1 \\ 1 \end{pmatrix}
 \end{aligned} \tag{2.5.14}$$

Likewise, the combination will transform the spatial mode of the photon entering port B to be,

$$|\varphi\rangle = \frac{1}{\sqrt{2}} \begin{pmatrix} 1 \\ -1 \end{pmatrix} \tag{2.5.15}$$

The Hadamard gate can be achieved by sending H - and V - polarized photons to port A and B, respectively, which executes the operation of transforming an initial qubit $|0\rangle$ to $\frac{1}{\sqrt{2}}(|0\rangle + |1\rangle)$ and $|1\rangle$ to $\frac{1}{\sqrt{2}}(|0\rangle - |1\rangle)$.

2.5.4 Mach-Zehnder interferometer

In the Sec. 2.3.7, Mach-Zehnder interferometer (MZI) has been revealed to be a common photonic operator for measuring the indistinguishability of photons from QDs. Fig. 2.25 shows the sketch of the common MZI consisting of two BSs, the spatial transformation matrix is,

$$\mathbf{R}_{MZI} = \mathbf{R}_{12}^{(BS)} \cdot \mathbf{R}_{12}^{(BS)} = \frac{1}{\sqrt{2}} \begin{pmatrix} i & 1 \\ 1 & i \end{pmatrix} \cdot \frac{1}{\sqrt{2}} \begin{pmatrix} i & 1 \\ 1 & i \end{pmatrix} = i \begin{pmatrix} 0 & 1 \\ 1 & 0 \end{pmatrix} \tag{2.5.16}$$

Suppose we have a single photon at input port A of the interferometer, the final state will be,

$$|\Psi\rangle_{final} = \mathbf{R}_{MZI} \cdot \begin{pmatrix} 1 \\ 0 \end{pmatrix} = \begin{pmatrix} 0 \\ i \end{pmatrix} = i \begin{pmatrix} 0 \\ 1 \end{pmatrix} \tag{2.5.17}$$

Above equation indicates that the photon will come out from port F with a $\pi/2$ phase shift of spatial mode comparing with the initial state of the photon.

As a comparison, if we replace the two BSs with PBSs, the polarization mode needs to

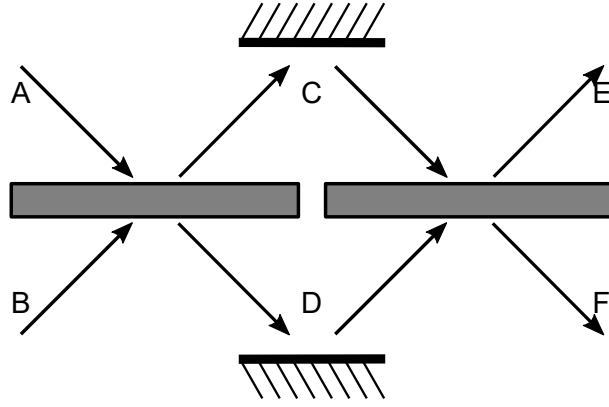


Figure 2.25: Sketch of the Mach-Zehnder interferometer.

be considered, thus leading to the transformation matrix of MZI to be,

$$\mathbf{R}_{MZI} = \mathbf{R}_{12}^{(PBS)} \cdot \mathbf{R}_{12}^{(PBS)} = \begin{pmatrix} 1 & 0 & 0 & 0 \\ 0 & 1 & 0 & 0 \\ 0 & 0 & 0 & i \\ 0 & 0 & i & 0 \end{pmatrix} \cdot \begin{pmatrix} 1 & 0 & 0 & 0 \\ 0 & 1 & 0 & 0 \\ 0 & 0 & 0 & i \\ 0 & 0 & i & 0 \end{pmatrix} = \begin{pmatrix} 1 & 0 & 0 & 0 \\ 0 & 1 & 0 & 0 \\ 0 & 0 & -1 & 0 \\ 0 & 0 & 0 & -1 \end{pmatrix} \quad (2.5.18)$$

When an H -polarized photon enters at port A, the final state of the photon after polarizing-MZI is,

$$|\Psi\rangle = \begin{pmatrix} 1 & 0 & 0 & 0 \\ 0 & 1 & 0 & 0 \\ 0 & 0 & -1 & 0 \\ 0 & 0 & 0 & -1 \end{pmatrix} \cdot \begin{pmatrix} 1 \\ 0 \\ 0 \\ 0 \end{pmatrix} = \begin{pmatrix} 1 \\ 0 \\ 0 \\ 0 \end{pmatrix} \rightarrow \begin{pmatrix} H_e \\ H_f \\ V_e \\ V_f \end{pmatrix} \quad (2.5.19)$$

The H -polarized photon will come out from the port E of the second PBS.

2.5.5 Hong-Ou-Mandel interferometer

As BS is a special optical element operating the spatial mode of state of photons, we can ignore the Jones matrix for polarization states when we study the spatial behavior. For example, in case two distinguishable photons (1 and 2) arrive at a 50:50 BS simultaneously

(Fig. 2.26(a)), the spatial state of photons from the BS is,

$$\begin{aligned}
 |\varphi\rangle_{cd} &= \mathbf{R}_{12}^{(BS)} |\varphi\rangle_{ab}^{(12)} = (\mathbf{R}_1 \otimes \mathbf{R}_2) |\varphi\rangle_{ab}^{(12)} \\
 &= \left[\frac{1}{\sqrt{2}} \begin{pmatrix} i & 1 \\ 1 & i \end{pmatrix}_1 \otimes \frac{1}{\sqrt{2}} \begin{pmatrix} i & 1 \\ 1 & i \end{pmatrix}_2 \right] \cdot \left[\begin{pmatrix} 1 \\ 0 \end{pmatrix}_1 \otimes \begin{pmatrix} 0 \\ 1 \end{pmatrix}_2 \right] \\
 &= \frac{1}{2} \begin{pmatrix} i \\ 1 \end{pmatrix}_1 \otimes \begin{pmatrix} 1 \\ i \end{pmatrix}_2 = \frac{1}{2} \begin{pmatrix} i \\ -1 \\ 1 \\ i \end{pmatrix} \equiv \begin{pmatrix} |c\rangle_1 \\ |d\rangle_1 \end{pmatrix} \otimes \begin{pmatrix} |c\rangle_2 \\ |d\rangle_2 \end{pmatrix} = \begin{pmatrix} |c\rangle_1 |c\rangle_2 \\ |c\rangle_1 |d\rangle_2 \\ |d\rangle_1 |c\rangle_2 \\ |d\rangle_1 |d\rangle_2 \end{pmatrix} \quad (2.5.20)
 \end{aligned}$$

where i denotes the phase of $\pi/2$ for V -polarized photons, the $|c\rangle_1 |c\rangle_2$, $|c\rangle_1 |d\rangle_2$, $|d\rangle_1 |c\rangle_2$, $|d\rangle_1 |d\rangle_2$ indicate the possibilities of photons outputting from the ports. As an example, $|c\rangle_1 |d\rangle_2$ means that photon 1 and 2 come out from port C and D of BS, respectively.

However, if two particles are indistinguishable in every degree of freedom, it means that no physical significance attaches to the labeling of these particles, and there is no observable effect if any two of them are interchanged. The two states $|ab\rangle$ and $|ba\rangle$ can only differ by a global phase, which has no influence on physical measurements. Relativistic quantum field theory shows that Bosons follow Bose-Einstein statistics and consequentially must be symmetric under particle exchange: $|ab\rangle = |ba\rangle$. As boson particles, photons need to follow that theory. We can define the exchange operator P which exchanges the coordinates of the two particles: $P_{ij} |ab\rangle = |ba\rangle$, with the eigenvalue λ of the exchange operator ($P_{ij} |ab\rangle = \lambda |ab\rangle$). According to $P_{ij}^2 |ab\rangle = \lambda^2 |ab\rangle$ and $P_{ij}^2 |ab\rangle = |ab\rangle$, it is therefore obtained that $\lambda = \pm 1$ and $P |\psi\rangle = \pm |\psi\rangle$. By determining the eigenfunction, the normalized eigenstates for the exchange operator for identical particles can be expressed as [181],

$$\begin{aligned}
 |\psi\rangle_{symmetric} &= \frac{1}{\sqrt{2}} (|ab\rangle + |ba\rangle) \\
 |\psi\rangle_{antisymmetric} &= \frac{1}{\sqrt{2}} (|ab\rangle - |ba\rangle)
 \end{aligned} \quad (2.5.21)$$

where symmetric condition is applicable for Bosons. Therefore, the spatial state for indistinguishable photon 1 and 2 at the BS is,

$$|\psi\rangle_{ab}^{(12)} = \frac{1}{\sqrt{2}} (|a\rangle_1 |b\rangle_2 + |a\rangle_2 |b\rangle_1) = \frac{1}{\sqrt{2}} \cdot \begin{pmatrix} 0 \\ 1 \\ 1 \\ 0 \end{pmatrix} \quad (2.5.22)$$

By applying the BS transformation 4x4-matrix above, the outcome state for the case of

two-qubits is,

$$|\psi\rangle_{cd}^{(indis)} = \mathbf{R}_{12}^{(BS)} |\psi\rangle_{ab}^{(12)} = \frac{i}{\sqrt{2}} \begin{pmatrix} 1 \\ 0 \\ 0 \\ 1 \end{pmatrix} \sim |c\rangle_1 |c\rangle_2 + |d\rangle_1 |d\rangle_2 \quad (2.5.23)$$

which immediately shows the result: no coincidences for a measurement in C and D, corresponding to the conclusion we propose in the Sec. 2.3.7 for HOM effect of indistinguishable photons impinging on the BS simultaneously. An alternative way of deducing the output state for indistinguishable photons meeting the symmetric exchange condition is given by,

$$|\varphi\rangle_{cd}^{(indis)} = \frac{1}{\sqrt{2}} (|\varphi_{cd}\rangle + |\varphi_{cd}\rangle) = \frac{1}{2\sqrt{2}} \left[\begin{pmatrix} i \\ -1 \\ 1 \\ i \end{pmatrix} + \begin{pmatrix} i \\ 1 \\ -1 \\ i \end{pmatrix} \right] \sim |c\rangle_1 |c\rangle_2 + |d\rangle_1 |d\rangle_2 \quad (2.5.24)$$

For the two-photon state, the argument of symmetry under exchange leads us to a basis different from the one using simple product states. When we extend our discussion about two-photon spatial state to be,

$$\begin{aligned} |\phi^\pm\rangle &= \frac{1}{\sqrt{2}} (|a\rangle_1 |a\rangle_2 \pm |b\rangle_1 |b\rangle_2) \\ |\psi^\pm\rangle &= \frac{1}{\sqrt{2}} (|a\rangle_1 |b\rangle_2 \pm |b\rangle_1 |a\rangle_2) \end{aligned} \quad (2.5.25)$$

which consist of the linear combinations of the 4 product states as similar as two-photon Bell states in polarization. With the transformation matrix of the beam splitter $\mathbf{R}_{BS}^{(12)}$, the input state would be transformed as,

$$\begin{aligned} |\psi^+\rangle &\rightarrow |\Phi^+\rangle \\ |\psi^-\rangle &\rightarrow |\Psi^-\rangle \\ |\phi^+\rangle &\rightarrow |\Psi^+\rangle \\ |\phi^-\rangle &\rightarrow |\Phi^-\rangle \end{aligned} \quad (2.5.26)$$

However, for two-photon qubits entering a PBS (Fig. 2.26(b)), we need to take the polarization into account, since a PBS manipulates both polarization and spatial mode of light. For a two-photon state, the transformation matrix for PBS is:

$$\mathbf{R}_{12}^{(PBS)} = \mathbf{R}_1^{(PBS)} \otimes \mathbf{R}_2^{(PBS)} \quad (2.5.27)$$

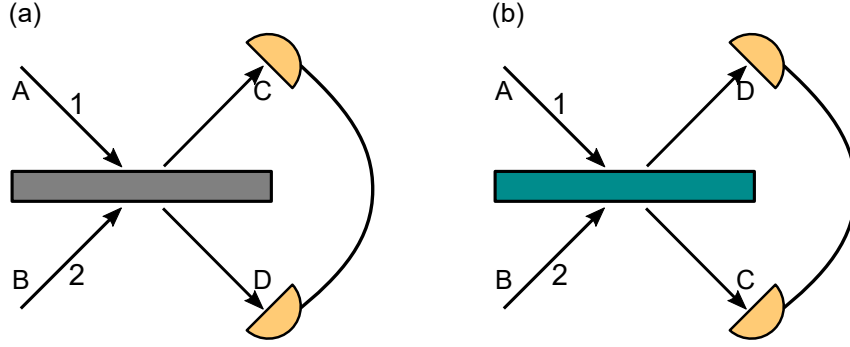


Figure 2.26: Sketch of two-photon state at a (a) BS (grey) or (b) PBS (green).

In case of two indistinguishable photons sent to each input port of PBS followed by a D -polarizer placed after the port C and D, respectively, the resultant state is,

$$\begin{aligned} |\varphi\rangle'_{cd} &= \mathbf{R}_{12}^{(polarizer)} \cdot |\varphi\rangle_{cd} \\ &= \mathbf{R}_{12}^{(polarizer)} \cdot \mathbf{R}_{12}^{(PBS)} \cdot |\varphi\rangle_{12} \end{aligned} \quad (2.5.28)$$

with the matrix of two D -polarization polarizers to be,

$$\begin{aligned} \mathbf{R}_{12}^{(polarizer)} &= \mathbf{R}_1^{(C)} \otimes \mathbf{R}_2^{(D)} \\ &= \frac{1}{2} \begin{pmatrix} 1 & 1 \\ 1 & 1 \end{pmatrix}_{1,pol} \otimes \begin{pmatrix} 1 & 0 \\ 0 & 1 \end{pmatrix}_{1,spat} \otimes \frac{1}{2} \begin{pmatrix} 1 & 1 \\ 1 & 1 \end{pmatrix}_{2,pol} \otimes \begin{pmatrix} 1 & 0 \\ 0 & 1 \end{pmatrix}_{2,spat} \end{aligned} \quad (2.5.29)$$

Therefore, the output state is,

$$\begin{aligned} |\varphi\rangle'_{cd} &= \frac{i}{4\sqrt{2}} \begin{pmatrix} 1 \\ 1 \end{pmatrix}_{1,pol} \otimes \begin{pmatrix} 1 \\ 1 \end{pmatrix}_{2,pol} \otimes \begin{pmatrix} 1 \\ 0 \\ 0 \\ 1 \end{pmatrix}_{12,spat} \\ &= \frac{i}{2\sqrt{2}} \cdot \begin{pmatrix} \frac{1}{\sqrt{2}} \\ \frac{1}{\sqrt{2}} \end{pmatrix}_{1,pol} \otimes \begin{pmatrix} \frac{1}{\sqrt{2}} \\ \frac{1}{\sqrt{2}} \end{pmatrix}_{2,pol} \otimes \left[\begin{pmatrix} 1 \\ 0 \end{pmatrix}_1 \otimes \begin{pmatrix} 1 \\ 0 \end{pmatrix}_2 + \begin{pmatrix} 0 \\ 1 \end{pmatrix}_1 \otimes \begin{pmatrix} 0 \\ 1 \end{pmatrix}_2 \right]_{spat} \\ &= \frac{i}{2} \cdot \frac{1}{\sqrt{2}} (|D\rangle_c |D\rangle_c + |D\rangle_d |D\rangle_d) \end{aligned} \quad (2.5.30)$$

For simplification of notation, here we write the ket for the first photon at first, and for photon 2 in second place. Thus, we write the polarization and spatial states now like $|H\rangle_1 |c\rangle_1 = |H\rangle |c\rangle$. As similar as the HOM interference happening at BS, it is impossible to observe coincidences between the output ports C and D, once the particles are indistinguishable. However, because of the D -projection in both arms, the measurement efficiency is reduced by a factor 1/4 comparing $|\varphi\rangle'_{cd}$ with Equ. 2.5.23 and 2.5.24.

When we go a step further and consider the input of a two-qubits polarization-based

Bell state:

$$|\psi^+\rangle_{polarization} = \frac{1}{\sqrt{2}} (|H\rangle_1 |V\rangle_2 + |V\rangle_1 |H\rangle_2) \quad (2.5.31)$$

with photon 1 entering port A and photon 2 entering port B. It is therefore possible to write the state in a simplified way as:

$$|\varphi_{in}\rangle = \frac{1}{\sqrt{2}} (|H\rangle_a |V\rangle_b + |V\rangle_a |H\rangle_b) \quad (2.5.32)$$

Then the state after the PBS is,

$$\begin{aligned} |\varphi\rangle_{cd} &= \mathbf{R}_{12}^{(PBS)} \otimes \frac{1}{\sqrt{2}} \left[\begin{pmatrix} 1 \\ 0 \\ 0 \\ 0 \end{pmatrix}_1 \otimes \begin{pmatrix} 0 \\ 0 \\ 0 \\ 1 \end{pmatrix}_2 + \begin{pmatrix} 0 \\ 0 \\ 1 \\ 0 \end{pmatrix}_1 \otimes \begin{pmatrix} 0 \\ 1 \\ 0 \\ 0 \end{pmatrix}_2 \right] \\ &= \frac{i}{\sqrt{2}} (|H\rangle_1 |c\rangle_1 |V\rangle_2 |c\rangle_2 + |V\rangle_1 |d\rangle_1 |H\rangle_2 |d\rangle_2) \\ &= \frac{i}{\sqrt{2}} (|H\rangle_c |V\rangle_c + |V\rangle_d |H\rangle_d) \end{aligned} \quad (2.5.33)$$

Now we make the state symmetric under particle exchange principle:

$$\begin{aligned} |\varphi\rangle'_{cd} &= \frac{1}{\sqrt{2}} (|\varphi\rangle_{cd,12} + |\varphi\rangle_{cd,21}) = \frac{i}{2} (|H\rangle_c |V\rangle_c + |V\rangle_d |H\rangle_d + |V\rangle_c |H\rangle_c + |H\rangle_d |V\rangle_d) \\ &= \frac{i}{2} [|cc\rangle (|HV\rangle + |VH\rangle) + |dd\rangle (|HV\rangle + |VH\rangle)] \\ &= i |\Phi^+\rangle_{12,spat} |\Psi^+\rangle_{12,pol} \end{aligned} \quad (2.5.34)$$

In a summary, we deduce the outcome of four polarization-entangled Bell states after sending into PBS,

$$\begin{aligned} |a\rangle_1 |b\rangle_2 |\psi^+\rangle_{pol} &\longrightarrow |\Phi^+\rangle_{spat} |\Psi^+\rangle_{pol} \\ |a\rangle_1 |b\rangle_2 |\psi^-\rangle_{pol} &\longrightarrow |\Phi^-\rangle_{spat} |\Psi^+\rangle_{pol} \\ |a\rangle_1 |b\rangle_2 |\phi^+\rangle_{pol} &\longrightarrow |\Psi^+\rangle_{spat} |\Phi^-\rangle_{pol} \\ |a\rangle_1 |b\rangle_2 |\phi^-\rangle_{pol} &\longrightarrow |\Psi^+\rangle_{spat} |\Phi^+\rangle_{pol} \end{aligned} \quad (2.5.35)$$

for both input states with polarization of $|\psi^+\rangle$ or $|\psi^-\rangle$, the PBS will transform them to $|\Psi^+\rangle_{pol}$! This should be the reason that we can only distinguish two out of four Bell states (Φ_{pol}^\pm) when using a linear optics based Bell state projection, consisting of a PBS, and a HWP with 22.5° and PBS in each output arm.

2.5.6 Entanglement teleportation with BS

In the Sec. 1.1, we introduce the implementation of photonic entanglement teleportation via the Bell state measurement (BSM). The measurement results are classically transferred to the remote part for Pauli unitary operation on the unknown qubits. However, it is physically impossible to measure all of four Bell states using linear optics at the same time. As displayed in the Fig. 2.27, assuming that the photon we are going to teleport is sent into port A of BS, and it has the polarization state,

$$|\varphi\rangle_a = \alpha |H\rangle_1 + |V\rangle_1 \quad (2.5.36)$$

And the polarization state of EPR pair is,

$$|\varphi\rangle_{EPR} = \gamma |H_2H_3\rangle + \sigma |V_2V_3\rangle \quad (2.5.37)$$

Before the beam splitter, the three photon quantum state can be expressed as,

$$\begin{aligned} |\varphi\rangle_{in} &= \alpha\gamma |H_1H_2H_3\rangle + \alpha\sigma |H_1V_2V_3\rangle + \beta\gamma |V_1H_2H_3\rangle + \beta\sigma |V_1V_2V_3\rangle \\ &= \alpha\gamma |H_3\rangle_1 |H_1H_2\rangle_1 + \alpha\sigma |V_3\rangle_2 |H_1V_2\rangle_2 + \beta\gamma |H_3\rangle_3 |V_1H_2\rangle_3 + \beta\sigma |V_3\rangle_4 |V_1V_2\rangle_4 \\ &= \sum_i^4 \sum_k^4 |\varphi_{12}\rangle_i |\varphi_3\rangle_k \end{aligned} \quad (2.5.38)$$

where $|\varphi_{12}\rangle_i |\varphi_3\rangle_k = 0$ if $i \neq k$. Once we consider both the polarization and spatial mode of photons, the above state can be rewritten as,

$$\begin{aligned} |\varphi\rangle_{in} &= \frac{1}{\sqrt{2}} (|\Phi_{12}^+\rangle (\alpha\gamma |H\rangle_3 + \beta\sigma |V\rangle_3) + |\Phi_{12}^-\rangle (\alpha\gamma |H\rangle_3 - \beta\sigma |V\rangle_3)) \\ &\quad + |\Psi_{12}^+\rangle (\alpha\sigma |H\rangle_3 + \beta\gamma |V\rangle_3) + |\Psi_{12}^-\rangle (\alpha\sigma |H\rangle_3 - \beta\gamma |V\rangle_3) \end{aligned} \quad (2.5.39)$$

Taking into account of the boson nature of photons. If the photon 1 and 2 arrive the BS at the same time, the complete expression for the Bell states should be [182],

$$\begin{aligned} |\Phi^+\rangle_{12} &= \frac{1}{2} (|H_1\rangle |H_2\rangle + |V_1\rangle |V_2\rangle) (|a_1\rangle |b_2\rangle + |b_1\rangle |a_2\rangle) \\ |\Phi^-\rangle_{12} &= \frac{1}{2} (|H_1\rangle |H_2\rangle - |V_1\rangle |V_2\rangle) (|a_1\rangle |b_2\rangle + |b_1\rangle |a_2\rangle) \\ |\Psi^+\rangle_{12} &= \frac{1}{2} (|H_1\rangle |V_2\rangle + |V_1\rangle |H_2\rangle) (|a_1\rangle |b_2\rangle + |b_1\rangle |a_2\rangle) \\ |\Psi^-\rangle_{12} &= \frac{1}{2} (|H_1\rangle |V_2\rangle - |V_1\rangle |H_2\rangle) (|a_1\rangle |b_2\rangle - |b_1\rangle |a_2\rangle) \end{aligned} \quad (2.5.40)$$

in which $|\Psi^-\rangle$ is the only one that is antisymmetric under particle exchange, all others are symmetric [179, 182, 183]. Because the BS only transform the spatial mode of the

photons, we ignore the polarization operation matrix. The output state is,

$$\begin{aligned}
 |\varphi\rangle_{out} &= \mathbf{R}_1^{(BS)} \otimes \mathbf{R}_2^{(BS)} \cdot |\varphi\rangle_{in} \\
 &= \frac{1}{4} \left[(|\phi_{12}^+\rangle \otimes \begin{pmatrix} \alpha\gamma \\ \beta\sigma \end{pmatrix}_{pol,3} + |\phi_{12}^-\rangle \otimes \begin{pmatrix} \alpha\gamma \\ -\beta\sigma \end{pmatrix}_{pol,3} + |\psi_{12}^+\rangle \otimes \begin{pmatrix} \alpha\sigma \\ \beta\gamma \end{pmatrix}_{pol,3} \right] \otimes \begin{pmatrix} i \\ 0 \\ 0 \\ i \end{pmatrix}_{spat,12} \\
 &\quad + \frac{1}{4} |\psi_{12}^-\rangle \otimes \begin{pmatrix} \alpha\sigma \\ -\beta\gamma \end{pmatrix}_{pol,3} \otimes \begin{pmatrix} 0 \\ -1 \\ 1 \\ 0 \end{pmatrix}_{spat,12}
 \end{aligned} \tag{2.5.41}$$

From above equations, it is obvious that the polarization state of photon 1 and 2 is $|\psi^-\rangle$, in case two photon come out from two different output ports. As a consequence, the polarization of photon 3 can be determined accordingly, if coincidence happen between detector 1 and 2.

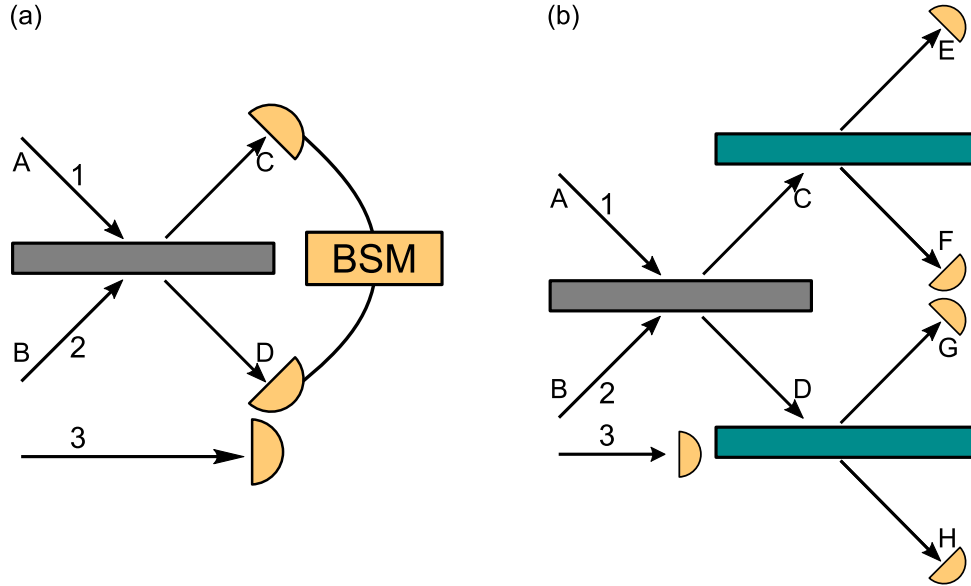


Figure 2.27: Sketch of quantum teleportation with BSM on (a) single- or (b) two- Bell states.

Moreover, when we consider there are another two PBSs after the beam splitter (Fig. 2.27(b)), two of four Bell states are then distinguishable in the teleportation experiment. Because the two PBS after the BS does not affect the state of photon 3, the operation of PBSs only works on the photons 1 and 2. According to the Equ. 2.5.41, we know the

quantum state of photons 1 and 2 after BS is

$$\begin{aligned}
 |\phi\rangle_{cd} = & \frac{1}{4\sqrt{2}} [i(|H_cH_c\rangle + |V_cV_c\rangle + |H_dH_d\rangle + |V_dV_d\rangle)(\alpha\gamma |H\rangle_3 + \beta\sigma |V\rangle_3) \\
 & + i(|H_cH_c\rangle - |V_cV_c\rangle + |H_dH_d\rangle - |V_dV_d\rangle)(\alpha\gamma |H\rangle_3 - \beta\sigma |V\rangle_3) \\
 & + i(|H_cV_c\rangle + |V_cH_c\rangle + |H_dV_d\rangle + |V_dH_d\rangle)(\alpha\sigma |H\rangle_3 + \beta\gamma |V\rangle_3) \\
 & - (|H_cV_d\rangle - |V_cH_d\rangle - |H_dV_c\rangle + |V_dH_c\rangle)(\alpha\sigma |H\rangle_3 - \beta\gamma |V\rangle_3)]
 \end{aligned} \tag{2.5.42}$$

The ultimate state can be obtained,

$$\begin{aligned}
 |\phi\rangle_{cd} = & \frac{1}{4\sqrt{2}} [i(|H_eH_e\rangle - |V_fV_f\rangle + |H_hH_h\rangle - |V_gV_g\rangle)(\alpha\gamma |H\rangle_3 + \beta\sigma |V\rangle_3) \\
 & + i(|H_eH_e\rangle + |V_fV_f\rangle + |H_hH_h\rangle + |V_gV_g\rangle)(\alpha\gamma |H\rangle_3 - \beta\sigma |V\rangle_3) \\
 & - (|H_eV_f\rangle + |V_fH_e\rangle + |H_hV_g\rangle + |V_gH_h\rangle)(\alpha\sigma |H\rangle_3 + \beta\gamma |V\rangle_3) \\
 & - i(|H_eV_g\rangle - |V_fH_h\rangle - |H_hV_f\rangle + |V_gH_e\rangle)(\alpha\sigma |H\rangle_3 - \beta\gamma |V\rangle_3)]
 \end{aligned} \tag{2.5.43}$$

Eventually, we can discriminate $|\psi\rangle_{\pm}$ by measuring any two of the four detectors. If the coincidence is detected between EG or FH, the state is $|\psi^{-}\rangle$. While the state is $|\psi^{+}\rangle$, if the coincidence happen between EF or GH.

2.5.7 Entanglement swapping with BS or PBS

For entanglement swapping, we assume the initial states of entangled photons are,

$$\begin{aligned}
 |\varphi\rangle_{12} &= \alpha |H_1H_2\rangle + \beta |V_1V_2\rangle \\
 |\varphi\rangle_{34} &= \gamma |H_1H_2\rangle + \sigma |V_1V_2\rangle
 \end{aligned} \tag{2.5.44}$$

then, the state of the quantum system is,

$$|\varphi\rangle_{1234} = \alpha\gamma |H_1H_2H_3H_4\rangle + \alpha\sigma |H_1H_2V_3V_4\rangle + \beta\gamma |V_1V_2H_3H_4\rangle + \beta\sigma |V_1V_2V_3V_4\rangle \tag{2.5.45}$$

which can be re-written as,

$$\begin{aligned}
 |\varphi\rangle_{1234} = & \frac{1}{\sqrt{2}} (|\Phi_{23}^{+}\rangle (\alpha\gamma |H_1H_4\rangle + \beta\sigma |V_1V_4\rangle) + |\Phi_{23}^{-}\rangle (\alpha\gamma |H_1H_4\rangle - \beta\sigma |V_1V_4\rangle)) \\
 & + |\Psi_{23}^{+}\rangle (\alpha\sigma |H_1V_4\rangle + \beta\gamma |V_1H_4\rangle) + |\Psi_{23}^{-}\rangle (\alpha\sigma |H_1V_4\rangle - \beta\gamma |V_1H_4\rangle)
 \end{aligned} \tag{2.5.46}$$

The entanglement swapping with BS is the same with teleportation. Once the coincidence happens between the ports 2 and 3 corresponding to polarization state $|\Psi\rangle_{23}^{-}$, photon 1 and 4 will be entangled with a maximally entangled pure state $|\varphi^{-}\rangle_{14} = \alpha\sigma |H_1V_4\rangle - \beta\gamma |V_1H_4\rangle$.

When two indistinguishable photons 2 and 3 arrive at PBS simultaneously as Fig. 2.28,

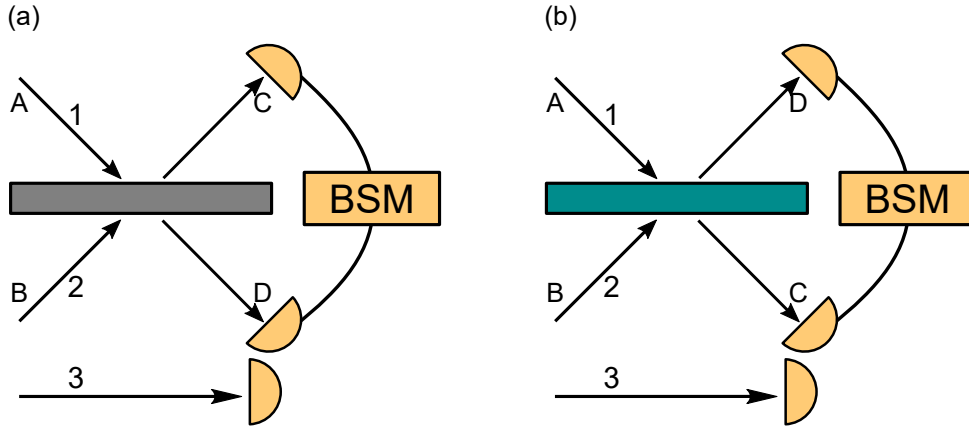


Figure 2.28: Sketch of the entanglement swapping using (a) BS (grey) or (b) PBS (green) for Bell state measurement.

the output state after PBS is,

$$\begin{aligned}
 |\varphi\rangle_{1234}^{(output)} &= \frac{1}{\sqrt{2}} [(|\Psi^+\rangle_{spat,23} |\Phi^-\rangle_{pol,23} (\alpha\gamma |H_1H_4\rangle + \beta\sigma |V_1V_4\rangle) \\
 &\quad + |\Psi^+\rangle_{spat,23} |\Phi^+\rangle_{pol,23} (\alpha\gamma |H_1H_4\rangle - \beta\sigma |V_1V_4\rangle) \\
 &\quad + i |\Phi^+\rangle_{spat,23} |\Psi^+\rangle_{pol,23} (\alpha\sigma |H_1V_4\rangle + \beta\gamma |V_1H_4\rangle) \\
 &\quad + i |\Phi^-\rangle_{spat,23} |\Psi^+\rangle_{pol,23} (\alpha\sigma |H_1V_4\rangle - \beta\gamma |V_1H_4\rangle)]
 \end{aligned} \tag{2.5.47}$$

Provided we insert a 45° polarizer at each output port of the PBS and detect the coincidence, it is equivalent to a projection measurement. The projection vector of the polarizer with the detection of coincidence is,

$$|\psi\rangle = |D_c\rangle |D_d\rangle = |H_c\rangle |H_d\rangle + |H_c\rangle |V_d\rangle + |V_c\rangle |H_d\rangle + |V_c\rangle |V_d\rangle \tag{2.5.48}$$

The state combinations in Equ. 2.5.47 can be separately written as,

$$\begin{aligned}
 |\Psi^+\rangle_{spat,23} |\Phi^-\rangle_{pol,23} &= |H_c\rangle |H_d\rangle - |V_c\rangle |V_d\rangle + |H_d\rangle |H_c\rangle - |V_d\rangle |V_c\rangle \\
 |\Psi^+\rangle_{spat,23} |\Phi^+\rangle_{pol,23} &= |H_c\rangle |H_d\rangle + |V_c\rangle |V_d\rangle + |H_d\rangle |H_c\rangle + |V_d\rangle |V_c\rangle \\
 |\Phi^+\rangle_{spat,23} |\Psi^+\rangle_{pol,23} &= |H_c\rangle |V_c\rangle + |V_c\rangle |H_c\rangle + |H_d\rangle |V_d\rangle + |V_d\rangle |H_d\rangle \\
 |\Phi^-\rangle_{spat,23} |\Psi^+\rangle_{pol,23} &= |H_c\rangle |V_c\rangle + |V_c\rangle |H_c\rangle - |H_d\rangle |V_d\rangle - |V_d\rangle |H_d\rangle
 \end{aligned} \tag{2.5.49}$$

Apparently, the final state when we apply the projector equation Equ. 2.5.48 on Equ. 2.5.47 will give the result of,

$$|\varphi\rangle_{1234}^{(output)} = \alpha\gamma |H_1H_4\rangle - \beta\sigma |V_1V_4\rangle \tag{2.5.50}$$

Therefore, the swapping can be achieved as well, a PBS and two 45° polarizers are used

for BSM. In addition, if the two polarizers are 45° and -45° respectively, the final state of photon 1 and 4 after the coincidence is $\alpha\gamma |H_1H_4\rangle + \beta\sigma |V_1V_4\rangle$ [184].

Entanglement swapping with single quantum dot

Transferring entangled states between photon pairs is essential in quantum communication. Semiconductor quantum dots are the leading candidate for generating polarization-entangled photons deterministically. In this chapter, the swapping of entangled states between two pairs of photons emitted by a single quantum dot is studied for the first time. A joint Bell measurement heralds the successful generation of the Bell state $|\Phi^+\rangle$, yielding a fidelity of 0.81 ± 0.04 and violating the CHSH and Bell inequalities.

This work is a collaboration with Michael Zopf, et al., which has been published in *Physics. Review. Lett.* [185] and dissertation from Michael Zopf [186].

Semiconductor light sources have revolutionized science and technology since laser diodes [187, 188] and vertical-cavity surface-emitting lasers (VCSELs) [189, 190] arrived in the 1960s. Quantum mechanics lies at the roots for these devices, yet quantum states of light have only been studied extensively in recent decades in their own rightsparking the second quantum revolution. Semiconductor sources can now emit single photons [109, 191] and entangled photons [192] on demand, more reliably and intensely than nonlinear crystals. They hold great potential for a range of applications in quantum communication [44], quantum metrology [193], and quantum computation [194].

The next step towards building quantum networks is to transfer entangled states between distinct pairs of photons [47, 195, 196]. This entails substituting the pairwise entanglement in two-photon states with entanglement between photons from different pairs [17, 48]. The first experiment to do this, two decades ago [49], used a technique based on spontaneous parametric down conversion in a nonlinear optical crystal [101, 197, 198]. Though such sources are widely used, for example, to entangle multiple photons [199], their brightness and therefore scalability are fundamentally limited owing to Poissonian emission statistics [82].

Semiconductor quantum dots (QDs), by contrast, are able to generate entangled photon pairs deterministically one by one [200]. However, until recently, QDs were too faint and of poor degree of entanglement and indistinguishability to use for advanced quantum applications. Improvements of the past three years have overcome these limitations. Highly coherent [201] and strongly entangled photons [128, 202] can now be generated with high brightness [26] and reproducibility [128] from QDs.

3.1 Overview of the experimental setup

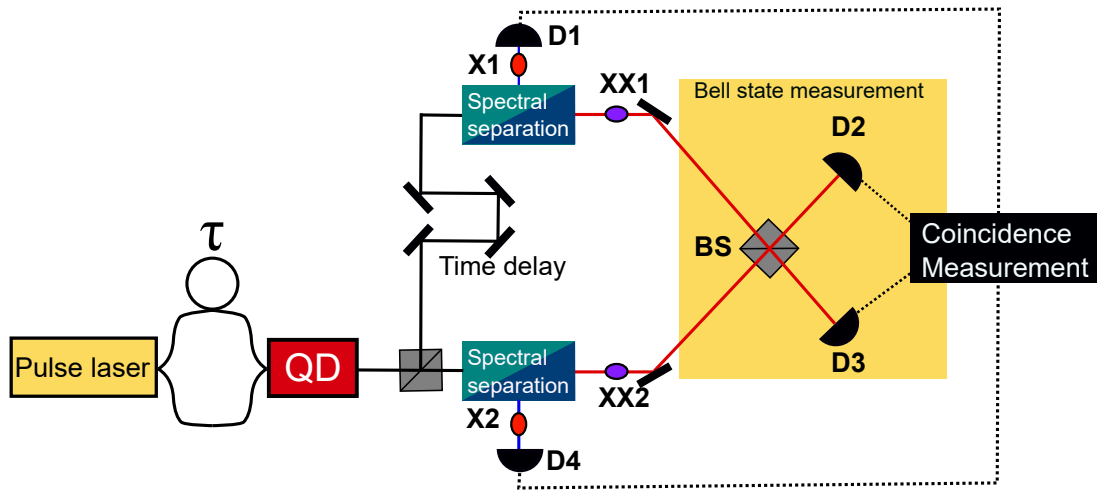


Figure 3.1: Schematic diagram of entanglement swapping with a single semiconductor QD as the entangled photon source. Two consecutive pairs of polarization-entangled photons $XX_i - X_i$ ($i=1,2$) are generated from a QD with a time delay of τ . The XX photons in the earlier pair of XX-X photons randomly reflected by the BS is interfered with the XX photons in latter pairs transmitted by the BS. Notch filters are utilized for spectrally splitting the path of XX and X photons. A time delay of τ is intentionally set up to ensure the concurrent arrival time of XX photons for BSM. The remaining X photons from both pairs are projected on a series polarization basis for tomography measurement.

Fig. 3.1 shows the sketch of first entanglement swapping between polarization-entangled photons emitted by a single semiconductor QD. Two pairs of polarization-entangled photons are consecutively emitted (emissions 1 and 2) by a single semiconductor QD. The polarization of one photon from each pair is measured by separate detectors. A joint Bell state measurement (BSM) is then made on the remaining two photons. Light from a pulsed Ti:sapphire laser is sent to the double pulse generation setup to excite the QD. The bright sources of entangled photons in our experiment are GaAs/AlGaAs QDs embedded in a broadband optical antenna, offering photon extraction efficiencies up to 65% while preserving a high single-photon purity and entanglement fidelity [138].

3.2 Sample information

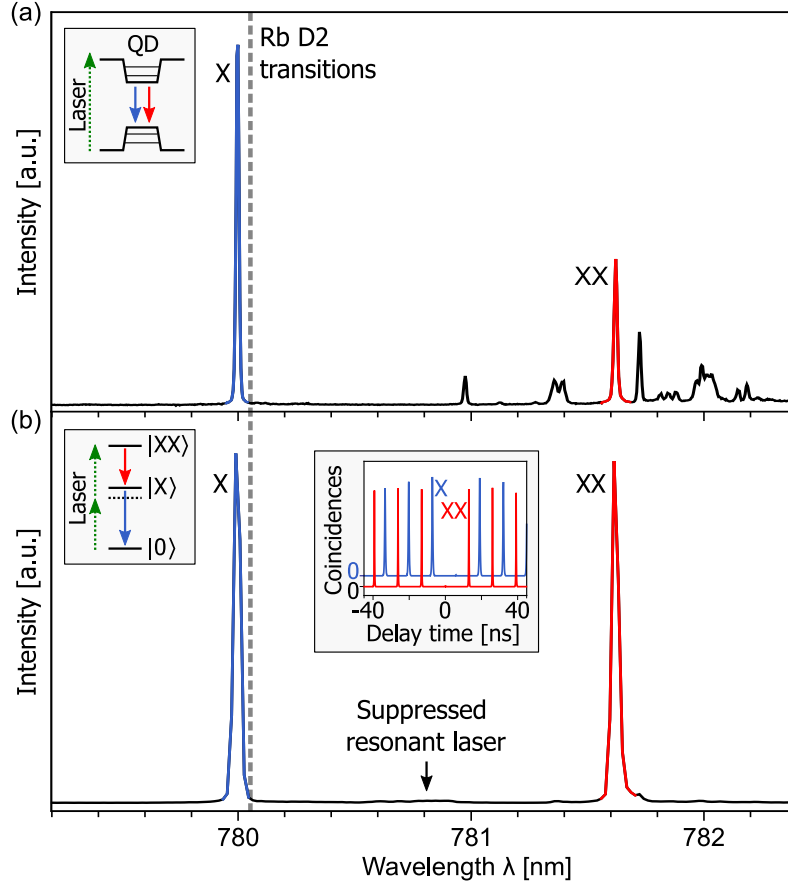


Figure 3.2: (a) QD photoluminescence spectrum under above-band-gap excitation highlighting the prominent X and XX emissions. (b) Emission spectrum under pulsed resonant two-photon excitation of the biexciton state. Decay via the intermediate exciton states results in the emission of polarization-entangled photon pairs XX-X. The inset shows the intensity auto-correlations, indicating a high single-photon purity of $g^{(2)}(0) < 0.005$. Reprinted figures with permission from [185]. Copyright 2019, American Physical Society, without any changes made.

At a sample temperature of $T = 4$ K, a selected QD is first triggered by optically pumping the surrounding host semiconductor material. The emission spectrum in Fig. 3.2(b) displays two prominent features: the neutral exciton (X) emission at 780.0 nm and the neutral biexciton (XX) emission at 781.6 nm. To generate polarization-entangled photon pairs, we exploit the XX-X radiative cascade [200]. Deterministic excitation of the XX state is ensured by resonant two photon excitation (TPE). A pair of photons is emitted in the successive decay via the intermediate X states to the ground state [left inset of Fig. 3.2(c)]. The photons share the polarization-entangled Bell state in the respective emission $i=1,2$,

$$|\Phi^+\rangle_i = \frac{1}{\sqrt{2}}(|H_{XX}H_X\rangle + |V_{XX}V_X\rangle) \quad (3.2.1)$$

with H and V representing horizontal and vertical polarization of the rectilinear basis. Figure 3.2 shows the resonant two-photon excitation spectrum of the XX cascade emission. The resonant laser is well suppressed using notch filters. Autocorrelation measurements [203] show high single-photon purities for X and XX emissions of $g_X^{(2)} = 0.0041 \pm 0.0003$ and $g_{XX}^{(2)} = 0.0050 \pm 0.0005$ (inset).

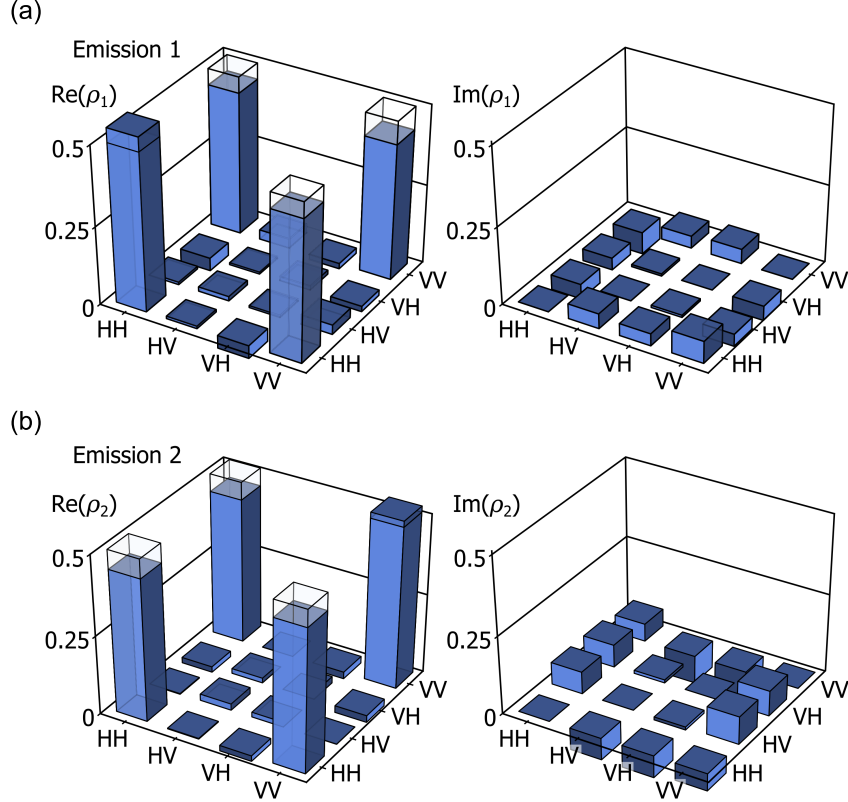


Figure 3.3: Two-photon density matrices of the photon pairs $XX_i - X_i$ from (a) emission $i=1$ and (b) emission $i=2$, resembling the Bell state $|\Phi^+\rangle$ (shaded areas) with fidelities f_i of $f_1 = 0.9369 \pm 0.0004$ and $f_2 = 0.9267 \pm 0.0004$. Reprinted figures with permission from [185]. Copyright 2019, American Physical Society, without any changes made.

Successful entanglement swapping relies on high entanglement fidelities f_i of the initial photon pairs (emission $i = 1, 2$) and on high photon indistinguishabilities I of the XX photons sent to the BSM. We perform quantum state tomography [160] to reconstruct the full two-photon density matrix ρ_i of emission $i = 1, 2$ as shown in Figs. 3.3(a) and 3.3(b), respectively. The real (left) and imaginary (right) parts clearly resemble the Bell state $|\Phi^+\rangle$. We obtain fidelities of $f_1 = 0.9369 \pm 0.0004$ (earlier pairs), and $f_2 = 0.9267 \pm 0.0004$, indicating highly entangled photon emission. To ensure successful quantum interference, the arrival times of XX_1 and XX_2 are matched by delaying the XX_1 photons before the BSM. The photons then pass through an H- or a V- oriented polarizer in each beam splitter output, which reduces the heralding efficiency but ensures that photons in the wrong polarization mode are discarded. Single-mode fibers deliver

the photons to superconducting nanowire single photon detector (SNSPD) with time resolutions of 50 ps.

3.3 Entanglement swapping with a single quantum dot

Figure 3.4 shows a coincidence histogram obtained in an indistinguishability measurement [204] based on Hong-Ou-Mandel interference [164]. The two consecutive XX photons are guided into a separate, unbalanced Mach-Zehnder interferometer featuring a time delay identical to that between XX_1 and XX_2 . Reduced coincidences are observed on two subsequent avalanche photodiodes with a time resolution of > 300 ps. The photon polarization is then changed by a HWP, rendering the photons distinguishable and increasing the coincidences. The coincidences for parallel polarizations (red) show a significant reduction in comparison with those for perpendicular polarizations (black). The visibility is obtained by,

$$V = 1 - \frac{A_{\parallel}}{A_{\perp}} = 0.539 \quad (3.3.1)$$

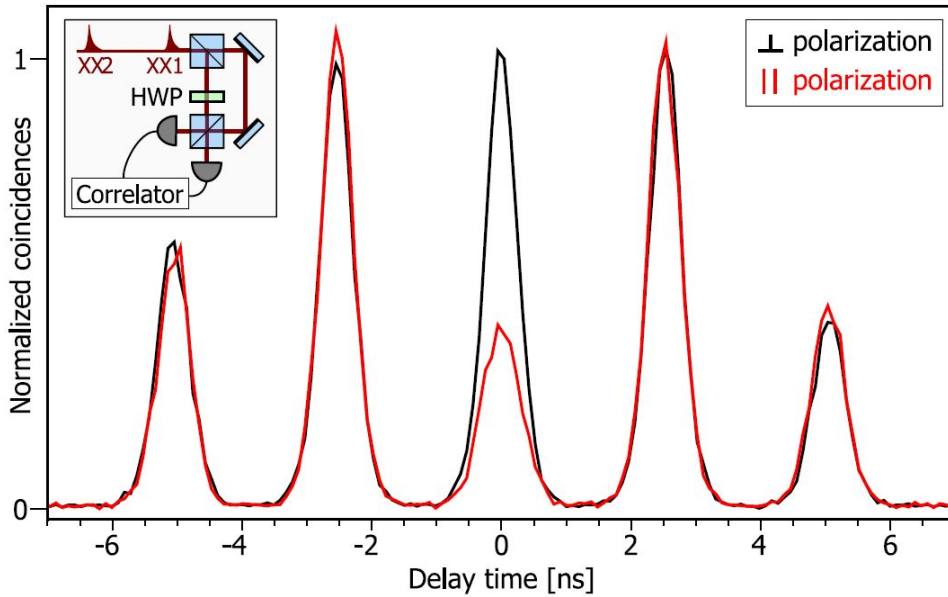


Figure 3.4: The indistinguishability $I = 0.569 \pm 0.009$ of photons XX_1 and XX_2 derived from a Hong-Ou-Mandel measurement using a separate, unbalanced Mach-Zehnder interferometer (inset) and avalanche photodiodes. By means of a HWP, copolarized photons yield reduced coincidences (red) compared with crossed polarizations (black). For entanglement swapping, the indistinguishability is further increased by time gating at the Bell state measurement. Reprinted figures with permission from [185]. Copyright 2019, American Physical Society, without any changes made.

Due to imperfections in the polarization optics, the polarizations cannot be set to be

fully orthogonal for measuring the case of distinguishable photons. A remaining interference visibility $V_{dist} = 0.108$ (measured with a narrow-band laser) is observed. Furthermore, the visibility is corrected from the unbalanced beam splitter transmission and reflection [170], in our case with a transmittance of $T = 0.477$ and a reflectance $R = 0.523$. By correcting the visibility from these effects, the photon indistinguishability (strictly speaking a lower bound to it) is obtained. The uncertainties are derived from Poissonian counting statistics and Gaussian error propagation.

$$I = \frac{R^2 + T^2}{2RT} - \frac{A_{\parallel} \cdot (1 - V_{dist})}{A_{\perp} - A_{\parallel} \cdot V_{dist}} = 0.569 \pm 0.009 \quad (3.3.2)$$

It directly specifies the success probability of the BSM in the entanglement swapping experiment. Time gating of BSM events further increases the photon indistinguishability.

3.4 Influence of indistinguishability on entanglement swapping fidelity

In order to estimate the final polarization state ρ of remaining X photon pairs, we developed a theoretical model that solely requires the density matrices ρ_1 and ρ_2 and the photon indistinguishability I . The final state ρ is written as weighted sum of the expected density matrices, when assuming zero and unity indistinguishability,

$$\rho = I\rho^{I=1} + (1 - I)\rho^{I=0} \quad (3.4.1)$$

Based on the measurement results obtained in Figs. 3.3(a) and 3.3(b), the fidelity to the Bell state $|\Psi^+\rangle$ is expected to be $f_{AB} = 0.71$. Distinguishable photons $I = 0$ result in a fidelity as high as $f_{AB} = 0.48$ since photon pairs that are in the right spatial but wrong polarization mode are discarded by the polarizers in our BSM (fig. 3.5(a)). We increase f_{AB} further by post-selecting BSM detection events that lie in a time gate width of 47 ps, at the expense of the total rate of heralding events. As shown in fig. 3.5(b), the ideal limit of $I = 1$ (zero gate width) would result in a fidelity of $f_{AB} = 0.89$. Figure 3.5(c) shows the fidelity of the swapped state as a function of photon indistinguishability I . The measured data point with $f_{AB} = 0.71 \pm 0.03$ (red square) fits well to the estimated value on the solid blue line. The determined density matrix shown in Fig. 3.4(d) closely resembles the Bell state $|\Psi^+\rangle$. The fidelity of $f_{AB} = 0.81 \pm 0.04$ clearly surpasses the classical limit of 0.5 and therefore testifies to the successful swapping of the entangled state. Based on our theoretical model, we estimate a photon indistinguishability of $I = 0.823 \pm 0.017$ in that case.

Figure 3.7(a) features the measurement of fourfold coincidences in the copolarized and cross-polarized diagonal bases as a function of the relative time delay between emissions 1 and 2. In this fashion the temporal overlap of the XX photons at the beam splitter in the

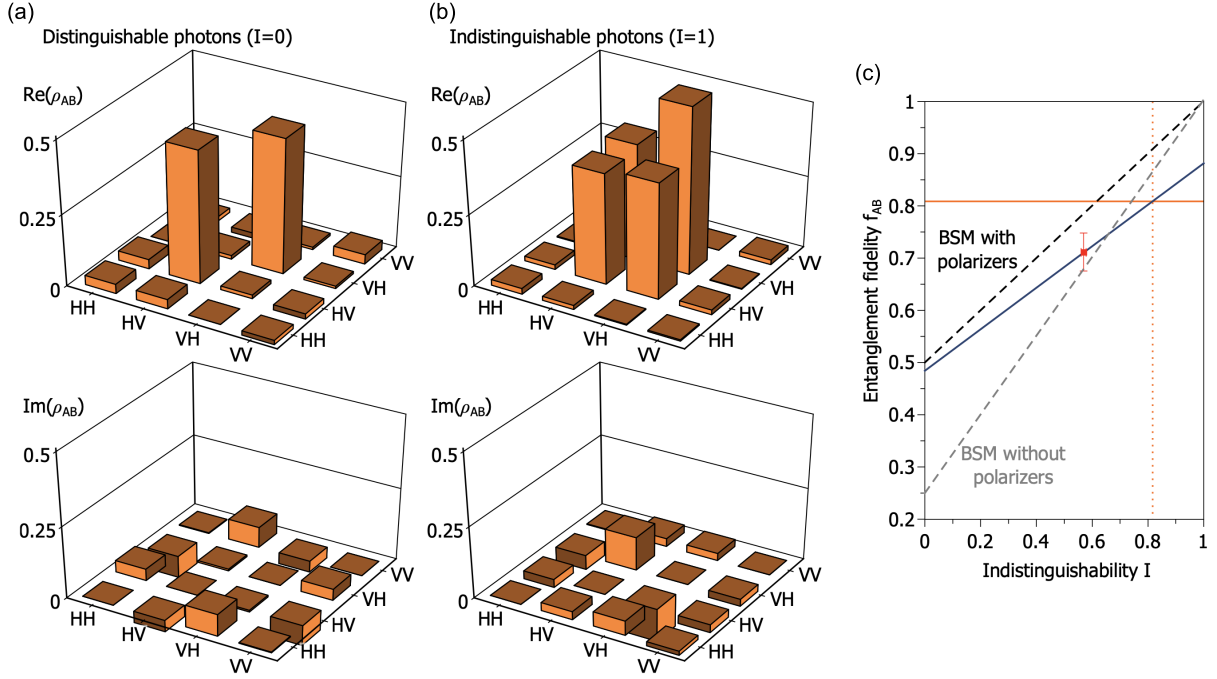


Figure 3.5: Estimated density matrices and entanglement fidelity for different photon indistinguishability. Real and imaginary part of the density matrix ρ_{AB} for (a) distinguishable and (b) indistinguishable photons at the Bell state measurement. (c) Estimated fidelity f_{AB} of the swapped state (blue solid line) as a function of the indistinguishability I including the measured data without time gating (red square) and with time gating (orange line). The black dashed line denotes the ideal case of perfect initial Bell states in our case of a BSM with polarizers. The gray dashed line shows the case of perfect initial Bell states and a BSM setup without polarizers. Reprinted figures with permission from [185]. Copyright 2019, American Physical Society, without any changes made.

BSM is tuned. The highest XX photon indistinguishability is found at zero delay, resulting in a distinct coincidence offset for copolarized and cross-polarized bases. As the delay time departs from zero, the BSM success starts to drop. This results in assimilating fourfold coincidences. The data, obtained without time gating at the BSM, can be well-fitted to double-sided exponential functions denoted as solid lines. In Fig. 3.7(b) the fidelity f_{AB} and the Bell parameter S , as used in the CHSH Bell inequalities are plotted against the temporal gate width. In perfect agreement with our theoretical model, the fidelity decreases to $f_{AB} = 0.71 \pm 0.03$ for large gate widths. Smaller gate widths result in values up to $f_{AB} = 0.81 \pm 0.04$. A further increase in the ideal fidelity of $f_{max} = 0.89$ for gate width approaching zero is unattainable due to the time resolution of the detectors. The Bell parameter $S = 2.28 \pm 0.13$ at the 47 ps gate violates the CHSH and Bell inequalities, $S \leq 2$, by more than 2 standard deviations. Assuming perfect indistinguishability, it reaches $S_{max} = 2.47$.

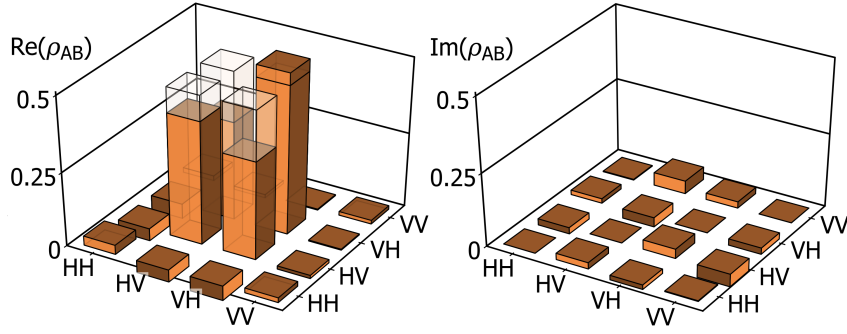


Figure 3.6: Density matrix of the two-photon state received by Alice and Bob with a heralding BSM. The shaded areas represent the difference from the ideally obtainable values. The real part (left) and imaginary part (right) of ρ_{mix} show three distinct signature of a perfect statistical mixture $\frac{1}{4}\mathbb{1}$, whereas ρ_{AB} closely resembles the entangled state $|\Psi^+\rangle$ with a fidelity of $f_{AB} = 0.81 \pm 0.04$ (with time gating at BSM). Reprinted figures with permission from [185]. Copyright 2019, American Physical Society, without any changes made.

3.5 Conclusion

In summary, we have realized the first entanglement swapping based on photons from a quantum dot, laying the foundations for scalable semiconductor based quantum networks. Therefore, the swapping of entanglement with photons from distant emitters or the realization of multiphoton entanglement comes into reach. As a comparison, we show the parameters of the spontaneous parametric down conversion (SPDC) and GaAs QDs-based quantum light sources in Fig. 3.8 from the publications in the recent years [143, 199, 205]. For SPDC source, the brightness is significantly limited in order to obtain a high degree of single photon purity. In contrast, the GaAs QDs embedded in the center of circular bragger grating structure can yield polarization-entangled photon pairs with higher qualities.

To further improve the properties of semiconductor QDs as the entangled photon sources towards the practical entanglement swapping, purification, or even quantum repeaters, advanced photonic techniques for optimizing the QDs properties are still necessary to be combined,

- **Photonic structures:** On one hand, structures such as the circular bragger grating give rise to the concentration of light and Purcell effect, which can improve the *photon collection efficiency and indistinguishability*. On the other hand, photonic waveguide is flexible for the on-chip integrated circuits with quantum gates in linear quantum computation applications.
- **Charge-tuning technique:** To stabilize the charge environment of the solid-state source, injection of charge carries with n-i-p gate structure allows the elimination of blinking and dephasing effect, leading to a high *brightness and indistinguishability*.

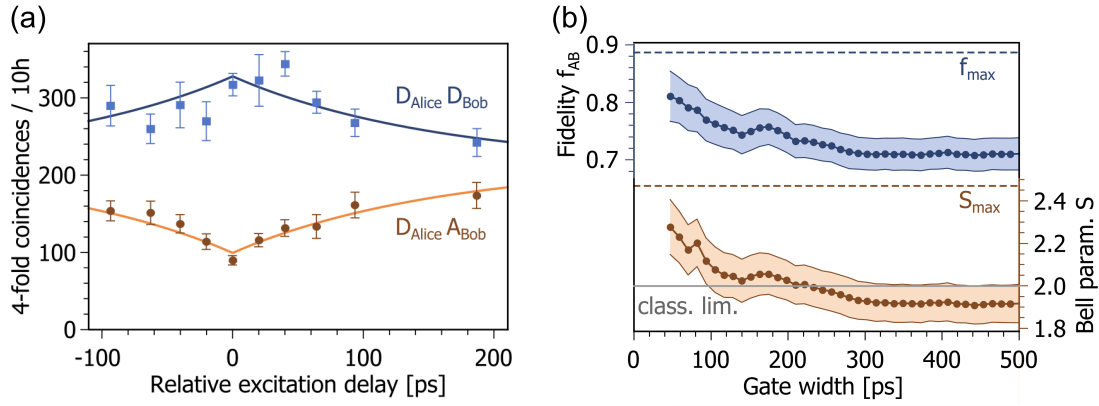


Figure 3.7: Fourfold coincidences as a function of the delay between photons XX1 and XX2 at the BSM (without time gating). Measurement settings of Alice and Bob in the copolarized (orange) and cross-polarized (blue) diagonal bases reveal a large difference at zero time delay, indicating successful entanglement swapping. The solid lines denote the double-sided exponential fit. (d) Fidelity f_{AB} and Bell parameter S as a function of gate width of photon detection at the BSM. Large gate widths result in a decreased fidelity of $f_{AB} = 0.71 \pm 0.03$. At 47 ps gate width, $S = 2.28 \pm 0.13$ is obtained, violating the CHSH and Bell inequalities. The dotted lines are the maximally achievable values in the case of perfect photon indistinguishability. Reprinted figures with permission from [185]. Copyright 2019, American Physical Society, without any changes made.

- **Anisotropic strain tuning:** External strain induced by the PMN-PT can adjust the shape and size of the QDs, which is important for getting a high degree of *entanglement and scalability*.

Figure 3.9 shows the tuning techniques required for an ideal quantum dots-based light source. It consists of circular bragger gating, isotropic strain-tuning and n-i-p charge tuning structure.

Apart from the requirements for fabrication, QDs based sources emitting high quality entangled photon pairs at telecommunication waveband to be compatible with current infrastructure still need to be improved. The most recent quantum teleportation based on InAs QDs is achieved by interfering the continuous single photon emission with telecom laser at C-band [206]. Average post-selected fidelity of $88.3 \pm 4.0\%$ is reached.

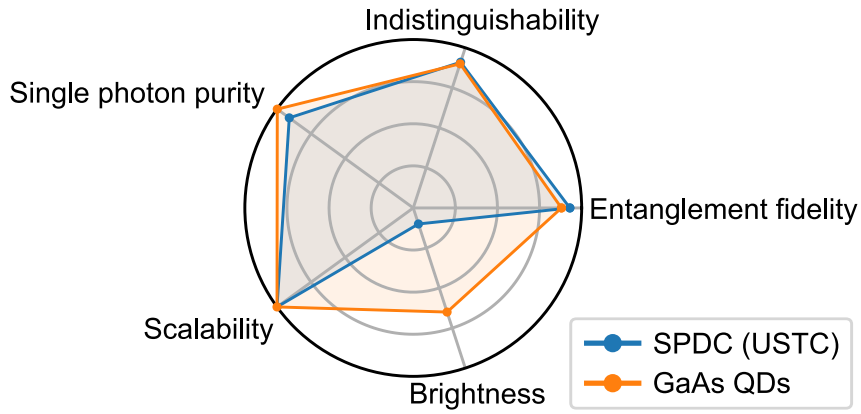


Figure 3.8: Comparison of properties of SPDC [199] and GaAs QDs [143, 205] based quantum light sources.

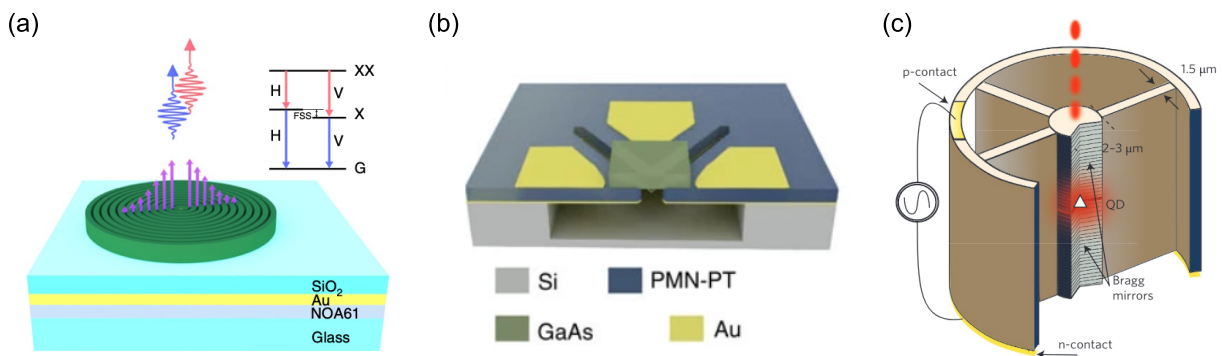


Figure 3.9: (a) GaAs quantum dots embedded in the circular Bragg grating structure. (b) Isotropic strain-tuning of the QDs-containing nanomembrane. (c) Charge-tuning device. Reprinted figures (a), (b) and (c) with permission from [205], [143] and [109], respectively. Copyright 2019 (Springer Nature), CC By 4.0[102], and Copyright 2016 (Springer Nature) without any changes made.

Statistical limits for entanglement swapping with independent quantum dots

In this chapter, the statistical limits for implementing a practical entanglement swapping with sources of polarization-entangled photons from the commonly used biexciton-exciton cascade is presented. The consequences of device fabrication, dynamic tuning techniques and statistical effects for practical network applications are investigated. We stress the necessity of tuning the exciton fine structure by explaining why the often observed time evolution of photonic entanglement in quantum dots is not applicable for large quantum networks. By identifying the critical device parameters, a numerical model for benchmarking the device scalability in order to bring the realization of distributed semiconductor-based quantum networks one step closer to reality.

This work is a collaboration with Michael Zopf, Pengji Li and has been published in Physics. Review. B. [207].

Entanglement is a fundamental resource in next-generation quantum technologies such as quantum communication [208, 209, 210] or quantum computing [24]. The efficient distribution of entanglement between remote parties is a key-enabling element for the realization of a global quantum internet [20, 21]. Photons are considered the best “flying” quantum bits for this goal since they can travel long distances with high resistance to decoherence from the environment [211]. Quantum information is encoded on the light by means of observables with continuous [212] or discrete eigenvalues [213]. The polarization degree of single photons has been utilized to transfer quantum states via optical fiber [214] or satellite signals [215]. However, the employed sources of single photons and polarization-entangled photon pairs are based on spontaneous parametric down-conversion (SPDC) [18, 49], a probabilistic process comprising a fundamental efficiency limit impeding practical applications [81, 82].

Self-assembled semiconductor QDs (QDs) have been studied extensively in the last decades and have become promising candidates for the generation of single photons

[169, 216], entangled pairs [114, 205], or linear cluster states [217]. However, distributed quantum networks based on QDs have yet to be demonstrated. Such networks may be realized using quantum repeater schemes [218] which, among others, rely on quantum interference between photons from independent sources and entanglement swapping [66]. Photon states generated by swapping entanglement of photon pairs emitted from a single QD have been shown to violate Bells inequality [185]. The individual properties of QDs that impact the success of entanglement swapping schemes have been well understood [167, 168, 219]. However, in the real-world application of distributed devices, it is impossible to choose the best possible values of each parameter simultaneously, since each parameter shows a statistical distribution in each device.

Here we show how the statistical distribution of QD properties limits their practical application in entanglement swapping between distributed nodes. Two separate dielectric antenna devices are studied, which have been reported to significantly enhance the photon extraction efficiency of QDs emitting at near-infrared [138] and telecom wavelengths [220]. The distribution of QD properties in the bare wafer and the changes induced by the device fabrication process are investigated. A suitable pair of QDs from the separate devices is tuned into resonance with each other as shown in Fig. 4.1. Two pairs of polarization-entangled photons are generated via the biexciton-exciton (XX-X) cascade from two individual QDs, which are excited by the separated pulses simultaneously. The XX photons are spectrally selected for two-photon interference in BSM, with remaining X photons for coincidence projection measurement.

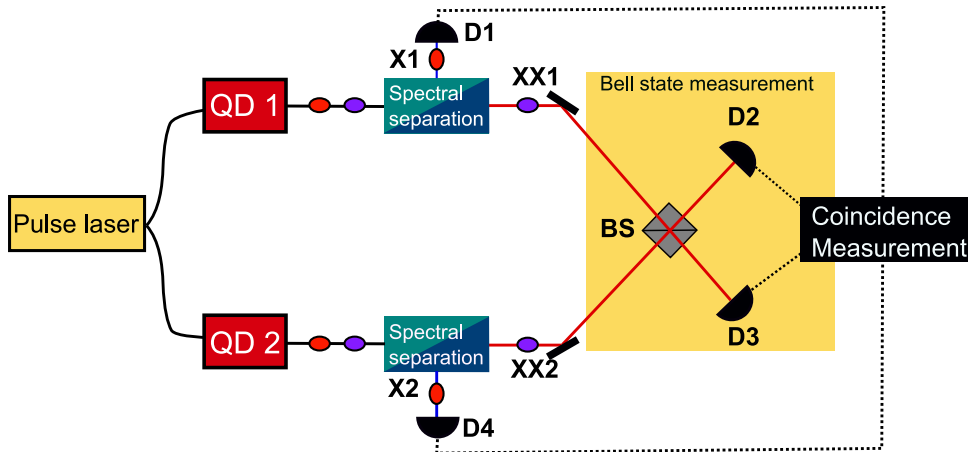


Figure 4.1: Sketch of entanglement swapping with independent semiconductor quantum dots as entangled photon sources.

We discuss the necessity of tuning the exciton fine structure of each individual device for network protocols involving Bell state measurements (BSMs). A numerical model is presented, by which the fidelity of entanglement swapping with two sources is estimated based on the statistically distributed QD parameters in each dielectric antenna device. The presented findings shed light on the roadmap for optimizing and utilizing semicon-

ductor photon sources in distributed quantum networks.

4.1 Spectral overlap between devices

Optical quantum interference lies at the heart of entanglement swapping schemes, requiring mode overlap of indistinguishable photons of the same wavelength for successful BSMs. In contrast to SPDC sources, whose emission wavelength can be easily adjusted, QDs exhibit discrete spectral lines which differ from dot to dot. Therefore, the emissions have to be tuned into resonance with each other, e.g., via quantum frequency conversion [221], which is, however, limited in efficiency due to coupling and conversion losses as well as higher operation complexity. Another possibility is applying external (e.g., strain or magnetic) fields [137, 143], for which it is important to understand the initial compatibility of two optical devices in wavelength: A too broad distribution of emission wavelengths increases the difficulty of finding similar QDs that can be tuned into resonance. Fig. 4.2(a) shows the distribution of X emission wavelengths of two dielectric antenna devices containing GaAs/AlGaAs QDs. This virtual strain-free QD system is known for the high level of control over the optical properties, resulting in similar emission spectra and low X fine structure splittings (FSSs) [128]. Most of the QDs in the fabricated antennas emit photons at wavelengths between 773 nm and 785 nm. On the one hand, this distribution is blue-shifted and broadened comparing with the as-grown sample, which can be attributed to different local strain conditions for the QDs after device fabrication. On the other hand, both wavelength distributions are very similar, rendering the fabrication process uniform and offering a certain probability of finding a QD in each device with close-by emission wavelengths. Now, two QDs (labelled A and B) in each dielectric antenna device are chosen with a small difference of emission wavelengths between XX_A and XX_B of 15.6 pm. Their spectral characteristics are illustrated in fig. 4.2(b), obtained by two-photon resonant excitation of the biexciton using π -pulses. They reveal the discrepancy of emission wavelengths between XX_A and XX_B with an uncertainty of 15.6 pm. External tuning techniques allow for tuning the emission wavelengths of QDs e.g., via temperature [134, 135], strain [143], electric fields [136], or magnetic fields [137].

Applying external fields often result in a mutual change of parameters, as shown exemplary in Fig. 4.2(c). Tuning the temperature from 3.4 K to 31.7 K results in a red-shift of the X emission by 0.445 nm. The temperature-induced change in the bandgap does typically not lead to changes in the X fine structure and lifetime. However, increased charge fluctuations and scattering process with phonons lead to degraded first-order coherence (increased linewidths), setting a limit to the visibility for quantum interference with photons from another device. The coherence time (T_2) of the neutral X emission as a function of the temperature was obtained with a Michelson interferometer and is shown. A more than threefold decrease in coherence time is observed when tuning the temperature from 3.4 to 31.4 K. While the wavelength barely changes for low temperatures, it shifts more

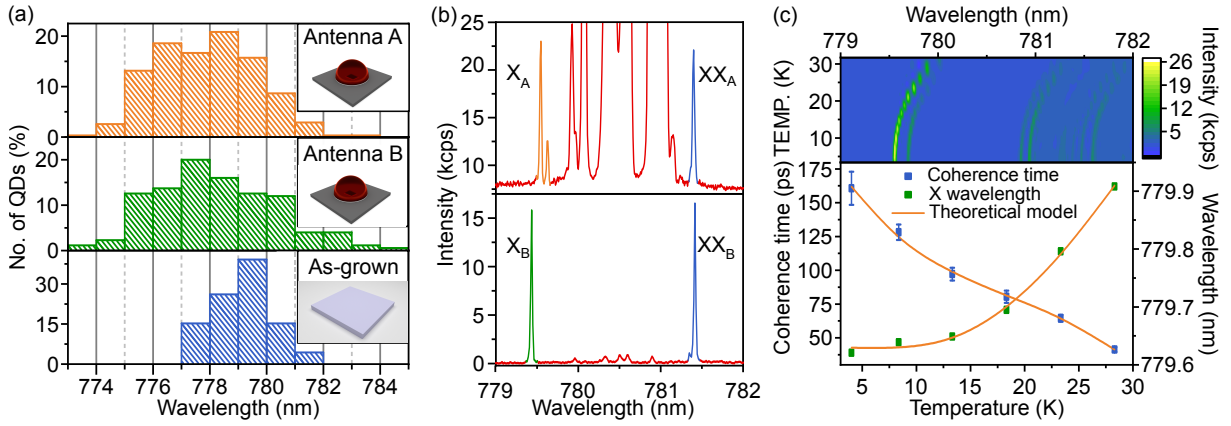


Figure 4.2: Emission wavelength characteristics and tuning. (a) Statistics of the emission wavelength in fabricated dielectric antenna structures A (orange) and B (green), compared to the as-grown sample (blue), revealing only a slight change after fabrication. (b) Spectra of two selected QDs with spectral proximity in each dielectric antenna device, excited via two-photon resonant pumping of the biexciton (XX). Different XX binding energies in each QD lead to different spectral distances between the XX and X emission. The signals in-between the XX and X peaks represent residual resonant laser background. (c) Tuning of QD emission characteristics via temperature, revealing simultaneous changes in emission wavelength, intensity, and coherence time. Photoluminescence spectra (top) and coherence time of the neutral X photons (bottom) under off-resonant excitation for different temperatures. Reprinted figures from [207]. Copyright CC BY 4.0 [102], American Physical Society, without any changes made.

efficiently for a temperature greater than 15 K (Fig. 4.2(c)).

4.2 Repeater-relevant device characteristics

We now investigate the parameters relevant for an entanglement swapping scheme with different sources. The temperature of QD B is now adjusted to 10.81 K, thereby realizing spectral overlap of the XX transitions of QD A and QD B. Due to slight differences in XX binding energies (in our case ≈ 0.26 meV) the X and XX transitions cannot be tuned in resonance with each other simultaneously. Fig. 4.3(a-c) show the relevant properties for quantum interference, i.e., the BSM in entanglement swapping, and figures. 4.3(d-f) for entanglement of the initial pair-wise entanglement. Fig. 4.3(a) illustrates the intensity auto-correlation $g^{(2)}(\tau)$ from the XX streams of device A and B. At zero time delay, $g_A^2(0) = g_B^2(0) \approx 0.03$ is determined, indicating a high single-photon purity leading to negligible degradation on quantum interference [222] between photons from the two devices. Apart from that, the data is superimposed by a bunching towards zero time delay, giving evidence to blinking. Such emission intermittence [201] can be explained by residual charges in the QD blocking the resonant excitation of the neutral XX. The “on”-fractions are $46.9(3) \pm 0.42\%$ and $51.1(2) \pm 0.83\%$ for device A and B (see Appendix), respectively [125]. Blinking [162, 223] is detrimental for the efficiency of quantum interference [224]

(in our case estimated to 48.9(4) %) and therefore also entanglement swapping.

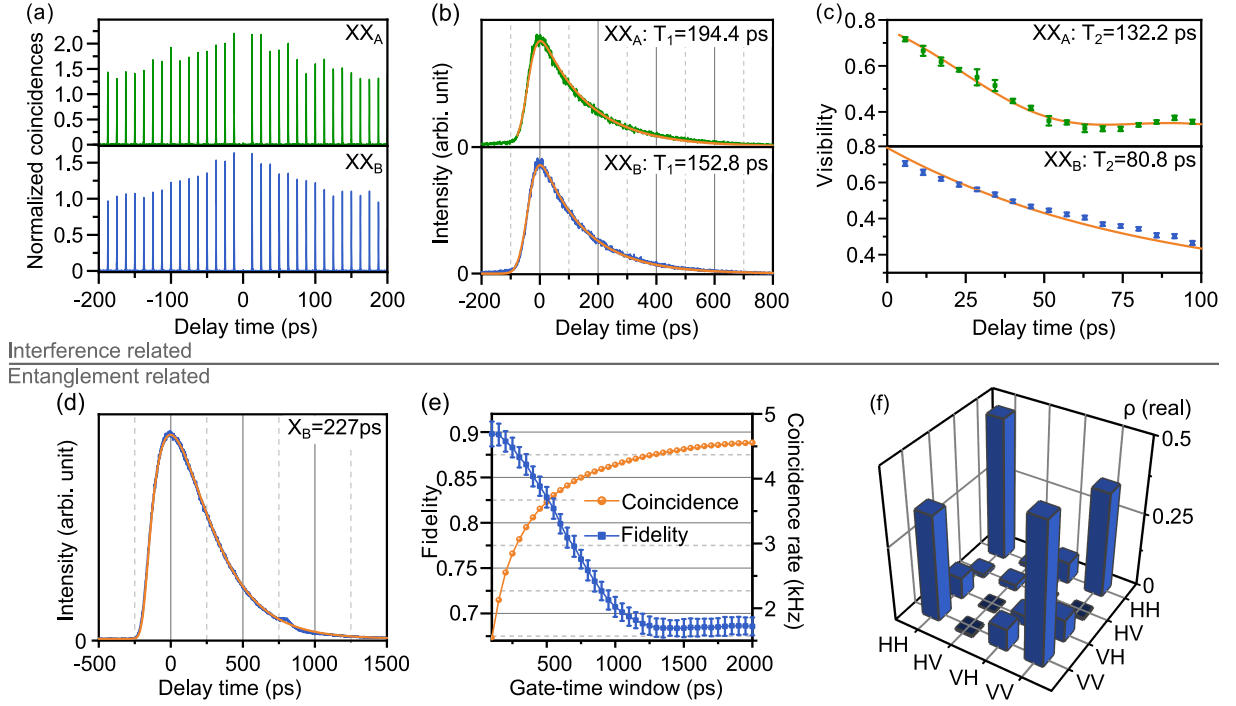


Figure 4.3: Optical properties from separate devices required for efficient entanglement swapping. (a-c) Quantum interference-related properties of the XX photons from two devices (A and B) that have been tuned into resonance via temperature tuning. (a) Second-order autocorrelation measurements for the XX photon streams of both devices, revealing pure single-photon emission and blinking. (b) Lifetime measurements and (c) coherence time measurements of both XX photon streams. (d-f) Entanglement-related properties of the QD in device B. (d) Radiative lifetime of X photons. (e) Entanglement fidelity and raw coincidence counts, obtained via quantum tomography based on polarization-resolved cross-correlation measurements between XX and X emissions, as a function of gate-time window size. (f) Real part of the two-photon density matrix obtained at a gate window size of 500 ps. Reprinted figures from [207]. Copyright CC BY 4.0 [102], American Physical Society, without any changes made.

The success of quantum interference is furthermore governed by the photon indistinguishability of each photon source, typically determined by $V_{\delta E} = T_2/2T_1$. Fig. 4.3(b) and (c) show the lifetime and coherence time measurements from the XX photons of each device. The indistinguishability are therefore estimated to $V_{\delta E}^{(XX_A)} = 34.0\%$ and $V_{\delta E}^{(XX_B)} = 26.4(4)\%$, respectively. The limited coherence is usually attributed to dephasing due to charge and spin noise or phonon scattering [165]. The ratio of the lifetimes of XX and X (i.e., 0.67(3) for QD in device B) is limiting the indistinguishability even further (in our case to $\sim 15.7\%$) due to intrinsic dephasing in the cascade emission [166, 167, 168]. A shortening of XX lifetime, e.g., by the Purcell effect, is therefore beneficial for addressing both discussed points that limit the indistinguishability simultaneously [167, 168].

The experimentally relevant degree of entanglement is determined by the X fine struc-

ture splitting, radiative lifetime, and spin scattering times. In the GaAs/AlGaAs material system, QDs can be found where spin scattering has only a small influence [128]. The X lifetime measurement of device B is shown in Fig. 4.3(d). Although a lower X lifetime would lead to less phase noise in the entangled state, it deteriorates quantum interference visibilities at the same time, and therefore the success of BSM required in the entanglement swapping scheme. The QD in device B exhibits a fine structure splitting of $4.22(8) \mu\text{eV}$. The polarization entanglement is obtained by polarization-resolved cross-correlation measurements and quantum tomography. Gating of detection events can be applied to enhance the measured degree of entanglement at the expense of coincidence counts [185]. This relationship is displayed in Fig. 4.3(e). The fidelity of the entanglement can be strongly enhanced when the gate-time window size is reduced to 500 ps. The corresponding real part of the two-photon density matrix is shown in Fig. 4.3(f). However, the coincidence counts also decrease significantly. Time-gating can also lead to the improved success of BSMs in entanglement swapping [185], also with the expense of reduced overall coincidences. The efficiency of entanglement swapping, i.e., the four-fold coincidence detection rate, is furthermore determined by the source efficiency, including the excitation and collection efficiency as well as the coupling efficiency into a single-mode fiber which depends on the mode profile of the emission.

We can eventually identify the most critical parameters that are statistically distributed in the QD devices, which affect entanglement swapping using polarization-entangled photon pairs from different devices, generated using the XX-X cascade. Based on these parameters we define initial values for a theoretical model to estimate entanglement swapping performance, as will be described in the next section. Typical values for GaAs/AlGaAs QDs found in the literature are listed in Tab. 4.1. Together with the experimental data obtained here, we now define initial values for a theoretical model to estimate entanglement swapping performance, as will be described in Sec. 4.4.

Although the pure dephasing times may be different for XX and X emission, we assume it to be identical here, since both transitions are affected by dephasing due to the solid-state environment, similarly. For actual networks of multiple sources or coupling to quantum memories, the binding energy of the XX also plays a role and is statistically distributed, but is not mentioned in the list above.

4.3 Necessity of fine structure tuning

For experiments such as entanglement swapping with QD-based light sources, a high swapping fidelity is accomplished only if the sources emit high-fidelity entangled photon pairs themselves. In recent years it has been shown several times that high degrees of entanglement persists even with larger X fine structure splittings if one experimentally

Table 4.1: Summary of typical GaAs/AlGaAs QD characteristics relevant in entanglement swapping, together with the used initial values for the model. (Given uncertainties denote the standard deviation of statistical measurements). Reprinted table from [207]. Copyright CC BY 4.0 [102], American Physical Society, without any changes made.

Parameters	Typical values	Initial values for our model
Wavelength (X) (nm)	779.8 ± 1.6 [128]	777.85 ± 2.19
Fine structure (X) (μeV)	4.8 ± 2.4 [128]	11 ± 6.5
X lifetime (ps)	213.75 ± 42.75	300 ± 50
XX lifetime (ps)	127.5 ± 14.67	150 ± 25
Pure dephasing time (ns)	0.41 ± 0.16	0.5 ± 0.25
$g^{(2)}(0)$ (XX)	0.02[128], 0.001[205]	-
Spin scattering time (X) (ns)	15 [128]	-
Pair collection efficiency (%)	37.2[138], 65.4 [205]	-

References [128, 138, 162, 167, 168, 202, 205, 225].

The statistics of dephasing time is estimated by the lifetime and linewidth of charge exciton of ten QDs in [226].

N.C., not considered in our model.

determines the phase factor for each emission [121]:

$$|\psi_{12}(t)\rangle = \frac{1}{\sqrt{2}} \left(|H_1 H_2\rangle + e^{-i\frac{S}{\hbar}t} |V_1 V_2\rangle \right) \quad (4.3.1)$$

where the phase factor is determined by the X fine structure splitting S and the time t that the exciton evolves. The distribution of the X fine structure splitting undergoes a strong change during fabrication. From Fig. 4.4(a), it is clear that the QDs in the as-grown sample have FSSs lower than $10 \mu\text{eV}$, much smaller than the ones in the dielectric antennas. A large FSS leads to two-photon states that oscillate between two Bell states with a randomized phase [121]. This phase can be determined by measuring the detection events of the XX and X photon from each emission and therefore obtaining t . However, it is important to note that these types of time-resolved measurements are accompanied by a significant loss in overall efficiency for any protocol that relies on BSMs with photons from different sources [206], i.e., quantum teleportation or entanglement swapping. This even accounts for experiments using photon pairs emitted by the same source but at different times. Let us consider an emission process of entangled pairs from two separate devices with subsequent detection events in an entanglement swapping scheme as illustrated in Fig. 4.4(b). Each emission from device A or B therefore carries its respective phase factor $\alpha = -\frac{S_A}{\hbar}t_A$ or $\beta = -\frac{S_B}{\hbar}t_B$

$$|\psi_{1234}(\alpha, \beta)\rangle = \frac{1}{2} \left(|H_1 H_2\rangle + e^{i\alpha} |V_1 V_2\rangle \right) \left(|H_3 H_4\rangle + e^{i\beta} |V_3 V_4\rangle \right) \quad (4.3.2)$$

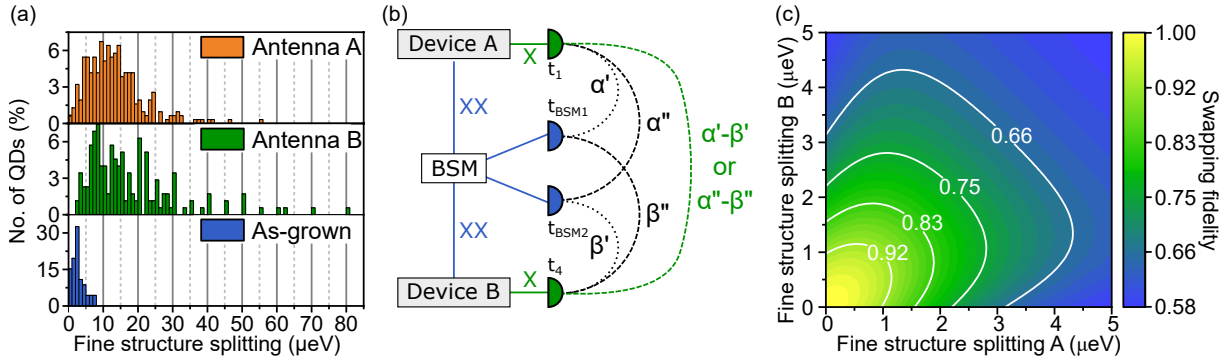


Figure 4.4: Exciton fine structure characteristics and influence on entanglement swapping. (a) Statistics of the X fine structure splitting in fabricated dielectric antenna structures A (orange) and B (green), compared to the as-grown sample (blue), revealing a significant broadening of the distribution after fabrication. (b) Scheme of entanglement swapping using QDs with finite exciton fine structure. The phases in the entangled states emitted by device A and B are not accessible via measuring detection times. Two possible solutions arise (α', β' and α'', β''), leading to two swapped states in a statistical superposition with the phases $\alpha' - \beta'$ and $\alpha'' - \beta''$, which cannot be experimentally distinguished. (c) Fidelity of an entanglement swapping scheme with ideal quantum interference at the BSM, taking into account the finite exciton fine structure of two separate QDs and an exciton lifetime of 300 ps. Reprinted figures from [207]. Copyright CC BY 4.0 [102], American Physical Society, without any changes made.

After projecting photons 2 and 3 on the Bell state $|\Psi_{2,3}^-\rangle = \frac{1}{\sqrt{2}} (|H_2V_3\rangle - |V_2H_3\rangle)$ one obtains the un-normalized state

$$\begin{aligned} |\psi_{1,4}(\alpha, \beta)\rangle &= \langle \Psi_{2,3}^- | \psi_{1234}(\alpha, \beta) \rangle \\ &= e^{i\beta} (|H_1V_4\rangle - e^{i(\alpha-\beta)} |V_1H_4\rangle) \end{aligned} \quad (4.3.3)$$

which means that similar to the case of entangled pair emission from a single device, the final (swapped) state is oscillating between two Bell states, here with the phase $\alpha - \beta$. In order to utilize this state, this phase has to be an experimentally accessible parameter. However, according to the principle of the indistinguishability of identical particles under particle exchange, the wave function of indistinguishable photons must obey the symmetric exchange condition at a non-polarizing beam splitter owing to the nature of Bosonic statistics. [182, 183] The BSM therefore removes the ‘which path’ information, making it impossible to determine from which source each photon originated. Therefore, two possible combinations of phase factors are possible:

$$\alpha' = -\frac{S_A}{\hbar} (t_1 - t_{BSM1}) \quad \text{and} \quad \beta' = -\frac{S_B}{\hbar} (t_4 - t_{BSM2}) \quad (4.3.4)$$

or

$$\alpha'' = -\frac{S_A}{\hbar} (t_1 - t_{BSM2}) \quad \text{and} \quad \beta'' = -\frac{S_B}{\hbar} (t_4 - t_{BSM1}) \quad (4.3.5)$$

where the indices $i = 1, 4$ in t_i correspond to the photons described in the state $|\psi_{1234}\rangle$, and the $i = (BSM1), (BSM2)$ correspond to the photons detected at the two respective detectors of a BSM. Independent of the present fine structure splittings it is impossible to experimentally determine which of the two cases occurs and therefore which of the two states

$$|\psi_{1,4}(\alpha', \beta')\rangle \neq |\psi_{1,4}(\alpha'', \beta'')\rangle \quad (4.3.6)$$

is present. The final state is therefore not a coherent, but a statistical superposition of the two possible states $|\psi_{1,4}(\alpha', \beta')\rangle$ and $|\psi_{1,4}(\alpha'', \beta'')\rangle$. The entanglement of the swapped state only persists in the case of low X fine structure splittings and radiative decay times or the case of $t_{BSM,1} = t_{BSM,2}$. The latter case is undesirable since it strongly lowers the efficiency of the BSM by discarding many detection events $t_{BSM,1} \neq t_{BSM,2}$ within the coincidence window. Physically, this is related to the quantum statistical nature of Bosonic particles such as indistinguishable photons hitting a non-polarizing beam splitter [182, 183]. A finite FSS in separate devices significantly lowers the fidelity of the two-photon states obtained in an entanglement swapping scheme. This is illustrated in Fig. 4.4(c) under the assumption of ideal quantum interference at the BSM for clarification of the theoretical concept. In reality, quantum interference is degraded by dephasing processes, the intrinsic dynamics of the three-level cascade decay as well as the imperfect spectral detuning with increasing X fine structure [227]. The latter 2 effects can be mitigated by selectively reducing the XX lifetime. Nevertheless, based on the above discussion, a scalable application of QD based entangled photon sources must rely on tuning the fine structure to remove the state oscillation. This can be achieved, e.g., via frequency-shifting optical setups [117, 228] or external fields such as anisotropic strain. Once such tuning is realized with high efficiency it allows for strong pair-wise photonic entanglement from individual QDs which can then be applied in quantum networks.

4.4 Prediction for a real-world quantum network

Even though prominent results have been obtained in optimizing individual parameters of single quantum dots, it is still unclear how to repeatably produce usable devices, due to statistical performance from device to device. To quantitatively investigate the requirements of the parameters from QDs-based photon sources for quantum networks, we now develop a theoretical model which takes into account the statistical effect on the fidelity of photons that result from entanglement swapping. We start by considering two independent sources, which are tunable in wavelength to target spectral overlap of the emission wavelengths. To estimate the magnitude of the overlap, first the probability density of finding a QD with a specific wavelength in device A and B is obtained (based on Fig. 4.2) and shown in 4.5(a). Under the assumption that the probability density of

the emission wavelengths obeys a standard distribution, we can describe it by

$$p(\lambda) = \frac{1}{\sqrt{2\pi}\sigma} \cdot e^{-\frac{(\lambda-\mu)^2}{2\sigma^2}} \quad (4.4.1)$$

where $p(\lambda)$ is the probability density, μ, σ are the expected and standard deviation values of the distribution. By fitting the data it is possible to extract the corresponding values (see Appendix). Next, the tuning range for the employed wavelength tuning of each device δ_λ is defined. Now we can analytically calculate the probability of tuning two devices into resonance (see Appendix). Fig. 4.5(b) shows the result, assuming an equal σ_λ in the devices, but different expected values with a difference of $\Delta\mu_\lambda$. Here, an exemplary wavelength tuning range of 1 nm for each device is assumed. The color-map shows that high probability can be obtained with a decreasing expected value difference $\Delta\mu_\lambda$ and narrower wavelength standard deviation σ_λ . Furthermore, for higher $\Delta\mu_\lambda$ and a fixed tuning range, it is beneficial to have σ_λ that is not too small, in order to increase the chance of tuning remote devices into resonance.

The model is now extended further, in order to obtain the fidelity of the swapped photon pairs based on the statistically distributed parameters in the devices. The exact nature of the distribution is not clear for every parameter and can be adapted for each specific QD material and fabricated device. Here we assume that the probability density for all parameters (e.g., X fine structure splitting) follows a (truncated) Gaussian distribution. This assumption models the fine structure well, as can be seen in Fig. 4.5(a). The rest of the parameters were approximated by reasonable experimental values (see Tab 4.1 and Appendix) based on the presented experiments and the existing literature.

The model is based on a numerical Monte Carlo approach. First, a random set of parameters is drawn for each parameter from device A and B. A tuning mechanism can now be considered which e.g., tunes the wavelengths from the different devices into resonance, potentially also affecting the other parameters. Then, the swapping fidelity is analytically calculated under the assumption of ideal projection in BSM, which has been demonstrated with high quality in practice [185]. This process of random sampling is repeated one million times. The resulting fidelities of the swapped state are then normalized to display a probability density. Fig. 4.5(c) shows the resulting probability distribution for obtaining a certain entanglement swapping fidelity for several considered cases. The integration of the probability density within a certain fidelity range then can yield the total probability for obtaining a fidelity within this range in a swapping experiment. Here, we consider a BSM with polarizing beam splitters, which is known to result in a lower limit of 0.5 in the swapping fidelity [185]. This coincides with the upper fidelity limit for classical two-photon states. Since we do not consider spin-scattering or limited single-photon purity here, the swapped fidelities will not fall below 0.5. The blue curve (1) shows the probability density considering the experimental parameters obtained in this work and assuming temperature tuning. It is clear that entanglement swapping is mostly not successful,

leading to fidelities close to 0.5. The reason is the limited tuning range via temperature and the simultaneous decrease in photon coherence. For the orange curve (2) we now assume that all QDs from both devices can be tuned into resonance with each other (e.g., by strain tuning) without affecting other properties. This leads to a visible increase of entanglement fidelity. However, the values are still located mostly below 0.6. The reason is the X fine structure in the devices. Therefore, we assume an additional tuning mechanism for the fine structure (e.g., anisotropic strain tuning) with a magnitude of $50 \mu\text{eV}$. The resulting green curve (3) now shows fidelities between 0.75 and 0.85. If furthermore a selective Purcell enhancement of the XX emission with a Purcell factor of $F_P = 10$ is added [229], the red curve (4) arises. Another significant increase in entanglement swapping fidelity is the result, with fidelities ranging between 0.85 and 0.97. To increase the probability of a high swapping fidelity, even more, the pure dephasing times can be increased to 4 ns. The result is shown by the violet curve (5), exhibiting fidelities between 0.9 and 0.99. Curve (6) shows the comparison to the expected probability density if the parameters would not be statistically distributed at all. Therefore, the statistical effect of QD properties on entanglement swapping is clear by comparing curves (5) and (6). Only a very small chance exists, that two QDs can be found such that the swapped fidelity is actually above those of curve (6). Due to the distribution of properties, the swapped entanglement deteriorates in almost all cases. How much lower the fidelity becomes is directly related to the relative uncertainties in the distributed parameters. It is worth mentioning that the same effect would be seen when using differently fabricated sources, e.g., based on circular Bragg gratings or diode structures. High fidelities can therefore only be obtained by either accepting very low sample yield (choosing only the best QDs) or by reducing the parameter uncertainties.

The developed model can be optimized further by implementing the following effects, leading to an even higher accuracy when estimating the fidelity of the swapped photonic states. X spin scattering times can be considered, though they are expected to be long enough to not strongly deteriorate the entanglement of the emitted photon pairs [128]. Furthermore, the single photon purity can be considered, which can be close to unity in GaAs/AlGaAs QDs [230]. The detrimental effect of the fine structure on the quantum interference at the BSM can be implemented. However, when the XX lifetime is decreased via asymmetric Purcell enhancement, this effect becomes less dominant due to the increased radiatively limited XX linewidths. Also, the total efficiency of the entanglement swapping operation can be included, based on the efficiency of each QD in each device and possibly applied post-selection of single photon counting events.

Now the question has to be raised where the advantage in using QD-based entangled photon sources lies. For SPDC sources, a match of emission wavelength between independent sources can be easily achieved by tuning the pump laser or phase-matching conditions. In the low-efficiency limit this can lead to the generation of highly indistinguishable photons and photon pairs with high fidelities [231], which is the reason why

these types of sources are used in various entanglement-related quantum applications. In contrast, QDs allow for a deterministic emission of photon pairs without any physical limits. However, to really offer an advantage over SPDC sources, QD-based sources must show better total efficiencies while offering the same possible fidelities of swapped photon pairs. For QD-based sources to achieve these fidelities, material growth and device fabrication have to be controlled to an extent that allows for highly narrow distributions in optical properties. Tuning methods of emission wavelength and fine structure are required. Simultaneously, QDs may need to be embedded in devices suppressing blinking and increasing coherence and photon indistinguishability.

We present insights on the scalability of semiconductor-enabled quantum photonic networks based on experimental observations and a developed numerical model. Considering QD-based dielectric optical antennas in an entanglement swapping scheme serves as an example for unraveling the challenges for employing semiconductor QDs in applications such as quantum repeaters. Two QDs from the separate devices are tuned into resonance with each other by temperature tuning, and the properties of the single and entangled photon characteristics are evaluated. We showed that the exciton fine structure is detrimental for scalable networks and therefore requires tuning. The statistical distribution of parameters (e.g., emission wavelengths and fine structures) in two separate devices are studied, and the influence on the achievable entanglement swapping fidelities investigated. Different tuning techniques are contemplated, revealing that the desired tuning of one parameter is often accompanied by a simultaneous tuning of others. Anisotropic strain tuning is most promising for independent tuning of independent parameters (i.e., wavelength and fine structure). Further, challenges such as blinking and limited coherence can be addressed e.g., by implementing QD devices with dynamic charge tuning [226]. A selective Purcell enhancement of the XX emission can be obtained using circular Bragg gratings [205]. However, the combination of all 3 techniques is technologically very demanding. In addition, since a large parameter space exists for generating polarization-entangled photon pairs from the XX-X cascade, not all important parameters can be tuned deterministically. A random sampling of several properties is thus unavoidable, posing intensified requirements to the material growth in order to obtain scalable semiconductor devices. Deviation of device parameters may necessitate entanglement purification, which uses up available resources in a quantum network and therefore may relativize the key advantage of source efficiency of QD-based sources. Therefore, the level of control over the parameter statistics directly translates to a potential advantage of QD-based sources in a quantum network. A possible alternative is to generate photonic entanglement with a significantly larger number of photons per individual QD first (e.g., cluster states) [217], before interfacing with photons from other sources.

This discussion and the numerical prediction can easily be extended to other types of solid-state quantum light emitters or quantum memories with photon interfaces (comprising entanglement generation via photon interference). The model incorporates well-known

analytical approaches for the independent physical problems (entangled two-photon states for individual QDs and subsequent entanglement swapping) whereas a numerical solution based on random sampling serves to evaluate the influence of statistical distributions of parameters in the chosen material system. This distribution eventually leads to the degradation of remote entanglement, necessitating time gating or correction protocols like entanglement purification which reduce the overall quantum network efficiency. It is therefore a key challenge for the scalable implementation of solid-state quantum light sources.

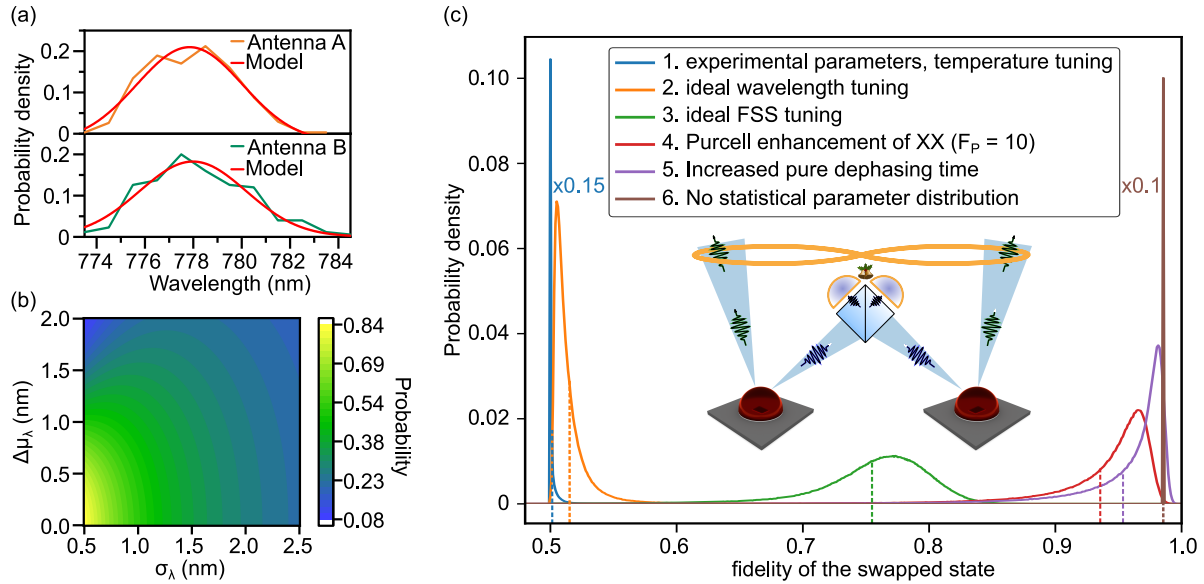


Figure 4.5: Estimated device performance in a quantum network based on entanglement swapping. The properties of individual QDs are defined by probability density distributions as exemplarily shown in (a) for the emission wavelengths from device A and B. The experimental data is fitted with a Gaussian curve. Other properties (FSS, T_1 , T_2 , not shown) are modeled by truncated Gaussian distributions. (b) Probability for tuning the emission wavelength of two randomly selected QDs from separate devices into resonance, assuming a wavelength tuning range of $\delta_\lambda = 1$ nm. The emission wavelength standard deviation σ_λ is set equal for both devices, while the expected value has a difference of $\Delta\mu_\lambda$. (c) Probability density of the entanglement fidelity after swapping entanglement between photon pairs emitted by separate devices. The semi-analytical model incorporates a random sampling of experimentally reasonable QD property distributions from both devices. One million samples are used to obtain the probability density. The blue line (curve 1) shows the fidelity distribution for the experimentally accessed parameters in this work. Possible improvements in the fidelity distribution by consecutively adding tuning mechanisms and optimizing device properties are shown in curves 2 to 5. Curve 6 shows the case with removed statistical parameter distribution (For an explicit display, heights of curve 1 and 6 are scaled-down with a factor of $\times 0.15$ and $\times 0.1$, respectively). Reprinted figures from [207]. Copyright CC BY 4.0 [102], American Physical Society, without any changes made.

High-brightness telecom O-band optical antenna

In the following chapter, the non-classical light source consists of a gallium phosphide solid immersion lens in combination with a quantum dot nanomembrane emitting single photons in the telecom O-band is studied, to overcome brightness limitation due to total internal reflection at the semiconductor/vacuum interface, based on the principle of dielectric antenna. With this device, the photon extraction is strongly increased in a broad spectral range. A brightness of 17% ($NA = 0.6$) is obtained experimentally, with a single photon purity of $g^2(0) = 0.049 \pm 0.020$ at saturation power. This brings the practical implementation of quantum communication networks one step closer.

*The experiment of this work is performed in collaboration with Cornelius Nawrath in the group of Prof. Dr. Peter Michler from the University of Stuttgart and has been published in *Opt. Express*. [220].*

Non-classical light sources are an essential element for secure photonic quantum information processing [195], quantum cryptography [45], or distributed quantum networks [81, 185]. Photons exhibit high stability against dephasing caused by the environment and can be transmitted over long distances with standard optical fibers. Semiconductor QDs can deterministically emit photons in the telecom wavelength bands around $1.31 \mu\text{m}$ [232, 233, 234, 235, 236, 237], and $1.55 \mu\text{m}$ [206, 238, 239, 240, 241, 242, 243], at which chromatic dispersion and transmission losses in optical fibers are at a respective minimum [244]. However, the high refractive index of the surrounding semiconductor results in total internal reflection (TIP) at the semiconductor/vacuum interface, thereby confining most of the photons in the host material [109, 245, 246].

Various approaches have been investigated in the last few years to enhance the extraction efficiency of QD emission in the wavelength range from 700 nm to 900 nm [131]. Making use of cavity quantum electrodynamics (cQED), the photons are efficiently emitted in the limited spectral width of the cavity mode. Multifarious nanoscale structures

are developed in that regard, such as micropillars [191, 247, 248] or circular Bragg gratings [249, 250]. Brightness values of up to 85 % have been observed in combination with high single-photon purity [205]. Moreover, the cavity-induced Purcell effect shortens the radiative lifetimes of the emitters, resulting in improved photon indistinguishability on short time scales [205, 229]. Another approach is to modify the photonic environment of the QDs, e.g., by embedding them in nanowires [251, 252] or making use of micro lenses [234, 253, 254, 255, 256]. This allows for a broadband and efficient extraction of photons from the semiconductor material. Alternatively, metal nanostructures can be placed close to the emitter [257, 258] which results in photoluminescence enhancement and directional emission by utilizing the localized surface plasmon resonance. These approaches generally require deterministic fabrication methods to ensure high yield and ideal performances, thereby increasing the overall fabrication complexity [255, 259, 260]. Recently, a new approach called dielectric antenna has been realized with GaAs/AlGaAs QDs grown by molecular beam epitaxy [138]. Based on a solid immersion lens (SIL) and the well-established fabrication of QD-containing nanomembranes, an emission brightness of up to 65 % was obtained for single photons emitted around 780 nm.

Increasing the photon extraction for QDs emitting in the telecom O-band has been investigated using nanowires and micropillars, with a brightness of up to 3.3 % [236, 261]. Using nanophotonic cavities, 36 % brightness in a narrow-band wavelength range was reported [232]. While this approach is also expected to be beneficial for the indistinguishability on short time scales, the resulting linewidth broadening could cause photon wave-packet dispersion during long-haul propagation, in particular in the near-infrared and also in the telecom C-band [221, 262]. With a mesa structure on top of the emitter, a brightness of 10 % has been experimentally realized in a broad wavelength range, but the position misalignment between the structure and the emitter significantly reduces the extraction efficiency [263]. Besides, deterministic Gaussian-shaped micro lenses fabricated via chemical etching were estimated to reach up to 17 % brightness. This method requires the use of sophisticated techniques with high accuracy and fabrication quality [234].

Herein, we present a similar dielectric antenna structure extracting single photons in the telecom O-band from InGaAs/GaAs QDs grown via metal-organic vapor-phase epitaxy (MOVPE). Based on simulations to optimize the antenna structure design, we experimentally fabricate and characterize this device. Compared to the as-grown sample, a 40 times brighter single-photon source is realized over a broadband spectral range, while maintaining a high single-photon purity.

5.1 Device fabrication

The InGaAs/GaAs QDs are grown by MOVPE, which is commonly employed for commercial semiconductor fabrication purposes. With careful optimization of the strain in the low-density QDs, photon emission in the telecom O-band has been realized [264]. The

initial GaAs (001) substrate is overgrown with a 50 nm buffer layer, followed by 100 nm AlGaAs, acting as a sacrificial layer for the intended membrane processing. The subsequent membrane structure consists of 190 nm GaAs, followed by InGaAs QDs which are embedded in a strain-reducing layer. The QDs are then capped with a 266 nm GaAs layer [265].

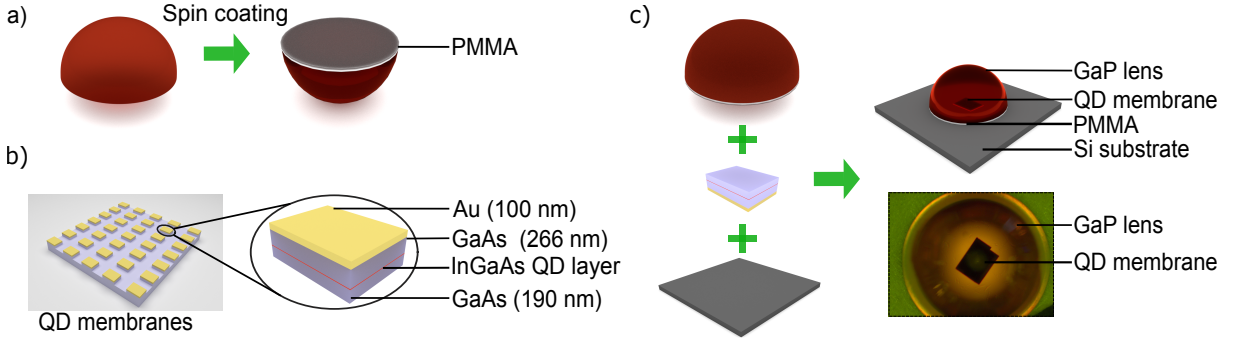


Figure 5.1: Fabrication steps of the telecom O-band dielectric antenna. (a) polymethyl methacrylate (PMMA) deposited on the flat surface of the GaP SIL. (b) Free-standing nanomembranes remain on the substrate after photolithography and wet chemical etching. The structure of a single nanomembrane is shown (right) (c) Combining the SIL, QD-nanomembrane and the silicon substrate (left), a dielectric antenna device is constructed (top right). The image taken by optical microscopy displayed in the bottom right corner shows the single nanomembrane glued centrally to the bottom of the SIL. Reprinted figures with permission from [220]. Copyright 2020, Optical Society of America, without any changes made.

Fig. 5.1 shows the fabrication procedure of the dielectric antenna device consisting of a commercial gallium phosphide (GaP) semi-spherical solid immersion lens, a nanomembrane containing InGaAs/GaAs QDs and a silicon carrier substrate. As shown in Fig. 5.1(a), a droplet of polymethyl methacrylate (PMMA) is deposited on the flat surface of a SIL with a diameter of 2 mm. Spin coating is then performed with a rotation speed of 7000 rpm, yielding a PMMA layer thickness of ~ 100 nm. To obtain a single nanomembrane containing QDs, a sequence of well-established fabrication methods is employed to the as-grown sample [138]. A square array of $160 \mu\text{m} \times 120 \mu\text{m}$ -sized rectangular metal pads is defined, by means of photolithography, followed by the deposition of 4 nm chromium and 100 nm gold and a subsequent lift-off process. Next, free-standing membranes are created by chemical etching method (Sec. 2.1.2). One single nanomembrane is transferred onto the bottom center of the SIL, with the PMMA layer acting as glue. Placing the whole structure on a silicon substrate (Fig. 5.1(c)) for convenient handling completes the device fabrication. The TIR at the semiconductor nano-membrane surface is greatly alleviated in this dielectric antenna structure due to the close contact of the nano-membrane ($n_{\text{GaAs}} \approx 3.40$) and the high refractive index GaP SIL ($n_{\text{GaP}} \approx 3.14$).

5.2 Simulation method for the antenna structure

To learn the performance of the dielectric antenna in theory, we perform finite-difference time-domain (FDTD) simulations of the device using the commercial FDTD software offered by Lumerical Solutions Inc. In the simulation, a three-dimensional simulation structure of the dielectric antenna is constructed according to the sketch depicted in Fig. 5.2(a). The wavelength-dependent refractive indices of Au, Cr, GaAs are provided by the software. The refractive index of PMMA is taken from the manufacturer's specification. The refractive index of GaP around $1.31 \mu\text{m}$ is taken from [266]. To ensure the accurate simulation result, a mesh accuracy of 6 with an auto non-uniform mesh type is used in the simulation settings, corresponding to mesh grid size of a 26th of the minimal wavelength [267]. The perfectly matched layer boundary condition for the x/y/z axes for the simulation area under consideration is applied. A mesh grid of $5 \times 5 \times 5 \text{ nm}^3$ is used to ensure sufficient precision at the interfaces between the multi-layers. An in-plane polarized dipole source is embedded in the GaAs layer. Fig. 5.2(b) shows the electric field intensity distribution of the dielectric antenna in a side view. A strong and directional emission pattern is observed in the GaP, indicating an increased photon extraction from the substrate.

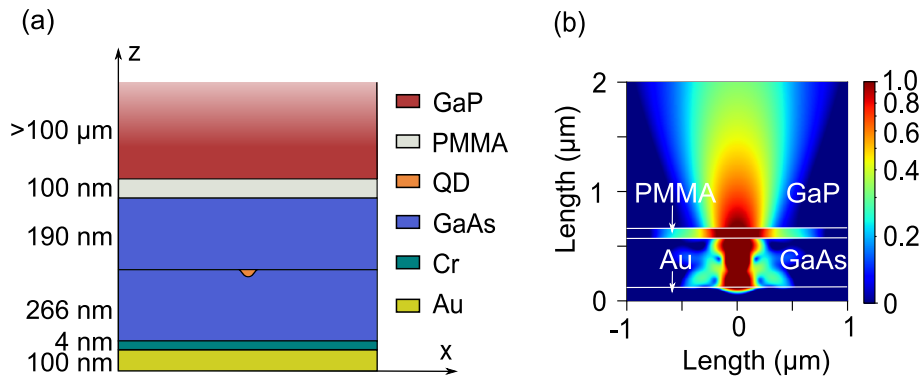


Figure 5.2: (a) Schematic of the simulation structure. (b) The side view of the electric field intensity distribution in the dielectric antenna. Reprinted figures with permission from [220]. Copyright 2020, Optical Society of America, without any changes made.

Fig. 5.3(a) shows the far-field extraction efficiency for different objective NAs as a function of PMMA layer thickness for the dielectric antenna operating at $1.31 \mu\text{m}$ used in this work. The efficiency is calculated using a monitor embedded in the GaP, considering only the radiation angle range determined by the NA. The reflection at the GaP/vacuum interface is taken into account by applying Fresnel equations. When the PMMA layer thickness is 0 nm, there is no antenna effect but only the lensing, which means the photons will spread over the full solid angle in the far-field. Therefore, the extraction efficiency is only determined by the NA of the objective. As shown in the figure, the device performs best with the extraction efficiency enhancement for a PMMA layer thickness of $\sim 290 \text{ nm}$

but lower than the case of 0 nm due to the antenna effect. This is ascribed by the partial total internal reflection at the GaAs-PMMA interface. The antenna effect starts to vanish for a PMMA layer thickness larger than 290 nm. The PMMA layer thickness for the simulations described in this work is 100 nm in accordance with the fabricated device. We tried to reduce the PMMA layer thickness to the minimum since obtaining a precise thickness by spin-coating on a small GaP SIL (2 mm diameter) is easier for lower thicknesses. This thickness was found to be more controllable and reproducible than larger thicknesses in the fabrication procedure.

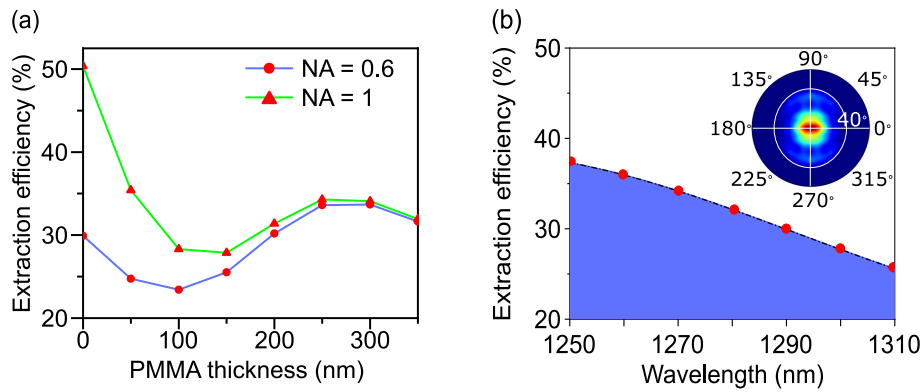


Figure 5.3: (a) Simulation results for the device operating at $1.31 \mu\text{m}$ used in this work. The far-field extraction efficiency is shown over the PMMA layer thickness for different NAs of the collection optics. (b) Simulated extraction efficiency as a function of the emission wavelength. The inset shows the polar view of the device radiation in the far-field. Reprinted figures with permission from [220]. Copyright 2020, Optical Society of America, without any changes made.

To verify further that the device operates in a broad wavelength range, we also perform the simulation with a PMMA layer thickness of 100 nm and do not include an anti-reflection coating on the GaP lens. The polar view of the device radiation in the far-field (inset in Fig. 5.3(b)) manifests that the majority of photons can be collected within a polar angle of 40° . Finally, the extraction efficiency of photons as a function of the emission wavelength is determined in the far-field, considering a numerical aperture of 0.6. In a wavelength range of 60 nm in which the QD ensemble is emitting, the dielectric antenna increases the photon extraction performance. This is much broader than cQED approaches, which usually enhance the emission in a spectral window of a few nm [191, 232, 247]

5.3 Brightness enhancement

To demonstrate the effectiveness of the device, we characterized the spectra and wavelength statistics of the as-grown sample and dielectric antenna, respectively. In Fig. 5.4(a), the spectra of two typical QDs are shown. A remarkable brightness enhancement is observed for the dielectric antenna. To demonstrate that the device fabrication only has

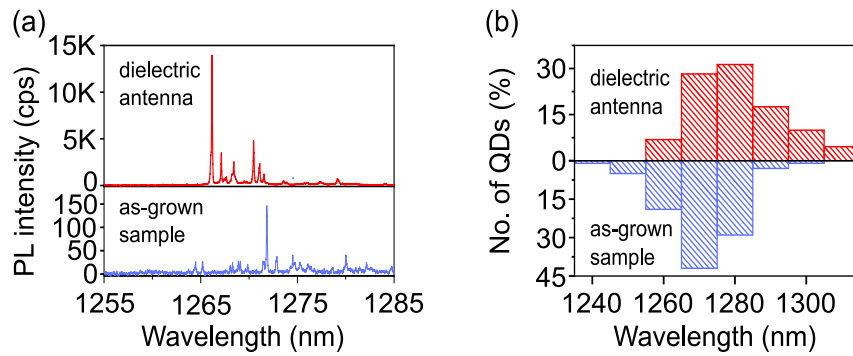


Figure 5.4: (a) Exemplary QD emission spectra from the dielectric antenna and the as-grown sample. (b) The wavelength distribution before and after the processing, for which 131 and 100 QDs are characterized, respectively. (Red: dielectric antenna; Blue: as-grown sample). Reprinted figures with permission from [220]. Copyright 2020, Optical Society of America, without any changes made.

a small effect on the emission wavelength, the QD emission in the dielectric antenna and as-grown sample is characterized. According to the wavelength statistics of the samples shown in the Fig. 5.4(b), the histograms show a similar central wavelength. Apart from possible fabrication-related effects like a difference in the strain situation in the surrounding of the QDs due to the change from a bulk sample to a nano-membrane, the 10 nm red-shift is ascribed to an inhomogeneity of QD sizes over the sample and the different subsets of randomly chosen QDs for the characterization.

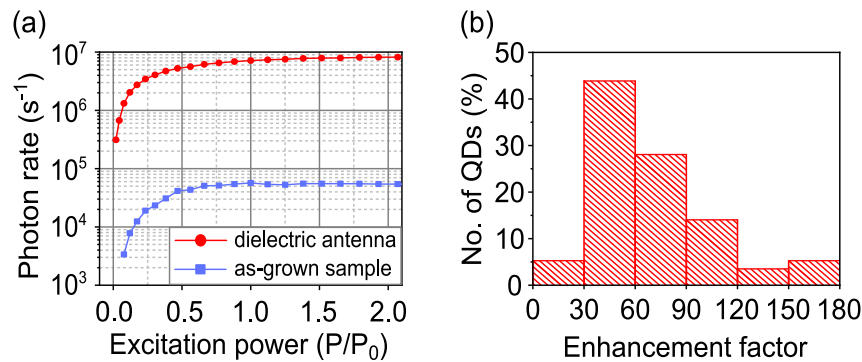


Figure 5.5: (a) Number of photons arriving at the objective as a function of excitation power for two exemplary QDs. The photon rate is determined by integrating the counts of the brightest transition peak shown on the CCD and correcting for the system losses. (b) The statistics of the brightness enhancement factor comparing the dielectric antenna (57 QDs) and the as-grown sample. Reprinted figures with permission from [220]. Copyright 2020, Optical Society of America, without any changes made.

Furthermore, we study the power-dependent photoluminescence under above-band excitation, using a pulsed laser at 633 nm with a repetition rate of 80 MHz (Fig. 5.5(a)). The recorded photon counts are obtained by integrating the brightest transition peak shown on the CCD of the spectrometer. Considering the system loss, we can calculate

the number of photons arriving at the objective in the photoluminescence measurement setup. Now we determine the brightness enhancement caused by the dielectric antenna: The photon count rate from 10 QDs in the as-grown sample, excited under saturation power P_0 , is averaged. Then the enhancement factor is given by the ratio between the photon counts of each characterized QD (in total 57) in the device and the value from the as-grown sample. The rate of collected photons is increased by up to two orders of magnitude compared to the as-grown sample. On average, the brightness is enhanced by more than a factor of 40 as displayed in the Fig. 5.5(b).

5.4 Evaluation of the single-photon purity

On the processed dielectric antenna sample, two bright QDs, labeled QD1 and QD2, are characterized in-depth regarding their single-photon purity under different pumping conditions to assess their suitability as single-photon sources. All measurements are performed under above-band excitation, creating free charge carriers in the barrier material. First, the most prominent spectral lines are assigned to the respective excitonic states, as shown in the insets of Fig. 5.6(a) and (b). This allocation is based on power- and polarization-dependent micro-photoluminescence series, time-resolved fluorescence and second-order cross-correlation measurements together with previous experimental and theoretical investigations on corresponding planar samples [264, 268, 269]. The most prominent spectral features result from charged excitonic states suggesting a background doping of the sample.

Next, the single-photon purity of the QDs is evaluated using a Hanbury-Brown and Twiss setup. The second-order correlation function $g^{(2)}(\tau)$ is measured under continuous-wave (cw) and pulsed excitation for different pump powers. The brightest transition at medium excitation powers, namely the double negatively charged exciton (X^{2-}), is investigated. As shown in Fig. 5.6(a), the expected antibunching dip at zero time delay for cw auto-correlation measurements is well preserved up to saturation. For 7% of the saturation power P_0 , the raw value excluding a correction for residual background emission yields $g_{\text{raw}}^{(2)}(0) = 0.063 \pm 0.005$, while for $P/P_0 = 1$ a value of $g_{\text{raw}}^{(2)}(0) = 0.214 \pm 0.006$ is obtained as displayed in the inset of Fig. 5.6(a). The uncertainty is obtained from the normalized standard deviation of the Poissonian level. This increase is attributed to the larger spectral background contribution at higher excitation powers. A bunching effect at small, non-zero time delays, observed for low excitation powers, becomes more pronounced for decreasing pump powers while exhibiting an increase of the corresponding time constant. This is attributed to the background doping and charge carrier trap states from which the QD can be refilled [270, 271, 272, 273] after an initial excitation and emission event. This assumption is corroborated by a time-resolved fluorescence measurement as displayed in the inset of Fig. 5.6(b), yielding two decay constants $T_f = 0.9$ ns and $T_s = 8.0$ ns. While the fast decay constant is connected to the radiative lifetime

of the transition, the secondary decay yields information on the time scale of the refilling process. Possible spin flips are excluded for the X^{2-} transition since it does not have a dark state. At low excitation powers, the possibility of refilling a QD on short time scales after an initial emission increases the probability of detecting two photons on these time scales i.e., yields values larger than the Poissonian level for small-time delays. At higher pump powers, this effect is no longer observed because a charge carrier reservoir created by the strong above-band excitation is large enough to provide carriers on all time scales.

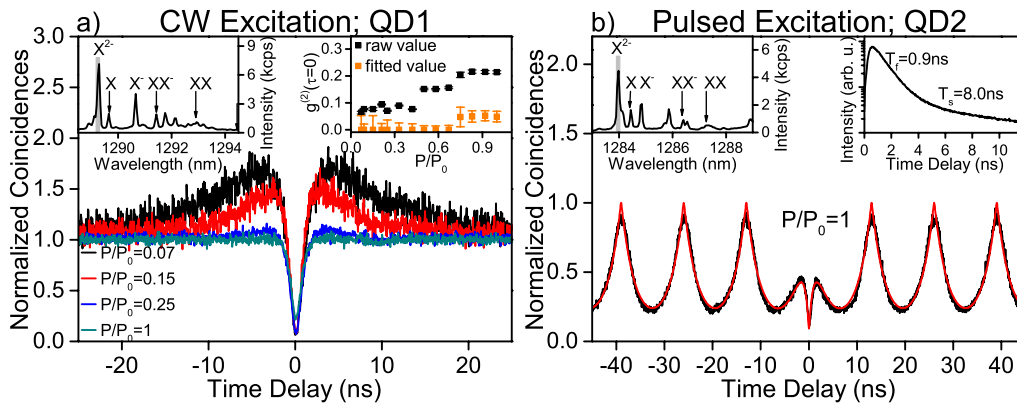


Figure 5.6: Measurements on the X^{2-} transition of QD1 and QD2 (spectra shown in the insets with the grey rectangle indicating the width of the spectral transmission window used for selecting individual transitions): (a) Second-order correlation measurements under continuous wave excitation for different pump powers. Inset: Single-photon purity as a raw value and after fitting (including the deconvolution with the system response function). (b) Pulsed second-order correlation measurement at saturation power with a fit function. The inset shows the time-resolved fluorescence measurement on a semi-logarithmic scale. Reprinted figures with permission from [220]. Copyright 2020, Optical Society of America, without any changes made.

To precisely estimate the single-photon purity, the data are fitted including a deconvolution with the system response function that is obtained from the auto-correlation of a 3 ps laser pulse. For the measurements with apparent bunching, this effect is included in the fit function [274, 275]. The values for $g^{(2)}(0)$ are displayed in the inset of Fig. 5.6(a), where the uncertainties are calculated via error propagation from the 1σ confidence bounds of the fit parameters determined by the non-linear fit algorithm. Even at saturation power, a value of $g^{(2)}(0) = 0.049 \pm 0.020$ is determined. For values below $P/P_0 = 0.75$ any residual two-photon contribution falls below the accuracy of the measurement and fit procedure, i.e., the excellent single-photon properties of the QDs [268] are not affected by the fabrication of the dielectric antenna.

While the single-photon purity is characterized by the evaluation of the $g^{(2)}(\tau)$ function under cw pumping, the suitability of the QDs for applications based on triggered single photons is evaluated by second-order correlation measurements under pulsed excitation. This is obtained by exciting the QD with a pulsed laser centered at 670 nm with a repe-

tion rate of 76.9 MHz. The result of this measurement for the X^{2-} transition of QD2 in saturation is displayed in Fig. 5.6(b) alongside a fit function. Due to the overlap of neighboring peaks separated by the repetition period of $\tau_{\text{rep}} = 13$ ns the signal does not decay to zero. Additionally, the above-mentioned refilling effect leads to a secondary radiative decay with a decay constant of 8.0 ns as observed in the time-resolved fluorescence measurement displayed in the inset of Fig. 5.6(b). This effect also explains the residual peak around zero time delay of the pulsed intensity auto-correlation measurement [276]. An antibunching dip owing to the single-photon nature of the emitted light is superimposed on this residual peak [270, 271, 272, 273, 275]. Hence, multi-photon emission events at vanishing time delays are strongly suppressed. A secondary emission event within a time period smaller than the repetition time τ_{rep} due to refilling, is found with a probability between 50 % and 70 % depending on the pump powers. Note that, for low excitation power a bunching of the first peaks at multiples of τ_{rep} is found and included in the respective fit functions. In other words, the QDs exhibit excellent single-photon emission properties but their suitability as a single-photon turnstile device [277] is limited by charge carriers refilling the QD [276]. Individual QDs [271] in spatial proximity to a charge carrier trap state have been found to be prone to refilling [264, 270, 271, 272, 273, 275, 276]. Considering the overall low spatial density of QDs [264] and the size of the area in which the SIL enhances the extraction efficiency optimally, the study at hand is limited to the investigation of these QDs. Hence, the refilling effect is assumed to be a property of the individual QDs under investigation rather than related to the transfer of the dielectric antenna approach to InGaAs QDs emitting in the telecom O-band.

5.5 Evaluation of extraction efficiency

So far, we considered only the dominant peak of the photoluminescence spectrum. In order to determine the brightness, i.e., the average number of photons emitted from the sample per excitation cycle, the emission from other excitonic states has to be taken into account. In the experiment, all the dominant transition lines of the brightest QD emission (labeled QD2 in Fig. 5.6(b)) are identified. We define the brightness B as the ratio of the photons per time emitted by the sample and the number of excitation pulses per time. The charge carriers are excited optically in pulsed mode with a repetition rate of $r_{\text{laser}} = 76.9$ MHz and a central wavelength of 670 nm above the band gap of the barrier material (above-band). The brightness for a given NA is calculated by comparing the measured count rate at the detector with the repetition rate of the laser accounting for a non-ideal setup efficiency. The NA of the objective lens employed for this evaluation is 0.6. Assuming each excitation laser pulse triggers the emission of one photon the brightness is equal to the extraction efficiency. If the state preparation fidelity is unequal to unity or non-radiative decay channels are present, the above-mentioned assumption does not hold, and the determined brightness will differ from the extraction efficiency [131].

Fig. 5.7 displays the sketch of optical characterization for the setup collection efficiency. Based on the ordinary photoluminescence (PL) setup (Fig. 2.6), a silver mirror is placed on top of the cryostat for reflecting the telecom 1.31 μm diode laser into the spectrometer. Powers of the laser at P1, P2, and P3 are detected, in order to define efficiencies of optics and detectors by $\eta_1 = P_2/P_1$, and $\eta_2 = P_3/P_2$, respectively. The setup efficiency is defined as,

$$\eta_{setup} = \eta_1 \cdot \eta_2 \quad (5.5.1)$$

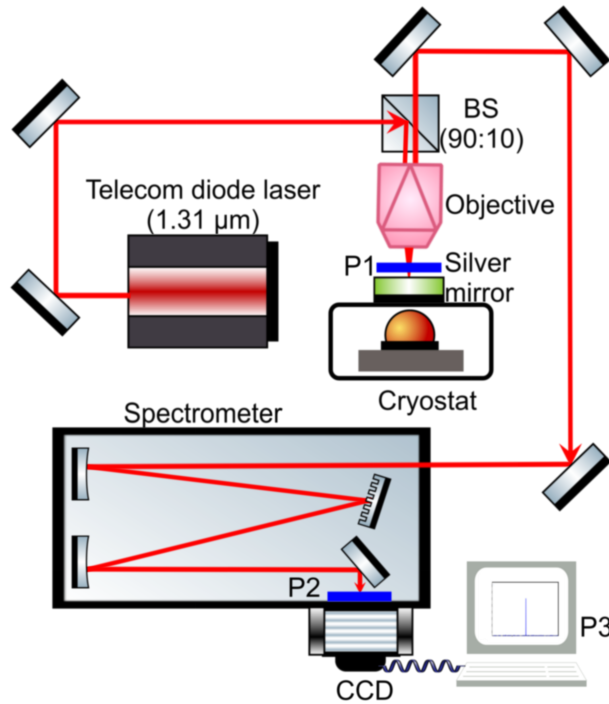


Figure 5.7: Sketch of experimental setup for characterizing the collection efficiency of the optical setup.

Since under above-band excitation different excitonic states can form constituting corresponding decay channels for the charge carriers, the photons arising from parallel, i.e., non-consecutive channels, need to be added up [273]. In the present case, these are the photons arising from the recombination of the exciton (X), the trion (X^-) and the double negatively charged exciton (X^{2-}). To exclude any background contributions, the spectrum at saturation is fitted with Gaussian functions for the transitions and a constant offset for the background emission. To correct the measured counts for background contributions, a factor f_{bgc} is calculated from the area of the respective Gaussian function A_G and the constant offset A_{bg} within the spectral transmission window of the setup via

$$f_{bgc} = \frac{A_G}{A_G + A_{bg}}. \quad (5.5.2)$$

As mentioned, a single excitation pulse can trigger more than one single-photon emission event due to refilling of the QD. To quantify this effect on the brightness [278], the pulsed second-order correlation measurement is fitted to extract the area of the central peak and the mean area of the outer peaks accounting for the temporal overlap and background contribution. The ratio of these areas $\tilde{g}_{\text{pulsed}}^{(2)}(0)$ (excluding overlapping pulses and background contributions) represents the probability for a secondary emission event in response to a single excitation pulse. This evaluation is performed for the X^{2-} and X^- transitions and yields $\tilde{g}_{\text{pulsed}}^{(2)}(0) = 0.69$ and $\tilde{g}_{\text{pulsed}}^{(2)}(0) = 0.73$ in saturation, respectively. Since due to a lower count rate this evaluation was not feasible for the X transition, the larger of the two previous values is assumed as a conservative estimate. The overall extraction efficiency is then calculated via

$$B = \frac{1}{r_{\text{laser}}\eta_{\text{setup}}} \cdot \sum_i r_{\text{raw},i} \cdot f_{\text{bgc},i} \cdot \sqrt{1 - \tilde{g}_{\text{pulsed},i}^{(2)}(0)}, \quad (5.5.3)$$

where the index i sums over all parallel decay channels and r_{raw} refers to the measured count rate at the detector. A brightness of 17% is finally obtained in a conservative estimate for an objective numerical aperture (NA) of 0.6, considering corrections for background emission, collection efficiency and multiphoton contributions. Possible reasons for the discrepancy include the roughness of the lens surface and the uncertainty of the PMMA laser thickness. Moreover, due to the overall low density of quantum emitters in the sample, only a few QDs are located in the very center of the GaP SIL in which the device is expected to perform optimally. Therefore, the observed dots provide a lower bound of the determined brightness.

In conclusion, we fabricated a dielectric antenna structure based on a GaP SIL, enhancing the extraction efficiency of InGaAs/GaAs QDs emitting in the technologically important telecom O-band. The brightness is experimentally determined to 17% for an objective NA of 0.6. FDTD simulations suggest a maximum extraction efficiency of up to 38% for the same NA and a structure with optimal PMMA layer thickness and low surface roughness of the SIL and QD membrane. Depositing an appropriately designed anti-reflection coating layer on the curved SIL surface can further enhance the brightness. The fabrication process of the dielectric antenna structure does not significantly alter the emission wavelength of the QDs. In-depth investigations of the transition lines of the two brightest QDs consistently point to a background doping and related charge carrier refilling effects. In order to exploit the demonstrated excellent single-photon purity values under cw excitation for single-photon turnstile operation, quasi-resonant or resonant excitation schemes should be employed.

This page intentionally left blank.

Neutralization of charge states for GaAs quantum dots

This chapter describe the investigation and adjustment of the emission properties of the neutral exciton of quantum dots as either single- or polarization-entangled photon sources. First, we investigate the spectral and quantum optical response of the quantum dot emission to an additional wavelength tunable gate laser, revealing blinking caused by the intrinsic Coulomb blockade due to charge capture processes. Our finding demonstrates that the emission quenching can be actively suppressed by controlling the balance of free electrons and holes in the vicinity of the quantum dot and thereby significantly increasing the quantum efficiency by 30%. In addition, we report the chemical surface passivation with sulfur compounds such as octadecanethiol performed on quantum dots with 20, 40, and 98 nm from the surface, resulting in improvements in linewidth and photoluminescence intensity as well as a well-preserved single photon emission.

*The work regarding the photoneutralization of the blinking is performed in collaboration with Tom Fandrich, Frederik Benthin and has been published in *Phys Rev. B* [279].*

*The work concerning the passivation of near-surface quantum dots is performed in collaboration with Xin Cao, and Pengji Li. It has been published in *Appl. Phys. Lett.* [280] and dissertation from X.Cao [281].*

Generating high-quality single photons and entangled photon states is considered a cornerstone for the development of photonic quantum technologies, e.g., quantum computing [24], quantum communication [282], or quantum simulation [283]. Although many mainstream demonstrations of quantum optical applications are implemented with spontaneous parametric down conversions (SPDCs) in the past decades [66, 68], they suffer from a fundamental trade-off between excitation efficiency (η_{ex}) and multiphoton emission probability, thereby encouraging the search of alternative sources. Semiconductor quantum dots (quantum dots (QDs)), referred to as artificial atoms, not only allow for

an on-demand generation of high-purity single photons [109], they also show high performance in terms of pairwise entanglement fidelity [110], large radiative decay rates and internal quantum efficiencies in contrast to other quantum systems (e.g., atoms and diamond defect centers) [111, 112]. However, an imperfect brightness and luminescence intermittence inhibits the application of such a source in quantum information processing schemes [224, 284, 285].

Tremendous efforts are invested to efficiently extract photons from the high refractive index matrix of QD based devices by modifying the photonic environment, e.g., by broadband micro lenses [254, 255], microcavities such as circular Bragg gratings [205] and micropillars [229], or metal antennas [257, 258] based on directional emission enhancement from surface plasmon resonance. The overall brightness of QD based photon sources is further influenced by the excitation efficiency, which corresponds to the probability of QDs being occupied at the desired state under resonant excitation [122, 123]. The degradation of excitation efficiency is typical for solid-state quantum emitters like single colloidal nanocrystals [286, 287] or organic molecules [288], manifesting as strong intermittency phenomena in the photon emission (called ‘blinking’). Even for III-V QDs, epitaxially grown in an ultrahigh vacuum atmosphere, it is impossible to fully avoid this effect without embedding QDs in devices such as n-i-p diode structures, which would allow for charge tuning [109, 226]. An all-optical approach to stabilize the solid-state charge environment for a resonantly excited QD is the concept of photoneutralization of charges by illumination with an additional weak gate laser, which has been investigated in self-assembled InAs/GaAs QDs [123, 124, 125]. In recent years, the emerging family of GaAs/AlGaAs QDs [128, 202] has shown intriguing features that benefit a high-quality entangled photon emission close to the rubidium D2 transitions [201, 289]. These include a high QD symmetry and homogeneity, low electron-nuclear spin hyperfine interaction [290], and reduced light- and heavy hole mixing [291].

Here we investigate the effect of a weak gate laser on entangled photon sources based on GaAs/AlGaAs quantum dots. For the generation of entangled photon pairs and investigating photoneutralization effects, we employ resonant two-photon pumping (TP) excitation to coherently drive the biexciton state in GaAs/AlGaAs quantum dots. Strong blinking and an additional emission from the positive exciton (X^+) transition are observed, indicating a degraded TP excitation efficiency. This effect is counteracted with a second, wavelength tunable gate laser in the low-power regime, allowing control over the charge carrier exchange rates between the barrier material and the QD. The impurity induced excess of holes in the QD ground state is therefore suppressed. Using photoluminescence excitation (photoluminescence excitation (PLE)) spectroscopy and second-order correlation measurements, we probe the continuum states in the barrier, and control the corresponding charging rate of the QD. The optical properties of semiconductor micro- and nano-structures are greatly affected by their surface. Defects in the crystal lattice usually result in additional electronic states in the bandgap (so-called surface states),

which is detrimental for radiative recombination processes and charge carrier transport. The past research and technological advance of optoelectronic devices based on gallium arsenide, therefore, kindled an interest in surface passivation [292, 293, 294]. An increase in photoluminescence (PL) intensity by more than one order of magnitude has been observed after passivating the GaAs surface with sulfur [295]. Up to now, although some groups worked on InAs or InGaAs QDs directly at the surface, all the obtained photoluminescence signals were from an ensemble of QDs and no single surface QD emission has been observed [296, 297]. We investigate the linewidth broadening and fluorescence quenching by reducing the capping layer thickness from 98 to 20 nm. We passivate the surface using octadecanethiol (ODT), a treatment that is applicable for many III-V material systems, such as InP [298], GaN [299], and GaSb [300]. The linewidth and intensity are partially restored, and single photon emission of the GaAs QDs is still preserved even with 20 nm capping. Bunching effects in the second-order intensity autocorrelation measurements are alleviated after ODT passivation, indicating the elimination of additional states and decay channels at the surface.

6.1 Dynamics of blinking in GaAs quantum dots

The GaAs/AlGaAs QDs under investigation are grown by molecular beam epitaxy with the in-suit droplet etching and nanohole infilling method [128, 301]. After the Al-droplet etching process on the 235 nm thick $Al_xGa_{1-x}As$ ($x=0.15$), a layer of 2 nm GaAs is deposited to fill the nanoholes, followed by 200 nm of $Al_xGa_{1-x}As$. In order to efficiently extract the photons out of the host material, a dielectric antenna device is fabricated [138]. Excitation of QDs is accomplished by illumination with 80 MHz Ti-Sapphire pulsed laser light, with a pulse length of ~ 9 ps. To realize TP excitation, the energy of the laser pulse is adjusted exactly at the half energy of the biexciton state $|XX\rangle$. Additionally, a weak continuous wave (cw) laser (FWHM ≈ 100 kHz) is applied with power around hundreds of nW for photoneutralization.

Fig. 6.1(a) illustrates the QD as a two and three-level system including the dynamics of charge capture processes related to the blinking behavior under optically gated TP excitation. If the QD is initially empty, described by the ground state $|g\rangle$, it can be pumped to the biexciton state $|XX\rangle$ using a TP excitation scheme with a pumping rate r_R (dashed line indicates the virtual energy level in TP excitation). Then, $|XX\rangle$ starts to decay via the exciton state $|X\rangle$ to the ground state by emitting a pair of polarization-entangled photons with spontaneous decay rates of γ_{XX} and γ_X , respectively. However, residual electrons and trapped by impurities (i.e., carbon acceptors) in the vicinity of the QDs can tunnel into the QDs with rates of $\gamma_e^{(d)}$ and $\gamma_h^{(d)}$ (not shown in the diagram) resulting in the charged ground state $|c\rangle$. The formation of the neutral biexciton will be blocked by the residual hole in the QD, similar to the Coulomb blockade effect [125]. According to the model of photoneutralization, holes and electrons are created in the

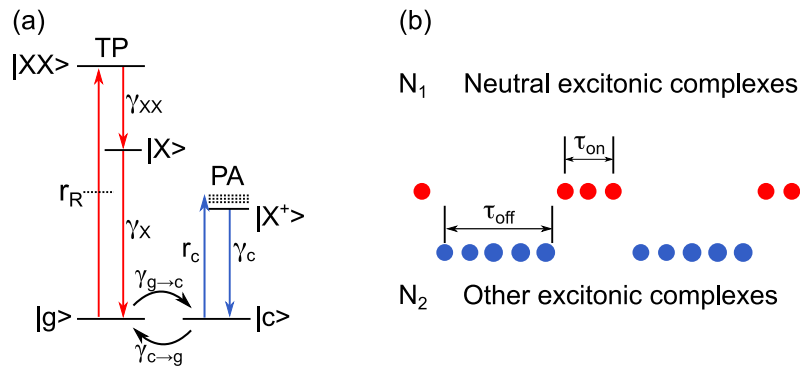


Figure 6.1: (a) Schematic of the charge carrier transition dynamics and (b) the effect on the emitted single photon stream. Reprinted figures with permission from [279]. Copyright 2022, American Physics Society, without any changes made.

barrier by an additional, weak and off-resonant gate laser with rates of $\gamma_h^{(b)}$ and $\gamma_e^{(b)}$, respectively. It modifies the rates $\gamma_{g \rightarrow c}$ and $\gamma_{c \rightarrow g}$ describing the transition between the neutral and charged ground state of the QD. The transfer rate between impurities and the QD is negligible if $\gamma_e^{(d)}, \gamma_h^{(d)} \ll \gamma_e^{(b)}, \gamma_h^{(b)}, \gamma_X, \gamma_{XX}$. Therefore, the neutral ground state $|g\rangle$ converts into the charged ground state $|c\rangle$ with an average number of electrons or holes in steady regime within a time range ($\tau_{off} = 1/\gamma_{g \rightarrow c}$). This leads to the phonon-assisted (PA) excitation of the trion state (i.e., $|X^+\rangle$) with a pumping and radiative rate of r_c and γ_c [302]. After a while ($\tau_{on} = 1/\gamma_{c \rightarrow g}$), the charged state is neutralized, leaving the QD empty and resulting in TP excitation of the $|XX\rangle$ state. Fig. 6.1(b) presents the blinking dynamics of the photon emission from the QD within the charge and neutralization process of the ground state. In a time range of τ_{on} , the QD stays neutral so that single photons are continuously emitted from the spontaneous transition processes. While neutral exciton photon emission is replaced by other excitonic state emission once the ground state is charged, until it is neutralized again.

6.2 Photoluminescence characterization of blinking

Fig. 6.2(a) shows the typical non-resonant (NR) and TP excitation photoluminescence (PL) spectra of a single QD, in which three dominant transitions of excitonic states are distinguished. By comparing the two spectra, it can be seen that the $|X^+\rangle$ state exists in TP excitation while the further red-shifted, weak transition lines around $|XX\rangle$ disappear. It demonstrates that the neutral and charged ground states are alternating, giving rise to bright $|X^+\rangle$ state emission and causing the intermittency of the neutral X photon emission. Fig. 6.2(b) displays the autocorrelation measurement of the neutral X photon emission from the QD under TP excitation using a Hanbury-Brown and Twiss setup. The anti-bunching at zero time delay reveals a pure single photon emission. At the same time, a superimposed bunching at a larger time delay demonstrates the switching of the QD

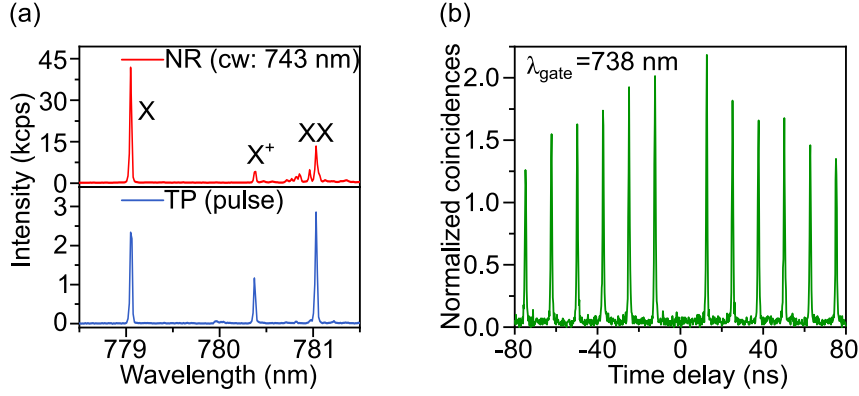


Figure 6.2: (a) Photoluminescence spectra of an exemplary QD under NR and TP excitation with cw and pulsed laser, respectively, showing the neutral exciton (X) and biexciton (XX) as well as the positively charged trion (X^+) emission. (b) Normalized autocorrelation histogram of X photons under TP excitation with an additional gate laser at 738 nm. Reprinted figures with permission from [279]. Copyright 2022, American Physics Society, without any changes made.

between a neutral and a charged ground state.

6.2.1 Photoluminescence excitation spectroscopy

Next, we implement an excitation spectroscopy measurement with the cw laser (Fig. 6.3) from 723 to 766 nm after the subtraction of the background, to explore how the excitation wavelength affects the excitation efficiency of the different excitonic complexes in the QD. In the upper panel of Fig. 6.3, the total intensity of the X and X^+ photons is shown, which keeps constant at wavelengths below 750 nm and then gradually increases. We attribute the increase at $\lambda > 750$ nm to a higher probability of the QD ground state to be either empty or populated with one residual hole. The probability of a negatively charged ground state or the formation of dark excitonic states is therefore expected to decrease.

The lower panel of Fig. 6.3 shows the intensity ratio of the $|X\rangle$ and $|X^+\rangle$ states as a function of the non-resonant laser wavelength. A strong contrast of the intensity ratio is observed at $\lambda \approx 738$ and 745 nm. Since the spontaneous decay rates of X and X^+ photons are assumed to be comparable [303], we can conclude that the QD tends to be empty at the ground state ($n_h^{(st)} = 0$) for these specific wavelengths.

6.2.2 Influence of gate-laser on photoluminescence intensity

For investigating the influence of the optical gate effect on the blinking, we first study the PL intensity dependence on the gate laser power and wavelength in the steady state regime. Fig. 6.4(a) shows the dependence of the neutral X photon counts on the power of the gate laser at a constant power of the pulsed TP excitation laser. To illustrate that the improvement of the intensity arises from the neutralization effect induced by the gate laser instead of the simultaneous off-resonant fluorescence, the photon counts emitted from the

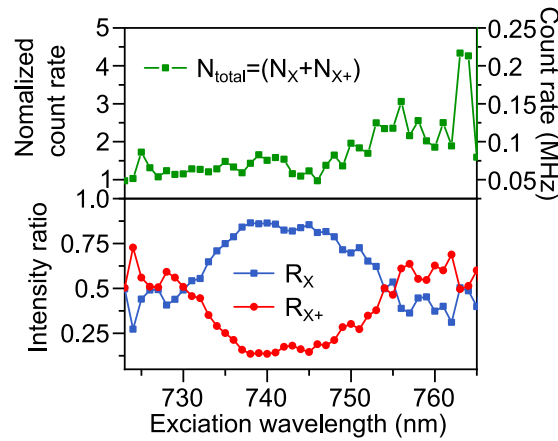


Figure 6.3: Excitation spectroscopy measurement in the absence of TP excitation under gate laser power $P_{gate} = 6.3 \mu\text{W}$, showing the total intensity and the intensity ratio of the X and X^+ transitions ($R_X = N_X/N_{total}$ and $R_{X^+} = N_{X^+}/N_{total}$). Reprinted figure with permission from [279]. Copyright 2022, American Physics Society, without any changes made.

QD when illuminated by two lasers (N_{Mix}) are subtracted by the counts present when solely excited by the gate laser (N_{gate}). The difference ($N_{Mix} - N_{gate}$) is then normalized to the X count rate (N_{TP}) when only the pulsed TP excitation is present. The curve increases and eventually saturates at around 1.3 with increasing gate laser power, proving the gate laser effect, aligned with a previous report [125].

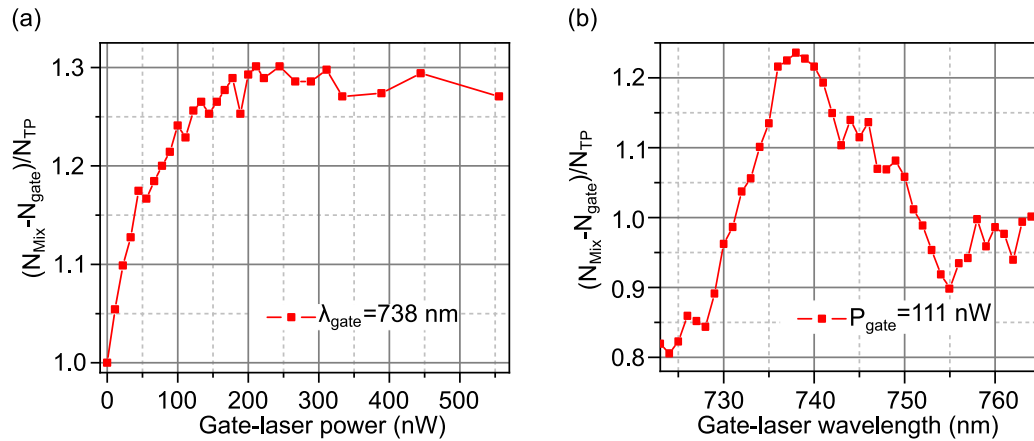


Figure 6.4: Dependence of QD emission intensity on gate laser power and wavelength. (a) Normalized gate laser power dependent fluorescence intensity of X photons from the QD under TP excitation. (b) Normalized gate laser wavelength dependent fluorescence intensity of X photons from the QD under TP excitation. Reprinted figures with permission from [279]. Copyright 2022, American Physics Society, without any changes made.

To demonstrate that the laser wavelength is able to control the charge state of the QD, we study the gate laser wavelength dependent emission intensity of neutral X photons (Fig. 6.4(b)) under TP excitation, in which most of the bright states are strictly from $|X^+\rangle$ and the cascade emission of the $|XX\rangle$ states. The power of the gate laser is kept

constant ($P_{gate} = 111 \text{ nW}$) below the power at which the optical gate effect saturates ($P_{sat} \sim 200 \text{ nW}$). We observe a similar intensity fluctuation (R_x) as shown in Fig. 6.3, revealing that the QD can be actively photoneutralized.

6.3 Second-order intensity correlation characterization

In the following we present the corresponding behavior as a function of gate laser wavelength and explain the blinking phenomena according to the proposed model, as intensity autocorrelation measurements reveal the photon emission properties in the dynamic regime. These correlations are shown in Fig. 6.5(a) for the X photon emission. It displays two exemplary histograms of the autocorrelation measurements (left) and the corresponding coincidence counts binned according to each laser pulse emission (right), normalized to the coincidences at large time delays. The missing peak in the center of the histograms resulting from anti-bunching is neglected during the binning of coincidence counts in the right graph. The remarkable bunching behavior (green curve) reflects the blinking dynamics for which photons emitted close to each other within the time range ($|\tau_B| \leq 1 \mu\text{s}$) have a higher chance to result in coincidence counts. By comparing the theoretical modeling of these two exemplary bunching curves, one can notice that the blinking dynamics is tuned when changing the gate laser wavelength. It deserves to be mentioned that the slight mismatch of the model with the central data points close to a time delay of $\tau = 0 \mu\text{s}$ is presumed to be the dark exciton transition [304].

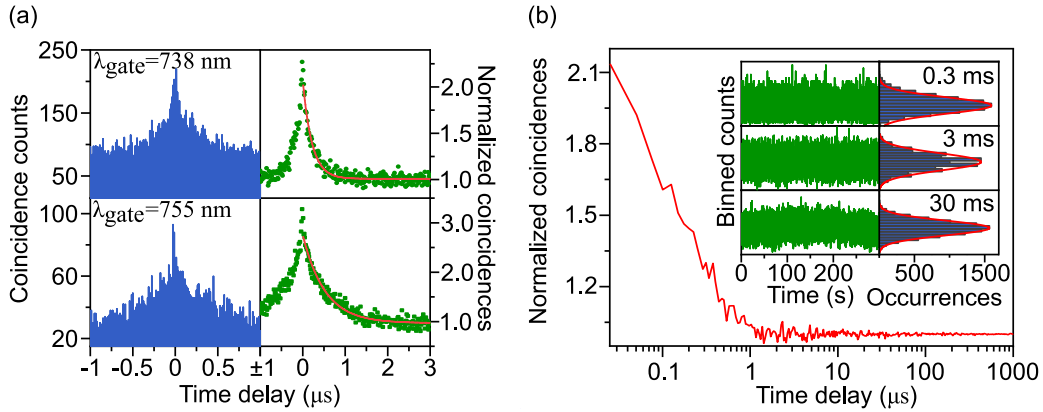


Figure 6.5: (a) Intensity autocorrelation histograms (left) for X photons revealing pure single-photon emission and a superimposed bunching due to blinking. Normalized histogram (right) with bin size set to the inverse of the laser repetition rate is used to apply an exponential decay model (red line). Measurements at two exemplary gate laser wavelengths are shown. (b) Normalized intensity autocorrelation of X photons in a logarithmic time delay scale up to one millisecond ($\lambda_{gate} = 738 \text{ nm}$). (Inset: Time trace (green) and histogram (blue) of detector count rates for 0.3 ms, 3 ms and 30 ms time bins, following Gaussian distribution with the statistics (red). Reprinted figures with permission from [279]. Copyright 2022, American Physics Society, without any changes made.

In Fig. 6.5(b), the normalized intensity autocorrelation of the X photons is plotted in a logarithmic time scale up to $1 \mu\text{s} \leq |\tau| \leq 1000 \mu\text{s}$. The first order linear decay at short delays ($|\tau| \leq 1 \mu\text{s}$) indicates that there are no other potential dark states causing the blinking of the photon emission [304]. The curve then remains flat up to 1 ms, indicating that there is no blinking observed at this time scale. To study the blinking on an even larger time scale, Fig. 6.5(b) shows the fluorescence intensity over time, under different time bin sizes of 0.3, 3 and 30 ms (left). From the histogram of the intensity values of each curve (right) it is clear that the intensity distribution exhibits a single Gaussian model behavior, verifying the absence of blinking at a longer time range $|\tau| \geq 1$ ms.

6.3.1 Auto-correlation of neutral exciton

Fig. 6.6(a) shows the gate laser wavelength and time-delay dependent normalized coincidences [each horizontal cut of the data corresponds to a green curve of the binned data in Fig. 6.5(a)] at different wavelengths in the form of a color-map. The bunching amplitude undergoes a descent and ascent with increasing gate laser wavelength, reaching the lowest value at ~ 740 nm. It implies a decreased blinking, qualitatively validating the behavior observed in Fig. 6.3 about the intensity change as a function of the gate laser wavelength.

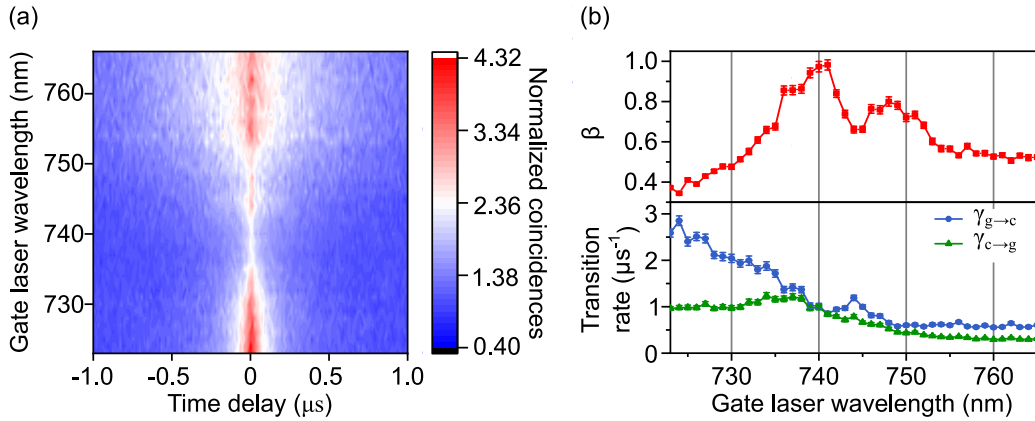


Figure 6.6: (a) Normalized coincidences as a function of time delay and gate laser wavelength, with fixed powers of the resonant and gate lasers ($P_{gate} = 166$ nW). (b) On-off time ratio β (top) and the charge capture rates (bottom) as a function of gate laser wavelength. Reprinted figures with permission from [279]. Copyright 2022, American Physics Society, without any changes made.

To quantitatively understand the blinking phenomenon related to the capture of charges in the QD, we extract the values of the parameters based on the modeling of the $g^{(2)}$, described by [201, 274],

$$g^{(2)}(\tau, \lambda) = \left[1 + \left(\frac{1}{\beta(\lambda)} \right) e^{-\gamma_B(\lambda)|\tau|} \right] \quad (6.3.1)$$

$$\gamma_B(\lambda) = \gamma_{g \rightarrow c}(\lambda) + \gamma_{c \rightarrow g}(\lambda) \quad (6.3.2)$$

with β denoting the blinking on-off ratio (τ_{on}/τ_{off}), γ_B the blinking rate ($\gamma_B = \sum_i \gamma_i, i = g \rightarrow c, c \rightarrow g$). The upper panel in Fig. 6.6(b) shows the average ratio of on and off times as a function of the gate laser wavelength, in which β follows exactly the tendency of intensity fluctuations in the steady state (Fig. 6.4 (b)). It verifies our previous assumption that the gate laser wavelength can tune the number of remaining charges in the QDs, thus affecting the excitation efficiency ($\eta_{ex}^{(min)} = 25.57(8) \pm 0.403\%$, $\eta_{ex}^{(max)} = 49.53(9) \pm 0.645\%$). A closer look at the effect of the gate laser on the charging and neutralization process is obtained by deducing the capture rates of holes and electrons as displayed in the lower panel. The charging rate (blue curve) generally stays higher than the neutralization rate (green curve) in the wavelength range from 723 ~ 765 nm, therefore, the ground state of the QD is charged with an excess of holes for most of the wavelengths. When the gate laser is tuned to ~ 740 nm, the two lines meet each other, corresponding to a balanced capture rate of holes and electrons between the barrier and the QD. ($\gamma_e^{(b)} = \gamma_h^{(b)}$). Simultaneously, the low transition of charges tunnelled from defects to the QD with rates of $\gamma_e^{(d)}, \gamma_h^{(d)}$ dominates. To completely eliminate the excess of charges in the QDs, a slightly higher ejection rate of electrons is preferred, in order to neutralize the holes additionally induced by the impurities.

6.3.2 Cross-correlation between neutral and charged exciton

The total capture rate of charges (γ_B) between QDs and barrier material decreases with increasing gate laser wavelength, and not only under TP excitation. For NR excitation, the charging rate is affected by the excitation laser wavelength, explaining the excitation spectroscopy in Fig. 6.3. The color map in Fig. 6.7(a) shows the normalized coincidences from a cross-correlation measurement between X and X^+ photons as a function of wavelength of the cw excitation laser. The excitation wavelength is limited to values below 755 nm, due to the observed laser background at higher wavelengths. Similar to the bunching envelope in the autocorrelation measurement, the here generally symmetric anti-bunching reveals the effect of the laser wavelength on the charge capture rate of the QD from its surrounding environment. The anti-bunching in the cross-correlation can be modelled with the below formula [223, 274],

$$g_{X,X^+}^{(2)}(\tau) = (1 - e^{\gamma_B(\lambda)|\tau|})g_{cross}^{(2)}(\tau) \quad (6.3.3)$$

$$g_{cross}^{(2)}(\tau) = [H(\tau)g_{X^+}^{(2)}(\tau) + H(-\tau)g_X^{(2)}(\tau)] \quad (6.3.4)$$

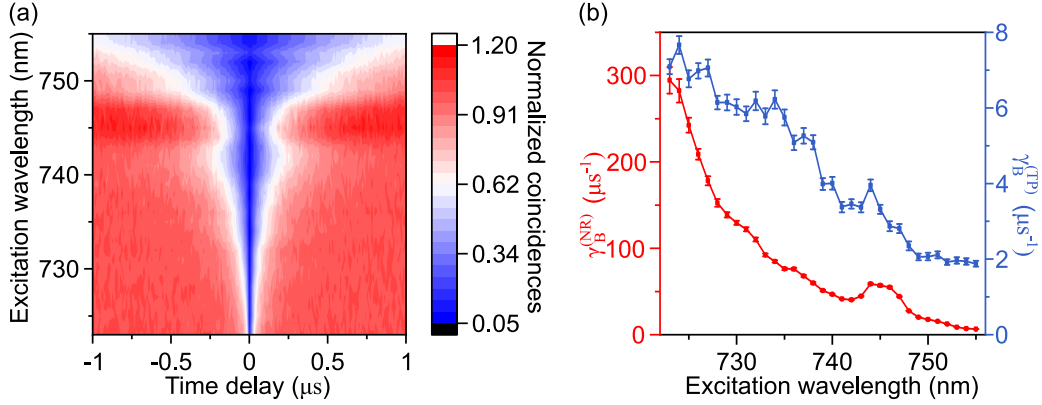


Figure 6.7: (a) Normalized coincidences from a cross-correlation measurement between X and X^+ photons as a function of time delay and excitation laser wavelength. (b) Average blinking rates γ_B under TP and NR excitation as a function of the wavelength of the non-resonant excitation laser. Reprinted figures with permission from [279]. Copyright 2022, American Physics Society, without any changes made.

where the first term in Eq. (6.3.3) is the total capture rate describing a charging of the ground state of the QD with one hole (related X^+ photon emission), followed by a return to the neutralized state ($|g\rangle \rightarrow |c\rangle \rightarrow |g\rangle$). The second term is the conventional anti-bunching, a result from the single photon character of the X and X^+ emissions. This is expressed in Eq. (6.3.4), where H is the Heaviside step function while $g_{X^+}^{(2)}$ and $g_X^{(2)}$ are the anti-bunching functions of X^+ and X , respectively. At lower excitation wavelengths it can be seen that the anti-bunching shows an asymmetric dip in the center.

This can be explained by the different rates contributing to the dynamics of X and X^+ emission, taking into account the pumping and decay processes under NR excitation. The decay processes (described by $r_c, \gamma_R, r_X, \gamma_{X^+}$) are much faster than the blinking rate of the ground state (γ_B) [223]. With increased wavelength, the asymmetric anti-bunching can not be distinguished anymore because of the low signal-to-noise ratio and the dominating blinking rate, leading to a broader and more symmetric anti-bunching.

Fig. 6.7(b) shows the comparison of the extracted γ_B from the autocorrelation of Fig. 6.6(a) and the cross-correlation of Fig. 6.7(a), respectively. Overall, the capture rate of the empty ground state and charged state with one hole is reduced with increasing gate/excitation laser wavelength. However, γ_B under NR excitation is much higher than the rate under TP excitation due to the different dynamics and possible formation of other excitonic states (e.g., X^- state) in NR excitation.

6.4 Influence of photon-neutralization on entangled states

After the investigation of photon-neutralization on the charge environment in the vicinity of QDs, we further try to learn more about the influence of the gate effect on the quality of

the polarization-entanglement of photons, by performing the quantum state tomography. Fig. 6.8(a) presents the polarization-resolved $XX - X$ density matrices measurement for the emission from the same QD under TP excitation without and with gate laser ($\lambda_{gate} = 738$ nm, $P_{gate} = 111$ nW), respectively. Without any post-selection method, we obtain the raw fidelities of $f_{without\ gate} = 0.61(6) \pm 0.020$, $f_{with\ gate} = 0.65(5) \pm 0.008$ by projecting the state to the Bell state $|\Phi^+\rangle$ in Fig. 6.8(b). Utilizing the maximum-likelihood estimation method, fidelities of $f_{without\ gate} = 0.63(8) \pm 0.020$, $f_{with\ gate} = 0.65(8) \pm 0.008$ are hereby extracted from the reconstructed density matrices, which are nearly constant. Therefore, we can conclude that the fidelity to the Bell state is not dependent on the excitation scheme [302].

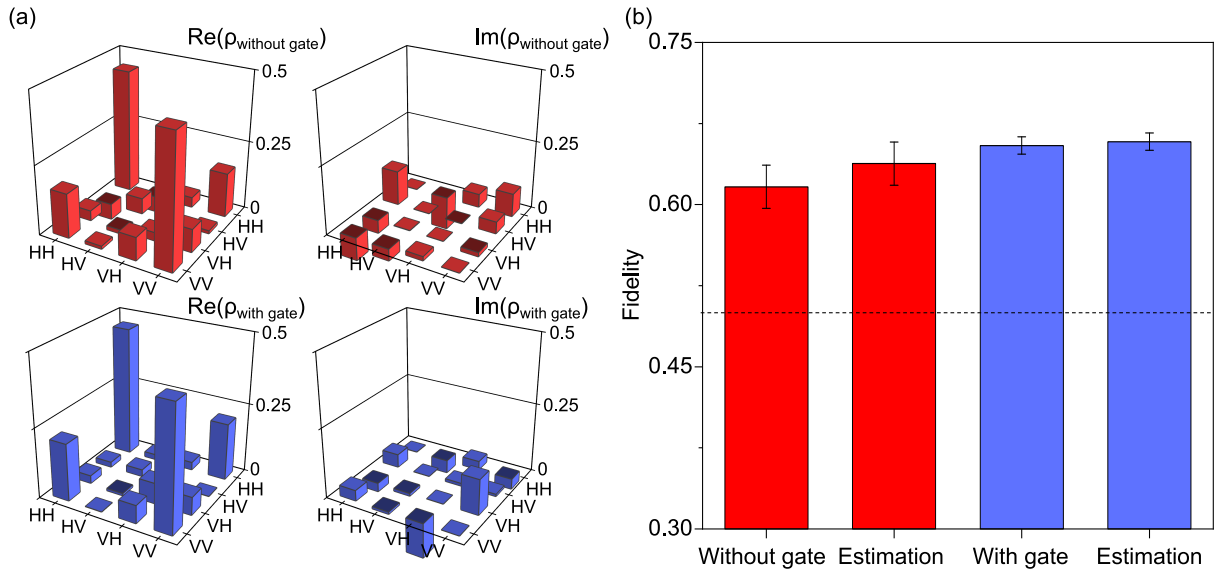


Figure 6.8: (a) Real (left) and imaginary (right) of reconstructed two-photon density matrices between XX and X photons under TP excitation without (top) and with (bottom) gate laser. (b) Fidelity to the expected Bell state $|\Phi^+\rangle$ for TP excitation without (red) and with (blue) gate laser. Reprinted figures with permission from [279]. Copyright 2022, American Physics Society, without any changes made.

Until now, we have shown that the electronic environment and material impurities play a pivotal role in obtaining an efficient optical response from a semiconductor QD based photon source. Charge capture processes are identified to be the major cause of luminescence intermittence in GaAs/AlGaAs QDs subject to two-photon excitation to the biexciton. The power and wavelength of a gate laser acts on the capture rate of holes and electrons, particularly close to the band gap of the barrier material (~ 740 nm for $Al_{0.15}Ga_{0.85}As$). An enhancement of up to 30% in excitation efficiency is observed, and the entanglement fidelity of the emitted photon pairs is maintained by applying the optical gate. The intensity of the QD emission in the steady state is well explained by investigating the charge capture dynamics with auto-/cross- correlation measurements from NR and TP excitation schemes. Our finding demonstrates that photo-generated charge carriers

modify the electronic environment of the QDs and thus increase the efficiency of the source while maintaining the degree of photonic entanglement. One possibility to gain further control of the charge in the QD is embedding it in n-i-p type charge tunable devices[226]. Since such devices also increase the fabrication complexity, especially in combination with nanostructure fabrication [205, 229] or, e.g., strain-field tuning [143, 144], an all optical and easily implementable method to control the charge population of the QD ground state is beneficial [305, 306, 307].

6.5 ODT passivation for near-surface quantum dots

The QD sample in the ODT passivation study is grown on an undoped GaAs (001) substrate (Wafer Technology Ltd.) with solid source molecular beam epitaxy (MBE, Riber, Compact 21) via the local droplet etching method as well [308]. The substrate is deoxidized and overgrown with a GaAs buffer, followed by the deposition of AlGaAs as a base for the subsequent QD growth. After interrupting As_4 for a short period to create a low arsenic environment, Al droplets are deposited on the AlGaAs surface. After the local droplet etching process introduced in Sec. 2.1.1, the QDs are capped with AlGaAs again with a thickness of 98, 40, and 20 nm, respectively, as shown in Fig. 6.9.

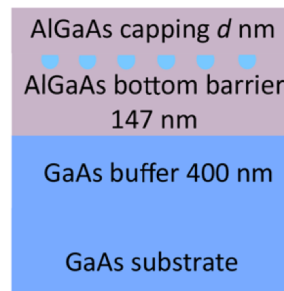


Figure 6.9: Schematic of the sample structures. Reprinted figure with permission from [280]. Copyright 2021, AIP Publishing, without any changes made.

After sample growth, the samples are cut into pieces. Chemical treatment is performed by immersing the sample pieces in 0.05 mol L^{-1} 1-Octadecanethiol (ODT, Sigma-Aldrich)/ethanol (Carl Roth GmbH) for 3 h to passivate the surface. The following optical measurements were performed at 4 K by inserting the different pieces of sample (with and without passivation) into a closed-cycle helium flow cryostat (Montana Instruments, Cryostation C2). Single QDs are excited using continuous wave diode laser at 675 nm (Thorlabs) which is focused by an objective (MicroscopeWorld, M Plan Apo NIR 100 \times) with a numerical aperture of 0.7 before irradiating the sample.

Fig. 6.10 displays the PL spectra of GaAs QDs with three capping thicknesses, before and after ODT passivation, obtained under an excitation laser power of 550 nW. It clearly shows the dominant neutral exciton peak and several charged exciton peaks at the red-

shifted side. By reducing the capping thickness, the intensity of the exciton peaks of the as-grown sample is significantly decreased and the linewidth is broadened. This indicates the presence of extra decay channels caused by surface states as well as the influence of electric fields from the charge carrier fluctuations at the surface via the DC Stark effect. After ODT passivation, it is difficult to observe any change from the PL spectra for the sample with 98 nm capping. For 40 and 20 nm, the intensity of the exciton emission is enhanced after passivation. Even at a low capping thickness of 20 nm, the different excitonic peaks can be clearly resolved.

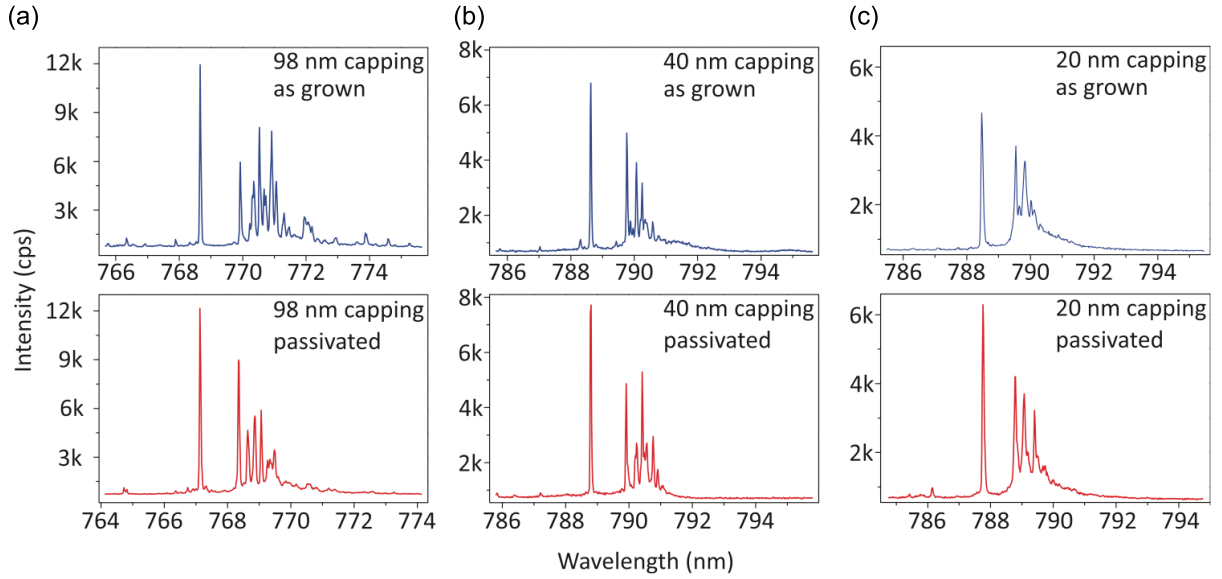


Figure 6.10: PL spectra of different GaAs QDs representing the average emission of each sample before and after passivation for different capping thicknesses. Top: as grown sample; bottom: passivated sample. Linewidth and intensities decrease with lower capping thickness. These properties are partially restored after surface passivation. Reprinted figures with permission from [280]. Copyright 2021, AIP Publishing, without any changes made.

To further illustrate the influence of surface passivation on the neutral exciton, both the linewidth and PL intensity are investigated in Fig. 6.11(a) and (b), showing no change after passivation since the QDs are deeply buried inside the AlGaAs matrix beyond the influence of the surface states. For 40 nm capping, the surface states start to affect the exciton recombination (linewidth of about $48 \mu\text{eV}$). When further reducing the capping thickness to 20 nm, the peak shows an additional threefold broadening compared with 40 nm capping. This can be explained by two mechanisms. On the one hand, due to the abrupt end of the crystal lattice at the surface, charge carriers may accumulate at the surface and will occupy and de-occupy surface states. Such moving charge carriers will result in a fluctuating electric field and therefore affect the exciton emission energy on short timescales (typically $< \text{ms}$) due to the DC Stark effect, causing peak broadening on longer timescales ($> \text{ms}$). When the QD is closer to the surface, the stronger electric field fluctuations will induce larger peak broadening. On the other hand, AlGaAs is easily

oxidized in air. The oxides will result in additional charge carrier trap states, leading to an increase in non-radiative transitions of the exciton.

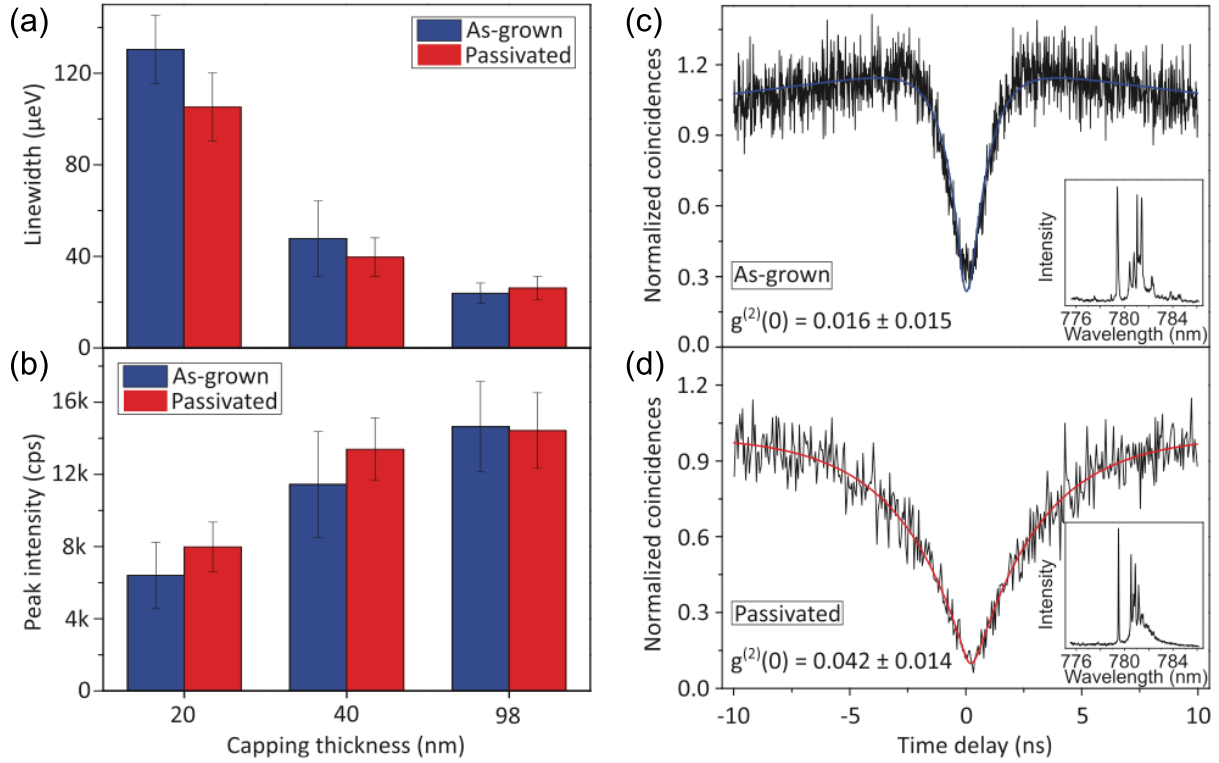


Figure 6.11: Left panel: comparison of linewidth (a) and saturated peak intensity (b) of the neutral exciton emission from GaAs near-surface QD samples before and after passivation. 30, 30, and 29 quantum dots were measured for 20, 40, and 98 nm capping thickness, respectively. The linewidth is $23.9/26.1 \mu\text{eV}$ for 98 nm capping, $47.8/39.6 \mu\text{eV}$ for 40 nm capping and $130.3/105.1 \mu\text{eV}$ for 20 nm capping for the as grown/passivated samples, respectively. The peak intensity is measured at saturated excitation power of $1.6 \mu\text{W}$. Right panel: second-order autocorrelation measurement of as grown (c) and passivated (d) sample with 20 nm capping. The anti-bunching dip at zero-time delay indicates single photon emission, with $g^{(2)}(0) = 0.016 \pm 0.015$ and 0.042 ± 0.014 for as grown and passivated, respectively. Slight bunching for the as-grown sample is attributed to the blinking effect, which is not present after ODT passivation. Surface passivation also reduces non-radiative transitions, resulting in the broadening of the anti-bunching dip. Inset: PL spectra of the measured QDs. Reprinted figures with permission from [280]. Copyright 2021, AIP Publishing, without any changes made.

However, after ODT treatment sulfur can partially replace the oxides [309], decreasing the trap state density. Studying an average of 30 dots reveals a reduction of the linewidth of the 40 and 20 nm capping samples by 8 and $25 \mu\text{eV}$, respectively, after ODT passivation. The intensity of the neutral exciton emission is also enhanced as the passivation reduces non-radiative transitions.

Fig. 6.11 (c) and (d) show the second-order autocorrelation measurement of the as-grown and passivated sample with 20 nm capping. The coincidence histogram is fitted

with the following correlation function, convoluted with the instrument response function of the APD (closely resembles a Gaussian function with a FWHM of: ~ 350 ps):

$$g^{(2)}(\tau) = \left(1 + \frac{1 - \beta}{\beta} e^{-\frac{|\tau|}{\tau_c}}\right) g_{ideal}^{(2)}(\tau) \quad (6.5.1)$$

$$g_{ideal}^{(2)}(\tau) = (g_0 - 1) e^{-\frac{|\tau|}{\tau_{corr}}} + 1 \quad (6.5.2)$$

where τ_c corresponds to the correlation time of the characteristic blinking effect, τ_{corr} is the characteristic correlation timescale, b is the fraction of time when the QD is in an on state, and g_0 is the $g^{(2)}$ value at time equal to zero. The autocorrelation measurement on the as grown sample shows a slight bunching effect. This is attributed to blinking in the exciton emission induced by trap states. After ODT passivation, the bunching effect is not observed, indicating a reduction of the density of trap states. In addition, the anti-bunching dip is broadened after ODT passivation. On the one hand, this is a clear indication that the non-radiative transition channels have been reduced, and the lifetime of the exciton is prolonged, consistent with the previous linewidth measurements. On the other hand, the passivation may lead to a stronger phonon bottleneck in the QDs [310] since excited exciton recombination dynamics can be affected by surface states.

In conclusion, we have shown that the quantum dot emission is not influenced by surface states when the dots are buried around 100 nm beneath the surface. By applying chemical passivation with ODT, the surface states are partially eliminated, inducing a partial recovery of linewidth and intensity. The single photon emission properties and excitonic spectral features are very well preserved even for 20 nm capping. The presence of blinking in the single photon emission is reduced with ODT passivation.

This page intentionally left blank.

Conclusions and Outlook

7.1 Conclusions

So far, the potential of epitaxial semiconductor QDs in the application of quantum information science has been presented, as the on-demand non-classical photon sources. Representative examples in quantum communication with the prevalently based on SPDC sources are discussed. In contrast, the family of III-V Quantum dots have been extensively studied for twenty years by now. Due to their great potential as sources of single photons and entangled photon pairs, tremendous efforts have been spent in optimizing the optical quality and brightness. In theory, it exhibits physical advantages over the SPDCs, especially the GaAs/AlGaAs QDs grown by local droplet etching and nanoholes infilling techniques. They own the features of inherently low exciton fine structure splitting, high radiative rates, and highly deterministic optical properties due to the virtually strain-free and weak charge carrier confinement [128, 202], rendering them to be the promising single- or entangled- photon sources in the quantum network applications.

7.1.1 Entanglement swapping with a single semiconductor QDs

Transferring entangled states between distinct pairs of photons is a core element in quantum networks. In the first part of the thesis, the first experimental evidence of entanglement swapping achieved with a single GaAs/AlGaAs quantum dots is presented. Deterministically generated and strongly entangled photon pairs interact very effectively with each other, resulting in a swapped photonic state which violates Bell's inequality. Over 80% entanglement fidelity is obtained for the swapped state with a source providing two pairs of entangled photon which is initially 90%. This is the first and a key step for scalable quantum technologies based on semiconductor light sources.

7.1.2 Predicating the outcome of swapping with two QDs devices

The efficient distribution of entanglement is deemed to be a key-enabling element in the next-generation of quantum technologies. The practical realization of such quantum networks is directly related to the properties of the underlying quantum light sources. Even though the semiconductor quantum dots have been demonstrated to be feasible for entanglement swapping scheme. Their scalable application is still lacking. In the second part of the thesis, the first comprehensive study on the practical requirements and limits of quantum networks based on semiconductor entangled photon sources is proposed. In contrast to existing literature, which mostly focuses on optimizing singular quantum dot properties, herein the thesis elucidate the discussion of full complexity of integrating practical solid-state devices in a scalable quantum network. In all current and proposed devices, the same challenges remain: several quantum dot properties will naturally be statistically distributed, leading to random parameter choices. By taking into account of the statistical effect of fabrication, a numerical simulation would provide a straightforward roadmap for the performance optimization of the devices.

7.1.3 Extraction of photons at telecom waveband

An efficient QDs based photon source emitting photons at telecom waveband is highly requested to be adapted into the real-world fiber-based infrastructures for quantum communication. However, the epitaxial QDs sources inherently suffer the low extraction efficiency of photons From the total internal reflection, which is caused by the high refractive index of the QDs embedded matrix. In the third part, the fabrication of a dielectric antenna structure consisting of a GaP solid immersion lens and a InGaAs/GaAs QDs nanomembrane is demonstrated in simulation and experiment. The device can broadly enhance the extraction efficiency up to 17% for the single photon emissions at telecom O-band range. With the advantage of the easier fabrication procedures comparing with other fabrication methods, i.e., photonic structures, one envision such a technique to be an essential step for the development of a high brightness QDs photon source at telecom band.

7.1.4 Efficient excitation of the source

Apart from the extraction of photons from the bulk substrate, the brightness of QDs sources are also limited by the excitation efficiency, which is commonly determined by the emission probability of photons at a certain resonantly excited state. ‘Blinking’, which describe the on/off emission of the QDs at studied transition state, is caused by the occupation of the QD by additional charge carriers induced by either by the impurities in the vicinity of the dot or surface state. In the last study of this thesis, the elimination of passive effects on excitation efficiency caused by the impurities in the grown sample and the defect states on the sample surface is investigated. Beside n-i-p charge tuning

technique, an additional weak gate laser on an entangled photon source under two photon excitation (TPE) give rise to the generation of charges carriers surrounding the QD. The redundant electrons and holes in the QD are neutralized, so that the QD can continuously emits photons at neutral transition states. Quantum dots grown close to the surface are prone to charge carrier fluctuations and trap states on the surface, degrading the brightness, coherence, and stability of the emission. Chemical surface passivation with sulfur compounds such as octadecanethiol has been performed on quantum dots near the surface. The reduction of the density and influence of surface states leads to the improvements in linewidth and photoluminescence intensity as well as a well-preserved single photon emission.

7.2 Outlook

In this thesis, we depict that the QDs are the promising candidates to be the next generation quantum light sources. To date, several breakthroughs of quantum information applications have been verified based on the epitaxial QDs [185, 210, 225, 285, 311, 312]. In the future, we envisioned the development and implementation of the sources as follows,

7.2.1 Optimization of the device performance

As we discuss in Chap. 3 and 4, the realization of quantum information applications necessitates high- efficiency and quality quantum light sources, i.e., brightness, single photon purity, indistinguishability, scalability and fidelity. Therefore, high- yield and quality solid-state quantum light sources should be reached with more efforts under advanced fabrication techniques.

7.2.2 On-chip integrated photonic circuits

Benefiting from the property of flexibility, the solid-state light sources own the intrinsic advantage in the real-world applications, comparing with atom/ion sources and SPDCs which requests either bulky instruments or lasers. Therefore, the development of integrated photonic circuits is promising for linear quantum computation technologies by use of the on-chip photonic waveguides. The key point of linear quantum computation is the cluster states of photons. It can be generated either from the internal states of the source with coherent interaction of dark excitons and biexcitons, or photonic interference between the photons in waveguides by BSMs.

7.2.3 Quantum communication in real-world

With the development of semiconductor quantum dots emitting photons at telecom waveband, the first demonstration of quantum communication is the quantum key distribution

by either fiber- or free-space channels. This technology can be reached in practice with the assistance of quantum repeater schemes, when the quality and efficiency of the source is satisfied. To construct a global quantum information transfer, quantum teleportation will enable a physically secure communication era.

Appendix

Temperature dependent emission wavelength and coherence time

In order to achieve spectral overlap of the biexciton (XX) photons emitted by quantum dots (QD)s in two independent devices, we adjust the temperature of the closed-cycle helium cryostats. However, an increase in temperature will also lead to a higher phonon population, thereby causing linewidth broadening. Theoretical models from the literature are used to fit the temperature-dependent emission wavelength and coherence times (Fig. 4.2(c) in the main text). The emission energy as a function of the temperature T is determined according to [313, 314]

$$E_g(T) = E_g(0) - S \langle \hbar\omega \rangle \left[\coth\left(\frac{\langle \hbar\omega \rangle}{2k_B T}\right) - 1 \right] \quad (7.2.1)$$

where $E_g(0)$ is the band gap energy at $T = 0$ K, S is the electron-phonon coupling constant, $\langle \hbar\omega \rangle$ is the average phonon energy and k_B is the Boltzmann constant. After performing least square regression, the following values are obtained: $E_g(0) = 1.58(7) \pm 0.77$ eV, $S = 0.4(8) \pm 0.18$, $\langle \hbar\omega \rangle = 5.8(1) \pm 0.59$ meV.

The coherence time T_2 has been measured by single-photon interference in a Michelson interferometer. The obtained first-order coherence function $g^{(1)}(\tau)$ of the X photon emission line has then been modelled by an exponential decay (corresponding to a Lorentzian line shape), which is modulated due to the remaining exciton fine structure S :

$$g^{(1)}(\tau) = \exp\left(-\frac{|\tau|}{\tau_c}\right) \sqrt{C_1^2 + C_2^2 + 2C_1 C_2 \cos\left(\frac{S}{\hbar} \tau\right)}, \quad (7.2.2)$$

with \hbar denoting the reduced Plank constant, τ the time difference of light traveling in the different interferometer arms and C_1 and C_2 (with $C_1 + C_2 = 1$) describing the intensity of the two respective Lorentzian lines that are split by S .

The data for the temperature dependence of the coherence time (T_2) is fitted with Equ. 7.2.3 in the usual regime of low temperature and low excitation power, where the line width broadening is mainly caused by the coupling with acoustic and optical phonons

[315].

$$\begin{aligned}
 T_2 &= \frac{2\hbar}{\Gamma(T)} \\
 &= \frac{2\hbar}{\Gamma_0 + aT + be^{-\frac{\Delta E}{k_B T}}}
 \end{aligned}
 \tag{7.2.3}$$

with \hbar being the reduced Plank constant, Γ_0 the line width at 0K, ΔE the activation energy and a denoting a coefficient related to the trapping/de-trapping process by emission/absorption of acoustic phonons. After least square regression, we extract the values of the parameters as $\Gamma_0 = 5.9(1) \pm 0.24 \mu\text{eV}$, $a = 0.5(5) \pm 0.03 \mu\text{eV/K}$, $\Delta E = 21.0(9) \pm 8.23 \text{meV}$. We find that the values extracted from the parameter estimation aligned well (in the order of magnitude) with the ones reported in the literature [313, 314, 315].

Blinking

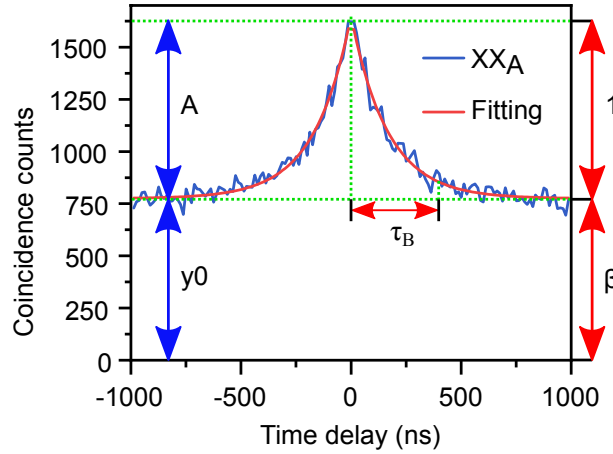


Fig. S1: Intensity autocorrelation measurement on the XX photons from the QD in device A, with a time bin size set to the repetition period of the laser (12.5 ns). The theoretical model (red line) is shown together with an illustration of the fit parameters. Reprinted figure from [207]. Copyright CC BY 4.0 [102], American Physics Society, without any changes made.

To get insight into the internal quantum efficiency of the QDs under a resonant two-photon pumping excitation scheme, we integrate the coincidence counts of each peak in the second-order autocorrelation measurement in Fig. 4.3(a) in the main text (the antibunching peak at zero time delay is neglected). The blue curve of the coincidence counts in Fig. S1 is fitted with the exponentially decaying function,

$$y = y_0 + A \cdot e^{-\frac{|t|}{\tau_B}}
 \tag{7.2.1}$$

$$A = y_0 \cdot \frac{1}{\beta} \quad (7.2.2)$$

where A , y_0 , τ_B , and β indicate the amplitude of the exponential decay, the baseline of the coincidence counts, the characteristic blinking timescale, and the ratio of the times that the QD is in an on and off state, respectively. $\tau_B = 166.2(2) \pm 5.13$ ns, $\beta = 0.8(8) \pm 0.02$ are extracted, implying the QD can emit a neutral XX photon stream in a characteristic blinking timescale of 313.2(6) ns [201].

Choice of parameters for the theoretical model of entanglement swapping

Fig. S2 shows the probability density distribution of FSS for QDs in device A (blue line). By using Gaussian modelling on the distribution (red line), we extract the expectation (μ_s) and standard deviation (σ_s) values as $11.0(9) \pm 0.26$ μeV and $6.5(2) \pm 0.30$ μeV , respectively.

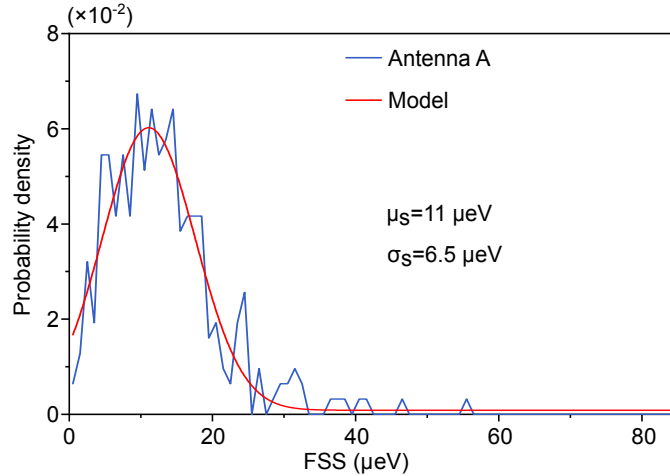


Fig. S2: Probability density distribution of FSSs property from antenna device A. Reprinted figure from [207]. Copyright CC BY 4.0 [102], American Physics Society, without any changes made.

The tuning range of the parameters used in our model has been implemented as Tab. S1 in the following. A higher entanglement swapping fidelity is achievable by means of implementations of isotropic strain-field, nanophotonic structures, and charge-tuning device techniques.

Tab. S1: Tunability of parameters for the prediction of the ideal entanglement swapping.

Parameters	value
Wavelength tuning range δ_λ (nm)	5 [145]
FSS tuning range δ_S (μeV)	10 [145]
Purcell factor of XX F_p	10 [168]
Increased dephasing time T_2^* (ns)	4 ± 0.8 [165]

Analytical calculation on the probability of tuning two independent devices into resonance

Assuming a normal distribution of parameters, the joint probability density of two independent devices can be written as:

$$\begin{aligned}
 p_{AB}(\lambda_A, \lambda_B) &= p_A(\lambda_A) \cdot p_B(\lambda_B) \\
 &= \frac{1}{2\pi \cdot \sigma_A \sigma_B} \cdot e^{-\frac{1}{2} \cdot \left[\frac{(\lambda_A - \mu_A)^2}{\sigma_A^2} + \frac{(\lambda_B - \mu_B)^2}{\sigma_B^2} \right]}
 \end{aligned} \tag{7.2.1}$$

Therefore, the probability of tuning two devices into resonance can be calculated within the area (G):

$$\begin{aligned}
 P_{AB}(\mu_A, \mu_B, \sigma_A, \sigma_B, \delta_\lambda) &= \iint_G p_{AB}(\lambda_A, \lambda_B) d\lambda_A d\lambda_B \\
 &= \frac{1}{2\pi \cdot \sigma_A \sigma_B} \cdot \iint_G e^{-\frac{1}{2} \cdot \left[\frac{(\lambda_A - \mu_A)^2}{\sigma_A^2} + \frac{(\lambda_B - \mu_B)^2}{\sigma_B^2} \right]} d\lambda_A d\lambda_B
 \end{aligned} \tag{7.2.2}$$

$$G = \left\{ \begin{array}{l} |\lambda_A - \lambda_B| \leq 2\delta_\lambda \\ \lambda_1 \leq \lambda_A \leq \lambda_2 \\ \lambda_1 \leq \lambda_B \leq \lambda_2 \end{array} \right\} \tag{7.2.3}$$

λ_1 and λ_2 are the wavelength range of searching for the suitable QDs, which are 773 nm and 785 nm in our analytical simulation. As an example, a wavelength tuning range of $\delta_\lambda = 1.5$ nm can be reached with a strain field [143], corresponding to the probability of 0.653.

Theoretical model for the probability density of entanglement swapping

As discussed in the main text, the performance of entanglement swapping is mainly determined by the two-photon interference (TPI) visibility of two independent sources and

the intrinsic entanglement fidelity of the photon pairs from each source. In case that the photons are perfectly overlapped in frequency temporally and spatially, the visibility of TPI is influenced by three components. The first are dephasing processes ($V_{\delta E}$) caused by e.g., charge noise due to the imperfections in the solid-state environment, resulting in inhomogeneous broadening of the emission.

$$\frac{1}{T_2} = \frac{1}{2T_1} + \frac{1}{T_2^*} = \frac{1}{2}\gamma_{T1} + \gamma^* \quad (7.2.1)$$

where γ_{T1} is the spontaneous decay rate, γ^* denotes the dephasing rate corresponding to dephasing time T_2^* . The second one is the time jitter in the XX-X cascade process (V_{casc}), stemming from the cascade emission in three-level quantum ladder systems [168]. First, we give an approximation on the effective dephasing rate base on the indistinguishability of an individual QD,

$$\gamma_{effect}^* = \frac{\gamma_{T1}(1-V)}{2V} \quad (7.2.2)$$

with indistinguishability $V = V_{\delta E}V_{casc}$, where $V_{\delta E}$ is the degraded indistinguishability caused by the energy jittering from charge noise, and V_{casc} is the limited indistinguishability due to the decay cascade for the generation of entangled photons [167]. Afterward, we can calculate the HOM interference of the two photo interference as follows [170],

$$M = \frac{\gamma_A \gamma_B}{\gamma_A + \gamma_B} \cdot \frac{\gamma_A + \gamma_B + \gamma_{A(effect)}^* + \gamma_{B(effect)}^*}{\Delta w^2 + [(\gamma_A + \gamma_B + \gamma_{A(effect)}^* + \gamma_{B(effect)}^*)/2]^2} \quad (7.2.3)$$

with the radiative rates γ_A , γ_B , effective pure dephasing rates $\gamma_{A(effect)}^*, \gamma_{B(effect)}^*$ from sources A, B and angular frequency mismatch Δw (zero in the numerical model Fig. 4.5(c), curves 2-6), respectively. Therefore, this explains the third component that influences the TPI visibility: If little dephasing is present, different radiative lifetimes (or rates) will also degrade the visibility. The density matrices of the initially emitted XX-X photon pairs from each of the two devices are calculated by each time drawing a random sample from the distributions given in Tab. 4.1. The time evolution of the density matrix is given by [121]:

$$\rho_{XX-X} = \frac{1}{2} \begin{pmatrix} 1 & 0 & 0 & \exp(-\frac{iSt}{\hbar}) \\ 0 & 0 & 0 & 0 \\ 0 & 0 & 0 & 0 \\ \exp(\frac{iSt}{\hbar}) & 0 & 0 & 1 \end{pmatrix} \quad (7.2.4)$$

where S is the fine structure splitting of the exciton, t is the time that the exciton evolves and \hbar is the reduced Plank constant. Since evaluating the time evolution of the exciton is not feasible in a swapping scheme (as discussed in the main text), the averaged density matrix has to be determined by multiplying the probability for t and then integrating

over it:

$$\rho_{XX-X,average} = \int_{t=0}^{t=\infty} dt \gamma e^{-\gamma t} \frac{1}{2} \begin{pmatrix} 1 & 0 & 0 & \exp(-\frac{iSt}{\hbar}) \\ 0 & 0 & 0 & 0 \\ 0 & 0 & 0 & 0 \\ \exp(\frac{iSt}{\hbar}) & 0 & 0 & 1 \end{pmatrix} \quad (7.2.5)$$

$$\rho_{XX-X,average} = \frac{1}{2} \begin{pmatrix} 1 & 0 & 0 & \frac{\gamma\hbar}{\gamma\hbar+iS} \\ 0 & 0 & 0 & 0 \\ 0 & 0 & 0 & 0 \\ \frac{\gamma\hbar}{\gamma\hbar-iS} & 0 & 0 & 1 \end{pmatrix} \quad (7.2.6)$$

In the case that polarization optics are applied in a Bell state measurement (BSM), the fidelity of the swapped two-photon state can be calculated as follows [185],

$$\rho_{swapped} = V \rho_{swapped,V=1} + (1 - V) \rho_{swapped,V=0} \quad (7.2.7)$$

V is the BSM success probability (equal to the TPI visibility discussed above), determined by the indistinguishability of photons from each QD in our simulation. The density matrix $\rho_{swapped}$ is calculated from the averaged density matrices $\rho_{XX-X,average}$ from the initial pairs from each device (according to [185]) and describes the state of swapped photon pairs considering indistinguishable ($V=1$) or distinguishable ($V=0$) photons at the BSM.

Probability of entanglement swapping

In addition to the discussion in the main paper regarding the probability of tuning two transitions into resonance, we also look at the dependence on other parameters (Fig. S3(a) and (b)). On one hand, more effective tunability on emission wavelength (δ_λ) for performance-defined devices yields higher resonance probability. On the other hand, the probability is higher with a decreased standard deviation ($\Delta\sigma_\lambda = \Delta\sigma_\lambda^{(B)} - \Delta\sigma_\lambda^{(A)}, \mu_\lambda^{(A)} \neq \mu_\lambda^{(B)}$ in our case), while a better overlap of the distribution generates higher resonance possibility ($\Delta\mu_\lambda \simeq 0$). Besides, the estimation of entanglement swapping fidelity as a function of various parameters ((c), (d), (e), (f)) is simulated based on Fig. 4.5(c) in the main text. Here, the expectation value for the swapping fidelity is encoded in the color. Devices with higher FSS tunability, lower expectation and standard deviation values in FSS and radiative X lifetime yield a higher fidelity of the initially emitted pairs, thereby improving the swapping fidelity (Fig. S3(c-d)). Meanwhile, better TPI between separate devices is obtained with lower XX lifetime (μ_{T_1}, σ_{T_1}) and longer XX dephasing time ($\mu_{T_2^*}, \sigma_{T_2^*}$), leading to higher photon coherence.

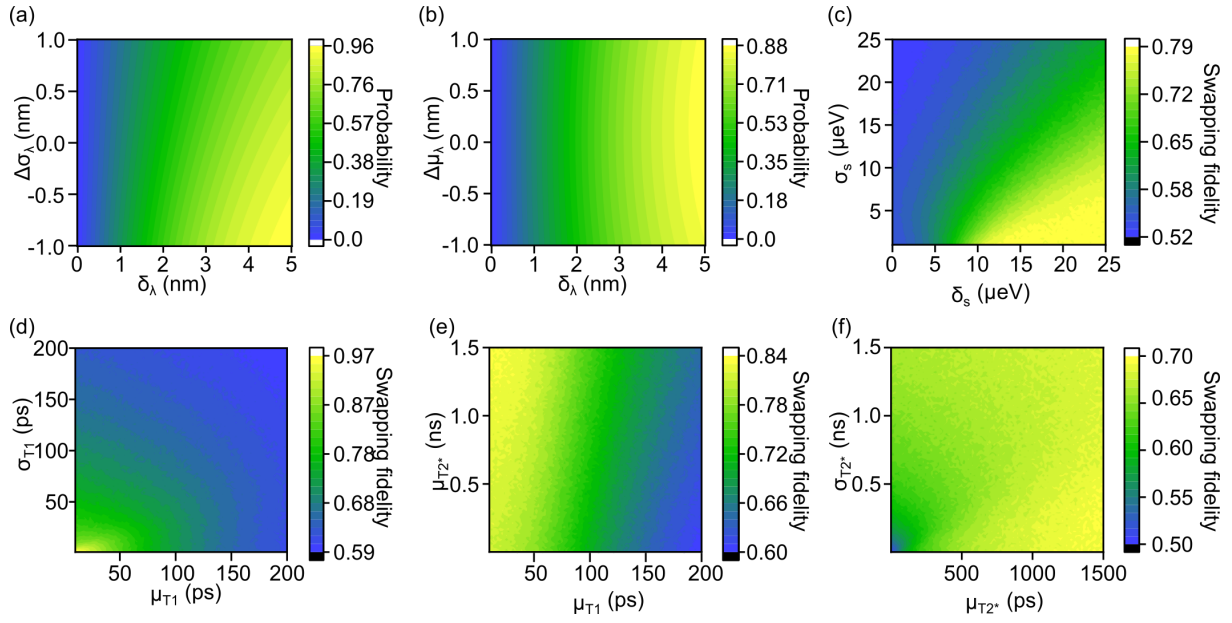


Fig. S3: (a-b) Probability of tuning two independent antenna devices into resonance and (c-f) expectation values of the entanglement swapping fidelity, as a function of different parameters. (a) and (b) show the probability of resonance tuning between two devices as a function of the wavelength tuning range (δ_λ) and difference of standard deviation (σ_λ) / expectation value (μ_λ), respectively. (c), (d), (e) and (f) show the expectation value of the entanglement swapping fidelity as a function of variables of interest, such as fine structure (FSS) tuning range (δ_s), standard deviation of FSSs in the device (σ_s), expectation and standard deviation of XX lifetimes (μ_{T1} and σ_{T1}), and expectation value and standard deviation of the dephasing time (σ_{T2^*} and μ_{T2^*}). Reprinted figures from [207]. Copyright CC BY 4.0 [102], American Physics Society, without any changes made.

This page intentionally left blank.

Bibliography

- [1] GILBERT N. LEWIS. The conservation of photons. *Nature*, 118(2981):874–875, dec 1926.
- [2] *Interference fringes with feeble light*, volume 15. Camb. Phil. Soc., 1909.
- [3] P Grangier, G Roger, and A Aspect. Experimental evidence for a photon anticorrelation effect on a beam splitter: A new light on single-photon interferences. *Europhys. Lett.*, 1(4):173–179, feb 1986.
- [4] R. HANBURY BROWN and R. Q. TWISS. Correlation between photons in two coherent beams of light. *Nature*, 177(4497):27–29, jan 1956.
- [5] Stuart J. Freedman and John F. Clauser. Experimental test of local hidden-variable theories. *Phys. Rev. Lett.*, 28(14):938–941, apr 1972.
- [6] Alain Aspect, Philippe Grangier, and Gérard Roger. Experimental tests of realistic local theories via bell's theorem. *Phys. Rev. Lett.*, 47(7):460–463, aug 1981.
- [7] Alain Aspect, Philippe Grangier, and Gérard Roger. Experimental realization of einstein-podolsky-rosen-BohmGedankenexperiment: A new violation of bell's inequalities. *Phys. Rev. Lett.*, 49(2):91–94, jul 1982.
- [8] Alain Aspect, Jean Dalibard, and Gérard Roger. Experimental test of bell's inequalities using time- varying analyzers. *Phys. Rev. Lett.*, 49(25):1804–1807, dec 1982.
- [9] A. Einstein, B. Podolsky, and N. Rosen. Can quantum-mechanical description of physical reality be considered complete? *Phys. Rev.*, 47(10):777–780, may 1935.
- [10] R.R. Schaller. Moore's law: past, present and future. *IEEE Spectrum*, 34(6):52–59, jun 1997.
- [11] Richard P. Feynman. Simulating physics with computers. *Int. J. Theoret. Phys.*, 21(6-7):467–488, jun 1982.
- [12] David Deutsch. Quantum theory, the church–turing principle and the universal quantum computer. *Proceedings of the Royal Society of London. A. Mathematical and Physical Sciences*, 400(1818):97–117, jul 1985.

- [13] Lov K. Grover. A fast quantum mechanical algorithm for database search. In *Proceedings of the twenty-eighth annual ACM symposium on Theory of computing - STOC '96*. ACM Press, 1996.
- [14] P.W. Shor. Algorithms for quantum computation: discrete logarithms and factoring. In *Proceedings 35th Annual Symposium on Foundations of Computer Science*. IEEE Comput. Soc. Press, 1994.
- [15] C. H. Bennett and G. Brassard. Quantum cryptography: Public key distribution and coin tossing. In *Proceedings of IEEE International Conference on Computers, Systems, and Signal Processing*, page 175, India, 1984.
- [16] Charles H. Bennett, Gilles Brassard, and N. David Mermin. Quantum cryptography without bell’s theorem. *Phys. Rev. Lett.*, 68(5):557–559, feb 1992.
- [17] Charles H. Bennett, Gilles Brassard, Claude Crépeau, Richard Jozsa, Asher Peres, and William K. Wootters. Teleporting an unknown quantum state via dual classical and einstein-podolsky-rosen channels. *Phys. Rev. Lett.*, 70(13):1895–1899, mar 1993.
- [18] Dik Bouwmeester, Jian-Wei Pan, Klaus Mattle, Manfred Eibl, Harald Weinfurter, and Anton Zeilinger. Experimental quantum teleportation. *Nature*, 390(6660):575–579, dec 1997.
- [19] David C. Burnham and Donald L. Weinberg. Observation of simultaneity in parametric production of optical photon pairs. *Phys. Rev. Lett.*, 25(2):84–87, jul 1970.
- [20] Ji-Gang Ren, Ping Xu, Hai-Lin Yong, Liang Zhang, Sheng-Kai Liao, Juan Yin, Wei-Yue Liu, Wen-Qi Cai, Meng Yang, Li Li, Kui-Xing Yang, Xuan Han, Yong-Qiang Yao, Ji Li, Hai-Yan Wu, Song Wan, Lei Liu, Ding-Quan Liu, Yao-Wu Kuang, Zhi-Ping He, Peng Shang, Cheng Guo, Ru-Hua Zheng, Kai Tian, Zhen-Cai Zhu, Nai-Le Liu, Chao-Yang Lu, Rong Shu, Yu-Ao Chen, Cheng-Zhi Peng, Jian-Yu Wang, and Jian-Wei Pan. Ground-to-satellite quantum teleportation. *Nature*, 549(7670):70–73, aug 2017.
- [21] Qi-Chao Sun, Ya-Li Mao, Yang-Fan Jiang, Qi Zhao, Si-Jing Chen, Wei Zhang, Wei-Jun Zhang, Xiao Jiang, Teng-Yun Chen, Li-Xing You, Li Li, Yi-Dong Huang, Xian-Feng Chen, Zhen Wang, Xiongfeng Ma, Qiang Zhang, and Jian-Wei Pan. Entanglement swapping with independent sources over an optical-fiber network. *Phys. Rev. A*, 95(3):032306, mar 2017.
- [22] Robert Raussendorf and Hans J. Briegel. A one-way quantum computer. *Phys. Rev. Lett.*, 86(22):5188–5191, may 2001.
- [23] Zhi Zhao, Yu-Ao Chen, An-Ning Zhang, Tao Yang, Hans J. Briegel, and Jian-Wei Pan. Experimental demonstration of five-photon entanglement and open-destination teleportation. *Nature*, 430(6995):54–58, jul 2004.

- [24] Han-Sen Zhong, Hui Wang, Yu-Hao Deng, Ming-Cheng Chen, Li-Chao Peng, Yi-Han Luo, Jian Qin, Dian Wu, Xing Ding, Yi Hu, Peng Hu, Xiao-Yan Yang, Wei-Jun Zhang, Hao Li, Yuxuan Li, Xiao Jiang, Lin Gan, Guangwen Yang, Lixing You, Zhen Wang, Li Li, Nai-Le Liu, Chao-Yang Lu, and Jian-Wei Pan. Quantum computational advantage using photons. *Science*, 370(6523):1460–1463, dec 2020.
- [25] Robert B. Griffiths. Hilbert space quantum mechanics, 2014.
- [26] J.B. Altepeter, E.R. Jeffrey, and P.G. Kwiat. Photonic state tomography. In *Advances In Atomic, Molecular, and Optical Physics*, pages 105–159. Elsevier, 2005.
- [27] Richard Jozsa. Fidelity for mixed quantum states. *J. Modern Opt.*, 41(12):2315–2323, dec 1994.
- [28] Nicholas A Peters. *One-and two-photon states for quantum information*. phdthesis, University of Illinois at Urbana-Champaign, 2006.
- [29] William K. Wootters. Entanglement of formation of an arbitrary state of two qubits. *Phys. Rev. Lett.*, 80(10):2245–2248, mar 1998.
- [30] Valerie Coffman, Joydip Kundu, and William K. Wootters. Distributed entanglement. *Phys. Rev. A*, 61(5):052306, apr 2000.
- [31] Michael A. Nielsen and Isaac L. Chuang. *Quantum Computation and Quantum Information*. Cambridge University Press, 2009.
- [32] John von Neumann, editor. *Mathematical Foundations of Quantum Mechanics*. Princeton University Press, feb 2018.
- [33] S. Bose and V. Vedral. Mixedness and teleportation. *Phys. Rev. A*, 61(4):040101, mar 2000.
- [34] G. Vidal and R. F. Werner. Computable measure of entanglement. *Phys. Rev. A*, 65(3):032314, feb 2002.
- [35] J. S. Bell. On the einstein podolsky rosen paradox. *Physics Physique Fizika*, 1(3):195–200, nov 1964.
- [36] J F Clauser and A Shimony. Bell's theorem. experimental tests and implications. *Reports On Progress in Physics*, 41(12):1881–1927, dec 1978.
- [37] J. Leach, R. E. Warburton, D. G. Ireland, F. Izdebski, S. M. Barnett, A. M. Yao, G. S. Buller, and M. J. Padgett. Quantum correlations in position, momentum, and intermediate bases for a full optical field of view. *Phys. Rev. A*, 85(1):013827, jan 2012.
- [38] L. K. Shalm, D. R. Hamel, Z. Yan, C. Simon, K. J. Resch, and T. Jennewein. Three-photon energy–time entanglement. *Nat. Phys.*, 9(1):19–22, nov 2012.

- [39] Alois Mair, Alipasha Vaziri, Gregor Weihs, and Anton Zeilinger. Entanglement of the orbital angular momentum states of photons. *Nature*, 412(6844):313–316, jul 2001.
- [40] Harishankar Jayakumar, Ana Predojević, Thomas Kauten, Tobias Huber, Glenn S. Solomon, and Gregor Weihs. Time-bin entangled photons from a quantum dot. *Nat. Commun.*, 5(1), jun 2014.
- [41] Menas Kafatos, editor. *Bell’s Theorem, Quantum Theory and Conceptions of the Universe*. Springer Netherlands, 1989.
- [42] G. Vernam. Cipher printing telegraph systems. *American Institute of Electrical Engineers*, XLV:109–115, 1926.
- [43] R. L. Rivest, A. Shamir, and L. Adleman. A method for obtaining digital signatures and public-key cryptosystems. *Commun ACM*, 21(2):120–126, feb 1978.
- [44] Nicolas Gisin, Grégoire Ribordy, Wolfgang Tittel, and Hugo Zbinden. Quantum cryptography. *Rev. Mod. Phys.*, 74(1):145–195, mar 2002.
- [45] Artur K. Ekert. Quantum cryptography based on bell’s theorem. *Phys. Rev. Lett.*, 67(6):661–663, aug 1991.
- [46] D. Bouwmeester and A. Zeilinger. The physics of quantum information: Basic concepts. In *The Physics of Quantum Information*, pages 1–14. Springer Berlin Heidelberg, 2000.
- [47] H.-J. Briegel, W. Dür, J. I. Cirac, and P. Zoller. Quantum repeaters: The role of imperfect local operations in quantum communication. *Phys. Rev. Lett.*, 81(26):5932–5935, dec 1998.
- [48] M. Żukowski, A. Zeilinger, M. A. Horne, and A. K. Ekert. “event-ready-detectors” bell experiment via entanglement swapping. *Phys. Rev. Lett.*, 71(26):4287–4290, dec 1993.
- [49] Jian-Wei Pan, Dik Bouwmeester, Harald Weinfurter, and Anton Zeilinger. Experimental entanglement swapping: Entangling photons that never interacted. *Phys. Rev. Lett.*, 80(18):3891–3894, may 1998.
- [50] Charles H. Bennett, Gilles Brassard, Sandu Popescu, Benjamin Schumacher, John A. Smolin, and William K. Wootters. Purification of noisy entanglement and faithful teleportation via noisy channels. *Phys. Rev. Lett.*, 76(5):722–725, jan 1996.
- [51] David Deutsch, Artur Ekert, Richard Jozsa, Chiara Macchiavello, Sandu Popescu, and Anna Sanpera. Quantum privacy amplification and the security of quantum cryptography over noisy channels. *Phys. Rev. Lett.*, 77(13):2818–2821, sep 1996.
- [52] Jian-Wei Pan, Christoph Simon, Āaslav Brukner, and Anton Zeilinger. Entanglement purification for quantum communication. *Nature*, 410(6832):1067–1070, apr 2001.

- [53] Jian-Wei Pan, Sara Gasparoni, Rupert Ursin, Gregor Weihs, and Anton Zeilinger. Experimental entanglement purification of arbitrary unknown states. *Nature*, 423(6938):417–422, may 2003.
- [54] Alexander I. Lvovsky, Barry C. Sanders, and Wolfgang Tittel. Optical quantum memory. *Nat. Photonics*, 3(12):706–714, dec 2009.
- [55] C. Simon, M. Afzelius, J. Appel, A. Boyer de la Giroday, S. J. Dewhurst, N. Gisin, C. Y. Hu, F. Jelezko, S. Kröll, J. H. Müller, J. Nunn, E. S. Polzik, J. G. Rarity, H. De Riedmatten, W. Rosenfeld, A. J. Shields, N. Sköld, R. M. Stevenson, R. Thew, I. A. Walmsley, M. C. Weber, H. Weinfurter, J. Wrachtrup, and R. J. Young. Quantum memories. *Eur. Phys. J. D*, 58(1):1–22, apr 2010.
- [56] W. Tittel, M. Afzelius, T. Chanelière, R.L. Cone, S. Kröll, S.A. Moiseev, and M. Sellars. Photon-echo quantum memory in solid state systems. *Laser & Photonics Reviews*, 4(2):244–267, may 2009.
- [57] Félix Bussi eres, Nicolas Sangouard, Mikael Afzelius, Hugues de Riedmatten, Christoph Simon, and Wolfgang Tittel. Prospective applications of optical quantum memories. *J. Modern Opt.*, 60(18):1519–1537, oct 2013.
- [58] C.W. Thiel, Thomas Böttger, and R.L. Cone. Rare-earth-doped materials for applications in quantum information storage and signal processing. *J. Lumin.*, 131(3):353–361, mar 2011.
- [59] M. V. Gurudev Dutt, L. Childress, L. Jiang, E. Togan, J. Maze, F. Jelezko, A. S. Zibrov, P. R. Hemmer, and M. D. Lukin. Quantum register based on individual electronic and nuclear spin qubits in diamond. *Science*, 316(5829):1312–1316, jun 2007.
- [60] Torsten Gaebel, Michael Domhan, Iulian Popa, Christoffer Wittmann, Philipp Neumann, Fedor Jelezko, James R. Rabeau, Nikolas Stavrias, Andrew D. Greentree, Steven Prawer, Jan Meijer, Jason Twamley, Philip R. Hemmer, and Jörg Wrachtrup. Room-temperature coherent coupling of single spins in diamond. *Nat. Phys.*, 2(6):408–413, may 2006.
- [61] K. C. Lee, B. J. Sussman, M. R. Sprague, P. Michelberger, K. F. Reim, J. Nunn, N. K. Langford, P. J. Bustard, D. Jaksch, and I. A. Walmsley. Macroscopic non-classical states and terahertz quantum processing in room-temperature diamond. *Nat. Photonics*, 6(1):41–44, dec 2011.
- [62] D. F. Phillips, A. Fleischhauer, A. Mair, R. L. Walsworth, and M. D. Lukin. Storage of light in atomic vapor. *Phys. Rev. Lett.*, 86(5):783–786, jan 2001.
- [63] M Hosseini, B M Sparkes, G T Campbell, P K Lam, and B C Buchler. Storage and manipulation of light using a raman gradient-echo process. *J. Phys. B: At. Mol. Opt. Phys.*, 45(12):124004, jun 2012.

- [64] D. G. England, P. J. Bustard, D. J. Moffatt, J. Nunn, R. Lausten, and B. J. Sussman. Efficient raman generation in a waveguide: A route to ultrafast quantum random number generation. *Appl. Phys. Lett.*, 104(5):051117, feb 2014.
- [65] Philip J. Bustard, Rune Lausten, Duncan G. England, and Benjamin J. Sussman. Toward quantum processing in molecules: A THz-bandwidth coherent memory for light. *Phys. Rev. Lett.*, 111(8):083901, aug 2013.
- [66] Luo-Kan Chen, Hai-Lin Yong, Ping Xu, Xing-Can Yao, Tong Xiang, Zheng-Da Li, Chang Liu, He Lu, Nai-Le Liu, Li Li, Tao Yang, Cheng-Zhi Peng, Bo Zhao, Yu-Ao Chen, and Jian-Wei Pan. Experimental nested purification for a linear optical quantum repeater. *Nat. Photonics*, 11(11):695–699, oct 2017.
- [67] Koji Azuma, Kiyoshi Tamaki, and Hoi-Kwong Lo. All-photonic quantum repeaters. *Nat. Commun.*, 6(1), apr 2015.
- [68] Zheng-Da Li, Rui Zhang, Xu-Fei Yin, Li-Zheng Liu, Yi Hu, Yu-Qiang Fang, Yue-Yang Fei, Xiao Jiang, Jun Zhang, Li Li, Nai-Le Liu, Feihu Xu, Yu-Ao Chen, and Jian-Wei Pan. Experimental quantum repeater without quantum memory. *Nat. Photonics*, 13(9):644–648, jun 2019.
- [69] Rodney Loudon. *The Quantum Theory of Light*. OUP Oxford, September 2000.
- [70] Emil Wolf Leonard Mandel. *Optical Coherence and Quantum Optics*. Cambridge University Press, October 1995.
- [71] Roy J. Glauber. Photon correlations. *Phys. Rev. Lett.*, 10(3):84–86, feb 1963.
- [72] X. T. Zou and L. Mandel. Photon-antibunching and sub-poissonian photon statistics. *Phys. Rev. A*, 41(1):475–476, jan 1990.
- [73] J.G. Rarity, P.C.M. Owens, and P.R. Tapster. Quantum random-number generation and key sharing. *J. Modern Opt.*, 41(12):2435–2444, dec 1994.
- [74] Jeremy L. O'Brien, Akira Furusawa, and Jelena Vučković. Photonic quantum technologies. *Nat. Photonics*, 3(12):687–695, dec 2009.
- [75] Peter Lodahl, Sahand Mahmoodian, and Søren Stobbe. Interfacing single photons and single quantum dots with photonic nanostructures. *Rev. Mod. Phys.*, 87(2):347–400, may 2015.
- [76] A. Femijs Koenderink, Andrea Alù, and Albert Polman. Nanophotonics: Shrinking light-based technology. *Science*, 348(6234):516–521, may 2015.
- [77] Igor Aharonovich, Dirk Englund, and Milos Toth. Solid-state single-photon emitters. *Nat. Photonics*, 10(10):631–641, sep 2016.

- [78] H. J. Kimble, M. Dagenais, and L. Mandel. Photon antibunching in resonance fluorescence. *Phys. Rev. Lett.*, 39(11):691–695, sep 1977.
- [79] Axel Kuhn, Markus Hennrich, and Gerhard Rempe. Deterministic single-photon source for distributed quantum networking. *Phys. Rev. Lett.*, 89(6):067901, jul 2002.
- [80] C. K. Hong and L. Mandel. Experimental realization of a localized one-photon state. *Phys. Rev. Lett.*, 56(1):58–60, jan 1986.
- [81] Jian-Wei Pan, Zeng-Bing Chen, Chao-Yang Lu, Harald Weinfurter, Anton Zeilinger, and Marek Żukowski. Multiphoton entanglement and interferometry. *Rev. Mod. Phys.*, 84(2):777–838, may 2012.
- [82] V. Scarani, H. de Riedmatten, I. Marcikic, H. Zbinden, and N. Gisin. Four-photon correction in two-photon bell experiments. *Eur. Phys. J. D*, 32(1):129–138, nov 2004.
- [83] Igor Aharonovich and Elke Neu. Diamond nanophotonics. *Adv. Opt. Mater.*, 2(10):911–928, jul 2014.
- [84] L.J. Rogers, K.D. Jahnke, T. Teraji, L. Marseglia, C. Müller, B. Naydenov, H. Schauffert, C. Kranz, J. Isoya, L.P. McGuinness, and F. Jelezko. Multiple intrinsically identical single-photon emitters in the solid state. *Nat. Commun.*, 5(1), aug 2014.
- [85] S. Castelletto, B. C. Johnson, V. Ivády, N. Stavrias, T. Umeda, A. Gali, and T. Ohshima. A silicon carbide room-temperature single-photon source. *Nat. Mater.*, 13(2):151–156, nov 2013.
- [86] T. Umeda, N. T. Son, J. Isoya, E. Janzén, T. Ohshima, N. Morishita, H. Itoh, A. Gali, and M. Bockstedte. Identification of the carbon antisite-vacancy pair in 4h-SiC. *Phys. Rev. Lett.*, 96(14):145501, apr 2006.
- [87] R. Kolesov, K. Xia, R. Reuter, R. Stöhr, A. Zappe, J. Meijer, P.R. Hemmer, and J. Wrachtrup. Optical detection of a single rare-earth ion in a crystal. *Nat. Commun.*, 3(1), jan 2012.
- [88] Kangwei Xia, Roman Kolesov, Ya Wang, Petr Siyushev, Rolf Reuter, Thomas Kornher, Nadezhda Kukharchyk, Andreas D. Wieck, Bruno Villa, Sen Yang, and Jörg Wrachtrup. All-optical preparation of coherent dark states of a single rare earth ion spin in a crystal. *Phys. Rev. Lett.*, 115(9):093602, aug 2015.
- [89] Anthony J. Morfa, Brant C. Gibson, Matthias Karg, Timothy J. Karle, Andrew D. Greetree, Paul Mulvaney, and Snjezana Tomljenovic-Hanic. Single-photon emission and quantum characterization of zinc oxide defects. *Nano Lett.*, 12(2):949–954, jan 2012.
- [90] Nicholas R. Jungwirth, Hung-Shen Chang, Mingde Jiang, and Gregory D. Fuchs. Polarization spectroscopy of defect-based single photon sources in ZnO. *ACS Nano*, 10(1):1210–1215, dec 2015.

- [91] Constantin Dory, Kevin A. Fischer, Kai Müller, Konstantinos G. Lagoudakis, Tomas Sarmiento, Armand Rundquist, Jingyuan L. Zhang, Yousif Kelaita, and Jelena Vučković. Complete coherent control of a quantum dot strongly coupled to a nanocavity. *Sci. Rep.*, 6(1), apr 2016.
- [92] Shuo Sun, Hyeochul Kim, Glenn S. Solomon, and Edo Waks. A quantum phase switch between a single solid-state spin and a photon. *Nat. Nanotechnol.*, 11(6):539–544, feb 2016.
- [93] Mark J. Holmes, Kihyun Choi, Satoshi Kako, Munetaka Arita, and Yasuhiko Arakawa. Room-temperature triggered single photon emission from a III-nitride site-controlled nanowire quantum dot. *Nano Lett.*, 14(2):982–986, jan 2014.
- [94] Saniya Deshpande, Ayan Das, and Pallab Bhattacharya. Blue single photon emission up to 200 k from an InGaN quantum dot in AlGaIn nanowire. *Appl. Phys. Lett.*, 102(16):161114, apr 2013.
- [95] Yu-Ming He, Genevieve Clark, John R. Schaibley, Yu He, Ming-Cheng Chen, Yu-Jia Wei, Xing Ding, Qiang Zhang, Wang Yao, Xiaodong Xu, Chao-Yang Lu, and Jian-Wei Pan. Single quantum emitters in monolayer semiconductors. *Nat. Nanotechnol.*, 10(6):497–502, may 2015.
- [96] Ajit Srivastava, Meinrad Sidler, Adrien V. Allain, Dominik S. Lembke, Andras Kis, and A. Imamoglu. Optically active quantum dots in monolayer WSe₂. *Nat. Nanotechnol.*, 10(6):491–496, may 2015.
- [97] Toan Trong Tran, Kerem Bray, Michael J. Ford, Milos Toth, and Igor Aharonovich. Quantum emission from hexagonal boron nitride monolayers. *Nat. Nanotechnol.*, 11(1):37–41, oct 2015.
- [98] Alexander Högele, Christophe Galland, Martin Winger, and Atac Imamoglu. Photon antibunching in the photoluminescence spectra of a single carbon nanotube. *Phys. Rev. Lett.*, 100(21):217401, may 2008.
- [99] Xuedan Ma, Nicolai F. Hartmann, Jon K. S. Baldwin, Stephen K. Doorn, and Han Htoon. Room-temperature single-photon generation from solitary dopants of carbon nanotubes. *Nat. Nanotechnol.*, 10(8):671–675, jul 2015.
- [100] A. Jeantet, Y. Chassagneux, C. Raynaud, Ph. Roussignol, J. S. Lauret, B. Besga, J. Estève, J. Reichel, and C. Voisin. Widely tunable single-photon source from a carbon nanotube in the purcell regime. *Phys. Rev. Lett.*, 116(24):247402, jun 2016.
- [101] Paul G. Kwiat, Klaus Mattle, Harald Weinfurter, Anton Zeilinger, Alexander V. Sergienko, and Yanhua Shih. New high-intensity source of polarization-entangled photon pairs. *Phys. Rev. Lett.*, 75(24):4337–4341, dec 1995.

- [102] Creative commons attribution 4.0 international license.
- [103] Creative commons attribution sharealike 3.0 unported license.
- [104] L. E. Brus. Electron–electron and electron-hole interactions in small semiconductor crystallites: The size dependence of the lowest excited electronic state. *J. Chem. Phys.*, 80(9):4403–4409, may 1984.
- [105] T. Jesper Jacobsson and Tomas Edvinsson. Absorption and fluorescence spectroscopy of growing ZnO quantum dots: Size and band gap correlation and evidence of mobile trap states. *Inorg. Chem.*, 50(19):9578–9586, aug 2011.
- [106] T. Jesper Jacobsson and Tomas Edvinsson. Photoelectrochemical determination of the absolute band edge positions as a function of particle size for ZnO quantum dots. *The Journal of Physical Chemistry C*, 116(29):15692–15701, jul 2012.
- [107] Davies J. H. Davies. *The Physics of Low-Dimensional Semiconductors*. Cambridge University Press, April 2009.
- [108] T. Edvinsson. Optical quantum confinement and photocatalytic properties in two-, one- and zero-dimensional nanostructures. *R Soc Open Sci*, 5(9):180387, sep 2018.
- [109] N. Somaschi, V. Giesz, L. De Santis, J. C. Loredó, M. P. Almeida, G. Hornecker, S. L. Portalupi, T. Grange, C. Antón, J. Demory, C. Gómez, I. Sagnes, N. D. Lanzillotti-Kimura, A. Lemaître, A. Auffeves, A. G. White, L. Lanco, and P. Senellart. Near-optimal single-photon sources in the solid state. *Nat. Photonics*, 10(5):340–345, mar 2016.
- [110] Daniel Huber, Marcus Reindl, Saimon Filipe Covre da Silva, Christian Schimpf, Javier Martín-Sánchez, Huiying Huang, Giovanni Piredda, Johannes Edlinger, Armando Rastelli, and Rinaldo Trotta. Strain-tunable GaAs quantum dot: A nearly dephasing-free source of entangled photon pairs on demand. *Phys. Rev. Lett.*, 121(3):033902, jul 2018.
- [111] M. Körber, O. Morin, S. Langenfeld, A. Neuzner, S. Ritter, and G. Rempe. Decoherence-protected memory for a single-photon qubit. *Nat. Photonics*, 12(1):18–21, dec 2017.
- [112] M. H. Abobeih, J. Cramer, M. A. Bakker, N. Kalb, M. Markham, D. J. Twitchen, and T. H. Taminiau. One-second coherence for a single electron spin coupled to a multi-qubit nuclear-spin environment. *Nat. Commun.*, 9(1), jun 2018.
- [113] Oliver Benson, Charles Santori, Matthew Pelton, and Yoshihisa Yamamoto. Regulated and entangled photons from a single quantum dot. *Phys. Rev. Lett.*, 84(11):2513–2516, mar 2000.
- [114] R. M. Stevenson, R. J. Young, P. Atkinson, K. Cooper, D. A. Ritchie, and A. J. Shields. A semiconductor source of triggered entangled photon pairs. *Nature*, 439(7073):179–182, jan 2006.

- [115] Peter Michler, editor. *Single Semiconductor Quantum Dots*. Springer Berlin Heidelberg, October 2009.
- [116] R. Mark Stevenson, Andrew J. Hudson, Anthony J. Bennett, Robert J. Young, Christine A. Nicoll, David A. Ritchie, and Andrew J. Shields. Evolution of entanglement between distinguishable light states. *Phys. Rev. Lett.*, 101(17):170501, oct 2008.
- [117] A. Fognini, A. Ahmadi, S. J. Daley, M. E. Reimer, and V. Zwiller. Universal fine-structure eraser for quantum dots. *Opt. Express*, 26(19):24487, sep 2018.
- [118] E. Poem, Y. Kodriano, C. Tradonsky, N. H. Lindner, B. D. Gerardot, P. M. Petroff, and D. Gershoni. Accessing the dark exciton with light. *Nat. Phys.*, 6(12):993–997, nov 2010.
- [119] Charles Santori, David Fattal, Matthew Pelton, Glenn S. Solomon, and Yoshihisa Yamamoto. Polarization-correlated photon pairs from a single quantum dot. *Phys. Rev. B*, 66(4):045308, jul 2002.
- [120] Jiaxiang Zhang, Johannes S. Wildmann, Fei Ding, Rinaldo Trotta, Yongheng Huo, Eugenio Zallo, Daniel Huber, Armando Rastelli, and Oliver G. Schmidt. High yield and ultrafast sources of electrically triggered entangled-photon pairs based on strain-tunable quantum dots. *Nat. Commun.*, 6(1), dec 2015.
- [121] R. Winik, D. Cogan, Y. Don, I. Schwartz, L. Gantz, E. R. Schmidgall, N. Livneh, R. Rapaport, E. Buks, and D. Gershoni. On-demand source of maximally entangled photon pairs using the biexciton-exciton radiative cascade. *Phys. Rev. B*, 95(23):235435, jun 2017.
- [122] Charles Santori, David Fattal, Jelena Vučković, Glenn S. Solomon, Edo Waks, and Yoshihisa Yamamoto. Submicrosecond correlations in photoluminescence from InAs quantum dots. *Phys. Rev. B*, 69(20):205324, may 2004.
- [123] Tobias Huber, Ana Predojević, Glenn S. Solomon, and Gregor Weihs. Effects of photo-neutralization on the emission properties of quantum dots. *Opt. Express*, 24(19):21794, sep 2016.
- [124] H. S. Nguyen, G. Sallen, C. Voisin, Ph. Roussignol, C. Diederichs, and G. Cassabois. Optically gated resonant emission of single quantum dots. *Phys. Rev. Lett.*, 108(5):057401, jan 2012.
- [125] Hai Son Nguyen, Gregory Sallen, Marco Abbarchi, Robson Ferreira, Christophe Voisin, Philippe Roussignol, Guillaume Cassabois, and Carole Diederichs. Photoneutralization and slow capture of carriers in quantum dots probed by resonant excitation spectroscopy. *Phys. Rev. B*, 87(11):115305, mar 2013.
- [126] Hai-Son Nguyen. *Contrôle optique de l'émission résonnante de boîtes quantiques semiconductrices*. Theses, Université Pierre et Marie Curie - Paris VI, December 2011.

- [127] A. Y. Cho and I. Hayashi. P-n junction formation during molecular-beam epitaxy of ge-doped GaAs. *J. Appl. Phys.*, 42(11):4422–4425, oct 1971.
- [128] Robert Keil, Michael Zopf, Yan Chen, Bianca Höfer, Jiaxiang Zhang, Fei Ding, and Oliver G. Schmidt. Solid-state ensemble of highly entangled photon sources at rubidium atomic transitions. *Nat. Commun.*, 8(1), may 2017.
- [129] Debasis Bera, Lei Qian, Teng-Kuan Tseng, and Paul H. Holloway. Quantum dots and their multimodal applications: A review. *Materials*, 3(4):2260–2345, mar 2010.
- [130] Yong Ma, Peter E. Kremer, and Brian D. Gerardot. Efficient photon extraction from a quantum dot in a broad-band planar cavity antenna. *J. Appl. Phys.*, 115(2):023106, jan 2014.
- [131] Peter Michler, editor. *Quantum Dots for Quantum Information Technologies*. Springer International Publishing, 2017.
- [132] S. Bogdanov, M. Y. Shalaginov, A. Boltasseva, and V. M. Shalaev. Material platforms for integrated quantum photonics. *Opt. Mater. Express*, 7(1):111, dec 2016.
- [133] Robert W. Boyd. *Quantum photonics : pioneering advances and emerging applications*, volume 217 of *Springer series in optical sciences*. Cham, Switzerland : Springer, 2 2019.
- [134] A. Rastelli, A. Ulhaq, S. Kiravittaya, L. Wang, A. Zrenner, and O. G. Schmidt. In situ laser microprocessing of single self-assembled quantum dots and optical microcavities. *Appl. Phys. Lett.*, 90(7):073120, feb 2007.
- [135] Mohamed Benyoucef, Hong Seok Lee, Juliane Gabel, Tae Whan Kim, Hong Lee Park, Armando Rastelli, and Oliver G. Schmidt. Wavelength tunable triggered single-photon source from a single CdTe quantum dot on silicon substrate. *Nano Lett.*, 9(1):304–307, jan 2009.
- [136] F. Findeis, M. Baier, E. Beham, A. Zrenner, and G. Abstreiter. Photocurrent and photoluminescence of a single self-assembled quantum dot in electric fields. *Appl. Phys. Lett.*, 78(19):2958–2960, may 2001.
- [137] M. Bayer, G. Ortner, O. Stern, A. Kuther, A. A. Gorbunov, A. Forchel, P. Hawrylak, S. Fafard, K. Hinzer, T. L. Reinecke, S. N. Walck, J. P. Reithmaier, F. Klopff, and F. Schäfer. Fine structure of neutral and charged excitons in self-assembled in(ga)as/(al)GaAs quantum dots. *Phys. Rev. B*, 65(19):195315, may 2002.
- [138] Yan Chen, Michael Zopf, Robert Keil, Fei Ding, and Oliver G. Schmidt. Highly-efficient extraction of entangled photons from quantum dots using a broadband optical antenna. *Nat. Commun.*, 9(1), jul 2018.

- [139] F. Ding, R. Singh, J. D. Plumhof, T. Zander, V. Křápek, Y. H. Chen, M. Benyoucef, V. Zwiller, K. Dörr, G. Bester, A. Rastelli, and O. G. Schmidt. Tuning the exciton binding energies in single self-Assembled InGaAs/GaAs Quantum dots by piezoelectric-induced biaxial stress. *Phys. Rev. Lett.*, 104(6):067405, feb 2010.
- [140] Jiaxiang Zhang, Fei Ding, Eugenio Zallo, Rinaldo Trotta, Bianca Höfer, Luyang Han, Santosh Kumar, Yongheng Huo, Armando Rastelli, and Oliver G. Schmidt. A nanomembrane-based wavelength-tunable high-speed single-photon-emitting diode. *Nano Lett.*, 13(12):5808–5813, nov 2013.
- [141] Jiaxiang Zhang, Yongheng Huo, Armando Rastelli, Michael Zopf, Bianca Höfer, Yan Chen, Fei Ding, and Oliver G. Schmidt. Single photons on-demand from light-hole excitons in strain-engineered quantum dots. *Nano Lett.*, 15(1):422–427, dec 2014.
- [142] Yan Chen, Iman Esmaeil Zadeh, Klaus D. Jöns, Andreas Fognini, Michael E. Reimer, Jiaxiang Zhang, Dan Dalacu, Philip J. Poole, Fei Ding, Val Zwiller, and Oliver G. Schmidt. Controlling the exciton energy of a nanowire quantum dot by strain fields. *Appl. Phys. Lett.*, 108(18):182103, may 2016.
- [143] Yan Chen, Jiaxiang Zhang, Michael Zopf, Kyubong Jung, Yang Zhang, Robert Keil, Fei Ding, and Oliver G. Schmidt. Wavelength-tunable entangled photons from silicon-integrated III–v quantum dots. *Nat. Commun.*, 7(1), jan 2016.
- [144] Rinaldo Trotta, Javier Martín-Sánchez, Johannes S. Wildmann, Giovanni Piredda, Marcus Reindl, Christian Schimpf, Eugenio Zallo, Sandra Stroj, Johannes Edlinger, and Armando Rastelli. Wavelength-tunable sources of entangled photons interfaced with atomic vapours. *Nat. Commun.*, 7(1), jan 2016.
- [145] Jiaxiang Zhang, Eugenio Zallo, Bianca Höfer, Yan Chen, Robert Keil, Michael Zopf, Stefan Böttner, Fei Ding, and Oliver G. Schmidt. Electric-field-induced energy tuning of on-demand entangled-photon emission from self-assembled quantum dots. *Nano Lett.*, 17(1):501–507, dec 2016.
- [146] Michael Zopf, Tobias Macha, Robert Keil, Eduardo Uruñuela, Yan Chen, Wolfgang Alt, Lothar Ratschbacher, Fei Ding, Dieter Meschede, and Oliver G. Schmidt. Frequency feedback for two-photon interference from separate quantum dots. *Phys. Rev. B*, 98(16):161302, oct 2018.
- [147] Shun Lien Chuang. *Physics of Photonic Devices*. Wiley Publishing, 2 edition, 2009.
- [148] G. E. PIKUS. Effect of deformation on the hole energy spectrum of germanium and silicon. *Soviet Physics-Solid state*, 1:1502, 1960.
- [149] Grigorii Ezechielevich Pikus Gennadii Levikovich Bir. *Symmetry and Strain-induced Effects in Semiconductors*. Wiley, 1974.

- [150] S. Seidl, A. Högele, M. Kroner, K. Karrai, A. Badolato, P.M. Petroff, and R.J. Warburton. Tuning the cross-gap transition energy of a quantum dot by uniaxial stress. *Phys. E: Low-Dimens. Syst. Nanostructures*, 32(1-2):14–16, may 2006.
- [151] Garnett W. Bryant, M. Zieliński, Natalia Malkova, James Sims, W. Jaskólski, and Javier Aizpurua. Effect of mechanical strain on the optical properties of quantum dots: Controlling exciton shape, orientation, and phase with a mechanical strain. *Phys. Rev. Lett.*, 105(6):067404, aug 2010.
- [152] APE Angewandte Physik and Elektronik GmbH. Pulse slicer.
- [153] A. M. Weiner. Femtosecond pulse shaping using spatial light modulators. *Rev. Sci. Instrum.*, 71(5):1929–1960, may 2000.
- [154] Bahaa Saleh. *Fundamentals of photonics*. Wiley-Interscience, Hoboken, N.J, 2007.
- [155] George Greenstein. *The quantum challenge : modern research on the foundations of quantum mechanics*. Jones and Bartlett Publishers, Sudbury, Mass, 2006.
- [156] Donald L. Horrocks. Method for determining random coincidence count rate in a scintillation counter utilizing the coincidence technique, January 1978.
- [157] D. Pengra. *Counting statistics of random events: A tutorial*, April 2008.
- [158] Mark Fox. *Quantum Optics*. Oxford University Press, April 2006.
- [159] Desmond Connor. *Time-correlated single photon counting*. Academic Press, London Orlando, December 1984.
- [160] Daniel F. V. James, Paul G. Kwiat, William J. Munro, and Andrew G. White. Measurement of qubits. *Phys. Rev. A*, 64(5):052312, oct 2001.
- [161] Ujaan Purakayastha. Guide to quantum state tomography.
- [162] Caspar Hopfmann, Weijie Nie, Nand Lal Sharma, Carmen Weigelt, Fei Ding, and Oliver G. Schmidt. Maximally entangled and gigahertz-clocked on-demand photon pair source. *Phys. Rev. B*, 103(7):075413, feb 2021.
- [163] Christian Schimpf, Marcus Reindl, Daniel Huber, Barbara Lehner, Saimon F Covre Da Silva, Santanu Manna, Michal Vyblecka, Philip Walther, and Armando Rastelli. Quantum cryptography with highly entangled photons from semiconductor quantum dots. *Science advances*, 7(16):eabe8905, 2021.
- [164] C. K. Hong, Z. Y. Ou, and L. Mandel. Measurement of subpicosecond time intervals between two photons by interference. *Phys. Rev. Lett.*, 59(18):2044–2046, nov 1987.
- [165] Liang Zhai, Giang N. Nguyen, Clemens Spinnler, Julian Ritzmann, Matthias C. Löbl, Andreas D. Wieck, Arne Ludwig, Alisa Javadi, and Richard J. Warburton. Quantum interference of identical photons from remote quantum dots, 2021.

- [166] Tobias Huber, Ana Predojević, Hashem Zoubi, Harishankar Jayakumar, Glenn S. Solomon, and Gregor Weihs. Measurement and modification of biexciton-exciton time correlations. *Opt. Express*, 21(8):9890, apr 2013.
- [167] Christian Schimpf, Marcus Reindl, Francesco Basso Basset, Klaus D. Jöns, Rinaldo Trotta, and Armando Rastelli. Quantum dots as potential sources of strongly entangled photons: Perspectives and challenges for applications in quantum networks. *Appl. Phys. Lett.*, 118(10):100502, mar 2021.
- [168] Eva Schöll, Lucas Schweickert, Lukas Hanschke, Katharina D. Zeuner, Friedrich Sbresny, Thomas Lettner, Rahul Trivedi, Marcus Reindl, Saimon Filipe Covre da Silva, Rinaldo Trotta, Jonathan J. Finley, Jelena Vučković, Kai Müller, Armando Rastelli, Val Zwiller, and Klaus D. Jöns. Crux of using the cascaded emission of a three-level quantum ladder system to generate indistinguishable photons. *Phys. Rev. Lett.*, 125(23):233605, dec 2020.
- [169] Pascale Senellart, Glenn Solomon, and Andrew White. High-performance semiconductor quantum-dot single-photon sources. *Nat. Nanotechnol.*, 12(11):1026–1039, nov 2017.
- [170] V. Giesz, S. L. Portalupi, T. Grange, C. Antón, L. De Santis, J. Demory, N. Somaschi, I. Sagnes, A. Lemaître, L. Lanco, A. Auffèves, and P. Senellart. Cavity-enhanced two-photon interference using remote quantum dot sources. *Phys. Rev. B*, 92(16):161302, oct 2015.
- [171] Hans Mueller. Memorandum on the polarization optics of the photoelastic shutter. *Report of the OSRD project OEMsr-576*, 2, 1943.
- [172] José Jorge Gil and Eusebio Bernabeu. Obtainment of the polarizing and retardation parameters of a non-depolarizing optical system from the polar decomposition of its mueller matrix. *Optik*, 76:67–71, 1986.
- [173] Shih-Yau Lu and Russell A. Chipman. Homogeneous and inhomogeneous jones matrices. *J. Opt. Soc. Amer. A*, 11(2):766, feb 1994.
- [174] Shih-Yau Lu and Russell A. Chipman. Interpretation of mueller matrices based on polar decomposition. *J. Opt. Soc. Amer. A*, 13(5):1106, may 1996.
- [175] Shane R. Cloude. Group theory and polarisation algebra. *Optik*, 75:26–36, 1986.
- [176] Zhang-Fan Xing. On the deterministic and non-deterministic mueller matrix. *J. Modern Opt.*, 39(3):461–484, mar 1992.
- [177] R. Sridhar and R. Simon. Normal form for mueller matrices in polarization optics. *J. Modern Opt.*, 41(10):1903–1915, oct 1994.
- [178] A. L. Fymat. Jones’s matrix representation of optical instruments i: Beam splitters. *Appl. Opt.*, 10(11):2499, nov 1971.

- [179] Qiang Zhang Yu'ao Chen. Transformation of optical state through linear systems. *College Physics*, 22(6):39, 2003.
- [180] Adriano Barenco, Charles H. Bennett, Richard Cleve, David P. DiVincenzo, Norman Margolus, Peter Shor, Tycho Sleator, John A. Smolin, and Harald Weinfurter. Elementary gates for quantum computation. *Phys. Rev. A*, 52(5):3457–3467, nov 1995.
- [181] J. Broida. Identical particles, 2009.
- [182] GREGOR Weihs and ANTON Zeilinger. Photon statistics at beam-splitters: an essential tool in quantum information and teleportation. *Coherence and Statistics of Photons and Atoms*, pages 262–288, 2001.
- [183] C. H. Holbrow, E. Galvez, and M. E. Parks. Photon quantum mechanics and beam splitters. *Amer. J. Phys.*, 70(3):260–265, mar 2002.
- [184] E. Megidish, A. Halevy, T. Shacham, T. Dvir, L. Dovrat, and H. S. Eisenberg. Entanglement swapping between photons that have never coexisted. *Phys. Rev. Lett.*, 110(21):210403, may 2013.
- [185] Michael Zopf, Robert Keil, Yan Chen, Jingzhong Yang, Disheng Chen, Fei Ding, and Oliver G. Schmidt. Entanglement swapping with semiconductor-generated photons violates bell's inequality. *Phys. Rev. Lett.*, 123(16):160502, oct 2019.
- [186] Hartmut Michael Zopf. *Semiconductor-generated entangled photons for hybrid quantum networks*. phdthesis, Chemnitz, Technische Universität Chemnitz, 2020, 2020.
- [187] R. N. Hall, G. E. Fenner, J. D. Kingsley, T. J. Soltys, and R. O. Carlson. Coherent light emission from GaAs junctions. *Phys. Rev. Lett.*, 9(9):366–368, nov 1962.
- [188] H. Kroemer. A proposed class of hetero-junction injection lasers. *Proceedings of the IEEE*, 51(12):1782–1783, dec 1963.
- [189] Ivars Melngailis. LONGITUDINAL INJECTION-PLASMA LASER OF InSb. *Appl. Phys. Lett.*, 6(3):59–60, feb 1965.
- [190] Haruhisa Soda, Ken ichi Iga, Chiyuki Kitahara, and Yasuharu Suematsu. GaInAsP/InP surface emitting injection lasers. *Jpn. J. Appl. Phys.*, 18(12):2329–2330, dec 1979.
- [191] Xing Ding, Yu He, Z.-C. Duan, Niels Gregersen, M.-C. Chen, S. Unsleber, S. Maier, Christian Schneider, Martin Kamp, Sven Höfling, Chao-Yang Lu, and Jian-Wei Pan. On-demand single photons with high extraction efficiency and near-unity indistinguishability from a resonantly driven quantum dot in a micropillar. *Phys. Rev. Lett.*, 116(2):020401, jan 2016.
- [192] C. L. Salter, R. M. Stevenson, I. Farrer, C. A. Nicoll, D. A. Ritchie, and A. J. Shields. An entangled-light-emitting diode. *Nature*, 465(7298):594–597, jun 2010.

- [193] Jonathan P. Dowling. Quantum optical metrology – the lowdown on high-n00n states. *Contemporary Physics*, 49(2):125–143, mar 2008.
- [194] E. Knill, R. Laflamme, and G. J. Milburn. A scheme for efficient quantum computation with linear optics. *Nature*, 409(6816):46–52, jan 2001.
- [195] H. J. Kimble. The quantum internet. *Nature*, 453(7198):1023–1030, jun 2008.
- [196] S. Bose, V. Vedral, and P. L. Knight. Multiparticle generalization of entanglement swapping. *Phys. Rev. A*, 57(2):822–829, feb 1998.
- [197] Y. H. Shih and C. O. Alley. New type of einstein-podolsky-rosen-bohm experiment using pairs of light quanta produced by optical parametric down conversion. *Phys. Rev. Lett.*, 61(26):2921–2924, dec 1988.
- [198] Evan Meyer-Scott, Nidhin Prasannan, Christof Eigner, Viktor Quiring, John M. Donohue, Sonja Barkhofen, and Christine Silberhorn. High-performance source of spectrally pure, polarization entangled photon pairs based on hybrid integrated-bulk optics. *Opt. Express*, 26(25):32475, nov 2018.
- [199] Xi-Lin Wang, Luo-Kan Chen, W. Li, H.-L. Huang, C. Liu, C. Chen, Y.-H. Luo, Z.-E. Su, D. Wu, Z.-D. Li, H. Lu, Y. Hu, X. Jiang, C.-Z. Peng, L. Li, N.-L. Liu, Yu-Ao Chen, Chao-Yang Lu, and Jian-Wei Pan. Experimental ten-photon entanglement. *Phys. Rev. Lett.*, 117(21):210502, nov 2016.
- [200] N. Akopian, N. H. Lindner, E. Poem, Y. Berlatzky, J. Avron, D. Gershoni, B. D. Gerardot, and P. M. Petroff. Entangled photon pairs from semiconductor quantum dots. *Phys. Rev. Lett.*, 96(13):130501, apr 2006.
- [201] Jan-Philipp Jahn, Mathieu Munsch, Lucas Béguin, Andreas V. Kuhlmann, Martina Renggli, Yongheng Huo, Fei Ding, Rinaldo Trotta, Marcus Reindl, Oliver G. Schmidt, Armando Rastelli, Philipp Treutlein, and Richard J. Warburton. An artificial rb atom in a semiconductor with lifetime-limited linewidth. *Phys. Rev. B*, 92(24):245439, dec 2015.
- [202] Daniel Huber, Marcus Reindl, Yongheng Huo, Huiying Huang, Johannes S. Wildmann, Oliver G. Schmidt, Armando Rastelli, and Rinaldo Trotta. Highly indistinguishable and strongly entangled photons from symmetric GaAs quantum dots. *Nat. Commun.*, 8(1), may 2017.
- [203] R. HANBURY BROWN and R. Q. TWISS. A test of a new type of stellar interferometer on sirius. *Nature*, 178(4541):1046–1048, nov 1956.
- [204] Charles Santori, David Fattal, Jelena Vučković, Glenn S. Solomon, and Yoshihisa Yamamoto. Indistinguishable photons from a single-photon device. *Nature*, 419(6907):594–597, oct 2002.

- [205] Jin Liu, Rongbin Su, Yuming Wei, Beimeng Yao, Saimon Filipe Covre da Silva, Ying Yu, Jake Iles-Smith, Kartik Srinivasan, Armando Rastelli, Juntao Li, and Xuehua Wang. A solid-state source of strongly entangled photon pairs with high brightness and indistinguishability. *Nat. Nanotechnol.*, 14(6):586–593, apr 2019.
- [206] M. Anderson, T. Müller, J. Huwer, J. Skiba-Szymanska, A. B. Krysa, R. M. Stevenson, J. Heffernan, D. A. Ritchie, and A. J. Shields. Quantum teleportation using highly coherent emission from telecom c-band quantum dots. *npj Quantum Inf*, 6(1), jan 2020.
- [207] Jingzhong Yang, Michael Zopf, Pengji Li, Nand Lal Sharma, Weijie Nie, Frederik Benthin, Tom Fandrich, Eddy P. Rugeramigabo, Caspar Hopfmann, Robert Keil, Oliver G. Schmidt, and Fei Ding. Statistical limits for entanglement swapping with semiconductor entangled photon sources. *Phys Rev B*, 105(23):235305, jun 2022.
- [208] Anton Zeilinger. Quantum entanglement: A fundamental concept finding its applications. *Phys. Scripta*, T76(1):203, 1998.
- [209] Mihir Pant, Hari Krovi, Don Towsley, Leandros Tassiulas, Liang Jiang, Prithwish Basu, Dirk Englund, and Saikat Guha. Routing entanglement in the quantum internet. *npj Quantum Inf*, 5(1), mar 2019.
- [210] Francesco Basso Basset, Mauro Valeri, Emanuele Rocchia, Valerio Muredda, Davide Poderini, Julia Neuwirth, Nicolò Spagnolo, Michele B. Rota, Gonzalo Carvacho, Fabio Sciarrino, and Rinaldo Trotta. Quantum key distribution with entangled photons generated on demand by a quantum dot. *Sci. Adv.*, 7(12), mar 2021.
- [211] Paul G. Kwiat, Andrew J. Berglund, Joseph B. Altepeter, and Andrew G. White. Experimental verification of decoherence-free subspaces. *Science*, 290(5491):498–501, oct 2000.
- [212] Yichen Zhang, Ziyang Chen, Stefano Pirandola, Xiangyu Wang, Chao Zhou, Binjie Chu, Yijia Zhao, Bingjie Xu, Song Yu, and Hong Guo. Long-distance continuous-variable quantum key distribution over 202.81 km of fiber. *Phys. Rev. Lett.*, 125(1):010502, jun 2020.
- [213] Ulrik L. Andersen, Jonas S. Neergaard-Nielsen, Peter van Loock, and Akira Furusawa. Hybrid discrete- and continuous-variable quantum information. *Nat. Phys.*, 11(9):713–719, sep 2015.
- [214] Danna Rosenberg, Jim W. Harrington, Patrick R. Rice, Philip A. Hiskett, Charles G. Peterson, Richard J. Hughes, Adriana E. Lita, Sae Woo Nam, and Jane E. Nordholt. Long-distance decoy-state quantum key distribution in optical fiber. *Phys. Rev. Lett.*, 98(1):010503, jan 2007.
- [215] R. Ursin, F. Tiefenbacher, T. Schmitt-Manderbach, H. Weier, T. Scheidl, M. Lindenthal, B. Blauensteiner, T. Jennewein, J. Perdigues, P. Trojek, B. Ömer, M. Fürst, M. Meyenburg, J. Rarity, Z. Sodnik, C. Barbieri, H. Weinfurter, and A. Zeilinger. Entanglement-based quantum communication over 144 km. *Nat. Phys.*, 3(7):481–486, jun 2007.

- [216] Hui Wang, Yu-Ming He, T.-H. Chung, Hai Hu, Ying Yu, Si Chen, Xing Ding, M.-C. Chen, Jian Qin, Xiaoxia Yang, Run-Ze Liu, Z.-C. Duan, J.-P. Li, S. Gerhardt, K. Winkler, J. Jurkat, Lin-Jun Wang, Niels Gregersen, Yong-Heng Huo, Qing Dai, Siyuan Yu, Sven Höfling, Chao-Yang Lu, and Jian-Wei Pan. Towards optimal single-photon sources from polarized microcavities. *Nat. Photonics*, 13(11):770–775, aug 2019.
- [217] I. Schwartz, D. Cogan, E. R. Schmidgall, Y. Don, L. Gantz, O. Kenneth, N. H. Lindner, and D. Gershoni. Deterministic generation of a cluster state of entangled photons. *Science*, 354(6311):434–437, sep 2016.
- [218] Peter Loock, Wolfgang Alt, Christoph Becher, Oliver Benson, Holger Boche, Christian Deppe, Jürgen Eschner, Sven Höfling, Dieter Meschede, Peter Michler, Frank Schmidt, and Harald Weinfurter. Extending quantum links: Modules for fiber- and memory-based quantum repeaters. *Adv. Quantum Technol.*, 3(11):1900141, oct 2020.
- [219] Michele Beniamino Rota, Francesco Basso Basset, Davide Tedeschi, and Rinaldo Trotta. Entanglement teleportation with photons from quantum dots: towards a solid-state based quantum network. *IEEE J. of Sel. Top. Quantum Electron.*, pages 1–1, 2020.
- [220] Jingzhong Yang, Cornelius Nawrath, Robert Keil, Raphael Joos, Xi Zhang, Bianca Höfer, Yan Chen, Michael Zopf, Michael Jetter, Simone Luca Portalupi, Fei Ding, Peter Michler, and Oliver G. Schmidt. Quantum dot-based broadband optical antenna for efficient extraction of single photons in the telecom o-band. *Opt. Express*, 28(13):19457, jun 2020.
- [221] Jonas H. Weber, Benjamin Kambs, Jan Kettler, Simon Kern, Julian Maisch, Hüseyin Vural, Michael Jetter, Simone L. Portalupi, Christoph Becher, and Peter Michler. Two-photon interference in the telecom c-band after frequency conversion of photons from remote quantum emitters. *Nat. Nanotechnol.*, 14(1):23–26, oct 2018.
- [222] H. Ollivier, S. E. Thomas, S. C. Wein, I. Maillette de Buy Wenniger, N. Coste, J. C. Loredó, N. Somaschi, A. Harouri, A. Lemaitre, I. Sagnes, L. Lanco, C. Simon, C. Anton, O. Krebs, and P. Senellart. Hong-ou-mandel interference with imperfect single photon sources. *Phys. Rev. Lett.*, 126(6):063602, feb 2021.
- [223] Caspar Hopfmann, Nand Lal Sharma, Weijie Nie, Robert Keil, Fei Ding, and Oliver G. Schmidt. Heralded preparation of spin qubits in droplet-etched GaAs quantum dots using quasiresonant excitation. *Phys. Rev. B*, 104(7):075301, aug 2021.
- [224] Klaus D. Jöns, Katarina Stensson, Marcus Reindl, Marcin Swillo, Yongheng Huo, Val Zwiller, Armando Rastelli, Rinaldo Trotta, and Gunnar Björk. Two-photon interference from two blinking quantum emitters. *Phys. Rev. B*, 96(7):075430, aug 2017.
- [225] F. Basso Basset, M. B. Rota, C. Schimpf, D. Tedeschi, K. D. Zeuner, S. F. Covre da Silva, M. Reindl, V. Zwiller, K. D. Jöns, A. Rastelli, and R. Trotta. Entanglement swapping with photons generated on demand by a quantum dot. *Phys. Rev. Lett.*, 123(16):160501, oct 2019.

- [226] Liang Zhai, Matthias C. Löbl, Giang N. Nguyen, Julian Ritzmann, Alisa Javadi, Clemens Spinnler, Andreas D. Wieck, Arne Ludwig, and Richard J. Warburton. Low-noise GaAs quantum dots for quantum photonics. *Nat. Commun.*, 11(1), sep 2020.
- [227] Julia Neuwirth, Francesco Basso Basset, Michele B Rota, Emanuele Roccia, Christian Schimpf, Klaus D Jöns, Armando Rastelli, and Rinaldo Trotta. Quantum dot technology for quantum repeaters: from entangled photon generation toward the integration with quantum memories. *Mater. Quantum Technol.*, 1(4):043001, dec 2021.
- [228] Xiang-Bin Wang, Cheng-Xi Yang, and Yan-Bing Liu. On-demand entanglement source with polarization-dependent frequency shift. *Appl. Phys. Lett.*, 96(20):201103, may 2010.
- [229] Hui Wang, Hai Hu, T.-H. Chung, Jian Qin, Xiaoxia Yang, J.-P. Li, R.-Z. Liu, H.-S. Zhong, Y.-M. He, Xing Ding, Y.-H. Deng, Qing Dai, Y.-H. Huo, Sven Höfling, Chao-Yang Lu, and Jian-Wei Pan. On-demand semiconductor source of entangled photons which simultaneously has high fidelity, efficiency, and indistinguishability. *Phys. Rev. Lett.*, 122(11):113602, mar 2019.
- [230] Lucas Schweickert, Klaus D. Jöns, Katharina D. Zeuner, Saimon Filipe Covre da Silva, Huiying Huang, Thomas Lettner, Marcus Reindl, Julien Zichi, Rinaldo Trotta, Armando Rastelli, and Val Zwiller. On-demand generation of background-free single photons from a solid-state source. *Appl. Phys. Lett.*, 112(9):093106, feb 2018.
- [231] Chao Zhang, Yun-Feng Huang, Cheng-Jie Zhang, Jian Wang, Bi-Heng Liu, Chuan-Feng Li, and Guang-Can Guo. Generation and applications of an ultrahigh-fidelity four-photon greenberger-horne-zeilinger state. *Opt. Express*, 24(24):27059, nov 2016.
- [232] Je-Hyung Kim, Tao Cai, Christopher J. K. Richardson, Richard P. Leavitt, and Edo Waks. Two-photon interference from a bright single-photon source at telecom wavelengths. *Optica*, 3(6):577, jun 2016.
- [233] J. Huwer, R. M. Stevenson, J. Skiba-Szymanska, M. B. Ward, A. J. Shields, M. Felle, I. Farrer, D. A. Ritchie, and R. V. Penty. Quantum-dot-based telecommunication-wavelength quantum relay. *Phys. Rev. Applied*, 8(2):024007, aug 2017.
- [234] Marc Sartison, Lena Engel, Sascha Kolatschek, Fabian Olbrich, Cornelius Nawrath, Stefan Hepp, Michael Jetter, Peter Michler, and Simone Luca Portalupi. Deterministic integration and optical characterization of telecom o-band quantum dots embedded into wet-chemically etched gaussian-shaped microlenses. *Appl. Phys. Lett.*, 113(3):032103, jul 2018.
- [235] Ł. Dusanowski, P. Holewa, A. Maryński, A. Musiał, T. Heuser, N. Srocka, D. Quandt, A. Strittmatter, S. Rodt, J. Misiewicz, S. Reitzenstein, and G. Sek. Triggered high-purity telecom-wavelength single-photon generation from p-shell-driven InGaAs/GaAs quantum dot. *Opt. Express*, 25(25):31122, nov 2017.

- [236] Ze-Sheng Chen, Ben Ma, Xiang-Jun Shang, Hai-Qiao Ni, Jin-Liang Wang, and Zhi-Chuan Niu. Bright single-photon source at $1.3 \mu\text{m}$ based on InAs bilayer quantum dot in micropillar. *Nanoscale Res Lett*, 12(1), may 2017.
- [237] M. B. Ward, O. Z. Karimov, D. C. Unitt, Z. L. Yuan, P. See, D. G. Gevaux, A. J. Shields, P. Atkinson, and D. A. Ritchie. On-demand single-photon source for $1.3\mu\text{m}$ telecom fiber. *Appl. Phys. Lett.*, 86(20):201111, may 2005.
- [238] T. Miyazawa, K. Takemoto, Y. Nambu, S. Miki, T. Yamashita, H. Terai, M. Fujiwara, M. Sasaki, Y. Sakuma, M. Takatsu, T. Yamamoto, and Y. Arakawa. Single-photon emission at $1.5 \mu\text{m}$ from an InAs/InP quantum dot with highly suppressed multi-photon emission probabilities. *Appl. Phys. Lett.*, 109(13):132106, sep 2016.
- [239] Matthias Paul, Fabian Olbrich, Jonatan Höschel, Susanne Schreier, Jan Kettler, Simone Luca Portalupi, Michael Jetter, and Peter Michler. Single-photon emission at $1.55 \mu\text{m}$ from MOVPE-grown InAs quantum dots on InGaAs/GaAs metamorphic buffers. *Appl. Phys. Lett.*, 111(3):033102, jul 2017.
- [240] Fabian Olbrich, Jonatan Höschel, Markus Müller, Jan Kettler, Simone Luca Portalupi, Matthias Paul, Michael Jetter, and Peter Michler. Polarization-entangled photons from an InGaAs-based quantum dot emitting in the telecom c-band. *Appl. Phys. Lett.*, 111(13):133106, sep 2017.
- [241] T. Müller, J. Skiba-Szymanska, A. B. Krysa, J. Huwer, M. Felle, M. Anderson, R. M. Stevenson, J. Heffernan, D. A. Ritchie, and A. J. Shields. A quantum light-emitting diode for the standard telecom window around $1,550 \text{ nm}$. *Nat. Commun.*, 9(1), feb 2018.
- [242] M. Benyoucef, M. Yacob, J. P. Reithmaier, J. Kettler, and P. Michler. Telecom-wavelength ($1.5 \mu\text{m}$) single-photon emission from InP-based quantum dots. *Appl. Phys. Lett.*, 103(16):162101, oct 2013.
- [243] Katharina D. Zeuner, Klaus D. Jöns, Lucas Schweickert, Carl Reuterskiöld Hedlund, Carlos Nuñez Lobato, Thomas Lettner, Kai Wang, Samuel Gyger, Eva Schöll, Stephan Steinhauer, Mattias Hammar, and Val Zwiller. On-demand generation of entangled photon pairs in the telecom c-band with InAs quantum dots. *ACS Photonics*, 8(8):2337–2344, jul 2021.
- [244] G. P. Agrawal. *Fiber-optic communication systems*. Wiley, Hoboken, N.J, 2010.
- [245] A. Beveratos, S. Kühn, R. Brouri, T. Gacoin, J.-P. Poizat, and P. Grangier. Room temperature stable single-photon source. *The European Physical Journal D - Atomic, Molecular and Optical Physics*, 18(2):191–196, feb 2002.
- [246] J. P. Hadden, J. P. Harrison, A. C. Stanley-Clarke, L. Marseglia, Y.-L. D. Ho, B. R. Patton, J. L. O'Brien, and J. G. Rarity. Strongly enhanced photon collection from diamond

- defect centers under microfabricated integrated solid immersion lenses. *Appl. Phys. Lett.*, 97(24):241901, dec 2010.
- [247] O. Gazzano, S. Michaelis de Vasconcellos, C. Arnold, A. Nowak, E. Galopin, I. Sagnes, L. Lanco, A. Lemaître, and P. Senellart. Bright solid-state sources of indistinguishable single photons. *Nat. Commun.*, 4(1), feb 2013.
- [248] Sebastian Unsleber, Yu-Ming He, Stefan Gerhardt, Sebastian Maier, Chao-Yang Lu, Jian-Wei Pan, Niels Gregersen, Martin Kamp, Christian Schneider, and Sven Höfling. Highly indistinguishable on-demand resonance fluorescence photons from a deterministic quantum dot micropillar device with 74% extraction efficiency. *Opt. Express*, 24(8):8539, apr 2016.
- [249] M. Davanço, M. T. Rakher, D. Schuh, A. Badolato, and K. Srinivasan. A circular dielectric grating for vertical extraction of single quantum dot emission. *Appl. Phys. Lett.*, 99(4):041102, jul 2011.
- [250] Luca Sapienza, Marcelo Davanço, Antonio Badolato, and Kartik Srinivasan. Nanoscale optical positioning of single quantum dots for bright and pure single-photon emission. *Nat. Commun.*, 6(1), jul 2015.
- [251] Joël Bleuse, Julien Claudon, Megan Creasey, Nitin. S. Malik, Jean-Michel Gérard, Ivan Maksymov, Jean-Paul Hugonin, and Philippe Lalanne. Inhibition, enhancement, and control of spontaneous emission in photonic nanowires. *Phys. Rev. Lett.*, 106(10):103601, mar 2011.
- [252] Michael E. Reimer, Gabriele Bulgarini, Nika Akopian, Moïra Hocevar, Maaike Bouwes Bavinck, Marcel A. Verheijen, Erik P.A.M. Bakkers, Leo P. Kouwenhoven, and Val Zwiller. Bright single-photon sources in bottom-up tailored nanowires. *Nat. Commun.*, 3(1), jan 2012.
- [253] Xue-Wen Chen, Stephan Götzinger, and Vahid Sandoghdar. 99% efficiency in collecting photons from a single emitter. *Opt. Lett.*, 36(18):3545, sep 2011.
- [254] A. Schlehahn, M. Gaafar, M. Vaupel, M. Gschrey, P. Schnauber, J.-H. Schulze, S. Rodt, A. Strittmatter, W. Stolz, A. Rahimi-Iman, T. Heindel, M. Koch, and S. Reitzenstein. Single-photon emission at a rate of 143 MHz from a deterministic quantum-dot microlens triggered by a mode-locked vertical-external-cavity surface-emitting laser. *Appl. Phys. Lett.*, 107(4):041105, jul 2015.
- [255] M. Gschrey, A. Thoma, P. Schnauber, M. Seifried, R. Schmidt, B. Wohlfeil, L. Krüger, J. H. Schulze, T. Heindel, S. Burger, F. Schmidt, A. Strittmatter, S. Rodt, and S. Reitzenstein. Highly indistinguishable photons from deterministic quantum-dot microlenses utilizing three-dimensional in situ electron-beam lithography. *Nat. Commun.*, 6(1), jul 2015.

- [256] Sergii Morozov, Michele Gaio, Stefan A. Maier, and Riccardo Sapienza. Metal–dielectric parabolic antenna for directing single photons. *Nano Lett.*, 18(5):3060–3065, mar 2018.
- [257] Hossam Galal and Mario Agio. Highly efficient light extraction and directional emission from large refractive-index materials with a planar yagi-uda antenna. *Opt. Mater. Express*, 7(5):1634, apr 2017.
- [258] F. Bigourdan, F. Marquier, J.-P. Hugonin, and J.-J. Greffet. Design of highly efficient metallo-dielectric patch antennas for single-photon emission. *Opt. Express*, 22(3):2337, jan 2014.
- [259] A. Dousse, L. Lanco, J. Suffczyński, E. Semenova, A. Miard, A. Lemaître, I. Sagnes, C. Roblin, J. Bloch, and P. Senellart. Controlled light-matter coupling for a single quantum dot embedded in a pillar microcavity using far-field optical lithography. *Phys. Rev. Lett.*, 101(26):267404, dec 2008.
- [260] S. Ates, L. Sapienza, M. Davanco, A. Badolato, and K. Srinivasan. Bright single-photon emission from a quantum dot in a circular bragg grating microcavity. *IEEE J. of Sel. Top. Quantum Electron.*, 18(6):1711–1721, nov 2012.
- [261] Sofiane Haffouz, Katharina D. Zeuner, Dan Dalacu, Philip J. Poole, Jean Lapointe, Daniel Poitras, Khaled Mnaymneh, Xiaohua Wu, Martin Couillard, Marek Korkusinski, Eva Schöll, Klaus D. Jöns, Valery Zwiller, and Robin L. Williams. Bright single InAsP quantum dots at telecom wavelengths in position-controlled InP nanowires: The role of the photonic waveguide. *Nano Lett.*, 18(5):3047–3052, apr 2018.
- [262] Hüseyin Vural, Simone L. Portalupi, Julian Maisch, Simon Kern, Jonas H. Weber, Michael Jetter, Jörg Wrachtrup, Robert Löw, Ilja Gerhardt, and Peter Michler. Two-photon interference in an atom–quantum dot hybrid system. *Optica*, 5(4):367, mar 2018.
- [263] N. Srocka, A. Musiał, P.-I. Schneider, P. Mrowiński, P. Holewa, S. Burger, D. Quandt, A. Strittmatter, S. Rodt, S. Reitzenstein, and G. Şek. Enhanced photon-extraction efficiency from InGaAs/GaAs quantum dots in deterministic photonic structures at 1.3 μm fabricated by in-situ electron-beam lithography. *AIP Adv.*, 8(8):085205, aug 2018.
- [264] Matthias Paul, Jan Kettler, Katharina Zeuner, Caterina Clausen, Michael Jetter, and Peter Michler. Metal-organic vapor-phase epitaxy-grown ultra-low density InGaAs/GaAs quantum dots exhibiting cascaded single-photon emission at 1.3 μm . *Appl. Phys. Lett.*, 106(12):122105, mar 2015.
- [265] B. Höfer, F. Olbrich, J. Kettler, M. Paul, J. Höschele, M. Jetter, S. L. Portalupi, F. Ding, P. Michler, and O. G. Schmidt. Tuning emission energy and fine structure splitting in quantum dots emitting in the telecom o-band. *AIP Adv.*, 9(8):085112, aug 2019.
- [266] Sadao Adachi. Optical dispersion relations for GaP, GaAs, GaSb, InP, InAs, InSb, $\text{Al}_x\text{Ga}_{1-x}\text{As}$, and $\text{In}_{1-x}\text{Ga}_x\text{As}_y\text{P}_{1-y}$. *J. Appl. Phys.*, 66(12):6030–6040, dec 1989.

- [267] Jingzhong Yang, Taisheng Wang, Zuolong Chen, Bingliang Hu, and Weixing Yu. Super-resolution imaging at mid-infrared waveband in graphene-nanocavity formed on meta-surface. *Sci. Rep.*, 6(1), nov 2016.
- [268] Jan Kettler, Matthias Paul, Fabian Olbrich, Katharina Zeuner, Michael Jetter, and Peter Michler. Single-photon and photon pair emission from MOVPE-grown In(Ga)As quantum dots: shifting the emission wavelength from 1.0 to 1.3 μm . *Appl. Phys. B*, 122(3), mar 2016.
- [269] Jan Kettler, Matthias Paul, Fabian Olbrich, Katharina Zeuner, Michael Jetter, Peter Michler, Matthias Florian, Christian Carmesin, and Frank Jahnke. Neutral and charged biexciton-exciton cascade in near-telecom-wavelength quantum dots. *Phys. Rev. B*, 94(4):045303, jul 2016.
- [270] Thomas Aichele, Valéry Zwiller, and Oliver Benson. Visible single-photon generation from semiconductor quantum dots. *New J. Phys.*, 6:90–90, jul 2004.
- [271] P. A. Dalgarno, J. McFarlane, D. Brunner, R. W. Lambert, B. D. Gerardot, R. J. Warburton, K. Karrai, A. Badolato, and P. M. Petroff. Hole recapture limited single photon generation from a single n-type charge-tunable quantum dot. *Appl. Phys. Lett.*, 92(19):193103, may 2008.
- [272] Hidekazu Kumano, Takumi Harada, Ikuo Suemune, Hideaki Nakajima, Takashi Kuroda, Takaaki Mano, Kazuaki Sakoda, Satoru Odashima, and Hirotaka Sasakura. Stable and efficient collection of single photons emitted from a semiconductor quantum dot into a single-mode optical fiber. *Appl. Phys. Express*, 9(3):032801, feb 2016.
- [273] Sarah Fischbach, Alexander Schlehahn, Alexander Thoma, Nicole Srocka, Timo Gissibl, Simon Ristok, Simon Thiele, Arsenty Kaganskiy, André Strittmatter, Tobias Heindel, Sven Rodt, Alois Herkommer, Harald Giessen, and Stephan Reitzenstein. Single quantum dot with microlens and 3d-printed micro-objective as integrated bright single-photon source. *ACS Photonics*, 4(6):1327–1332, jun 2017.
- [274] G. Sallen, A. Tribu, T. Aichele, R. André, L. Besombes, C. Bougerol, M. Richard, S. Tatarenko, K. Kheng, and J.-Ph. Poizat. Subnanosecond spectral diffusion measurement using photon correlation. *Nat. Photonics*, 4(10):696–699, jul 2010.
- [275] Jan Kettler. *Telecom-wavelength nonclassical light from single In(Ga)As quantum dots*. Dr. Hut, München, 2017.
- [276] E. Peter, S. Laurent, J. Bloch, J. Hours, S. Varoutsis, I. Robert-Philip, A. Beveratos, A. Lemaître, A. Cavanna, G. Patriarche, P. Senellart, and D. Martrou. Fast radiative quantum dots: From single to multiple photon emission. *Appl. Phys. Lett.*, 90(22):223118, may 2007.

- [277] P. Michler, A. Imamoglu, M. D. Mason, P. J. Carson, G. F. Strouse, and S. K. Buratto. Quantum correlation among photons from a single quantum dot at room temperature. *Nature*, 406(6799):968–970, aug 2000.
- [278] Matthew Pelton, Charles Santori, Jelena Vučković, Bingyang Zhang, Glenn S. Solomon, Jocelyn Plant, and Yoshihisa Yamamoto. Efficient source of single photons: A single quantum dot in a micropost microcavity. *Phys. Rev. Lett.*, 89(23):233602, nov 2002.
- [279] Jingzhong Yang, Tom Fandrich, Frederik Benthin, Robert Keil, Nand Lal Sharma, Weijie Nie, Caspar Hopfmann, Oliver G. Schmidt, Michael Zopf, and Fei Ding. Photoneutralization of charges in GaAs quantum dot based entangled photon emitters. *Phys. Rev. B*, 105(11):115301, mar 2022.
- [280] Xin Cao, Jingzhong Yang, Pengji Li, Yiteng Zhang, Eddy P. Rugeramigabo, Benedikt Brechtken, Rolf J. Haug, Michael Zopf, and Fei Ding. Single photon emission from ODT passivated near-surface GaAs quantum dots. *Appl. Phys. Lett.*, 118(22):221107, may 2021.
- [281] Xin Cao. *Growth and characterization of epitaxial quantum dots: from visible to telecom wavelength range*. phdthesis, Leibniz University of Hannover, June 2022.
- [282] Hua-Lei Yin, Teng-Yun Chen, Zong-Wen Yu, Hui Liu, Li-Xing You, Yi-Heng Zhou, Si-Jing Chen, Yingqiu Mao, Ming-Qi Huang, Wei-Jun Zhang, Hao Chen, Ming Jun Li, Daniel Nolan, Fei Zhou, Xiao Jiang, Zhen Wang, Qiang Zhang, Xiang-Bin Wang, and Jian-Wei Pan. Measurement-device-independent quantum key distribution over a 404 km optical fiber. *Phys. Rev. Lett.*, 117(19):190501, nov 2016.
- [283] Hui Wang, Jian Qin, Xing Ding, Ming-Cheng Chen, Si Chen, Xiang You, Yu-Ming He, Xiao Jiang, L. You, Z. Wang, C. Schneider, Jelmer J. Renema, Sven Höfling, Chao-Yang Lu, and Jian-Wei Pan. Boson sampling with 20 input photons and a 60-mode interferometer in a 1014 -dimensional hilbert space. *Phys. Rev. Lett.*, 123(25):250503, dec 2019.
- [284] Yu-Hao Deng, Hui Wang, Xing Ding, Z.-C. Duan, Jian Qin, M.-C. Chen, Yu He, Yu-Ming He, Jin-Peng Li, Yu-Huai Li, Li-Chao Peng, E. S. Matekole, Tim Byrnes, C. Schneider, M. Kamp, Da-Wei Wang, Jonathan P. Dowling, Sven Höfling, Chao-Yang Lu, Marlan O. Scully, and Jian-Wei Pan. Quantum interference between light sources separated by 150 million kilometers. *Phys. Rev. Lett.*, 123(8):080401, aug 2019.
- [285] Xiang You, Ming-Yang Zheng, Si Chen, Run-Ze Liu, Jian Qin, M. C. Xu, Z. X. Ge, T. H. Chung, Y. K. Qiao, Y. F. Jiang, H. S. Zhong, M. C. Chen, H. Wang, Y. M. He, X. P. Xie, H. Li, L. X. You, C. Schneider, J. Yin, T. Y. Chen, M. Benyoucef, Yong-Heng Huo, S. Hoefling, Qiang Zhang, Chao-Yang Lu, and Jian-Wei Pan. Quantum interference between independent solid-state single-photon sources separated by 300 km fiber, 2021.
- [286] M. Nirmal, B. O. Dabbousi, M. G. Bawendi, J. J. Macklin, J. K. Trautman, T. D. Harris, and L. E. Brus. Fluorescence intermittency in single cadmium selenide nanocrystals. *Nature*, 383(6603):802–804, oct 1996.

- [287] Alexander L. Efros and David J. Nesbitt. Origin and control of blinking in quantum dots. *Nat. Nanotechnol.*, 11(8):661–671, aug 2016.
- [288] Jacob P. Hoogenboom, Jordi Hernando, Erik M. H. P. van Dijk, Niek F. van Hulst, and Maria F. García-Parajó. Power-law blinking in the fluorescence of single organic molecules. *ChemPhysChem*, 8(6):823–833, apr 2007.
- [289] N. Akopian, L. Wang, A. Rastelli, O. G. Schmidt, and V. Zwiller. Hybrid semiconductor-atomic interface: slowing down single photons from a quantum dot. *Nat. Photonics*, 5(4):230–233, feb 2011.
- [290] Erik Welander, Julia Hildmann, and Guido Burkard. Influence of hyperfine interaction on the entanglement of photons generated by biexciton recombination. *arXiv preprint arXiv:1409.6521*, 2014.
- [291] Y. H. Huo, B. J. Witek, S. Kumar, J. R. Cardenas, J. X. Zhang, N. Akopian, R. Singh, E. Zallo, R. Grifone, D. Kriegner, R. Trotta, F. Ding, J. Stangl, V. Zwiller, G. Bester, A. Rastelli, and O. G. Schmidt. A light-hole exciton in a quantum dot. *Nat. Phys.*, 10(1):46–51, nov 2013.
- [292] C. J. Sandroff, M. S. Hegde, L. A. Farrow, C. C. Chang, and J. P. Harbison. Electronic passivation of GaAs surfaces through the formation of arsenic—sulfur bonds. *Appl. Phys. Lett.*, 54(4):362–364, jan 1989.
- [293] Takahisa Ohno. Sulfur passivation of GaAs surfaces. *Phys. Rev. B*, 44(12):6306–6311, sep 1991.
- [294] Vasily N. Bessolov. Solvent effect on the properties of sulfur passivated GaAs. *Journal of Vacuum Science & Technology B: Microelectronics and Nanometer Structures*, 14(4):2761, jul 1996.
- [295] H. A. Budz and R. R. LaPierre. Properties of octadecanethiol self-assembled monolayers deposited on GaAs from liquid and vapor phases. *Journal of Vacuum Science & Technology A: Vacuum, Surfaces, and Films*, 26(6):1425–1431, nov 2008.
- [296] Qing Yuan, Baolai Liang, Chuan Zhou, Ying Wang, Yingnan Guo, Shufang Wang, Guangsheng Fu, Yuriy I. Mazur, Morgan E. Ware, and Gregory J. Salamo. Interplay effect of temperature and excitation intensity on the photoluminescence characteristics of In-GaAs/GaAs surface quantum dots. *Nanoscale Res Lett*, 13(1), nov 2018.
- [297] Guodong Wang, Baolai Liang, Bor-Chau Juang, Aparna Das, Mukul C Debnath, Diana L Huffaker, Yuriy I Mazur, Morgan E Ware, and Gregory J Salamo. Comparative study of photoluminescence from In_{0.3}Ga_{0.7}As/GaAs surface and buried quantum dots. *Nanotechnology*, 27(46):465701, oct 2016.

- [298] M Schwartzman, V Sidorov, D Ritter, and Y Paz. Surface passivation of (100) InP by organic thiols and polyimide as characterized by steady-state photoluminescence. *Semicond. Sci. Technol.*, 16(10):L68–L71, sep 2001.
- [299] Chao Zhao, Tien Khee Ng, Aditya Prabaswara, Michele Conroy, Shafat Jahangir, Thomas Frost, John O'Connell, Justin D. Holmes, Peter J. Parbrook, Pallab Bhattacharya, and Boon S. Ooi. An enhanced surface passivation effect in InGaN/GaN disk-in-nanowire light emitting diodes for mitigating shockley–read–hall recombination. *Nanoscale*, 7(40):16658–16665, 2015.
- [300] E. Papis-Polakowska, J. Kaniewski, J. Jureńczyk, A. Jasik, K. Czuba, A. E. Walkiewicz, and J. Szade. Surface passivation of (100) GaSb using self-assembled monolayers of long-chain octadecanethiol. *AIP Adv.*, 6(5):055206, may 2016.
- [301] Saimon Filipe Covre da Silva, Gabriel Undeutsch, Barbara Lehner, Santanu Manna, Tobias M. Krieger, Marcus Reindl, Christian Schimpf, Rinaldo Trotta, and Armando Rastelli. GaAs quantum dots grown by droplet etching epitaxy as quantum light sources. *Appl. Phys. Lett.*, 119(12):120502, sep 2021.
- [302] Marcus Reindl, Klaus D. Jöns, Daniel Huber, Christian Schimpf, Yongheng Huo, Val Zwiller, Armando Rastelli, and Rinaldo Trotta. Phonon-assisted two-photon interference from remote quantum emitters. *Nano Lett.*, 17(7):4090–4095, jun 2017.
- [303] Eva Schöll, Lukas Hanschke, Lucas Schweickert, Katharina D. Zeuner, Marcus Reindl, Saimon Filipe Covre da Silva, Thomas Lettner, Rinaldo Trotta, Jonathan J. Finley, Kai Müller, Armando Rastelli, Val Zwiller, and Klaus D. Jöns. Resonance fluorescence of GaAs quantum dots with near-unity photon indistinguishability. *Nano Lett.*, 19(4):2404–2410, mar 2019.
- [304] Marcelo Davanço, C. Stephen Hellberg, Serkan Ates, Antonio Badolato, and Kartik Srinivasan. Multiple time scale blinking in InAs quantum dot single-photon sources. *Phys. Rev. B*, 89(16):161303, apr 2014.
- [305] W.-H. Chang, H.-S. Chang, W.-Y. Chen, T. M. Hsu, T.-P. Hsieh, J.-I. Chyi, and N.-T. Yeh. Optical control of the exciton charge states of single quantum dots via impurity levels. *Phys. Rev. B*, 72(23):233302, dec 2005.
- [306] Y. Benny, Y. Kodriano, E. Poem, S. Khatsevitch, D. Gershoni, and P. M. Petroff. Two-photon photoluminescence excitation spectroscopy of single quantum dots. *Phys. Rev. B*, 84(7):075473, aug 2011.
- [307] M. H. Baier, A. Malko, E. Pelucchi, D. Y. Oberli, and E. Kapon. Quantum-dot exciton dynamics probed by photon-correlation spectroscopy. *Phys. Rev. B*, 73(20):205321, may 2006.

- [308] Zh. M. Wang, B. L. Liang, K. A. Sablon, and G. J. Salamo. Nanoholes fabricated by self-assembled gallium nanodrill on GaAs(100). *Appl. Phys. Lett.*, 90(11):113120, mar 2007.
- [309] Yasuo Nannichi, Jia-Fa Fan, Haruhiro Oigawa, and Atsushi Koma. A model to explain the effective passivation of the GaAs surface by $(NH_4)_2S_x$ treatment. *Jpn. J. Appl. Phys.*, 27(Part 2, No. 12):L2367–L2369, dec 1988.
- [310] R. Heitz, H. Born, F. Guffarth, O. Stier, A. Schliwa, A. Hoffmann, and D. Bimberg. Existence of a phonon bottleneck for excitons in quantum dots. *Phys. Rev. B*, 64(24):241305, nov 2001.
- [311] Marcus Reindl, Daniel Huber, Christian Schimpf, Saimon F. Covre da Silva, Michele B. Rota, Huiying Huang, Val Zwiller, Klaus D. Jöns, Armando Rastelli, and Rinaldo Trotta. All-photonic quantum teleportation using on-demand solid-state quantum emitters. *Sci. Adv.*, 4(12), dec 2018.
- [312] Christian Schimpf, Santanu Manna, Saimon F. Covre da Silva, Maximilian Aigner, and Armando Rastelli. Entanglement-based quantum key distribution with a blinking-free quantum dot operated at a temperature up to 20 k. *Advanced Photonics*, 3(06), dec 2021.
- [313] K. P. O’Donnell and X. Chen. Temperature dependence of semiconductor band gaps. *Appl. Phys. Lett.*, 58(25):2924–2926, jun 1991.
- [314] Paweł Holewa, Marek Burakowski, Anna Musiał, Nicole Srocka, David Quandt, André Strittmatter, Sven Rodt, Stephan Reitzenstein, and Grzegorz Sek. Thermal stability of emission from single InGaAs/GaAs quantum dots at the telecom o-band. *Sci. Rep.*, 10(1), dec 2020.
- [315] Carole Diederichs. *The resonance fluorescence of single semiconductor quantum dots for the generation of indistinguishable photons*. Habilitation à diriger des recherches, Université Pierre et Marie Curie (UPMC), December 2016.
- [316] John Stevenson Mark Osborne. Kung fu panda. Paramount Pictures, 2008. United States.

This page intentionally left blank.

Publications and Presentations

Publications:

- Xin Cao*, **Jingzhong Yang***, Pengji Li, Tom Fandrich, Eddy P. Rugeramigabo, Vlastimil Křápek, Chenxi Ma, Frederik Benthin, Robert Keil, Benedikt Brechtken, Rolf J. Haug, Michael Oestreich, Yiteng Zhang, Constantin Schmidt, Zhao An, Michael Zopf, Fei Ding, “*Surface quantum dots with pure, coherent, and blinking-free single photon emission*”, arXiv:2207.13387v1 (2022)
- **Jingzhong Yang***, Tom Fandrich*, Frederik Benthin*, Robert Keil, Nand Lal Sharma, Weijie Nie, Caspar Hopfmann, Oliver G Schmidt, Michael Zopf, Fei Ding, “*Photo-neutralization of charges in GaAs quantum dot based entangled photon emitters*”, Phys. Rev. B. **105** 115301 (2022)
- **Jingzhong Yang***, Michael Zopf*, Pengji Li*, Nand Lal Sharma, Weijie Nie, Frederik Benthin, Tom Fandrich, Eddy Patrick Rugeramigabo, Caspar Hopfmann, Robert Keil, Oliver G Schmidt, Fei Ding, “*Statistical limits for quantum networks with semiconductor entangled photon sources*”, submitted to Phys. Rev. B. journal
- Weijie Nie, Nand Lal Sharma, Carmen Weigelt, Robert Keil, **Jingzhong Yang**, Fei Ding, Caspar Hopfmann, Oliver G. Schmidt, “*Experimental optimization of the fiber coupling efficiency of GaAs quantum dot-based photon sources*”, Appl. Phys. Lett. **119** 244003 (2021)
- Xin Cao*, **Jingzhong Yang***, Pengji Li*, Yiteng Zhang, Eddy P Rugeramigabo, Benedikt Brechtken, Rolf J Haug, Michael Zopf, Fei Ding, “*Single photon emission from ODT passivated near-surface GaAs quantum dots*”, Appl. Phys. Lett. **118** 221107 (2021)
- **Jingzhong Yang***, Cornelius Nawrath*, Robert Keil, Raphael Joos, Xi Zhang, Bianca Höfer, Yan Chen, Michael Zopf, Michael Jetter, Simone Luca Portalupi, Fei Ding, Peter Michler, Oliver G Schmidt, “*Quantum dot-based broadband optical antenna for efficient extraction of single photons in the telecom O-band*”, Opt. Express. **28** 19457 (2020)
- **Jingzhong Yang**, Michael Zopf, Fei Ding, “*Strain tunable quantum dot based non-classical photon sources*”, J. Semicond. **41** 011901 (2020)

- Michael Zopf, Robert Keil, Yan Chen, **Jingzhong Yang**, Disheng Chen, Fei Ding, Oliver G Schmidt, “*Entanglement Swapping with Semiconductor-generated Photons Violates Bell’s Inequality*”, Phys. Rev. Lett. **123** 160502 (2019)

Scientific talks and posters:

- **Talk:** Deutsche Physikalische Gesellschaft (DPG) Frühjahrstagung der Sektion Kondensierte Materie (SKM). “*Statistical limits for entanglement swapping with independent semiconductor quantum dots*”. Regensburg, Germany. Sep 4th-9th, 2022
- **Talk:** Annual NanoDay of the Laboratory of Nano and Quantum Engineering. “*Development of semiconductor entangled photon sources for quantum networks*”. Hannover, Germany. Sept. 30th, 2021
- **Poster:** The 11th International Conference on Quantum Dots. “*Quantum dot-based broadband optical antenna for efficient extraction of single photons in the telecom O-band*”. Munich, Germany. Dec 7th-11th, 2020
- **Poster:** Annual NanoDay of the Laboratory of Nano and Quantum Engineering. “*Entanglement swapping with semiconductor-generated photons*”. Hannover, Germany. Oct 10th, 2019
- **Poster and talk:** The international school on gravity from earth to space (ISGES). “*Entanglement swapping based on semiconductor-generated photons*”. Urbino, Italy. May 21st-24th, 2019
- **Poster:** Deutsche Physikalische Gesellschaft (DPG) Frühjahrstagung der Sektion Kondensierte Materie (SKM). “*High brightness quantum dot based source of telecom O-band photons*”. Regensburg, Germany. Mar 31st-Apr 5th, 2019

Acknowledgments

The Ph.D. thesis has been conducted under the supervision of Prof. Dr. Fei Ding in the Institute of Solid State Physics at Gottfried Wilhelm Leibniz Universität Hannover. I thank Prof. Fei Ding for allowing me to develop my knowledge of physics and enjoy the pleasure of science. Not only a supervisor, he is also a good friend in life, offering help and trust when I suffered the major depressive disorder.

I thank Prof. Dr. Oliver G. Schmidt for his support in providing me the opportunity to study and work at IFW-Dresden for one and a half years at the beginning of my Ph.D. career.

I particularly thank my colleague Dr. Michael Zopf for his patient instruction during my study. It is very impressive time to have fruitful discussion with him with respect to experiments and theories of physics. Besides, it is also my pleasure to be his friend, receiving enthusiastic reception from his whole family. There are so many impressive moments in participation of the celebration of Christmas with his parents, the family of his sister, and the kids.

I thank Dr. Robert Keil for his responsible supervision and instruction to the labs and mental support with his optimistic attitude for work and life.

I thank all the former colleagues in IFW-Dresden: Bianca Höfer, Dr. Yan Chen, Dr. Xi Zhang, Dr. Yuan Li and Dr. Disheng Chen for their instruction about my major in quantum optics and life during my stay in Dresden. Simultaneously, I would also appreciate the operation instruction and guidance for focused ion beam etching and fabrication techniques from Dr. Baunack and Barbara Eichler, respectively.

A huge thanks to all the former and current colleagues in Leibniz Universität Hannover: Dr. Eddy Patrick Rugeramigabo, Xin Cao, Zhao An, Pengji Li, Taoran Li, Chenxi Ma, Yiteng Zhang, Markus Kromrey, Frederik Benthin, Tom Fandrich, Constantin Schmidt, Zenghui Jiang, Muti Liu, Tao He, Ruolin Guan, Tingting Liang. It is pleasant to spend time with them in the labs, and enjoyed periodic barbecues, hiking activities, parties, etc. during after-work time.

Furthermore, I would also like to thank my former colleagues in the other group of IFW-Dresden for enjoyable basketball time every Saturday at the basketball court behind the institute. The team members are: Jinbo Pang, Yin Yin, Xueyi Lu, Jiawei Wang, Qi Hao and Guodong Li. As

the youngest member, I received plenty of concern from everyone. Additionally, I would also thank Lixiang Liu for her help of providing living help in Dresden.

I would like to express my gratitude to the successive team of Nano-photonics group in IFW-Dresden for the collaboration and discussion. The team members are: Dr. Caspar Hopfmann, Dr. Nand Lal. Sharma, Dr. Weijie Nie.

I would like to thank my collaborators in Universität Stuttgart, in particular Cornelius Nawrath and Dr. Simone Luca Portalupi, for the fruitful discussion of the collaborated telecom O- and C- band projects and experimental time in the labs together.

I would like to give my great thanks to my parents, brother/sister and other relatives for their support, trust and inspiration for all the time.

Po: Maybe I should just quit and go back to make noodles.

Grand Master Oogway: Quit, don't quit. Noodles, don't noodles. [...].

Yesterday is history, tomorrow is a mystery, but today is a gift.

That is why it's called the present.

“Kung Fu Panda”[316]

For everyone who asks receives, and the one who seeks finds, and to the one who knocks it will be opened.

Matthew. 7:7-8. Bible

Thank you very much!

Selbstständigkeitserklärung

Hiermit erkläre ich an Eides statt, dass ich die heute eingereichte Dissertation zum Thema “Development of semiconductor light sources for photonic-enabled quantum communication” unter der Betreuung von Prof. Dr. Fei Ding selbständig angefertigt und verfasst habe. Meine individuellen eigenen Beiträge und die Beiträge weiterer Autoren an den jeweiligen Publikationen im Ergebnisteil der Dissertation sind in der vorangestellten Erklärung korrekt dargelegt. Alle in dieser Dissertation veröffentlichten Ergebnisse und Zitate sind korrekt zitiert worden. Andere als die angegebenen Quellen habe ich nicht benutzt.

Die Dissertation wurde in dieser oder ähnlicher Form an keiner anderen Stelle zum Zwecke eines Promotionsverfahrens eingereicht. Es wurde von mir bisher kein Promotionsverfahren an anderer Stelle beantragt.

Hannover, 25. Mai 2022

Ort, Datum

Unterschrift

This page intentionally left blank.

Curriculum Vitae

Personal information:

Name Jingzhong Yang
Date of Birth 27.09.1991
Place of Birth Liaoning, China
Nationality Chinese

Education:

2017 - present PhD candidate, Semiconductor quantum optics
 Institute of Solid State Physics, Leibniz University of Hannover

2014 - 2017 Master of Natural Science, Optics
 China Changchun Institute of Optics Fine Mechanics and Physics, University of Chinese Academy of Science

2010 - 2014 Bachelor of Science, National base for fostering talents in basic science of Physics
 School of Physical Science and Technology, Lanzhou University